MACHINING DYNAMICS AND STABILITY ANALYSIS IN LONGITUDINAL TURNING INVOLVING WORKPIECE WHIRLING

A Dissertation

by

ACHALA VIOMY DASSANAYAKE

Submitted to the Office of Graduate Studies of
Texas A&M University
in partial fulfillment of the requirements for the degree of

DOCTOR OF PHILOSOPHY

August 2006

Major Subject: Mechanical Engineering

MACHINING DYNAMICS AND STABILITY ANALYSIS IN LONGITUDINAL TURNING INVOLVING WORKPIECE WHIRLING

A Dissertation

by

ACHALA VIOMY DASSANAYAKE

Submitted to the Office of Graduate Studies of
Texas A&M University
in partial fulfillment of the requirements for the degree of

DOCTOR OF PHILOSOPHY

Approved by:

Chair of Committee,	Chii-Der S. Suh
Committee Members,	Suhada Jayasuriya
	Arun Srinivasa
	Andrew K. Chan
Head of Department,	Dennis O'Neal

August 2006

Major Subject: Mechanical Engineering

ABSTRACT

Machining Dynamics and Stability Analysis in Longitudinal Turning

Involving Workpiece Whirling. (August 2006)

Achala Viomy Dassanayake, B.S., University of Peradeniya, Sri Lanka;

M.S., Texas A&M University

Chair of Advisory Committee: Dr. Chii-Der S. Suh

Tool chatter in longitudinal turning is addressed with a new perspective using a complex machining model describing the coupled tool-workpiece dynamics subject to nonlinear regenerative cutting forces, instantaneous depth-of-cut (DOC) and workpiece whirling due to material imbalance. The workpiece is modeled as a system of three rotors: unmachined, being machined and machined, connected by a flexible shaft. The model enables workpiece motions relative to the tool and tool motions relative to the machining surface to be three-dimensionally established as functions of spindle speed, instantaneous DOC, rate of material removal and whirling. Excluding workpiece vibrations from the cutting model is found improper. A rich set of nonlinear behaviors of both the tool and the workpiece including period-doubling bifurcation and chaos signifying the extent of machining instability at various DOCs is observed. Presented numerical results agree favorably with physical experiments reported in the literature. It is found that whirling is non-negligible if the fundamental characteristics of machining dynamics are to be fully understood. The 3D model is explored along with its 1D

counterpart, which considers only tool motions and disregards workpiece vibrations. Numerical simulations reveal diverse behaviors for the 3D coupled and 1D uncoupled equations of motion for the tool. Most notably, observations made with regard to the inconsistency in describing stability limits raise the concern for using 1D models to obtain stability charts.

The nonlinear 3D model is linearized to investigate the implications of applying linear models to the understanding of machining dynamics. Taylor series expansion about the operating point where optimal machining conditions are desired is applied to linearize the model equations of motion. Modifications are also made to the nonlinear tool stiffness term to minimize linearization errors. Numerical experiments demonstrate inadmissible results for the linear model and good agreement with available physical data in describing machining stability and chatter for the nonlinear model. Effects of tool geometry, feed rate, and spindle speed on cutting dynamics are also explored. It is observed that critical DOC increases with increasing spindle speed and small DOCs can induce cutting instability -- two of the results that agree qualitatively well with published experimental data.

ACKNOWLEDGMENTS

I would like to dedicate this dissertation to my beloved mother, Berney Dassanayake, who gave me guidance, love, strength, and encouragement throughout my life. I would not have come this far without the emotional support and love she gave me during the many difficult times of my life. Without the presence of my deceased father, she raised all six of us. Going through multitudes of incomprehensible hardships herself, still she made sure everyone of us receive the best education. I am forever indebted to her for everything she did for me.

I would also like to express my deepest gratitude to my academic advisor, Dr. C. Steve Suh, for his invaluable guidance and support for my doctoral career at Texas A&M. His broad knowledge and encouraging words always provided me the needed enthusiasm in my pursuit of knowledge and research solutions. My special appreciations go to Dr. Suhada Jayasuriya, who as my M.S. thesis advisor guided me through the first two years of my graduate career at the university. His understanding of my capability and interest directed me to the research area that I love.

Finally, I would like to express my sincere gratitude to Dr. Andrew Chan and Dr. Arun Srinivasa for serving as my advisory committee and for teaching me time-frequency analysis and advanced dynamics. The knowledge and attitude I learned from them benefited me greatly in reaching my research goals.

TABLE OF CONTENTS

Page

Page

LIST OF FIGURES

FIGURE Page

FIGURE Page

FIGURE Page

FIGURE Page

FIGURE Page

FIGURE Page

FIGURE Page

FIGURE Page

FIGURE Page

FIGURE Page

LIST OF TABLES

1. INTRODUCTION

1.1 Overview and Literature Review

Machining is one of the most significant operations in manufacturing industry. Machine tool chatter is an instability state commonly seen in machining operation involving material removal. Chatter has been identified as a detrimental problem that adversely impacts machine tool integrity, tool life, surface quality and dimensional precision of final products, thus significantly compromising productivity. Machining dynamics and machine tool chatter has long been studied [1-3]; nevertheless, chatter as a type of undesirable dynamic instability still persists. Stability charts are generated through the wisdoms collected over the years incorporating many factors that affect instability for machining operations in general [3-5] and turning in specific [6-8]. In contrast to conventional stability lobes, a recent literature [9] reported multiple stability regions verifying the low depth-of-cut (DOC) instability found experimentally in [10]. Theoretical investigation done by Kim and Lee [11], which was verified by experimental results, suggests critical width-of-cuts that differ from stability lobes. Ref. [12] used the experimental results along with their own experimental data to validate their theoretical model. However, even setting the suggested ranges of the cutting parameters according

---

This dissertation follows the style and format of the *Journal of Manufacturing Science and Engineering*.

to available stability charts, chatter could still elude one's effort [13]. This seems suggest that one or more factors that truly affects stability in turning process is still unaccounted for in the understanding of machining instability developed so far. Generally speaking, machining dynamics and stability in turning operation are yet to be fully understood.

Most machining operations have two distinct motions: rotary motion and translation that is either straight or curvilinear. In operations such as milling and drilling, the tool undergoes both the motions and, thus, is the only component that vibrates. In turning process, on the other hand, the workpiece has a rotary motion whereas the tool translates linearly. It is obvious that both the tool and workpiece vibrate in the process of material removal. However, through out the years, researchers considered only tool vibration in cutting dynamics [1, 8-11, 14-16]. Exception to the previous, workpiece deflection due to the exertion of 3–D cutting forces and correlated dimensional errors has been recently considered [17, 18]. Machining failures attributable to whirling-induced workpiece vibration are often observed in real world [19]. Tool whirling in line boring operations has also been reported [20]. Both hint at the magnitude of whirling on affecting machining dynamics. However, most published results do not consider whirling resulted from material imbalance of the workpiece. Workpiece vibration affects not only cutting instability but also product surface roughness, hence the quality. Most models developed for surface roughness [21–23] do not consider workpiece vibration, either. Thus it is import that both tool and workpiece vibrations are considered in modeling cutting dynamics.

Regenerative effect, nonlinearity and three-dimensionality are among major factors affecting machining instability. The importance of regeneration process in cutting dynamics has been recognized in the early stage of machining instability research [3, 24]. Since then regenerative effect has been considered as one of the primary factors determining stability in cutting process [10, 14, 25]. Literature review on turning operation shows that the recent trend is indeed in developing nonlinear models [8-10, 12, 14-16, 25-29] for the understanding of machining dynamics. However, many models are of single degree-of-freedom [14, 15, 25] developed to either study the regenerative chatter effects using time-delayed differential equations, explore machining responses using perturbation methods, or investigate the impact phenomenon between the tool and workpiece as a result of regenerative cutting. Of the recent 1-DOF models, the nonlinearity associated with turning operation of multiple cutters is considered in [26]. The nonlinearity caused by random cutting resistance that is due to workpiece material inhomogeneity is investigated in [27]. Among investigations employing 2-DOF models to study machining stability [9, 11, 16, 29], the nonlinearity inherent to the coupled tool-workpiece dynamics is rarely considered. Cutting force nonlinearity was considered in a three-dimensional cutting model presented by Rao and Shin to investigate stability [10]. They like most others did not consider workpiece vibration effect on cutting dynamics.

The importance of considering cutting nonlinearity is discussed in a recent publication [28], in which two nonlinear models are compared and the infeasibility of linearized models is implied. As far back as 1990, a comparison of linear and nonlinear stability performed in [30] observed that, while the vibration amplitude of the linear

version grew infinitely, the chatter amplitude of the nonlinear model was always finite and bounded, thus consistent with observations made in the real-world. Still, literature came along after [30] on the analysis of cutting stability abounds with various linearized models including the types involving linear delay differential equations [31].

Since nonlinearity is recognized as a governing factor in cutting, the use of a good characterization tool to analyze nonlinear signals is also crucial in capturing proper underlying dynamics. Ref. [32] points out that Fourier-based spectral methods are not effective for characterizing nonlinear signals. Also, force analyses performed in [10] using FFT fall short of resolving the inherent characteristics associated with the machining instabilities that were studied. As alternatives to FFT, the discrete wavelet transform is found to be a preferred tool for processing cutting force measurements [33] and the concept of instantaneous frequency [34] is shown to be highly effective for characterizing nonlinear rotor-dynamic responses [35]. Considering the above, the dissertation studies cutting instability using a 3-DOF system model developed to consider: (1) regenerative effect, (2) nonlinearity associated with the cutting force and structure, (3) simultaneous workpiece-tool vibrations, and (4) whirling due to material inhomogeneity of the workpiece. Mass and stiffness reduction of the workpiece due to material removal is also considered. Instantaneous frequency is used as the characterization tool for joint temporal-spectral domain analysis. As a support to the qualitative analysis using instantaneous frequency, quantitative measure of stability is done using the Largest Lyapunov Exponent according to the method developed by Wolf et al., [36] for nonlinear time series.

The next section describes the 3D nonlinear turning model. Nonlinear cutting forces are derived from chip flow angle, chip cross sectional area, normal and friction pressure components, and tool geometry, which are all identified as the main contributors acting in the tool-chip contact zone in material removal [9, 10, 37–40]. Although tool wear has been identified as a significant factor governing cutting forces [41-44], since the model developed in the dissertation simulates only the first 5 seconds of a machining process to study stability, tool geometry is considered unchanged. In the presented model, the chip flow angle is a function of the instantaneous depth-of-cut (DOC) while the normal and friction pressure components are functions of instantaneous chip thickness, which is also called "regenerative process." Modeling of regeneration process requires cautious thinking as there is a fundamental misinterpretation in published literature [25, 45, 46]. Unless it is face turning, regeneration occurs in the tool feed direction that is along the workpiece [47] direction and not in the radial direction. In Refs. [25] and [46], it is not clear if face turning instead of longitudinal turning is modeled. Ref. [45] models longitudinal turning with a long slender workpiece, but the tool is allowed to move radially inwards, thus is the regenerative process. Physically, as is set up in [45], if the tool feeds in radial inward direction by some amount for each revolution of the workpiece, the workpiece will soon be parted off to two pieces and cause a mechanical failure. Realizing this fundamental flaw, all equations presented in the following sections are carefully derived. The workpiece is modeled as a system of three rotors connected by a flexible weightless shaft. Whirling would then occur due to mass imbalance of the workpiece.

Section 3 is dedicated to discussing instantaneous frequency and the largest Lyapunov exponents, the characterization tools used for the research. Examples are given to demonstrate their feasibility. Newmark numerical scheme [48] in conjunction with Newton-Jacobi method [49] is used for solving the model equations. Sections 4 to 10 presents numerically simulated results for various cutting situations. The fourth section compares numerical results with experimental data in [10] for model validation. Considering various DOCs, the importance of modeling cutting dynamics with workpiece motion is also pointed out. This is followed by a section compares 3D and 1D models. The sixth section emphasizes whirling as an important issue in turning with detailed descriptions. Nonlinear and linearized models are compared in Section 7 whereas significance of tool geometry is presented in Section 8. Effect of chip thickness in turning process is comprehensively discussed in Section 9. The tenth section investigates effects of DOC and spindle speed on stability. It presents a stability diagram for a range of spindle speed and DOCs. The final section concludes the obtained results and elaborates the contributions the research has made. The section also suggests future work towards "chatter-free" machining.

1.2 Research Objectives

It is understood from the literature survey that (1) cutting dynamics models developed up to this date all fall short of grasping the underlying dynamics of turning operation and (2) stability charts developed using the models are ineffective in identifying the true stability regions. Despite decades of effort, machine tool chatter remains a major problem in industry. Thus, the objective of the research is to develop a

cutting dynamics model that considers all the essential key effects to fully capture the underlying dynamics associated with material removal and cutting. Realization of the objective will enable the true stability regions to be identified. To achieve the objective, a series of tasks is required:

- Develop a 3-D turning nonlinear dynamic model involving whirling
- Generate time domain response by using a numerical simulation scheme effective for solving coupled nonlinear equations
- Analyze time response data using instantaneous frequency
- Perform time series analysis to obtain the largest Lyapunov exponents (Lyapunov spectrum) to quantify instability
- Compare numerical results for models with and without whirling
- Compare numerical results with available experimental results in literature
- Identify the non-negligible effect of whirling on turning
- Compare numerical results for nonlinear and linearized models and thereby discuss the deficiency for applying linear models
- Establish the significance of developing models that consider simultaneous tool-workpiece vibrations
- Argue the imperative of modeling cutting system 3-dimensionally
- Investigate the effects and ranges of cutting parameters for stable cutting conditions
- Identify multiple stability regions (which will differ from conventional stability regions) through stability analysis

Successful completion of the tasks will help establish the fundamental knowledge of nonlinear cutting dynamics and provide guidelines for developing chatter-free machine tool design concepts for the future.

2. MODEL DESCRIPTION

Lathe turning involves two moving components; namely, the tool and the workpiece. The workpiece has a rotary motion while the tool moves along the spindle axial direction. Consider the workpiece given in Fig. 2.1, which is undergoing longitudinal tuning operation. As a result of the operation, the workpiece has three distinctive sections: unmachined, being machined and machined. In Fig. 2.1, the end of the unmachined section is fixed to the spindle; while the other end is pinned to the tailstock,

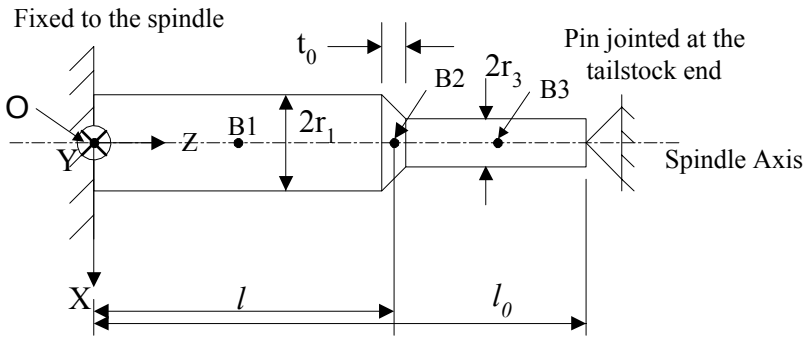

Fig. 2.1 Workpiece setup

where l_0 is the full length of the workpiece, l is a variable measuring the distance from the spindle end to the tool position, t_0 is the chip width in feed per revolution, r_1 is the radius of the unmachined section, and r_3 is the radius of the machined section. Variable l is an independent variable of time, which can be written as

$$l = l_i - \dot{l}\,t \tag{2.1}$$

with $\dot{l}$ being the constant feed rate of the tool and l_i being the value of l at time t = 0. Note that O is the coordinate origin placed at the spindle end of the workpiece, and B1, B2 and B3 are located midway of each section along the spindle axis. For simplicity, the three sections seen in Fig. 2.1 are assumed to be consisted of 3 rotors connected to each other with a shaft of negligible mass as shown in Fig. 2.2. Even though the mass of each section is assumed to act on their individual center of mass, the thickness of each rotor is kept the same as the length of each section.

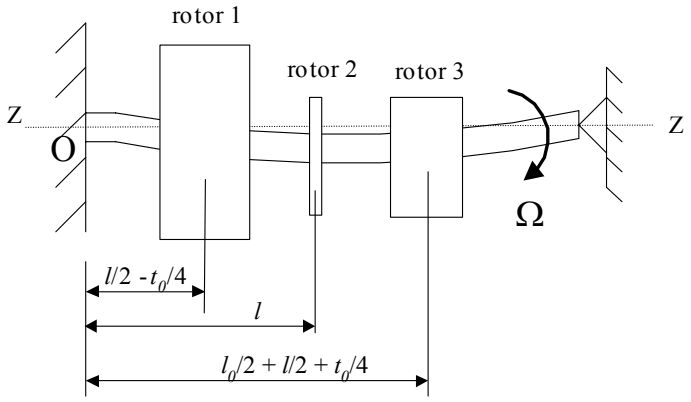

Fig. 2.2 Workpiece modeled as three rotors

Rotor 1 represents the unmachined section having a full length of (l-$t_0/2$) measuring from O. The tool is aligned with the spindle axis, ZZ. Rotor 2, having a thickness of t_0 , represents the section being machined. It is also where the current

position of the tool is. The machined section is represented by Rotor 3, which has a length measuring from ($l + t_0/2$) to l_0. It is also assumed that the rotors are rigid and remain vertical at all time. The configuration of Rotor 2 is not cylindrical and hence the center of mass of the section differs from the other two sections even if there is no deflection. The mass of each rotor can be determined using

$$m_1 = \rho \pi r_1^2 (l - t_0/2) \tag{2.2}$$

$$m_2 = \rho \pi r_3^2 t_0 + \rho \pi r_1 t_0 (r_1 - r_3) \tag{2.3}$$

$$m_3 = \rho \pi r_3^2 (l_0 - l - t_0/2) \tag{2.4}$$

where ρ is the density of the workpiece. Although its section thickness and mass are small compared with those of Rotors 1 and 3, nonetheless, Rotor 2 is where cutting forces exert and a new machined surface is being generated (Fig. 2.4). As such, the response of Rotor 2 dominates the dynamics of the 3-rotor system. In the followings, focus will be placed on Rotor 2 to develop an understanding for machining stability subject to the exertion of cutting force and whirling of the workpiece.

2.1 Accelerations and Velocities of Rotor Centers of Mass

As depicted in Fig. 2.3, Rotor 1 when subjected to a spindle speed, Ω, would see an angle $\alpha = \psi_0 + \Omega t$ (where ψ_0 is the angle between the X-axis and $\overrightarrow{C1G1}$ at t = 0) between the mass center (G1) and the geometric center (C1). Note that parameters ε_1, Ω and ψ_0 are all constants. At rest, C1 coincides with B1. While in motion, C1 has

x_1 and y_1 as its X- and Y-direction components, respectively. If $\overrightarrow{C1G1}$ coincides with the X-axis at t = 0, then $\psi_0 = 0$.

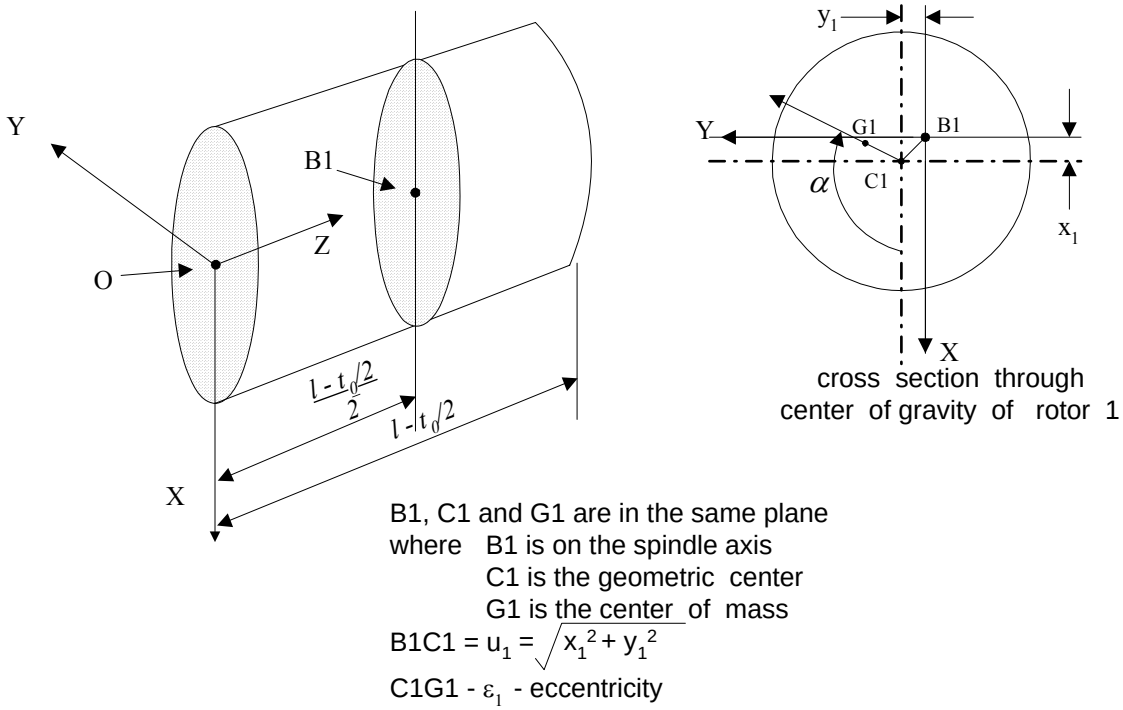

Fig. 2.3 Configuration for Rotor 1

From the figure, the position vector of the center of mass of Rotor 1 is therefore

$$\begin{aligned}\overrightarrow{OG1} &= \overrightarrow{OB1} + \overrightarrow{B1C1} + \overrightarrow{C1G1} \\ &= 1/2(l - t_0/2)\underline{k} + (x_1 + \varepsilon_1 \cos\alpha)\underline{i} + (y_1 + \varepsilon_1 \sin\alpha)\underline{j}\end{aligned} \tag{2.5}$$

By differentiating Eq. 5 once and twice, and collecting terms afterwards, the velocity and acceleration of G1 are then

$$v_1 = (\dot{x}_1 - \varepsilon_1 \Omega \sin \Omega t)\underline{i} + (\dot{y}_1 + \varepsilon_1 \Omega \cos \Omega t)\underline{j} - \frac{\dot{l}}{2}\underline{k} \tag{2.6}$$

$$\underline{a}_1 = (\ddot{x}_1 - \varepsilon_1 \Omega^2 \cos \Omega t)\underline{i} + (\ddot{y}_1 - \varepsilon_1 \Omega^2 \sin \Omega t)\underline{j} \tag{2.7}$$

Note that $\dot{\alpha} = \Omega$ and $\ddot{\alpha} = 0$ for constant spindle speed. Similarly, the velocity and acceleration of the center of mass of Rotor 3 are

$$v_3 = (\dot{x}_3 - \varepsilon_3 \Omega \sin \Omega t)\underline{i} + (\dot{y}_3 + \varepsilon_3 \Omega \cos \Omega t)\underline{j} - \frac{\dot{l}}{2}\underline{k} \tag{2.8}$$

$$\underline{a}_3 = (\ddot{x}_3 - \varepsilon_3 \Omega^2 \cos \Omega t)\underline{i} + (\ddot{y}_3 - \varepsilon_3 \Omega^2 \sin \Omega t)\underline{j} \tag{2.9}$$

Considering the reduction of eccentricity due to material removal, eccentricity is assumed to be proportional to the radius of each section. Thus,

$$\varepsilon_3 = \frac{r_3}{r_1}\varepsilon_1 \tag{2.10}$$

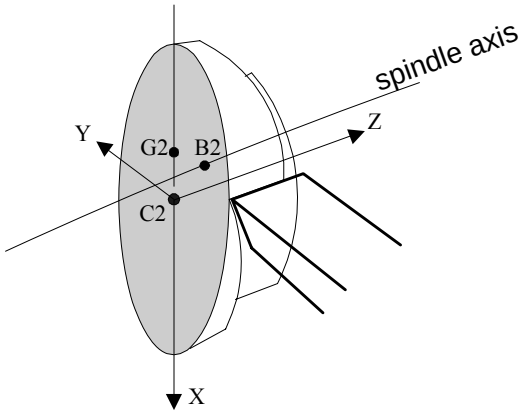

Fig. 2.4 Configuration for Rotor 2

From the shape of Rotor 2 presented in Fig. 2.4, it is understood that even if the material is uniformly distributed, its mass center does not coincide with its geometric center. Hence it is proper to assume that this mass center (which is determined by the shape) dominates the gravitational property of Rotor 2.

Assume that the asymmetric shape of Rotor 2 negates the effect of material inhomogeneity. Since the tool moves toward the spindle end in time, the location of Rotor 2 also changes in time. However, the configuration and orientation of Rotor 2 remain the same at all time. Thus, G2 is always above C2 as shown in Fig. 2.4 and $\overrightarrow{C2G2}$ is always parallel to the X-axis. Then $\overrightarrow{C2G2} = x_2' \underline{i} + y_2' \underline{j}$ and the position vector of the center of mass of Rotor 2, $\overrightarrow{OG2} = (l - t_0/2 + z_2')\underline{k} + x_2' \underline{i} + x_2 \underline{i} + y_2 j + y_2' \underline{j}$, where $x_2' = \dfrac{-r_1(r_1 - r_3)(2r_1 - r_3)}{2\pi(r_3^2 + r_1(r_1 - r_3))}$ = constant, $y_2' = 0$, and $z_2' = \dfrac{t_0}{6}\dfrac{(3r_3^2 + 2r_1^2 - 2r_1 r_3)}{(r_3^2 + r_1^2 - r_1 r_3)}$ = constant. Again, through differentiation and simplification, the acceleration of the center of mass of Rotor 2 becomes

$$\underline{a}_2 = \ddot{x}_2 \underline{i} + \ddot{y}_2 \underline{j} \tag{2.11}$$

Note that with respect to the geometric center, *G2* is fixed, meaning that Rotor 2 undergoes only a curvilinear translation, not a rotation. While the position of Rotor 2 changes continuously with time (as it is a function of *l*), with G2 always holding the same position with respect to C2, Rotor 2 maintains the same shape at all time. Thus, the angular velocity of Rotor 2 is zero. Also note that both the tool and Rotor 2 move towards the spindle end at a constant speed, $\dot{l}$, and that while Rotor 2 has a constant

section thickness, t_0, the thicknesses of Rotors 1 and 3 vary with time. Since all the depth-of-cuts considered in the study are smaller than 6% of the diameter of the cylindrical workpiece, for the purpose of finding the static deflections at certain locations of interest, the workpiece can be assumed to be a uniform shaft with an average diameter, d_{AV}, as

$$d_{AV} = \frac{1}{l_0}\left[d_1(l - t_0/2) + (\frac{d_1 + d_3}{2})t_0 + d_3(l_0 - l + t_0/2) \right] \tag{2.12}$$

where d_1 and d_3 are the diameters of Rotors 1 and 3, respectively. The average area moment of inertia of the shaft is therefore

$$I_{AV} = \frac{\pi\, d_{AV}}{64} \tag{2.13}$$

Consider the shaft as subject to a fixed-pinned boundary condition (Fig. 2.2) and a concentrated load, the static deflection of the center of gravity of each rotor can then be determined as follows [50]. Assume that δ_1, δ_2, and δ_3 are the deflections of Rotors 1, 2 and 3, respectively, and that vibration displacements, u_i, are proportional to static deflections, δ_i. Thus, $\frac{u_1}{\delta_1} = \frac{u_2}{\delta_2} = \frac{u_3}{\delta_3}$ [51]. Note that u_i is also the radial displacement of the center of gravity of Rotor i and the resultant cutting force acting radially on the shaft is the concentrated load. Since gravity is negligible compared to the cutting force, one has $\frac{x_1}{\delta_1} = \frac{x_2}{\delta_2} = \frac{x_3}{\delta_3}$ and $\frac{y_1}{\delta_1} = \frac{y_2}{\delta_2} = \frac{y_3}{\delta_3}$, or equivalently,

$$x_1 = \frac{\delta_1}{\delta_2}x_2\ ,\ \ x_3 = \frac{\delta_3}{\delta_2}x_2\ ,\ y_1 = \frac{\delta_1}{\delta_2}y_2 \text{ and } \ y_3 = \frac{\delta_3}{\delta_2}y_2 \tag{2.14}$$

Note that for particular t_0 and l_0 values, deflections are functions of l, the concentration load and the average area moment of inertia. As deflection ratios are functions of l and l in turn is a function of time, all accelerations $\underline{a}_i$ are also functions of x_2 , y_2 and time. Deflection ratios can then be expressed as

$$\delta_{12} = \frac{\delta_1}{\delta_2} = \frac{\dfrac{l^2}{2l_0^3}[3l_0 - l]\left[\left(l_0 - \dfrac{(l - t_0/2)}{2}\right)^3 - 3l_0^2\left(l_0 - \dfrac{(l - t_0/2)}{2}\right)\right] + 3l^2\left(l_0 - \dfrac{(l - t_0/2)}{2}\right) - \left(l - \dfrac{(l - t_0/2)}{2}\right)}{\dfrac{l^2}{2l_0^3}[3l_0 - l]\left[(l_0 - l)^3 - 3l_0^2(l_0 - l)\right] + 3l^2(l_0 - l)} \tag{2.15}$$

and

$$\delta_{32} = \frac{\delta_3}{\delta_2} = \frac{\dfrac{l^2}{2l_0^3}[3l_0 - l]\left[\left(l_0 - \dfrac{(l_0 - l - t_0/2)}{2}\right)^3 - 3l_0^2\left(l_0 - \dfrac{(l_0 - l - t_0/2)}{2}\right)\right] + 3l^2\left(l_0 - \dfrac{(l_0 - l - t_0/2)}{2}\right) - \left(l - \dfrac{(l_0 - l - t_0/2)}{2}\right)}{\dfrac{l^2}{2l_0^3}[3l_0 - l]\left[(l_0 - l)^3 - 3l_0^2(l_0 - l)\right] + 3l^2(l_0 - l)} \tag{2.16}$$

It should be noted that the reason that concentration load and average area moment of inertia were not explicitly included in Eqs. 2.15 and 2.16 is because they were cancelled out when taking the deflection ratios.

2.2. Forces Acting on Workpiece

Forces acting on the three rotors are considered separately. The forces acting on Rotors 1 and 3 are due to the stiffness of the shaft. Rotor 2 sees three more forces in the *X-*, *Y-*, and *Z*-direction, which together play the role of material removal. The force acting on Rotor 1 due to shaft stiffness is k_1u_1 and its orientation is shown in Fig. 2.5.

Here $u_1 = \overrightarrow{B1C1}$. Consider its component along the *X*- and *Y*-direction, the force acting on Rotor 1 is of the form: $(-k_1 u_1 \cos\theta)\underline{i} - (k_1 u_1 \sin\theta)\underline{j}$.

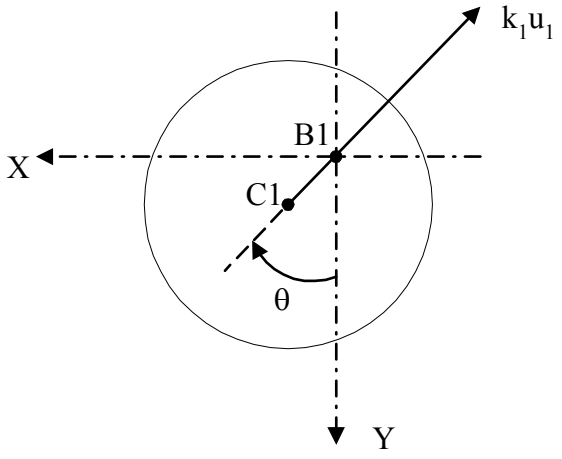

Fig. 2.5 Force acting on Rotor 1

But since $\cos\theta = x_1 / u_1$ and $\sin\theta = y_1 / u_1$, so the force acting on Rotor 1 is therefore

$$(-k_1 x_1)\underline{i} - (k_1 y_1)\underline{j} \tag{2.17}$$

Similarly, the force acting on Rotor 3 is

$$(-k_3 x_3)\underline{i} - (k_3 y_3)\underline{j} \tag{2.18}$$

Other than the forces due to shaft stiffness, a cutting force also acts on Rotor 2.

Referring to Fig. 2.6, Fx, Fy and Fz are three components of the cutting force on Rotor 2 and F_T is the force due to bending stiffness in the *k*-direction. Since the workpiece is not allowed to move along the *Z*-direction, the acceleration of Rotor 2 in the *Z*-direction is therefore zero. In other words, F_T = Fz. As a result, the force acting

on Rotor 2 becomes $(-k_2 u_2 \cos\theta)\underline{i} - (k_2 u_2 \sin\theta)\underline{j} - F_X \underline{i} + F_Y \underline{j}$, which can be further simplified to be

$$(-F_X - k_2 x_2)\underline{i} + (F_Y - k_2 y_2)\underline{j} \tag{2.19}$$

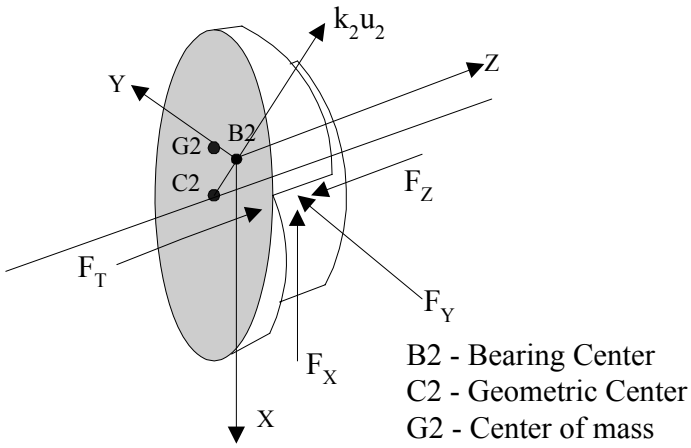

Fig. 2.6 Components of cutting forces acting on Rotor 2

Now applying Newton's 2nd law, $\vec{F} = m\frac{d\underline{v}}{dt} + \underline{v}\frac{dm.}{dt}$, in the *X*- and *Y*-directions and using Eqs. (2.6)-(2.11), (2.17)-(2.19) and the time derivatives of Eqs. (2.2) and (2.4), the following two equations can be obtained:

$$-k_1 x_1 - k_2 x_2 - k_3 x_3 - F_X = m_1 a_{1x} + m_2 a_{2x} + m_3 a_{3x} + v_{1x}\frac{dm_1}{dt} + v_{3x}\frac{dm_3}{dt} \tag{2.20}$$

$$-k_1 y_1 - k_2 y_2 - k_3 y_3 + F_Y = m_1 a_{1y} + m_2 a_{2y} + m_3 a_{3y} + v_{1y}\frac{dm_1}{dt} + v_{3y}\frac{dm_3}{dt} \tag{2.21}$$

Note that the mass of Rotor 2 does not change with time. Let M_Z be the equivalent mass of the machine tool and k_Z and k_{ZC} be the equivalent linear and nonlinear stiffness of the tool in the Z-direction, then the equation of motion for the tool in the *Z*-direction including nonlinear stiffness term can be written as

$$M_Z \ddot{z}_t + k_Z z_t + k_{ZC} z_t^3 = F_Z \tag{2.22}$$

where F_Z is the cutting force component in the *Z*-direction.

2.3. Calculation of Instantaneous Chip Thickness

Consider tool vibrations in the *Z*-direction. In Fig. 2.7 a PQ section of Rotor 2 actively engaging with the tool and showing a flatted outer surface on one side is given, where the lowercase z_t is the relative displacement of the tool at time t , and z'_t is the relative displacement of the tool one revolution before. Then the instantaneous chip width, t_i , can be found to be

$$t_i = t_0 - z_t + z_t^{'} \tag{2.23}$$

From Fig. 2.7 it is understood that the tool is engaged in vibration in the Z-direction only. Note that if the tool does not vibrate, the chip width (chip thickness) is equal to the feed rate [47]. It should be noted that the tool feed direction is along the workpiece. As in [45], any assumption assuming tool feed occurs along the inward radial direction is fundamentally incorrect. (See pages 12 and 13 of [47] for clarifications.) Since the tool is considered infinitely stiff in the X-Y plane and the workpiece is rigidly constrained along the Z-direction, only responses of the tool in the Z-direction and workpiece responses in the X- and Y-directions are considered in the study.

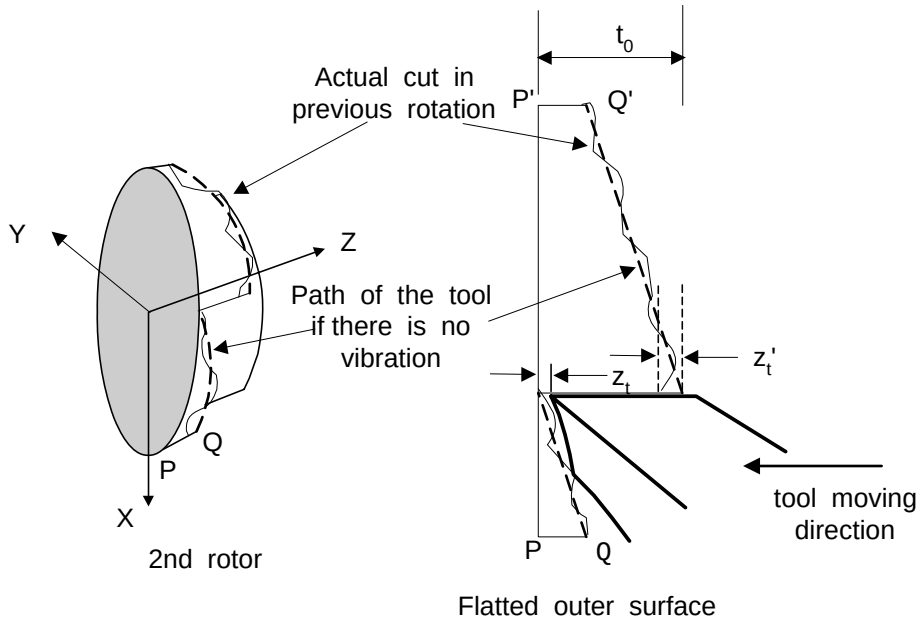

Fig. 2.7 Instantaneous chip width (instantaneous feed per revolution)

2.4. Calculation of Instantaneous Depth-of-Cut

If changes of instantaneous depth-of-cut (DOC) are only affected by the Y-direction vibrations, then DOC = $(r_1 - r_3 - y_2)$. However, X-direction vibrations also contribute to changing the DOC. Fig. 2.8 shows the changes of DOC due to vibration in the X-direction, in which DOC $= \sqrt{r_1^{\,2} - x_2^{\,2}} - r_3$. Therefore, considering vibrations in both the X- and Y-directions, the total instantaneous DOC, *s*, is

$$s = \sqrt{r_1^2 - x_2^2} - r_3 - y_2 \tag{2.24}$$

Note that the side cutting edge angle (lead angle) does not play a role in the instantaneous chip width or instantaneous DOC. But it does affect the chip load and

hence the cutting force. However, corner radius of the tool is not being taken into account in the study as it is much smaller than the DOCs considered herein.

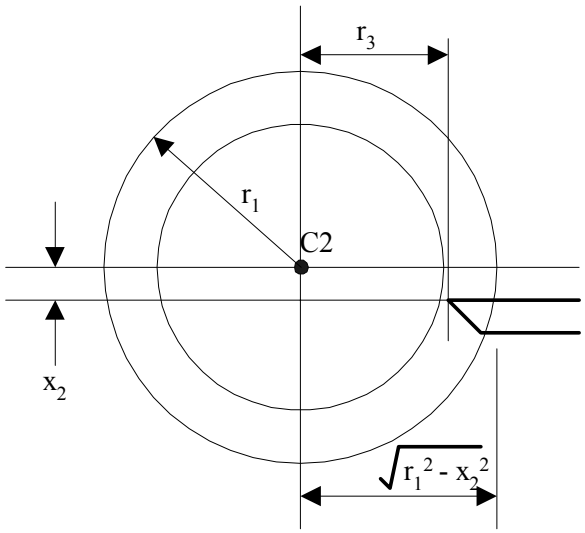

Fig. 2.8 Depth-of-cut affected by vibration along X-direction, where C2 is the geometric center

2.5. Calculation for Cutting Forces

Cutting force components, F_X, F_Y, and F_Z , exerted by the tool can be written in the following form [10],

$$F_X = F_f(b_{x1}\sin(\eta_c) + b_{x2}\cos(\eta_c)) + b_{x3}F_n \tag{2.25}$$

$$F_Y = F_f(b_{y1}\sin(\eta_c) + b_{y2}\cos(\eta_c)) + b_{y3}F_n \tag{2.26}$$

$$F_Z = F_f(b_{z1}\sin(\eta_c) + b_{z2}\cos(\eta_c)) + b_{z3}F_n \tag{2.27}$$

where F_f is the friction force, F_n is the normal force and η_c is the chip flow angle. The constants b_{rm}'s (r = x,y,z and m = 1,2,3) depend on the tool rake angle, side cutting edge angle and inclination angle. In this study, parameter values used in [10] for tool rake angle, side cutting edge angle and inclination angle are adopted for the objective of being able to compare with experimental (physical) data. By using a curve fitting for the experimental result found in [10], the chip flow angle can be formulated as a function of DOC valid for the range of 0.4mm < DOC < 2.5mm. Thus the chip flow angle is

$$\eta_c = \alpha_1 s^3 + \alpha_2 s^2 + \alpha_3 s + \alpha_4 \tag{2.28}$$

Here α_i's are constants. The normal force and the friction force are as follows,

$$F_n = k_n A_C \tag{2.29}$$

$$F_f = k_f A_C \tag{2.30}$$

in which k_n and k_f are normal and friction pressure components, respectively, and the chip cross sectional area, A_C, is defined using the instantaneous chip width, t_i, and the instantaneous DOC, s, as

$$A_C = t_i s \tag{2.31}$$

By substituting Eqs. (2.23) and (2.24) into (2.31), the chip cross sectional area becomes

$$A_C = (t_0 - z_t + z_t')(\sqrt{r_1^2 - x_2^2} - r_3 - y_2) \tag{2.32}$$

In the model presented herein, coefficients k_n and k_f are not constants. But rather they are functions of the instantaneous chip width, t_i. The relationships are modeled as follows

$$k_n = K_{nm} t_i + K_{nn} \tag{2.33}$$

$$k_f = K_{fm} t_i + K_{ff} \tag{2.34}$$

Table 2.1 lists the values along with their units for all *K*'s, which were determined using the experimental data available in [10].

Table 2.1 Various K values

K_{nm}	-6.0E+12	N/m^2
K_{nn}	2.9E+9	N/m^3
K_{fm}	-8.7E+12	N/m^2
K_{ff}	3.0E+9	N/m^3

With the aid of Eqs. (2.23), (2.24), and (2.28)-(2.34), cutting forces F_X, F_Y, and F_Z in Eqs. (2.25) - (2.27) can then be determined.

2.6. Calculation for Stiffness

Consider the shaft as a beam of a circular cross section being fixed to the chuck at one end and pinned to the tail stock at the other end. The stiffness at a particular cross section is $k = \frac{12EIl_0^3}{a^3b^2(3l_0 + b)}$, where *E* is the elastic modulus, *I* is the area moment of inertia, *a* is the length between the cross section considered and the fixed end, *b* is the length between the cross section considered and the pinned end, and l_0 is the length of the beam [52]. Using the same explanation given in Section 2.1, area moment of inertia, *I*, can be replaced with I_{AV} in Eq. (2.13). So the stiffness associated with each rotor is therefore of the form,

$$k_i = \frac{12EI_{AV}l_0^3}{a_{ii}^{\ 3}b_{ii}^{\ 2}(3l_0 + b_{ii})} \tag{2.35}$$

where a_{ii} is the distance between the fixed end and the cross section sliced through the center of gravity of the i-th rotor, and b_{ii} is the distance between the pinned end and the cross section cut through the center of gravity of the i-th rotor.

2.7. Equations of Motion

In order to compute accelerations, Eq. (2.1) is first substituted into Eqs. (2.15) and (2.16). Differentiating the two equations twice and using Eq. (2.14), the relationships between $\ddot{x}_1, \dot{x}_1, \ddot{x}_2, \dot{x}_2, \ddot{x}_3, \dot{x}_3$ and $\ddot{y}_1, \dot{y}_1, \ddot{y}_2, \dot{y}_2, \ddot{y}_3, \dot{y}_3$ can be established. These established relationships can then be substituted into Eqs. (2.6)-(2.9) and (2.11). The five resulted equations, along with Eqs. (2.2)-(2.4) & (2.35) and the derived equations for cutting forces, can then be substituted into Eqs. (2.20)-(2.22) to obtain three equations of motions that are functions of $\ddot{x}_2, \dot{x}_2, x_2, \ddot{y}_2, \dot{y}_2, y_2, \ddot{z}_t, z_t, z_t'$ and time, t, as follows

$$f_1(t)\ddot{x}_2 + f_2(t)\dot{x}_2 + f_3(t)x_2 = f_4(t, x_2, y_2, z_t, z_t') \tag{2.36}$$

$$f_5(t)\ddot{y}_2 + f_6(t)\dot{y}_2 + f_7(t)y_2 = f_8(t, x_2, y_2, z_t, z_t') \tag{2.37}$$

$$M_Z\ddot{z}_t + k_Z z_t + k_{ZC}z_t^{\ 3} = f_9(t, x_2, y_2, z_t, z_t') \tag{2.38}$$

Note that $f_i(t, x_2, y_2, z_t, z_t')$'s are nonlinear functions. Even though $f_j(t)$'s are also nonlinear functions, for a brief time period of the first 2-3 seconds, they behave linearly. Functions f_i*'s* and f_j's in their explicit forms are

$$f_1(t) = f_5(t) = A_2 \tag{2.39}$$

$$f_2(t) = f_6(t) = 2A_3 - A_6 \tag{2.40}$$

$$f_3(t) = f_7(t) = A_4 + A_5 - A_7 \tag{2.41}$$

$$f_4(t, x_2, y_2, z_t, z_t') = A_1\Omega^2 \cos(\Omega t) - A_8\Omega \sin(\Omega t) - F_X \tag{2.42}$$

$$f_8(t, x_2, y_2, z_t, z_t') = A_1\Omega^2 \sin(\Omega t) + A_8\Omega \cos(\Omega t) + F_Y \tag{2.43}$$

$$f_9(t, x_2, y_2, z_t, z_t') = F_Z \tag{2.44}$$

where

$$A_1 = m_1\varepsilon_1 + m_3\varepsilon_3 \tag{2.45}$$

$$A_2 = 2(m_1\delta_{12} + m_2 + m_3\delta_{32}) \tag{2.46}$$

$$A_3 = m_1\dot{\delta}_{12} + m_3\dot{\delta}_{32} \tag{2.47}$$

$$A_4 = m_1\ddot{\delta}_{12} + m_3\ddot{\delta}_{32} \tag{2.48}$$

$$A_5 = k_1\delta_{12} + k_2 + k_3\delta_{32} \tag{2.49}$$

$$A_6 = \pi\rho\dot{l}(r_1^{\,2}\ddot{\delta}_{12} - r_3^{\,2}\ddot{\delta}_{32}) \tag{2.50}$$

$$A_7 = \pi\rho\dot{l}(r_1^{\,2}\dot{\delta}_{12} - r_3^{\,2}\dot{\delta}_{32}) \tag{2.51}$$

$$A_8 = \pi\rho\dot{l}(r_1^{\,2}\varepsilon_1 - r_3^{\,2}\varepsilon_3) \tag{2.52}$$

The above system of equations can be solved using a proper numerical scheme for x_2 , y_2 , z_t and the cutting force components as functions of time. Hence, the system of equations represented by Eqs. (2.36)-(2.52) can be employed to study: (1) the motion of the workpiece relative to the tool in the X- and Y-directions and (2) the tool motion relative to the machining surface in the (spindle) Z-direction, all as functions of the cutting force and whirling. Note that the terms A_4, A_6, A_7, and A_8 are comparably negligible in magnitude. Fig. 2.9 shows that the errors of approximations even for the extreme cases are small enough to be omitted. Thus, in numerical experiments the following approximations are adopted to simplify the system of equations of motion above.

$$(2A_3 - A_6) \approx 2A_3 \tag{2.53}$$

$$(A_5 + A_4 - A_7) \approx A_5 \tag{2.54}$$

$$(A_1\Omega^2\cos(\Omega t) - A_8\Omega\sin(\Omega t)) \approx A_1\Omega^2\cos(\Omega t) \text{ and} \tag{2.55}$$

$$(A_1\Omega^2\sin(\Omega t) + A_8\Omega\cos(\Omega t)) \approx A_1\Omega^2\sin(\Omega t) \tag{2.56}$$

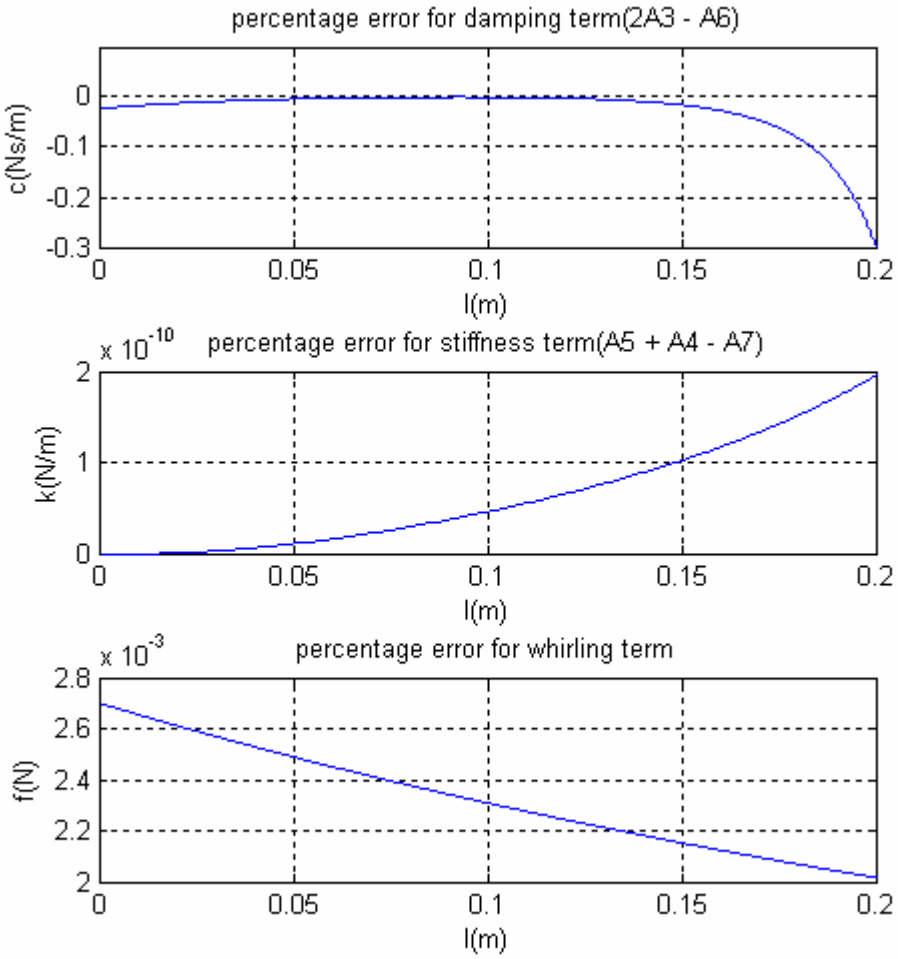

Fig. 2.9 Error diagrams for term approximation

3. CONCEPTS AND FUNDAMENTALS OF CHARACTERIZATION TOOLS

3.1 Fundamentals of Instantaneous Frequency

Fast Fourier Transform (FFT) is a characterization tool commonly used for vibration analysis in manufacturing industry. Fourier spectrum is the representation of a stationary signal in the frequency domain. However, if the signal's amplitude and frequency are modulated with time, Fourier analysis would become ineffective. Despite the fact that machining dynamic response is highly nonlinear with time varying amplitude and frequency, nonetheless, FFT remains popular for spectral domain vibration analysis. The need for resolving the progression of all individual spectral components in time prompted the use of instantaneous frequency for the study.

The fundamental notion of instantaneous frequency was first discussed half a century ago. In 1958, it was defined as a time derivative of a phase of a signal by Ville [53]. Consider a signal in general,

$$x(t) = a(t)\cos(\phi(t)) \tag{3.1}$$

where *a(t)* is amplitude and *Φ(t)* is frequency with one or both of them varying with time. Fourier approach is well defined for the case where both amplitude *a(t)* and frequency *Φ(t)* are constants. Taking the Hilbert transform of the signal, *H(x(t))*, the analytic form of it is,

$$z(t) = x(t) + iH(x(t)) \tag{3.2}$$

This can be rewritten as $z(t) = x(t) + iy(t)$ (3.3)

with $y(t) = H(x(t)) = \frac{p}{\pi} \int_{-\infty}^{\infty} \frac{x(\tau)}{t-\tau} d\tau$. Here the term P is Cauchy principle value. Then instantaneous amplitude *a(t)* and instantaneous phase *Φ(t)* can be expressed as follows

$$a(t) = \sqrt{x^2(t) + y^2(t)} \tag{3.4}$$

$$\phi(t) = \arctan(y(t)/x(t)) \tag{3.5}$$

The analytic function can be written as $z(t) = a(t)\exp i(\phi(t))$. According to Ville, the time derivative of *Φ(t)* is defined as instantaneous frequency:

$$InsFreq = f(t) = \frac{1}{2\pi}\frac{d\phi(t)}{dt} = \frac{1}{2\pi}\frac{d}{dt}(\arctan(x(t)/y(t))) \tag{3.6}$$

The definition works well for mono-component time varying signals, but not for multi-component signals. Since then numerous efforts have been carried out related to instantaneous frequency [35, 54-60]. As a remedy to the problem, Huang et al. [34] came up with a decomposition scheme that separates the individual spectral components from a multi-component signal. The method is called Empirical Mode Decomposition (EMD). It was developed with the assumption that the multi-component signal consists of a number of intrinsic modes of oscillations. Each intrinsic oscillation is called an Intrinsic Mode Function (IMF). IMF has to satisfy two conditions: (i) the number of extrema, the number of zero and the number of zero crossings must be either equal or differ at most by one, and (ii) at any point the mean value of the envelope defined by local minima and the local maxima is zero. Decomposing IMFs can be summarized in several steps as below:

Step 1. Connect all local maxima of the signal (x(t)) by a smooth function, maxfun1(t).

Step 2. Connect all local minima of the signal (x(t)) by a smooth function, minfun1(t).

Step 3. Find the average of maxfun1(t) and minfun1(t):

meanfun1(t) = (maxfun1(t)+minfun1(t))/2

Step 4. Subtract meanfun1(t) from the signal and find the remainder:

remfun1(t) = x(t)-meanfun1(t).

Step 5. Repeat above 4 Steps on remfun1(t) to get meanfun2(t) and remfun2(t) and then do the same procedure to find "remfun" functions 3, 4 and so on until the "n"th "remfun" becomes an IMF that satisfies the conditions mentioned above.

Step 6. Once the first IMF (IMF1(t)) is obtained, subtract it from the original function and get the new signal newx1(t).

Step 7. Repeat this process on newx1(t) to get IMF2(t) and newx2(t) and so on until an IMF cannot be extracted from the newx(t) function. This is called a residue, R(t).

The original signal can be restored by summing all the IMFs and the residue, R(t),

$$x(t) = \sum_{j=1}^{n} IMFj(t) + R(t) \tag{3.7}$$

After performing Hilbert transform on each IMF, the new representation of the analytic function can be expressed as

$$z(t) = \sum_{j=1}^{n} a_j(t) \exp(i \int \phi_j(t) dt) \tag{3.8}$$

There are four distinct cases consist in this function.

1) The mono-component signal has both amplitude modulation (AM) and frequency modulation (FM). In this case none of them is constant.

2) The mono-component signal has time varying amplitude but frequency is a constant. Then the function becomes $z(t) = \sum_{j=1}^{n} a_j(t) \exp(i\phi_j t)$.

3) The mono-component signal has constant amplitude but frequency varies with time. Then the function becomes $z(t) = \sum_{j=1}^{n} a_j \exp(i\int \phi_j(t)dt)$ with constant a_j.

4) Both amplitude and frequency are constants, so that the signal can be represented in Fourier format as $z(t) = \sum_{j=1}^{n} a_j \exp(i\phi_j t)$.

3.2 Examples and Descriptions

This subsection considers some simple examples with amplitude and frequency modulations. In general a signal can be a combination of several mono-components, which can have constant or time-varying amplitude and frequency. Some demonstrative examples are considered to compare FFT and instantaneous frequency. All the figures herein have three plots: (a) time domain history, (b) FFT spectrum, and (c) spectral analysis using instantaneous frequency. Fig. 3.1 is a simple signal of two mono-components with constant amplitude and constant frequency. As seen, both FFT and instantaneous frequency resolve the spectrum of the signal faithfully. A signal having an increasing frequency in time is shown in Fig 3.2. While the FFT shows a broadband behavior having many frequency components up to 40Hz, the corresponding instantaneous frequency plot resolves a time-increasing frequency. Moreover, Fig 3.3 shows that when signal frequency increases and decreases with time, instantaneous frequency again provides better resolution than does FFT, where unsatisfactory,

erroneous results are seen. Fig. 3.4 shows a signal with both amplitude and frequency modulation. Once again instantaneous frequency demonstrates that it is a preferred characterization tool over FFT.

A period doubling bifurcation is shown in Fig. 3.5. Up till 0.5 seconds, the signal is a pure oscillation of 50Hz. At 0.5 seconds, one more frequency component appears whose frequency is half of the previous one. The FFT plot represents both the frequencies. But the analysis lacks the knowledge about the temporal behavior of the frequencies. Instantaneous frequency as a time-frequency presentation shows the period doubling phenomena with exact timing. Overall, it is noted that instantaneous frequency is a better tool for characterizing signals with amplitude and frequency modulations. Since machining dynamics is oftentimes nonlinear with period-doublings, superharmonics or other types of bifurcations, instantaneous frequency is selected as the characterization tool for spectral domain analysis.

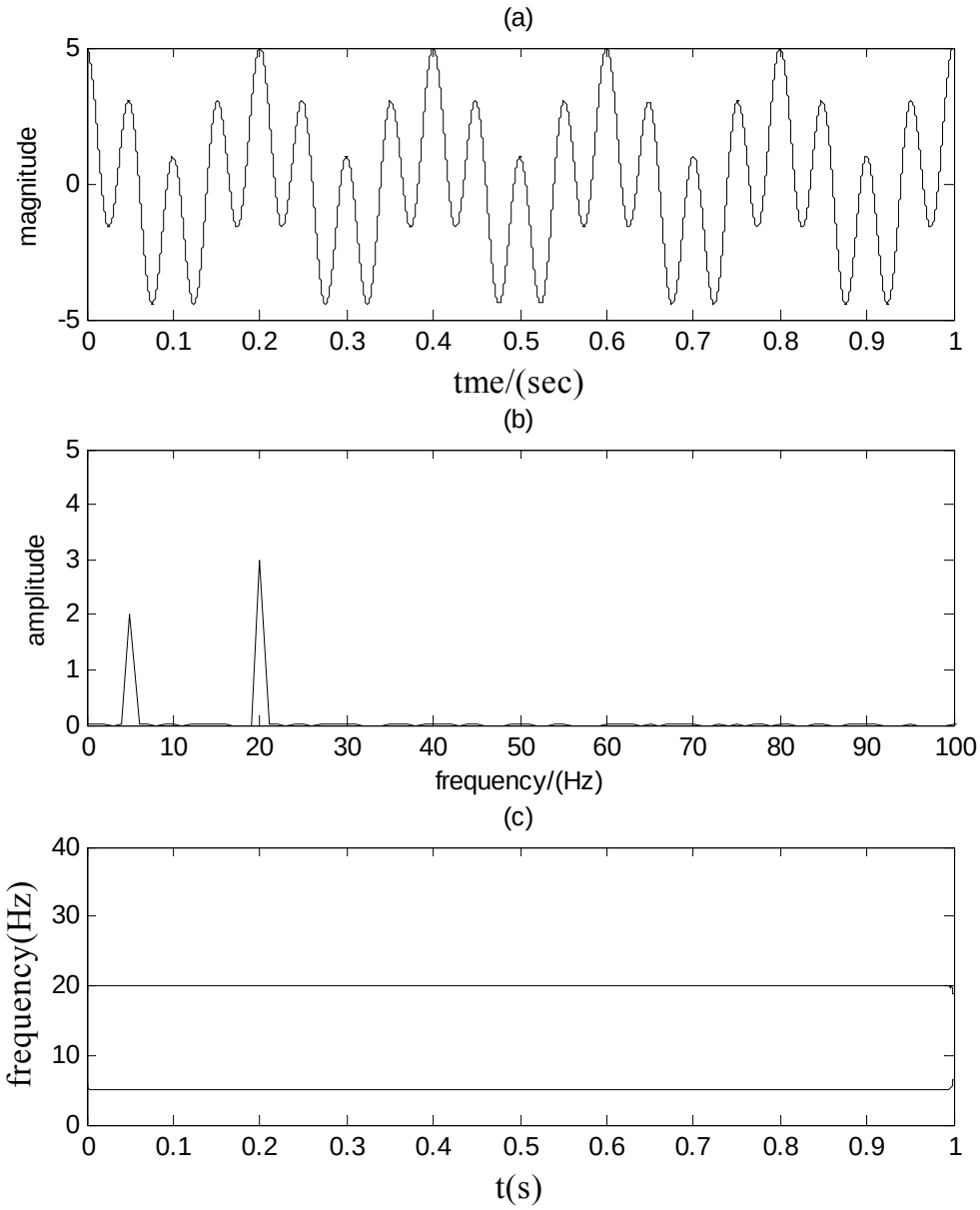

Fig 3.1 Time and frequency domain data for X(t) = 2cos (10t) +3cos (40t)

(a) Time history, (b) FFT graph and (c) Instantaneous frequency

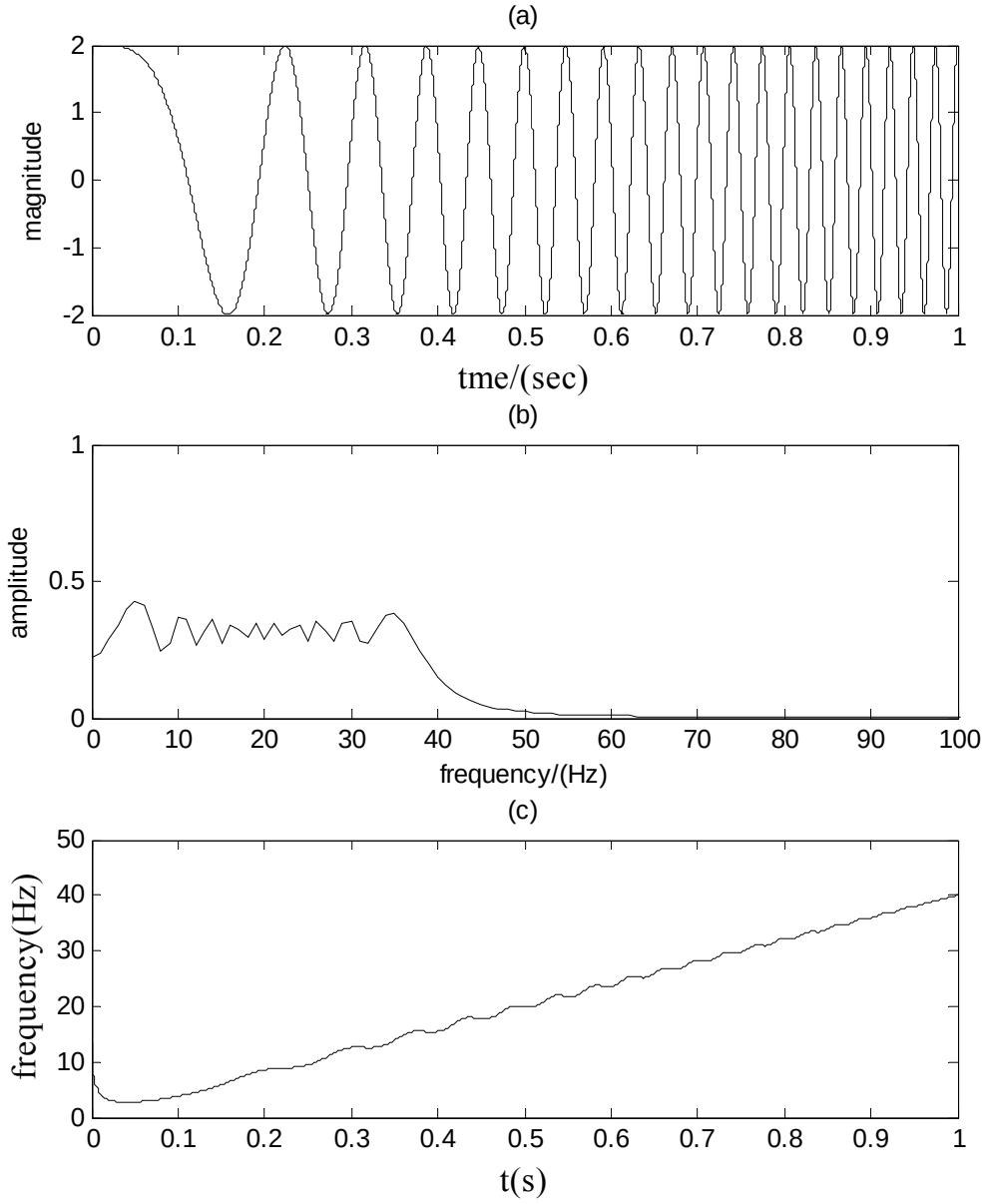

Fig 3.2 Time and frequency domain data for X(t) = 2cos ((40t) π t)

(a) Time history, (b) FFT graph and (c) Instantaneous frequency

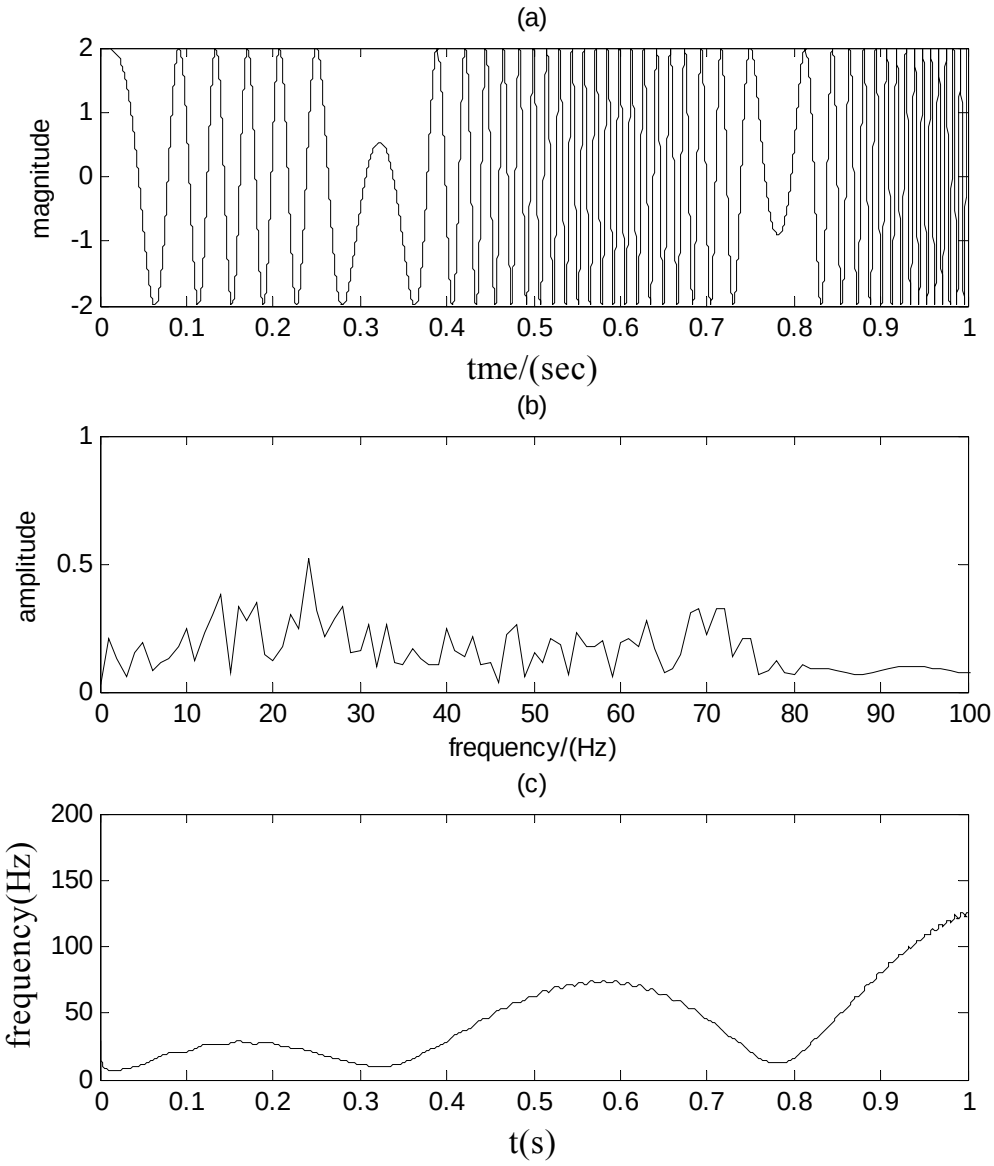

Fig 3.3 Time and frequency domain data for X(t) = 2cos ((40sin(2 π t) π t)

(a) Time history, (b) FFT graph and (c) Instantaneous frequency

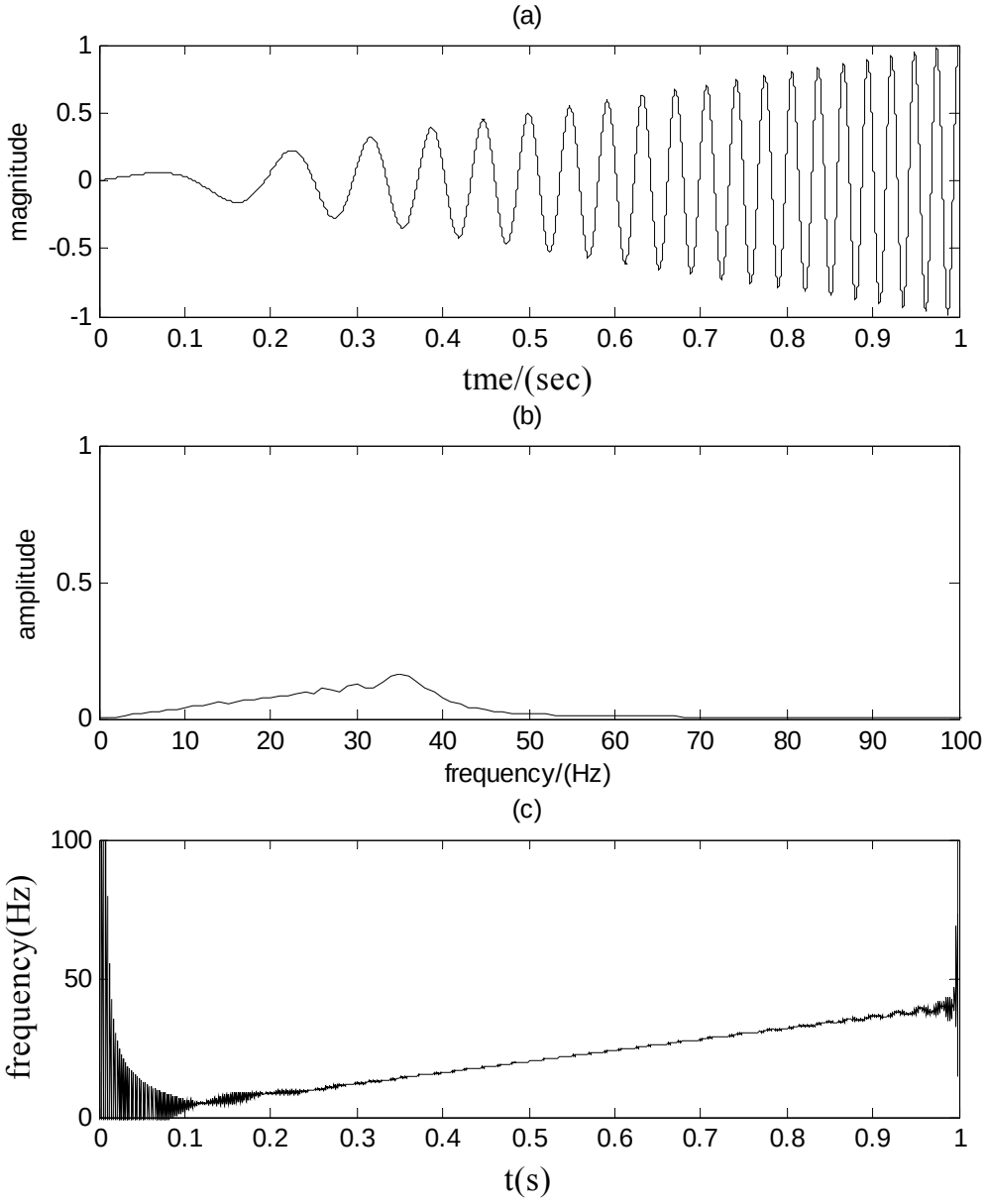

Fig 3.4 Time and frequency domain data for X(t) = t (cos(40 t) π t)

(a) Time history, (b) FFT graph and (c) Instantaneous frequency

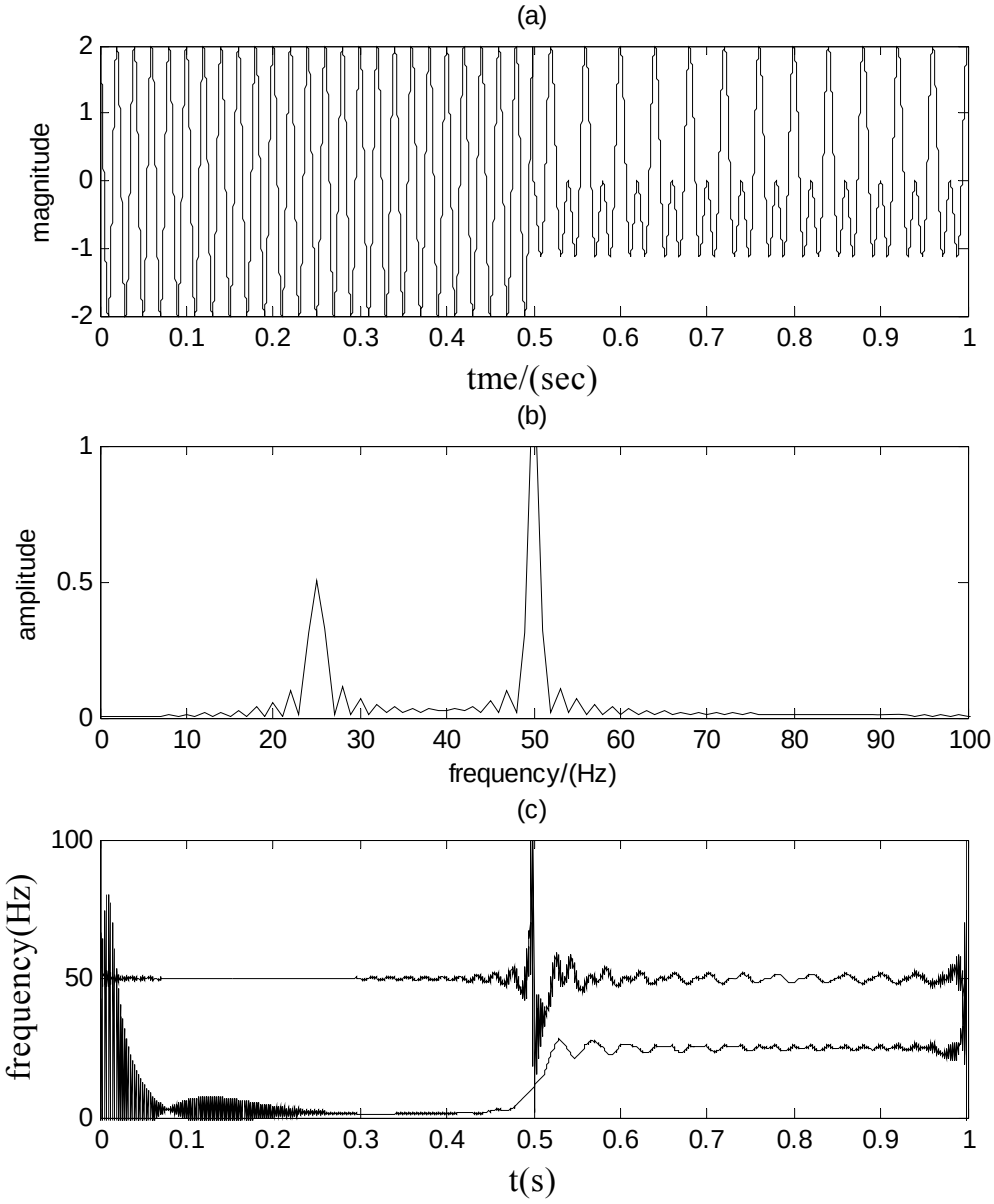

Fig 3.5 Time and frequency domain data for

$$X(t) = \begin{cases} 2\cos(100\pi t) & t < 0.5s \\ \cos(100\pi t) + \cos(50\pi t) & 0.5s \le t \le 1s \end{cases}$$

(a) Time history, (b) FFT graph and (c) Instantaneous frequency

3.3 Fundamentals and Examples of Largest Lyapunov Exponent

Lyapunov exponent is a quantitative measure of the average rate of exponential divergence or convergence of two neighboring trajectories in the phase space. If the initial separation is δX_0, then the divergence can be written as

$$\delta X(t) \approx e^{\lambda t} \delta X_0 \tag{3.9}$$

where λ is the Lyapunov exponent. The rate of divergence varies with the different orientations of the initial vector, δX_0. In other words, for n-dimensional state phase, the spectrum of Lyapunov exponents, $\{\lambda_1, \lambda_2, \ldots \lambda_n\}$, depends upon the starting point x_0. Lyapunov spectrum can be described as follows. Consider an infinitesimal small sphere with radius $d\rho_0$ positioning on the initial state of a trajectory. The flow of the dynamic system deforms this sphere into an ellipsoid in time (Fig. 3.6). In other words, all the orbits which have started in the sphere will be in the ellipsoid after a finite time, t.

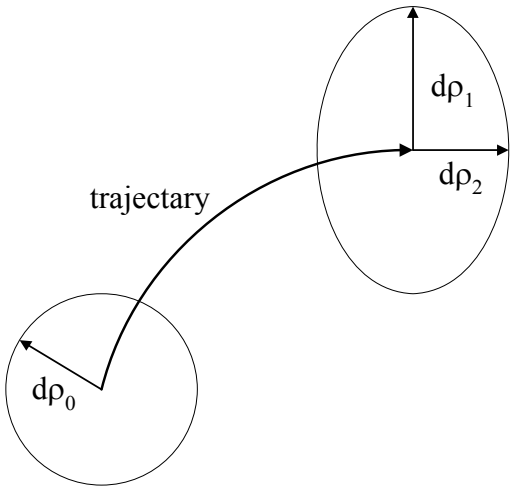

Fig 3.6 Obtaining Lyapunov spectrum

The ith Lyapunov exponent is defined by

$$\lambda_i = \lim_{t\to\infty} \frac{1}{t} \ln\left(\frac{d\rho_i(t)}{d\rho_0}\right) \tag{3.10}$$

where $d\rho_i(t)$ is the radius of the ellipsoid along its i-th principal axis. (i = 1, 2,…n for n-dimensional phase space). When the dynamics of a system becomes unpredictable, it will have at least one positive Lyapunov exponent and the system is defined as chaotic. Thus, finding the largest Lyapunov exponent will give a quantitative measure for system stability. Methods of calculating largest Lyapunov exponents and predicting chaos in nonlinear time series have been much explored [61–64]. Methods of computing Lyapunov exponents for a system with a set of differential equations of motion or logistic maps are comparably straightforward [64–66] than computing them for a time series data set. The commercially available "Chaos Data Analyzer" [67] and the free MATLAB add-in software, TSTOOL toolbox [68], both use the Wolf algorithm based techniques [69] to calculate the spectrum of Lyapunov exponents. They both have successfully applied to equation sets, and experimental and numerical time history data. Wolf et al. [69] defined the Lyapunov spectrum similarly to Eq. 3.10

$$\lambda_i = \lim_{t\to\infty} \frac{1}{t} \log_2\left(\frac{\rho_i(t)}{\rho_i(0)}\right) \tag{3.11}$$

Here λ_i is the i-th one dimensional Lyapunov exponent and $\rho_i(t)$ is the length of the i-th principal axis at time t.

Lyapunov exponents are arranged in such a way that

$$\lambda_1 \geq \lambda_2 \geq \cdots \lambda_n \tag{3.12}$$

where λ_1 and λ_n correspond to the most rapidly expanding to the most rapidly contracting principal axis, respectively, or in other words, the largest to the smallest Lyapunov exponents. The TSTOOL toolbox has been adopted by many [70, 71] for computing Lyapunov spectra. The command "largelyap" in the TSTOOL toolbox uses an algorithm very similar to the Wolf algorithm [69]. To estimate the largest Lyapunov exponent (LLE), the average growth of the distance between two neighboring trajectories is computed through scaling of prediction errors. The increasing error in predicted time represents the LLE. The system is stable if the prediction error is zero. The followings are two examples of stable and unstable conditions. Time histories and their Lyapunov spectra are shown in Figs. 3.7 and 3.8. The Lyapunov spectrum for the time series of an unstable dynamic system gives positive exponents (Fig. 3.7), while the zero-valued Lyapunov spectrum of the stable system demonstrates stability.

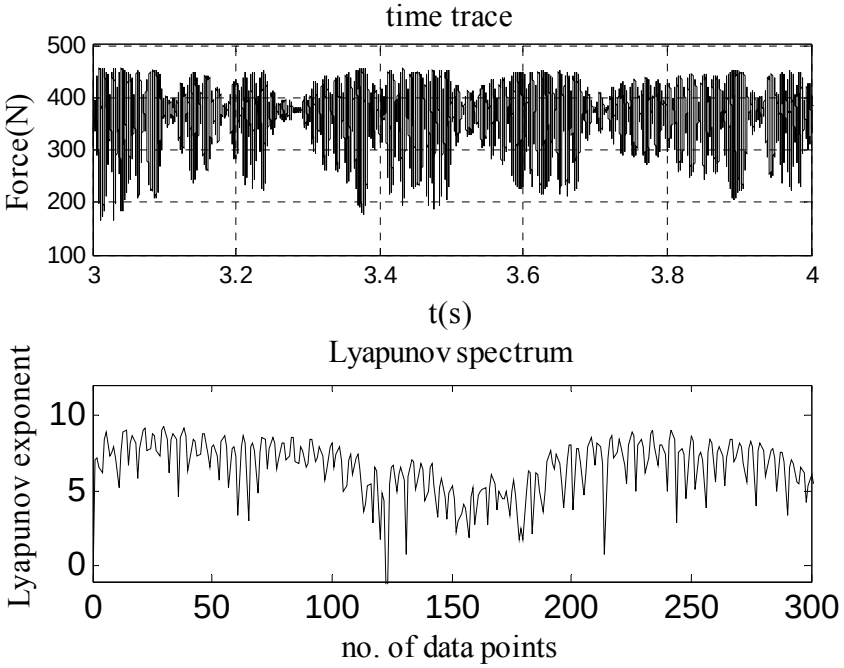

Fig 3.7 Lyapunov spectrum for chaotic data set

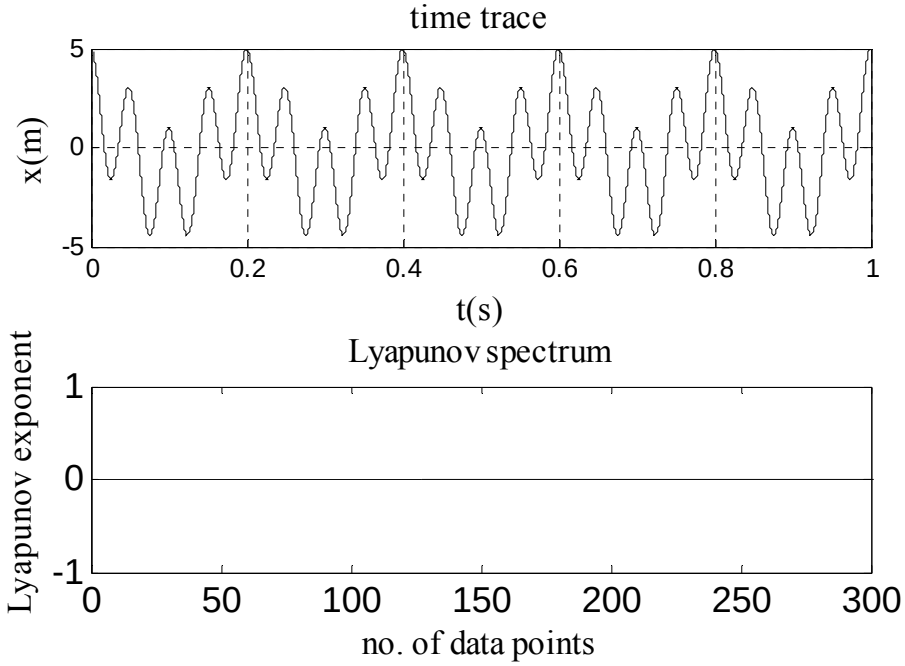

Fig 3.8 Lyapunov spectrum for stable data set

4. MODEL VALIDATION AND IMPORTANCE OF CONSIDERING WORKPIECE IN CUTTING DYNAMICS

4.1. Comparison with Experimental Results

The experimental result of Case #4 found in [10] is considered for the purpose of comparison. The paper suggested DOC = 1.75mm as the stable limit and DOC = 1.78mm as the unstable limit. The set of experimental data were taken 9% below the predicted stable limit at DOC = 1.62mm and 40% above the predicted unstable limit at DOC = 2.49mm. To compare with the physical results, the same DOCs, cutting parameter values and tool geometry are adopted in the numerical simulations presented in the followings. That is, a constant spindle speed of Ω = 1250rpm, a constant chip width of t_0 = 0.0965mm (feed per revolution), a 4140 steel workpiece with the radius of the machined section, r_3 = 20.095mm, and a tool with 45 degrees side cutting edge angle, 3.55 degrees rake angle and 3.55 inclination angle are used. In [10], cutting stability was investigated by analyzing the Y-direction cutting force component in the spectral domain. Fig. 4.1 shows the time histories, instantaneous frequency and the Lyapunov spectrum of the Y-direction force component, Fy, for DOC = 1.62mm and DOC = 2.49mm. Responses clearly convey a stable and a chaotic state of motion, agreeing well with the physical data in [10]. Furthermore, results for X- and Y-direction vibrations of the workpiece (Figs. 4.2 and 4.3) and Z-direction vibration of the tool (Fig 4.4) are in line with the two states of the system demonstrated by stability analysis of the Y-direction cutting force (Fig 4.1).

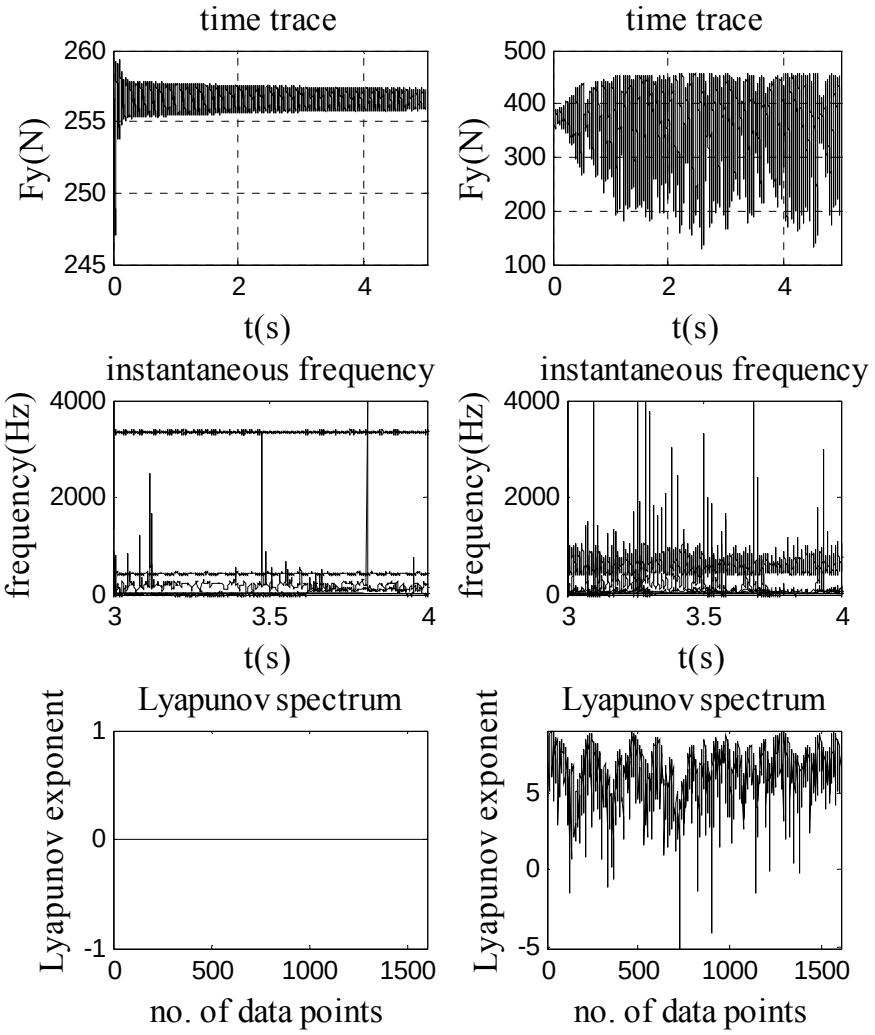

Fig. 4.1 Y–direction cutting force responses for DOC = 1.62mm (left column) and DOC = 2.49mm (right column) for Ω = 1250rpm with whirling

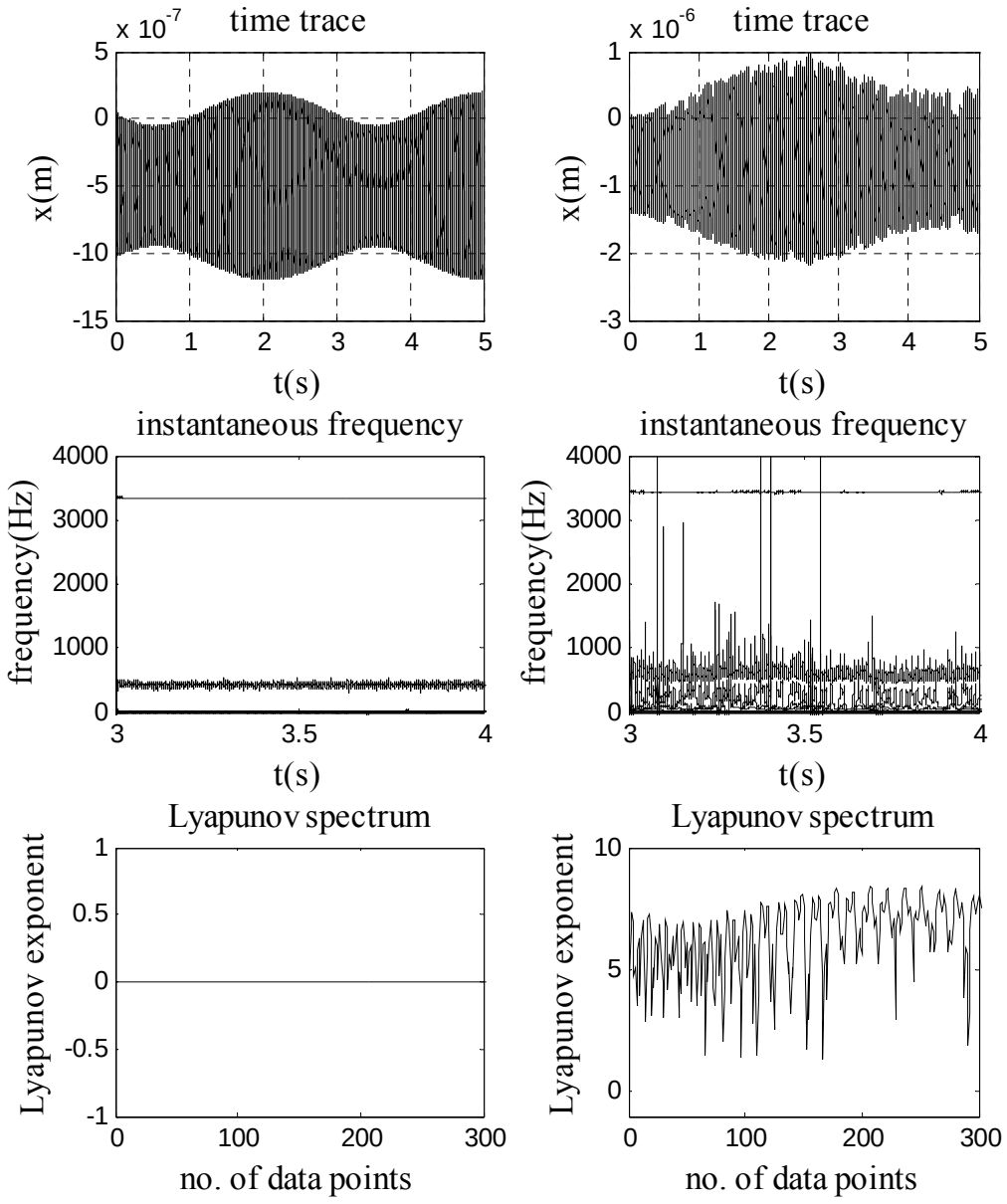

Fig. 4.2 X–direction workpiece responses for DOC = 1.62mm (left column) and DOC = 2.49mm (right column) for Ω = 1250rpm with whirling

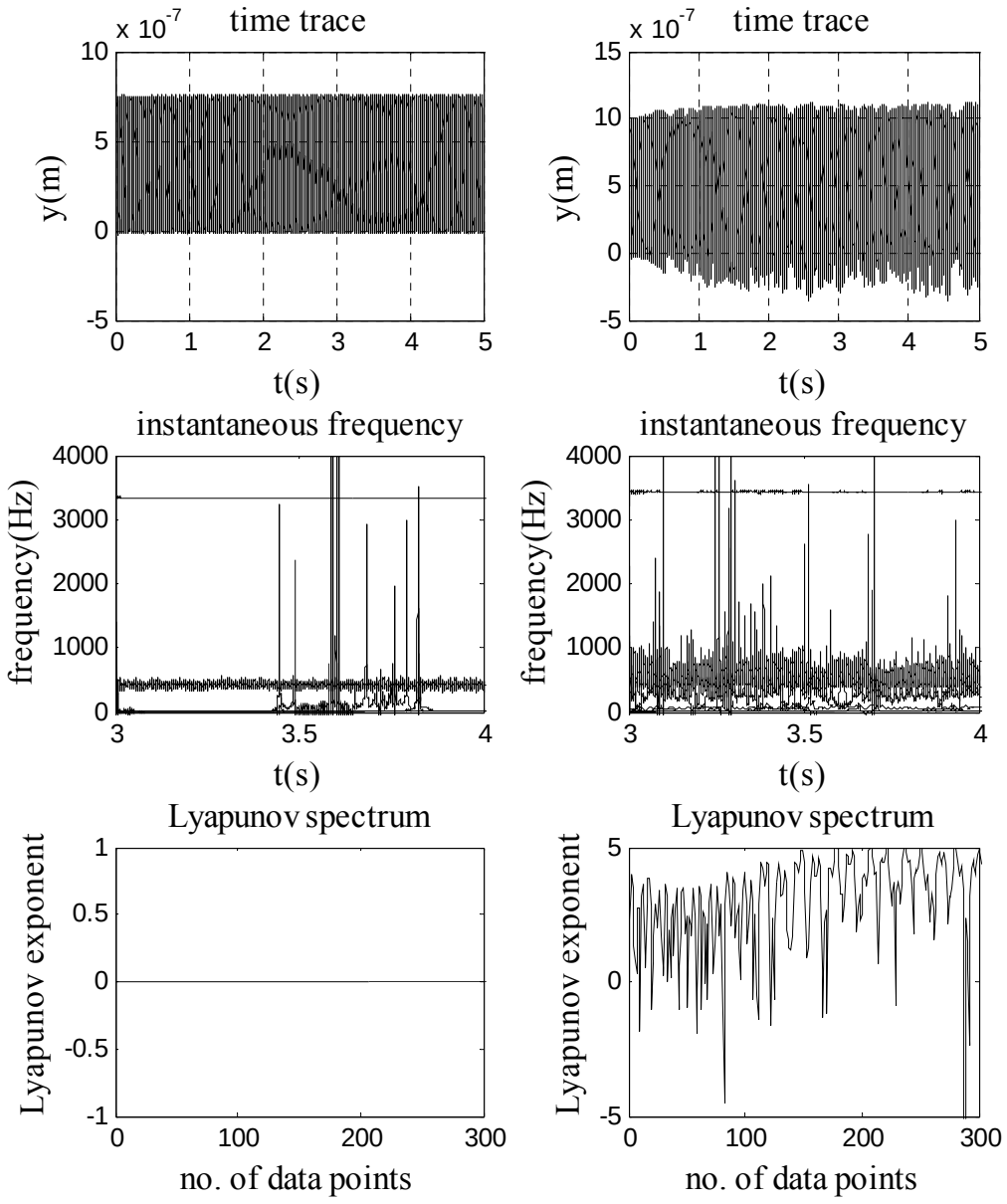

Fig. 4.3 Y–direction workpiece responses for DOC = 1.62mm (left column) and DOC = 2.49mm (right column) for Ω = 1250rpm with whirling

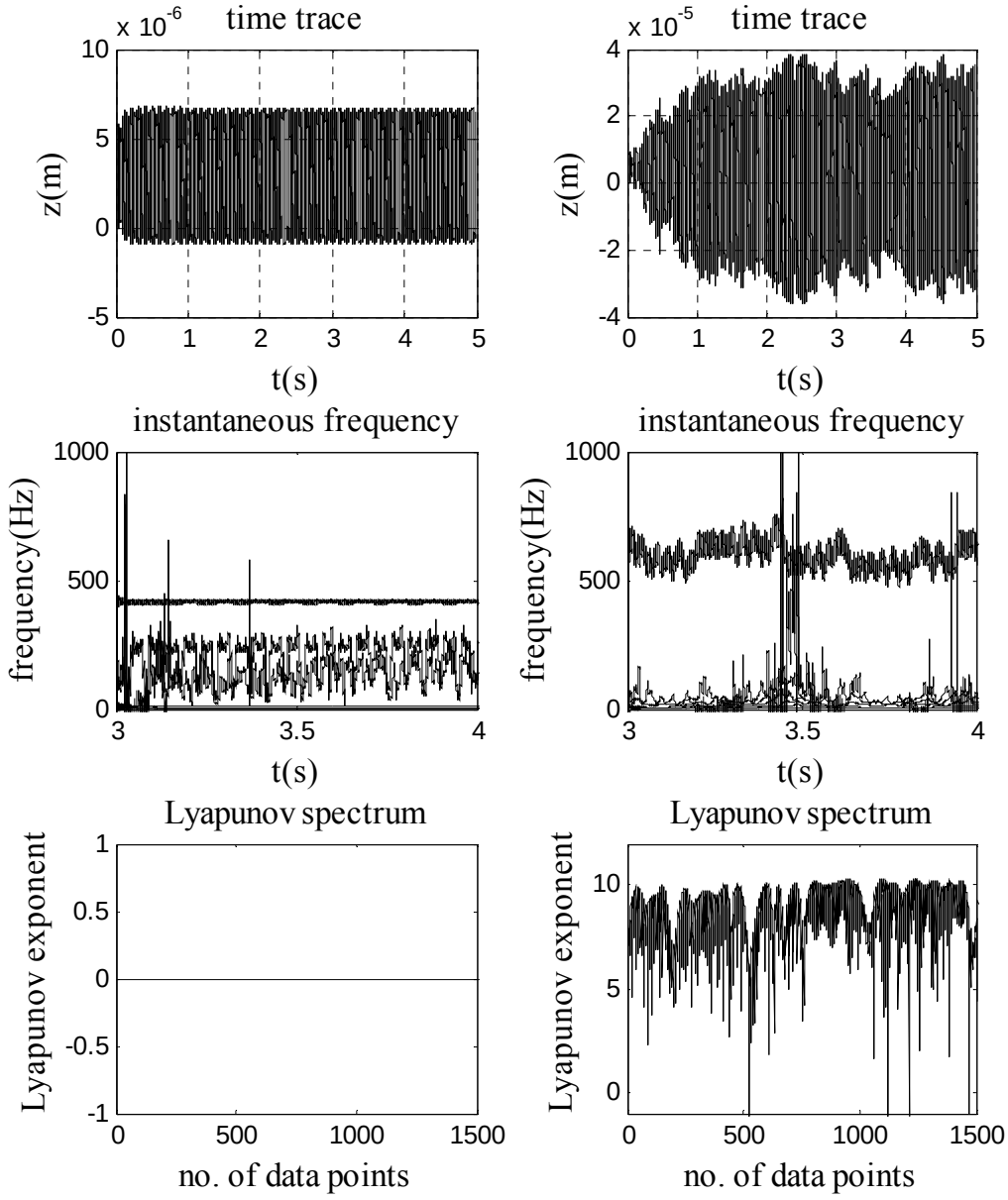

Fig. 4.4 Z–direction tool responses for DOC = 1.62mm (left column) and DOC = 2.49mm (right column) for Ω = 1250rpm with whirling

4.2. Importance of Considering Workpiece in Cutting Dynamics

4.2.1. Nonlinear 3D Model Responses with Increasing DOC

In this section 5 different DOCs between 1.00mm and 2.00mm are considered to compare the stability states of the tool and workpiece. All the responses are for constant spindle speed at Ω = 1250rpm. Workpiece behaviors in the X- and Y-direction are fairly similar. For this very reason, only the results associated with the X-direction are used to represent workpiece responses. There are three main frequencies dominating in the workpiece-tool machining model system. They are the workpiece natural frequency at 3300Hz, tool natural frequency at 420Hz, and whirling frequency at 20.8Hz. The workpiece characteristic frequency changes with its diameter and variation in stiffness due to material removal.

Fig. 4.5 gives workpiece (left) and tool (right) responses corresponding to DOC = 1.00mm. It seems that both time histories indicate a stable motion. However, the Lyapunov spectrum resolved using the time series show that the dynamic state of the workpiece is different from the tool. The workpiece response is clearly unstable with positive Lyapunov exponents, while the tool response shows a stable condition. Although lower frequencies vary with time, the instantaneous frequency of the tool does not illustrate broadband characteristics for the tool natural frequency. In contrast, the workpiece time-frequency response shows a broadband behavior at 420Hz, which is excited by the tool natural frequency. Moreover, another frequency at 1650Hz is seen to be present with the workpiece characteristic frequency at around 3280Hz. This is a case of period-doubling bifurcation. When DOC is increased to 1.25mm (Fig. 4.6), all the

workpiece and tool responses display a clear stable state of machining. While the tool response shows components near the tool natural frequency, the workpiece response has components at its characteristic frequency at 3300Hz and at tool natural frequency at 420Hz. The whirling frequency component at 20.8Hz is readily present in all the instantaneous frequency plots for the workpiece.

Further increment of DOC to 1.62mm (Fig. 4.7) displays a different stability state for the tool with bifurcations at low frequencies. The workpiece characteristic frequency has increased to 3340Hz with the increase of its diameter. However, the Lyapunov spectra for the tool and workpiece responses demonstrate a stable state of motion. It should be noted that the tool vibration amplitude is reduced with increasing DOCs (Figs. 4.5-4.8). Even though the tool responses show a very stable behavior in all the three plots (time, time-frequency and Lyapunov spectrum) in Fig. 4.8, the instantaneous frequency for the workpiece displays a highly bifurcated state of machining. Not only the workpiece natural frequency increases further to 3355Hz, the frequency component of the workpiece that is excited by the tool natural frequency also increases considerably to 650Hz. This is the case when system nonlinearity dominates. The second and third harmonics of the frequency at 1300Hz and 1950Hz, respectively, are also observed. This raises the concern for relying exclusively on models that consider only tool dynamics in machining that also involves workpiece. And, unless the system is unstable, Lyapunov exponents are not able to quantify the various states of bifurcation.

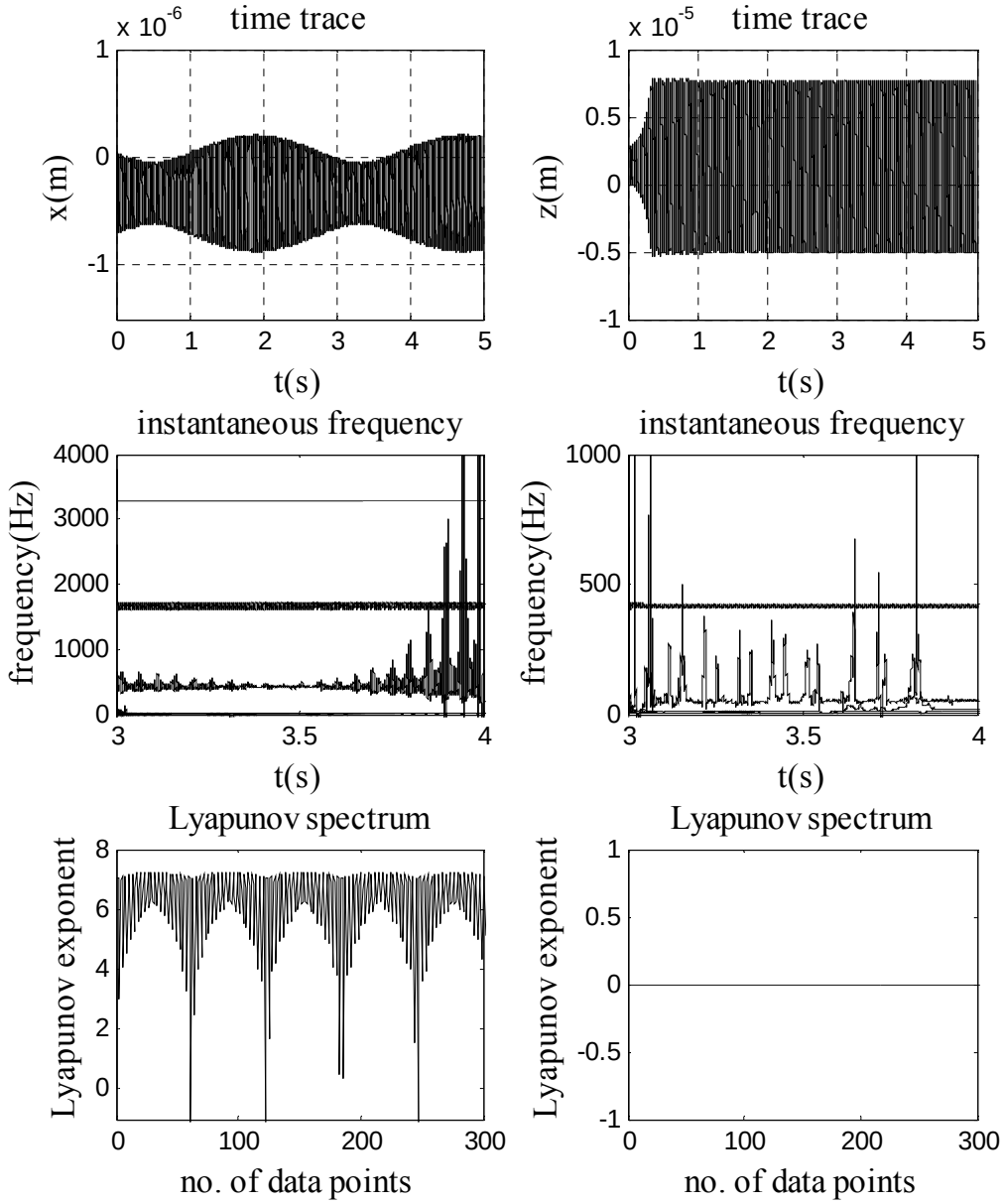

Fig. 4.5 X–direction workpiece responses (left) and Z-direction tool responses (right) for DOC = 1.00mm and Ω = 1250rpm

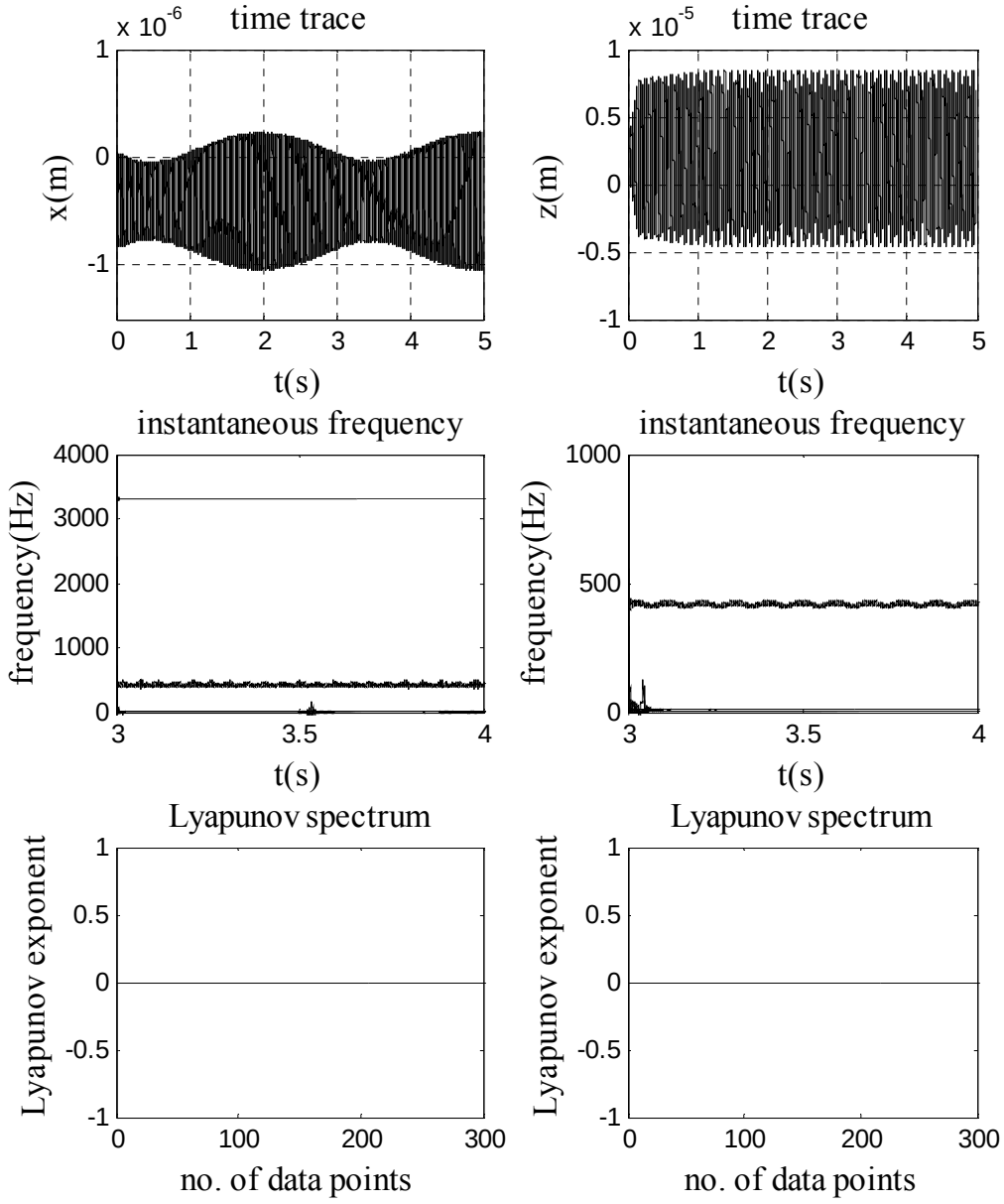

Fig. 4.6 X–direction workpiece responses (left) and Z-direction tool responses (right) for DOC = 1.25mm and Ω = 1250rpm

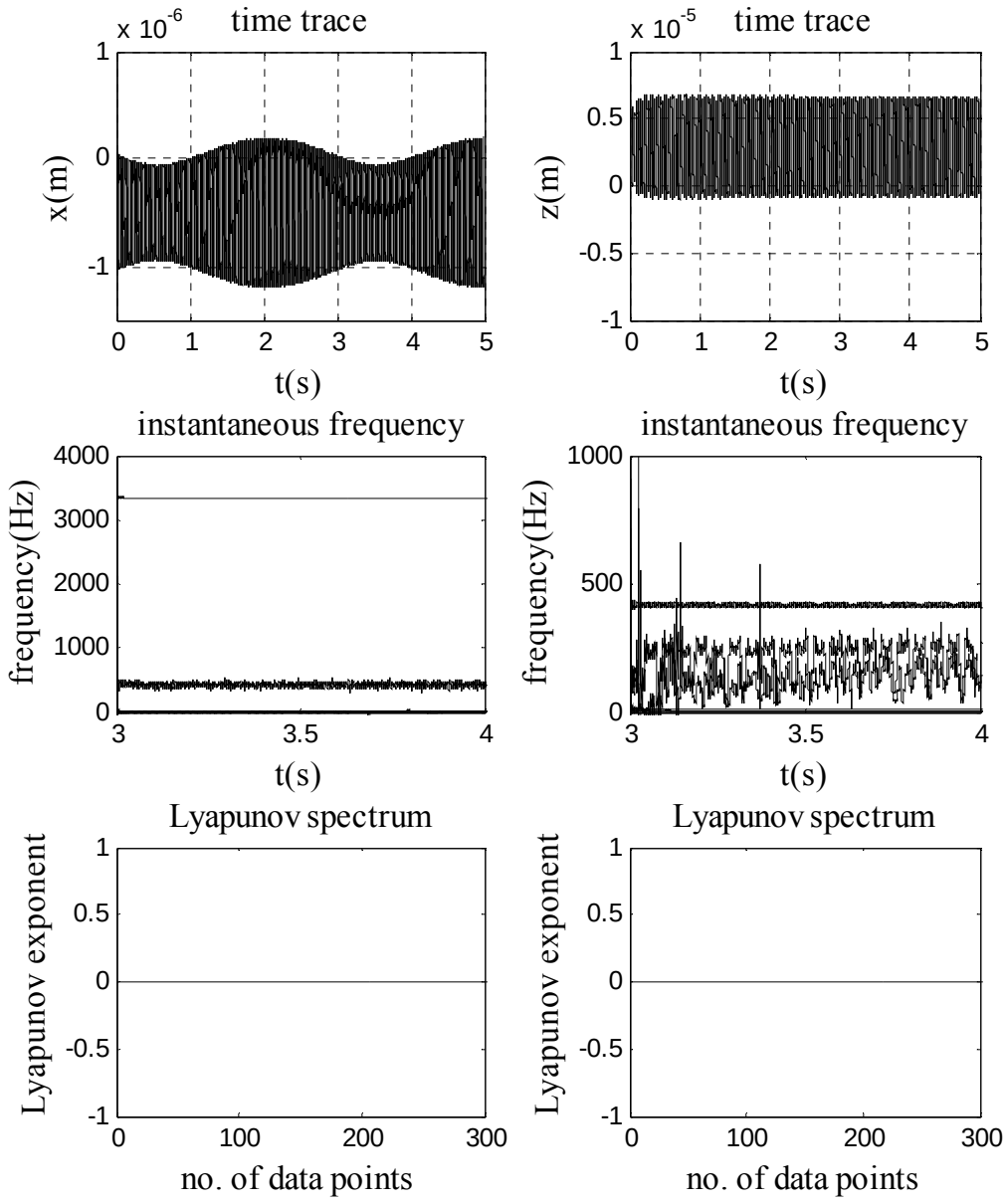

Fig. 4.7 X–direction workpiece responses (left) and Z-direction tool responses (right) for DOC = 1.62mm and Ω = 1250rpm

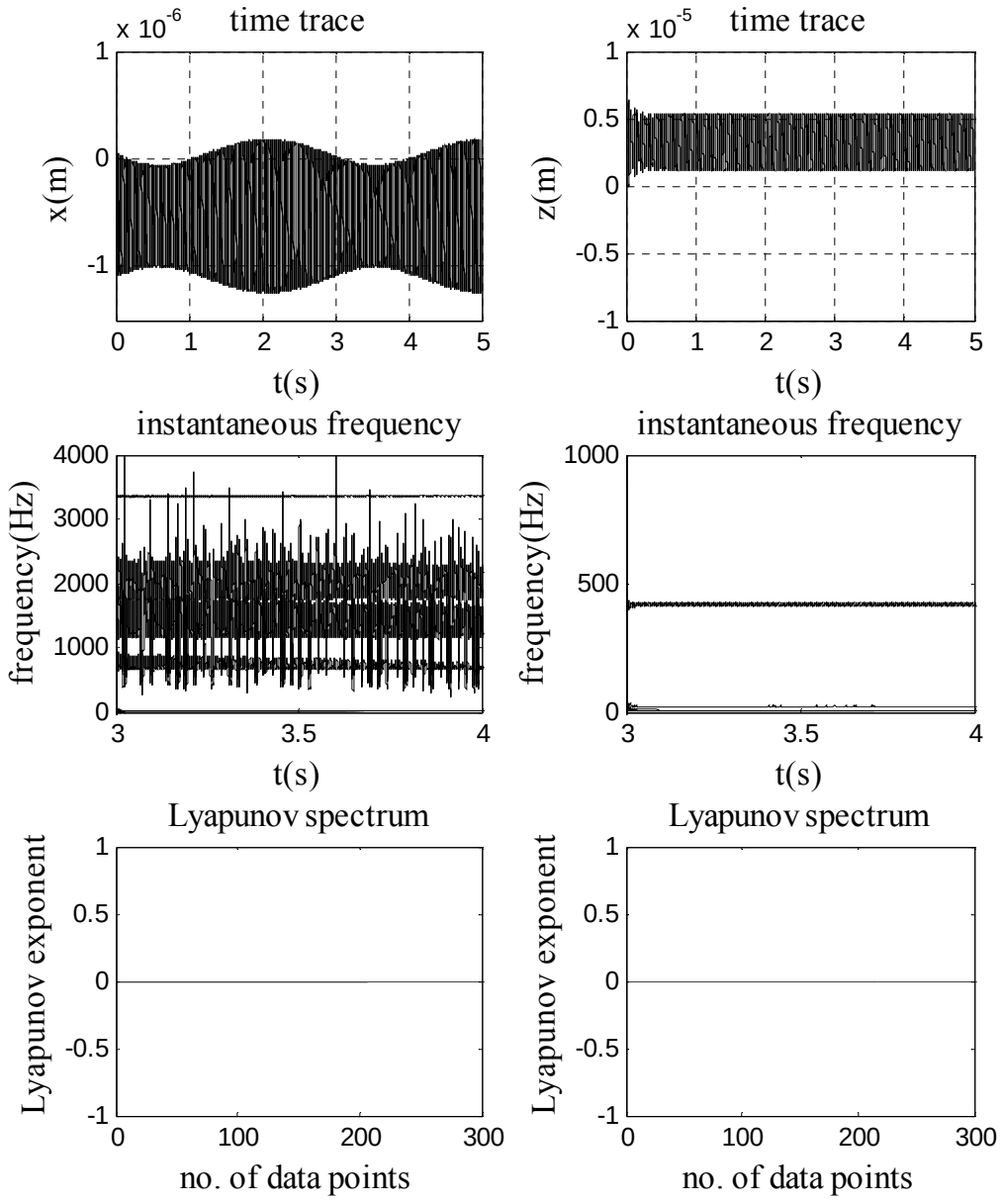

Fig. 4.8 X–direction workpiece responses (left) and Z-direction tool responses (right) for DOC = 1.75mm and Ω = 1250rpm

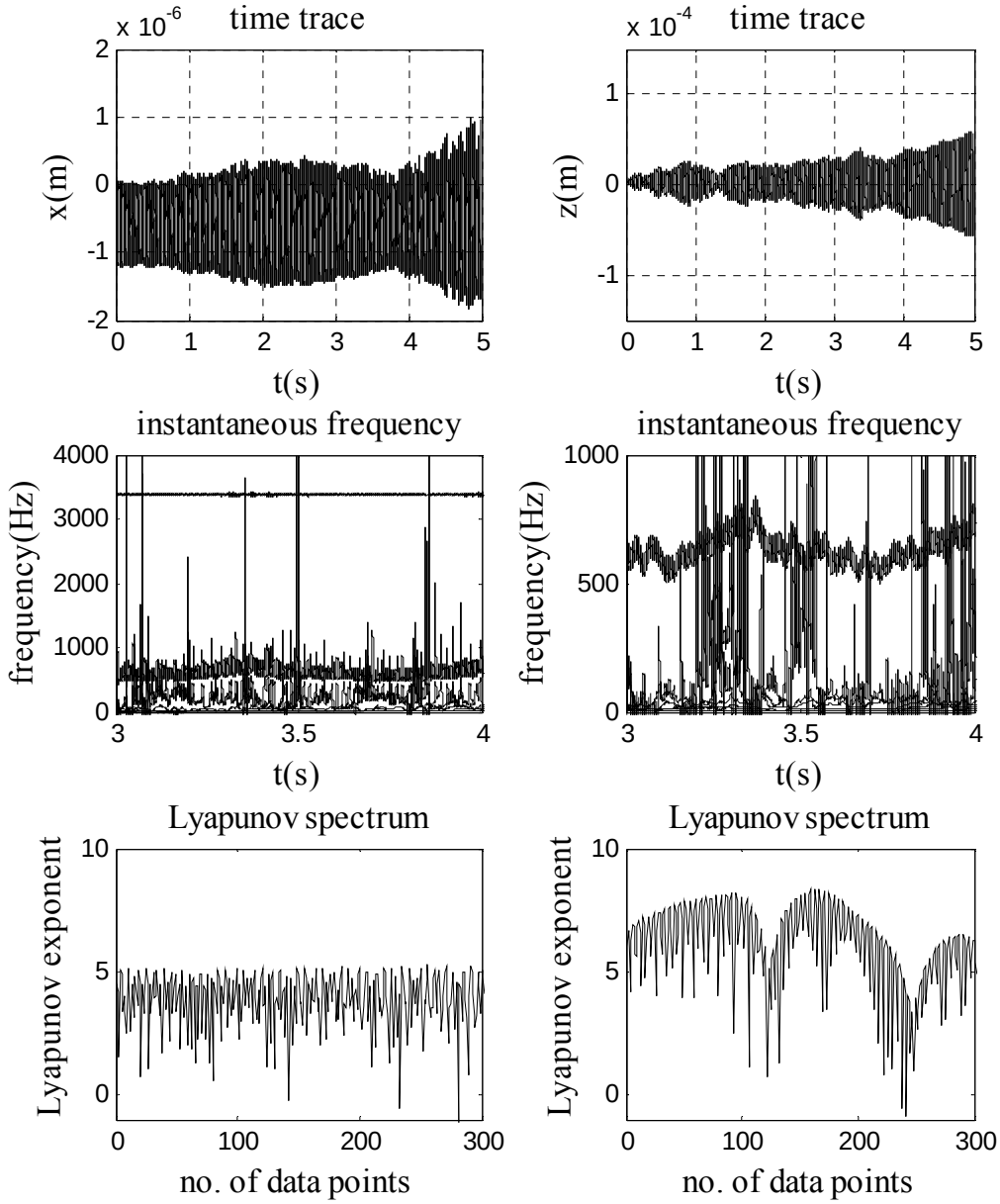

Fig. 4.9 X–direction workpiece responses (left) and Z-direction tool responses (right) for DOC = 2.00mm and Ω = 1250rpm

Fig. 4.9 presents the responses associated with DOC = 2.00mm. Both the tool and workpiece display the worst case of machining instability with large amplitude vibration and broadband spectra in the time-frequency domain. This unstable state of motion is confirmed by the positive exponents in the Lyapunov spectra. Note that the whirling frequency disappears when the workpiece starts to vibrate chaotically, thus indicating the workpiece no longer whirls in this cutting state. The broadband spectral responses excited by the tool natural frequency and the aperiodic vibrations of both the tool and workpiece clearly indicate that the system is in chaos. This leads the system to a complete failure that could result in a damaged tool and impact the workpiece quality and dimensional preciseness.

4.2.2. Effect of Workpiece Dimensions

Instead of spindle speed, cutting speed is the most common cutting parameter used in stability charts. For a workpiece having a machined section of D millimeters in diameter, the cutting speed is

$$cutting\_speed = \frac{\pi D \Omega}{1000 \times 60} ms^{-1} \tag{4.1}$$

where Ω is spindle speed in revolutions per minute. This means that there can be different spindle speeds and workpiece diameters to have the same cutting speed. In milling or drilling, milling cutters or drill bits have standard diameters. However, in turning process, the machined diameter can be any value depending on product requirements. Most literatures do not consider workpiece vibrations in modeling cutting dynamics that governs turning processes. In other words, stability charts generated using such models to predict stable DOCs with increasing cutting speed do not discern

as to which workpiece diameter a particular stability chart is proper and applicable. In a previous example where a 1250 rpm spindle speed and a machined workpiece of 20.095mm in radius were considered, the cutting speed was 2.63 ms^{-1}. Consider the case when DOC = 1.75mm is required. If the spindle speed decreases to 1000 rpm, to have the same cutting speed, the machined workpiece radius would need to be 25.12mm. Fig. 4.10 shows the responses in the X- and Z-direction corresponding to DOC = 1.75mm. Comparing with Fig. 4.8 where the same cutting speed and DOC were considered, even though the Lyapunov spectrum shows that the system is stable, the time histories and time-frequency plots demonstrate a different state of motion. While X-direction workpiece vibration frequencies are significantly different from each other, the Z-direction tool vibrations demonstrate significant instability. Fig. 4.11 shows the system dynamical behaviors associated with Ω = 1250 rpm, DOC = 1.75mm and machined workpiece radius r_2 = 15mm. Comparing with Fig 4.8 where the same spindle speed and DOC but a different workpiece diameter were considered, it is noted that though the tool responses are quite similar, workpiece vibration signatures are not. With the reduction of workpiece diameter, workpiece stiffness has reduced and thus the amplitude of vibration has increased (Fig 4.11). However, the instantaneous frequency plots corresponding to the workpiece of smaller diameter are visibly more stable. It is seen in Fig. 4.10 that the workpiece vibration amplitudes reduce with the increase in workpiece diameter. Moreover, the vibration amplitudes of the tool also increase with increasing workpiece diameter.

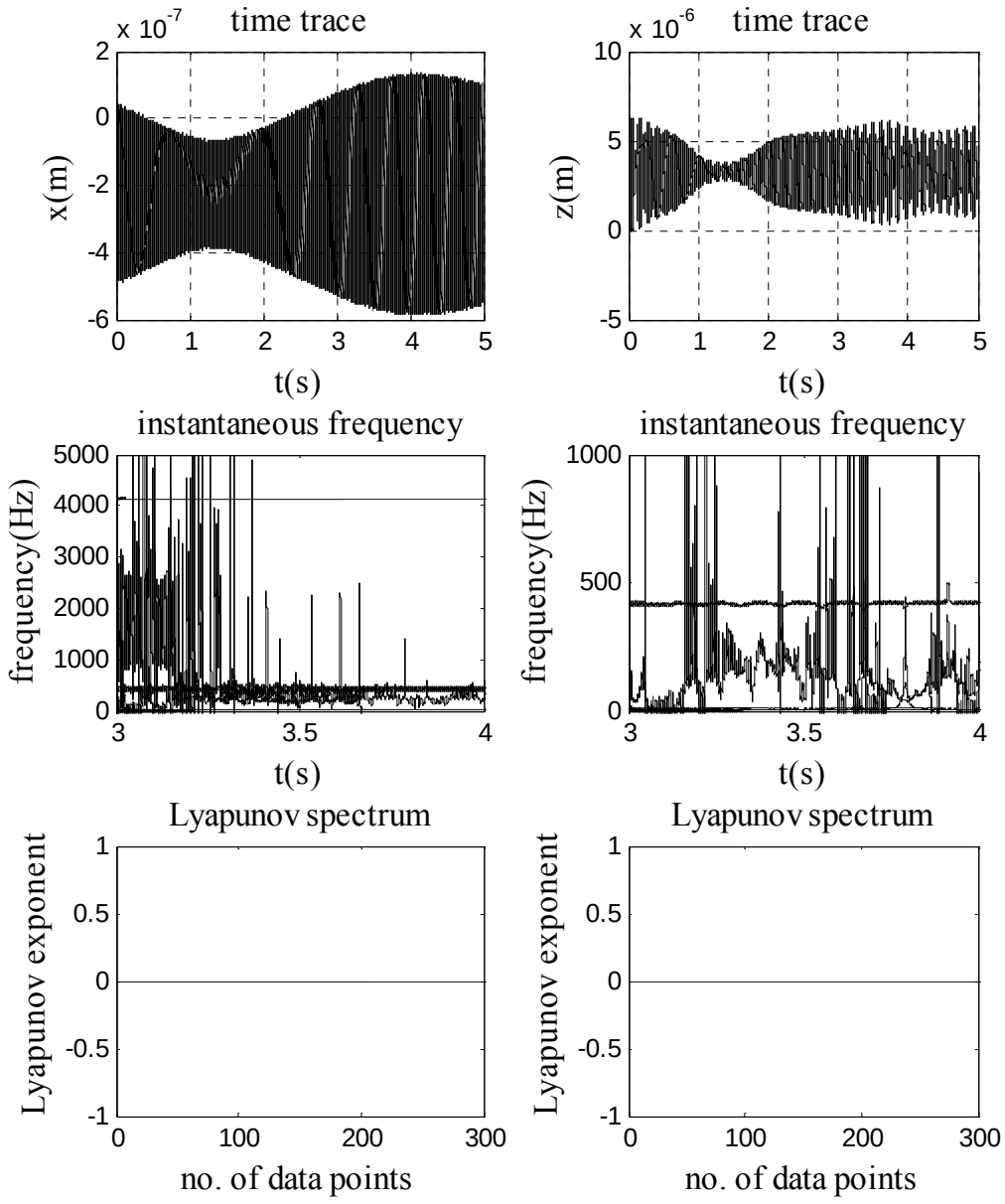

Fig. 4.10 X–direction workpiece responses (left) and Z-direction tool responses (right) for DOC = 1.75mm and Ω = 1000rpm with a machined workpiece radius = 25.12mm

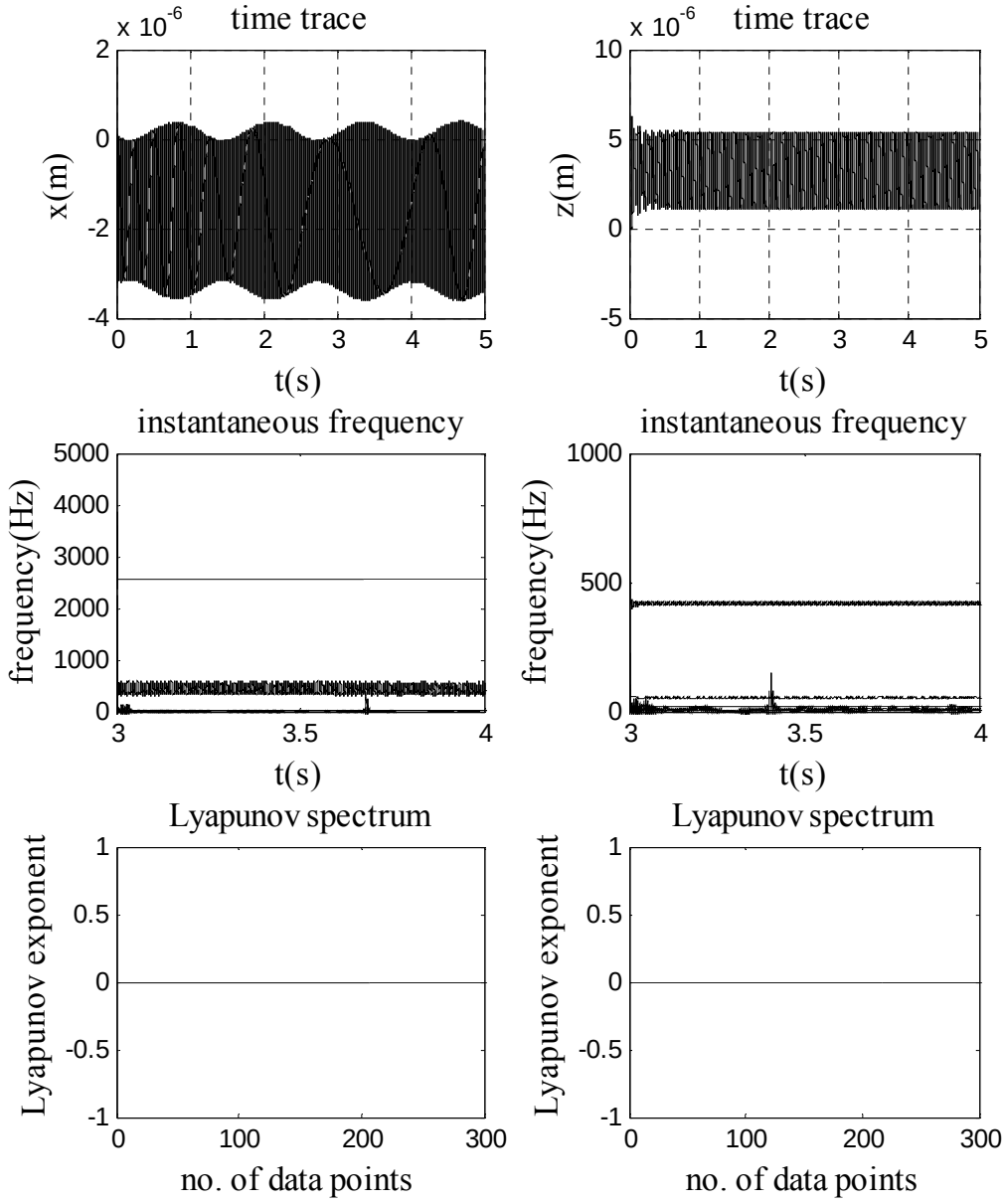

Fig. 4.11 X–direction workpiece responses (left) and Z-direction tool responses (right) for DOC = 1.75mm and Ω = 1250rpm with a machined workpiece radius = 15.00mm

4.3. Discussions

In the section, validation of the machining model was made by comparing numerical responses with experimental data. Concerns over neglecting workpiece vibrations in modeling turning dynamics were also raised and discussed. It was shown that the responses of the 3D cutting model agreed well with the experimental data in literature. Ref. [10] reported that no chatter was detected at DOC = 1.62mm and that chatter was prominent at DOC = 2.49mm. Numerical results presented in Figs. 4.1 through 4.4 were seen to be in line with the real-world observations. The case in Fig. 4.8 presented a significant observation that, while the 3D model described the tool response as one of stability motions, the corresponding workpiece response was not. It was of a highly bifurcated state. Fig. 4.5, on the other hand, was a case in which the workpiece showed cutting instability at DOC = 1.00mm when the tool response was comparably stable. Thus, ignoring workpiece vibrations in predicting stability bounds or anticipating machining instability is questionable at the fundamental level. The risk of experiencing cutting instability and tool failure would be significant even if conservative cutting parameters were chosen. Moreover, theoretical predictions [9] and experimental observations [10] in literature had reported chatter occurring at small DOCs. Fig. 4.5 was in support of these results. As it would impact workpiece surface roughness and geometrical tolerances, observations made with the figure also suggested that neglecting workpiece vibrations in modeling fine turning or finishing cuts is highly improper. Lastly, it was demonstrated in Figs. 4.10 and 4.11 that workpiece dimension was one of the primary parameters affecting cutting dynamics, as were DOC, cutting speed and

spindle speed. All these observations support the argument that workpiece motions need be considered to ensure proper insight into the dynamics of turning-based material cutting.

5. COMPARISON OF 3D AND SINGLE DOF MODEL RESPONSES

5.1 SDOF Model with Uncoupled EQM for the Tool

When workpiece vibrations are neglected, the cutting model system is reduced to one equation of motion governing the tool motions. The uncoupled equation of motion for the tool can be derived from Eq. (2.38) by eliminating the x and y terms as

$$M_Z \ddot{z}_t + k_Z z_t + k_{ZC} z_t^3 = F_{ZZ} \tag{5.1}$$

where F_{ZZ}, the new cutting force in the Z-direction only, is obtained from Eqs. (2.27) and (2.28) with the modified Eqs. (2.22) and (2.32) as follows

$$s_n = r_1 - r_3 \tag{5.2}$$

$$A_{Cn} = (t_0 - z_t + z_t')(r_1 - r_3) \tag{5.3}$$

Note that s_n , the new depth-of-cut, and A_{cn} , the new chip cross sectional area, are no longer functions of x and y. The uncoupled cutting force in the Z-direction can then be derived by modifying Eq. (2.27)

$$F_{ZZ} = F_{fn}(b_{z1}\sin(\eta_{cn}) + b_{z2}\cos(\eta_{cn})) + b_{z3}F_{nn} \tag{5.4}$$

where F_{nn} and F_{fn} are the new normal and friction forces. The new chip flow angle, η_{cn} , can be derived from modifying Eqs. (2.28), (2.29) and (2.30) with s_n and A_{cn} as follows

$$\eta_{cn} = \alpha_1 s_n^{\,3} + \alpha_2 s_n^{\,2} + \alpha_3 s_n + \alpha_4 \tag{5.5}$$

$$F_{nn} = k_n A_{Cn} \tag{5.6}$$

$$F_{fn} = k_f A_{Cn} \tag{5.7}$$

As a result, the final equation of motion is then

$$M_Z \ddot{z}_t + k_Z z_t + k_{ZC} z_t^3 = C_1(t_0 - z + z') + C_2(t_0 - z + z')^2 \tag{5.8}$$

where constants C_1 and C_2 depend on tool geometry, chip flow angle and DOC.

5.2 Numerical Results

The current section compares tool responses of the 3D model of 3 coupled EQMs with those of the 1D model of single EQM. Four different DOCs are considered for comparison. A constant speed of 1250rpm and constant feed of 0.0965mm per revolution are used in all numerical studies. In figures that follow, the left columns present tool responses for the coupled 3D system, whereas the right columns display tool behaviors of the SDOF system. Fig. 5.1 shows the dynamic responses of the tool at DOC = 1.00mm. Time histories demonstrate a similar state of stable motion. The observation of stability is further confirmed by the corresponding Lyapunov spectra of zero exponents for both cases. However, the instantaneous frequency plots reveal two different stability stages for the 3D (coupled) and 1D (uncoupled) versions. The tool response of the 3D model exhibits prominent broadband characteristics in the low frequency region with a component at 60Hz. Moreover, after 3.7 seconds, another frequency component appears at around 20Hz. On the other hand, the tool time-frequency response of the SDOF system shows a very stable state after 3.4 seconds. Other than the tool natural frequency, all instantaneous frequency components are less than 10Hz. Recall that the workpiece response in Fig. 4.5 demonstrated an unstable state of motion for DOC = 1.00mm.

In Fig. 5.2, the time responses, instantaneous frequencies and Lyapunov spectra associated with the case of DOC = 1.75mm all indicate a very stable tool motion for both models. Yet, the 1D model response reveals that the tool vibrates only with the tool natural frequency, while the 3D model describes a component other than the tool characteristic frequency at 20Hz. When DOC is increased to 1.83mm, a large reduction of the tool vibration amplitude can be observed in Fig. 5.3 for both models. In situations when time domain data seem suggest a stable motion of only a few nanometers in vibration amplitude, the corresponding instantaneous frequency and Lyapunov exponents might suggest a completely different state of motion. The tool time–frequency response for the 3D model illustrates a dynamical state of instability characterized by a broadband behavior at 3400Hz. In contrast, the 1D model demonstrates a comparably stable state with slight instability in the low frequency region. Additionally, the Lyapunov exponents are closer to zero for the SDOF system, while the 3D system has a positive spectrum, thus supporting the instability state illustrated in the corresponding time–frequency response.

Fig. 5.4 is a chaotic case for DOC = 1.84mm, where a mere hundredth of a millimeter increase in DOC (from 1.83mm) has resulted in an instability exhibiting a vibration amplitude 30,000 times larger than that of Fig. 5.3. All three plots in Fig. 5.4 for both the 3D and 1D models display chaotic behaviors with broadband characteristics. All the plots show that the 3D coupled model is dynamically more unstable than the corresponding SDOF uncoupled model at the particular DOC.

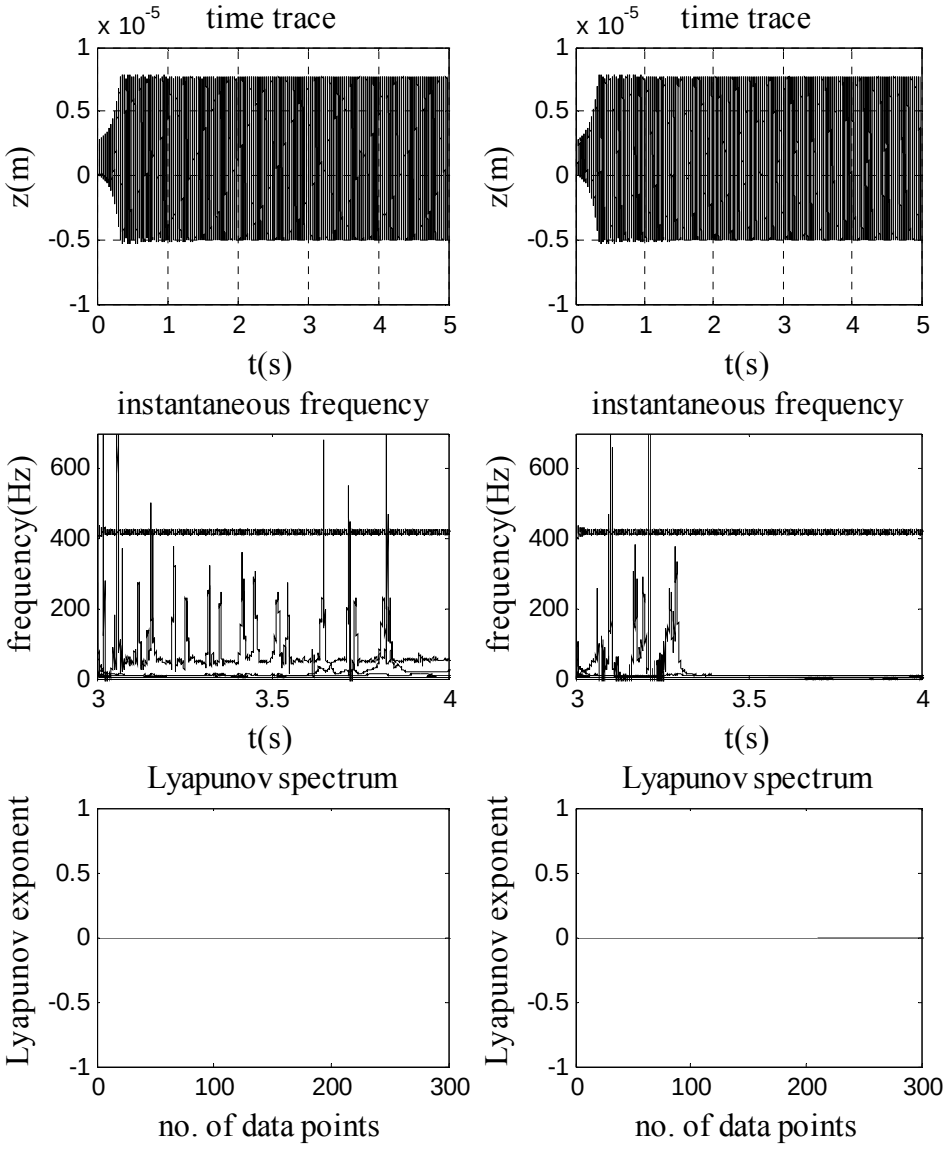

Fig. 5.1 Z – direction tool response of 3D coupled model (left) and Z- direction tool response of 1D uncoupled model (right) for DOC = 1.00mm and Ω = 1250rpm

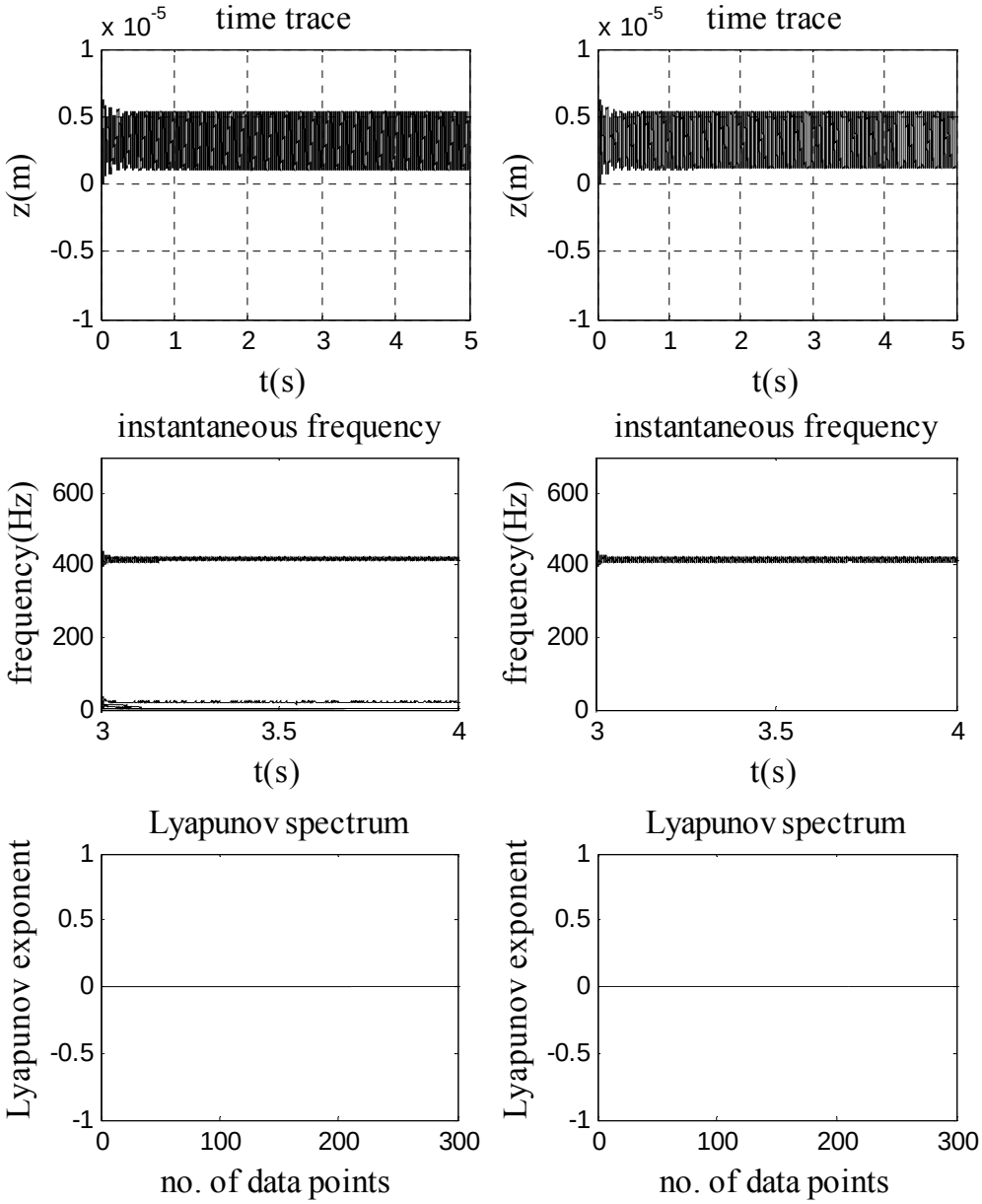

Fig. 5.2 Z – direction tool response of 3D coupled model (left) and Z- direction tool response of 1D uncoupled model (right) for DOC = 1.75mm and Ω = 1250rpm

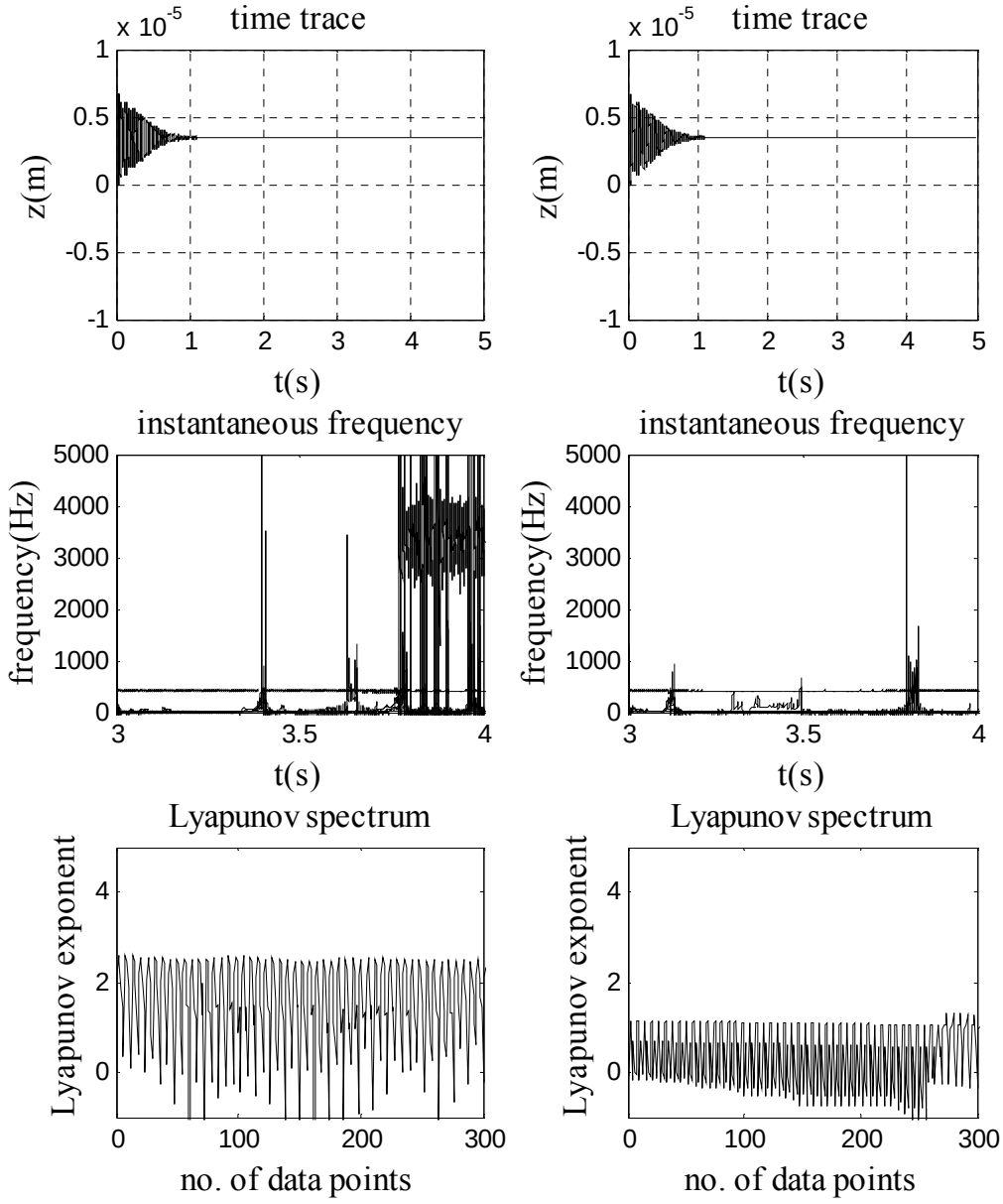

Fig. 5.3 Z – direction tool response of 3D coupled model (left) and Z- direction tool response of 1D uncoupled model (right) for DOC = 1.83mm and Ω = 1250rpm

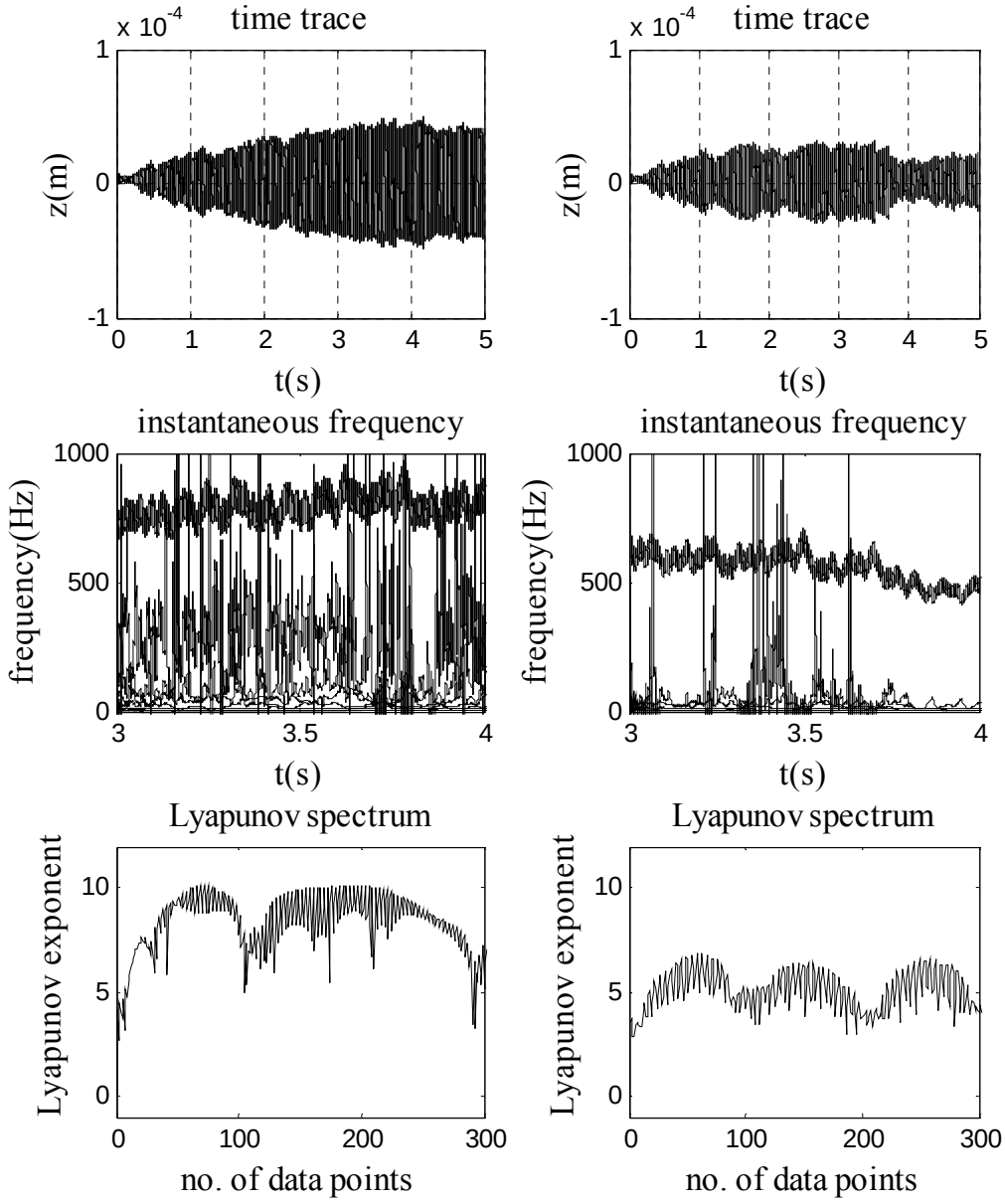

Fig. 5.4 Z – direction tool response of 3D coupled model (left) and Z- direction tool response of 1D uncoupled model (right) for DOC = 1.84mm and Ω = 1250rpm

5.3 Discussions

The tool responses of the 3D model with coupled EQMs demonstrated more frequency components indicative of instability than those of the SDOF model of a single uncoupled EQM (Figs. 5.1-5.4). The SDOF model was shown to be incapable of capturing various instabilities. It was evident that the SDOF model miscomprehended the underlying cutting dynamics. For example, when DOC = 1.83mm, the tool response predicted by the coupled model was one of instability. But the corresponding SDOF model response in Fig. 5.3 (where the tool was decoupled from the workpiece) was one of stability. Recall that in the previous section it was shown in Fig. 4.5 that the workpiece could be in instability while the tool vibrates in stability. These observations seem suggest against the use of one dimensional equation of motion for studying machining dynamics and for establishing stability limits. To better understand cutting dynamics, it is required that tool-workpiece interactions and workpiece whirling be considered simultaneously. These facts imply that 3D modeling with consideration of workpiece vibration is required for better understanding of cutting dynamics.

6. EFFECTS OF MATERIAL IMBALANCE INDUCED WHIRLING ON CUTTING STABILITY

The geometric center of a workpiece would not coincide with its gravitational center if the workpiece material is not uniformly distributed. This would then lead to mass imbalance. Eccentricity attributable to mass imbalance would cause the workpiece to whirl. In Section 2 one saw that (1) mass imbalance induced whirling, (2) deflections due to nonlinear cutting force, and (3) reduction of workpiece mass and stiffness due to material removal were among parameters affecting workpiece vibrations. To facilitate workpiece whirling, deflections and material removal, the workpiece was assumed to be a system of 3 rotors connected by a flexible, massless shaft. Each rotor represents a distinctive section in the workpiece. That is, a section that has been machined, a section that is being machined and a section that is yet to be machined. Using the model configuration, whirling was realized as the rotary motion of the mass center of each rotor about their respective geometric center. If material distribution along the workpiece is both uniform and homogeneous, there will be no whirling. Fig. 6.1 shows the location of center of gravity of Rotor 1 subject to whirling and whirling-free. Same as Rotor 1, the gravitational center of Rotor 3 also coincides with its geometric center if whirling is ignored. Because it is dominated by the shape of the rotor, not by material inhomogeneity as described in section 2, subject to whirling or not, the location of gravitational center of Rotor 2 does not vary.

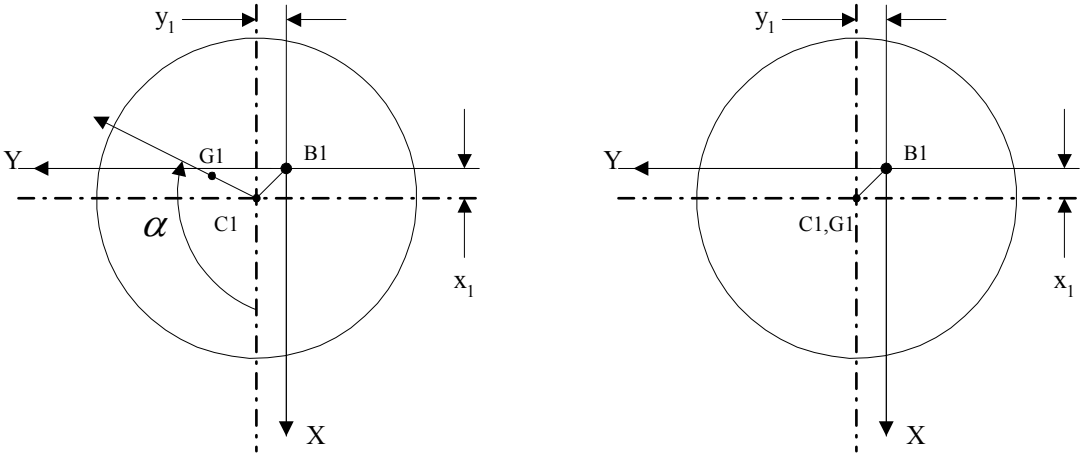

With whirling condition
C1G1=ε, eccentricity

Without whirling condition
C1G1=ε, eccentricity=0

Fig 6.1 Cross sections of Rotor 1 through its center of gravity

6.1 Numerical Results

In the sub-section 3 different spindle speeds (Ω = 1250rpm, 1500rpm and 1000rpm), 4 different eccentricities (ε_1 = 0.0mm, 0.2mm, 0.5mm, and 1.0mm), and 3 different DOCs (DOC = 1.25mm, 1.62mm and 1.75mm) are considered along with a constant chip width t_0 = 0.0965mm. Figs. 6.2-6.7 give the workpiece dynamical responses in the X- and Y-direction in response to the various DOCs, spindle speeds and eccentricities given above. Both with and without whirling cases are presented. As it is confined to the X-Y plane, whirling has a minimal effect on the Z-direction response. Therefore, the Z-direction time histories, instantaneous frequencies, and Lyapunov spectra for both with and without whirling cases do not differ discernibly. For this very reason only results associated with the X– and Y–direction are shown.

In Figs. 6.2 and 6.3, the left column plots time histories, whereas the right column shows the corresponding instantaneous frequency responses. The organization of Figs. 6.4 and 6.5 is slightly different, in which Lyapunov spectra are found at the bottom row. Since all Lyapunov spectra show zero exponents signifying dynamic stability, Figs. 6.6 and 6.7 have in their bottom rows plots that are zoom-ins of the instantaneous frequencies in the center row. This is done to better visualize the responses associated with the with- and without-whirling cases. It can be seen in Figs. 6.2 and 6.3 that the frequency responses of the with-whirling cases are better behaved than the without whirling cases. Also, for spindle speed Ω = 1250rpm and the relatively small eccentricity of 0.2mm, differences in the X-direction vibration magnitudes between the two cases are negligible (Figs. 6.2(a) and 6.2(b)). However, when eccentricity ε_1 = 1.0mm and Ω = 1500rpm are considered in Fig. 6.2(c), vibration amplitudes are seen to increase by 20 percent, thus negatively impacting the surface finish of the final product.

Similar behaviors are also observed in the Y-direction time histories in Fig. 6.3. Figs. 6.4 and 6.5 exhibit workpiece responses in the X- and Y-direction for Ω = 1500rpm, ε_1 = 1.0mm and DOC = 1.62mm. The plots illustrate that whirling due to material inhomogeneity results in slightly higher vibration amplitudes. Thus, whirling is seen to impact two essential qualities of the workpiece; namely, machining tolerance and true concentricity. However, when eccentricity is small and spindle speed is low, the effect of whirling on vibration amplitude is negligible (Figs. 6.2(a), 6.2(b), 6.3(a) and 6.3(b), 6.6(a), 6.7(a)). The two Lyapunov spectra in Figs. 6.4 and 6.5 indicate that the

responses are relatively stable even though they have bifurcations in the low frequency regions. In all the figures, the workpiece characteristic frequency at 3340Hz can be seen in both with- and without- whirling cases. However, whirling frequencies at 20.8Hz (Figs. 6.2(b) and 6.3(b)), at 25Hz (Figs. 6.2(c), 6.3(c), 6.4 and 6.5) or at 16.7Hz (Figs. 6.6 and 6.7) are observed only in the "with-whirling" case. In all the cases a 420Hz frequency component, which is the tool natural frequency, is also excited. The tendency for the "without whirling" case to further bifurcate is evident. This can be clearly seen in the "zoomed-ined" instantaneous frequency plots Figs. 6.6(c) and 6.7(c), where DOC = 1.75mm, Ω = 1000rpm and ε_1 = 0.5mm are considered. Even though machining stability is confirmed with Lyapunov spectra, these low frequency vibrations can affect the surface quality of the final product. All the above observations readily suggest that whirling is one of the dominant parameters impacting machining stability.

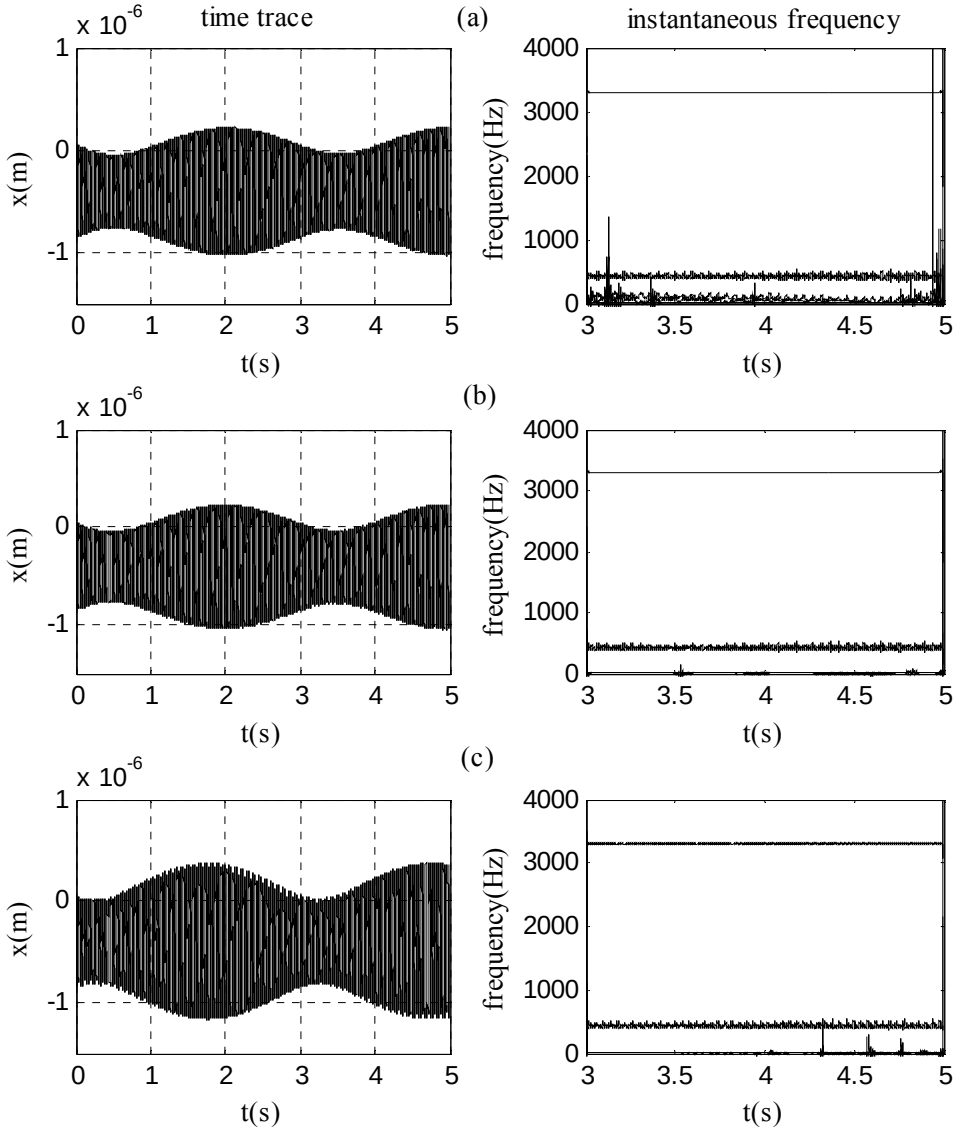

Fig.6.2 Workpiece vibration in X-direction for DOC = 1.25mm and (a) Ω = 1250 rpm without whirling (b) Ω = 1250 rpm with whirling and ε_1 = 0.2mm (c) Ω = 1500rpm with whirling and ε_1 = 1.0mm

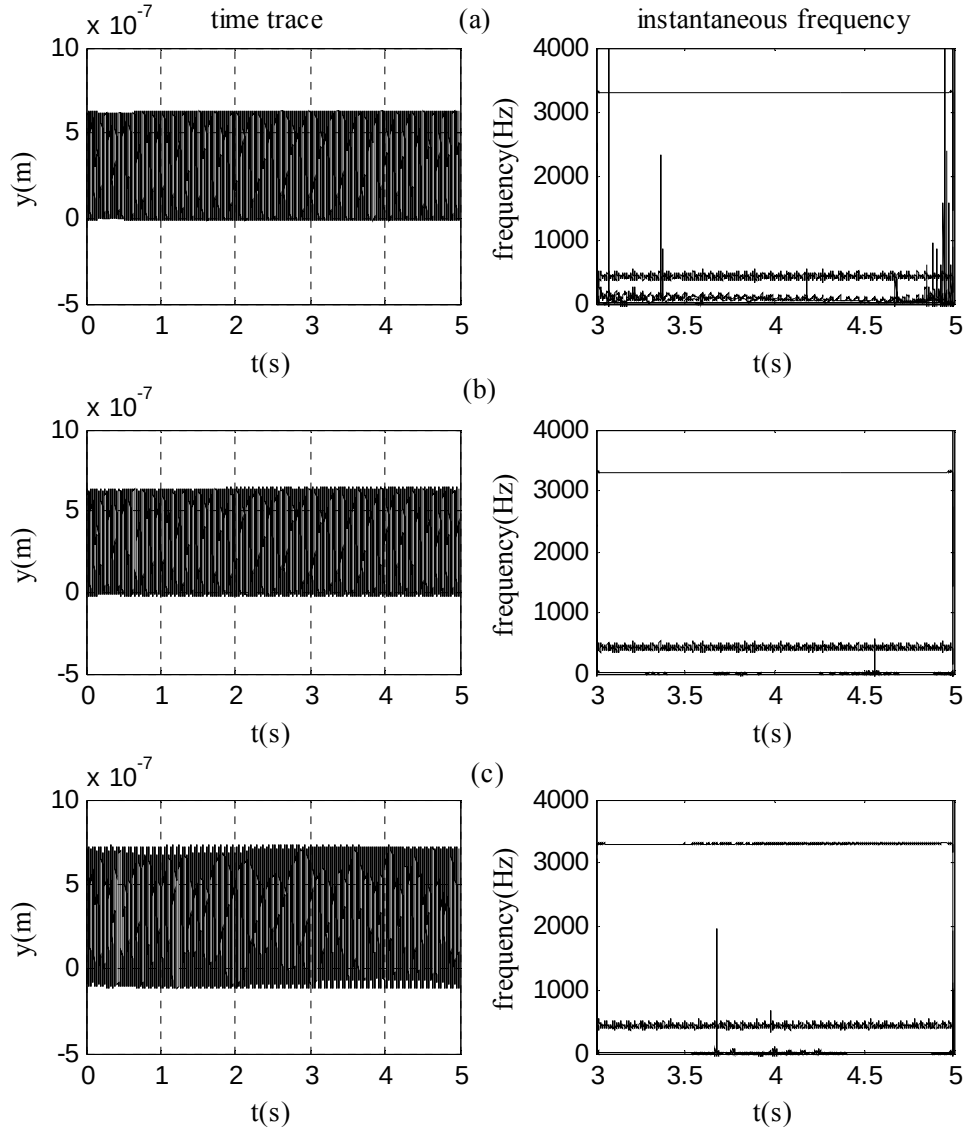

Fig.6.3 Workpiece vibration in Y - direction for DOC=1.25mm and (a) Ω = 1250 rpm without whirling (b) Ω = 1250 rpm with whirling and ε_1 = 0.2mm (c) Ω = 1500rpm with whirling and ε_1 = 1.0mm

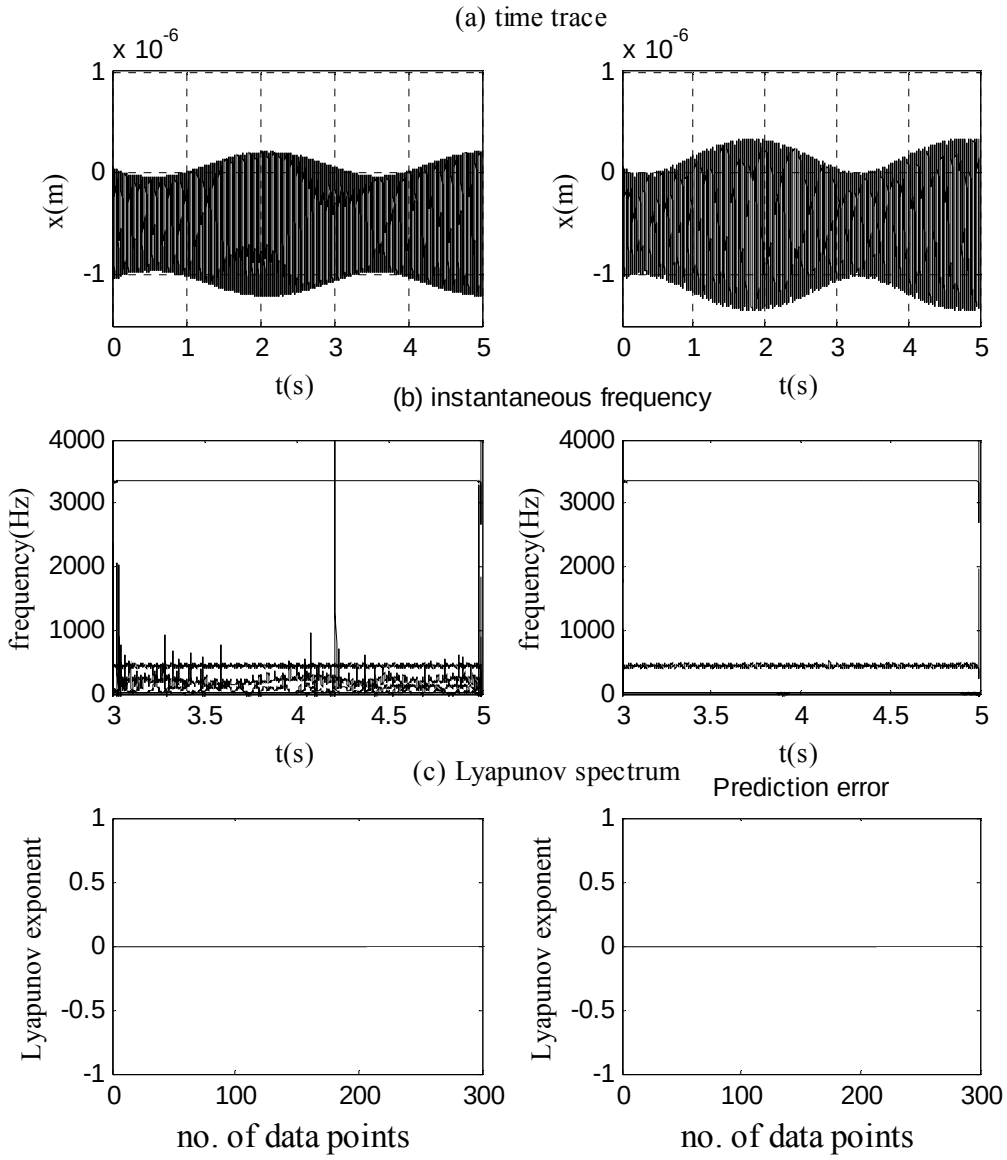

Fig.6.4 X - direction vibration response for DOC = 1.62mm and Ω = 1500rpm with whirling of ε_1 =1.00mm (right) and without whirling (left)

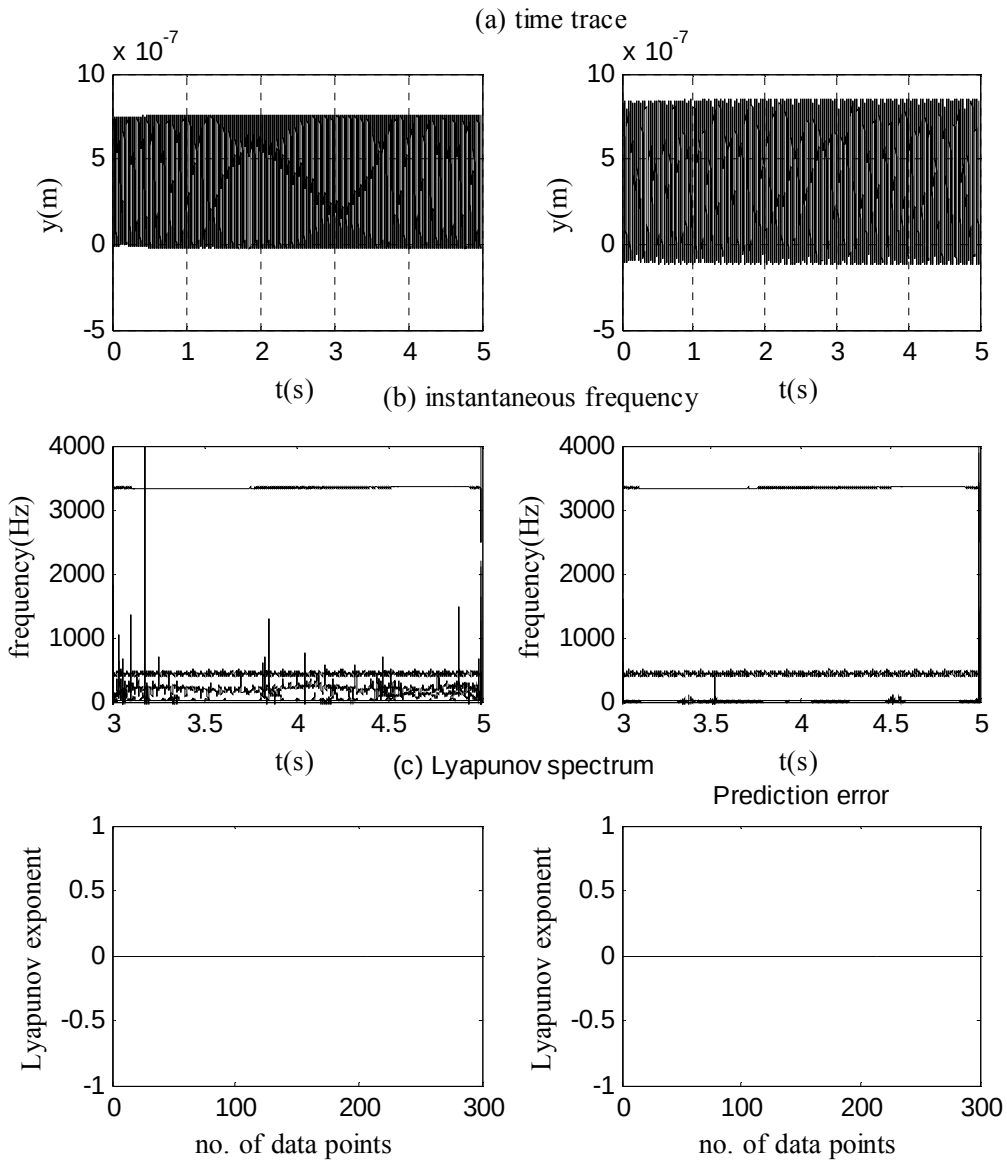

Fig.6.5 Y - direction vibration response for DOC = 1.62mm and Ω = 1500rpm with whirling of ε_1 =1.00mm (right) and without whirling (left)

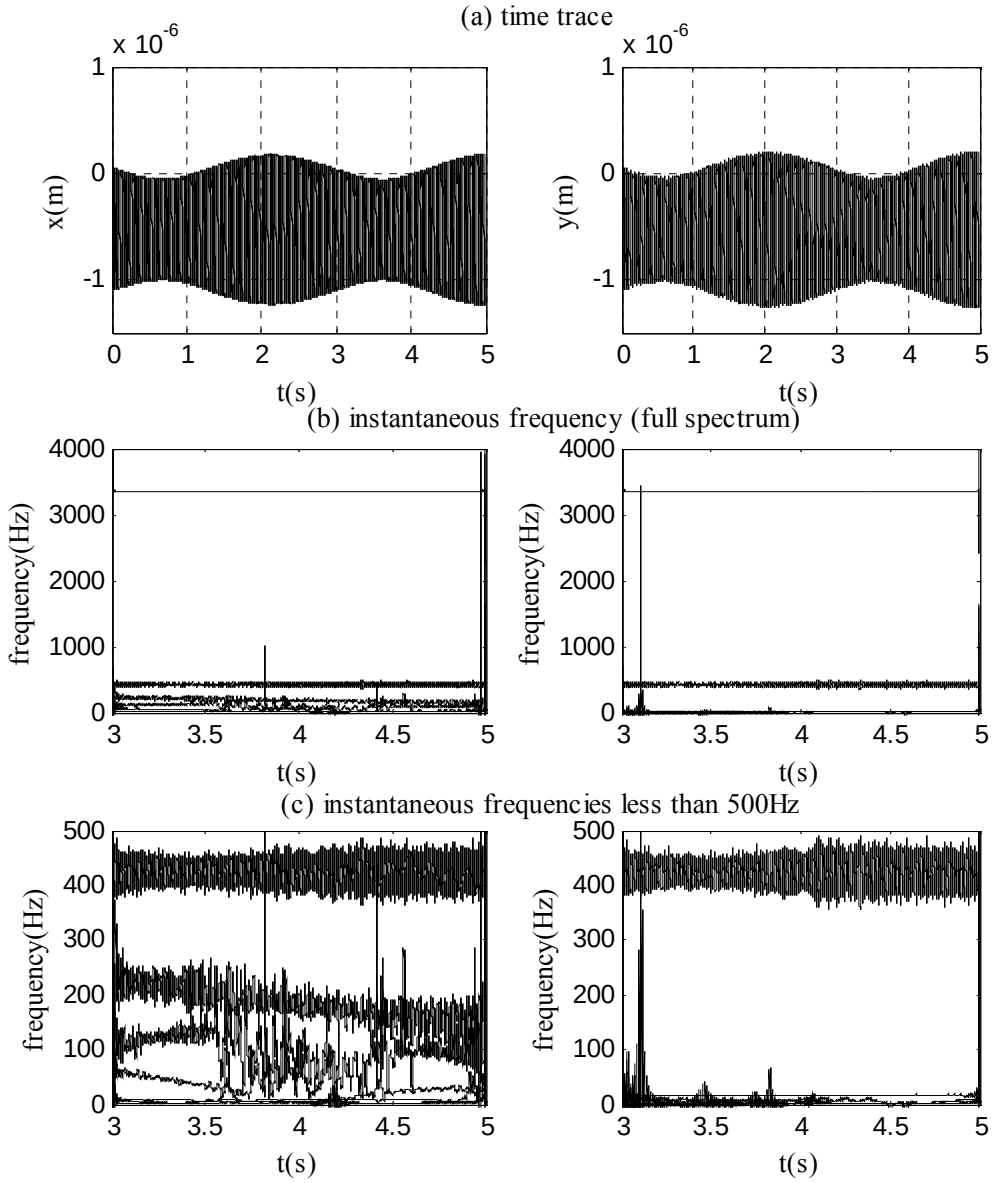

Fig.6.6 X - direction vibration response for DOC = 1.75mm and Ω = 1000rpm with whirling of ε_1 = 0.5mm (right) and without whirling (left)

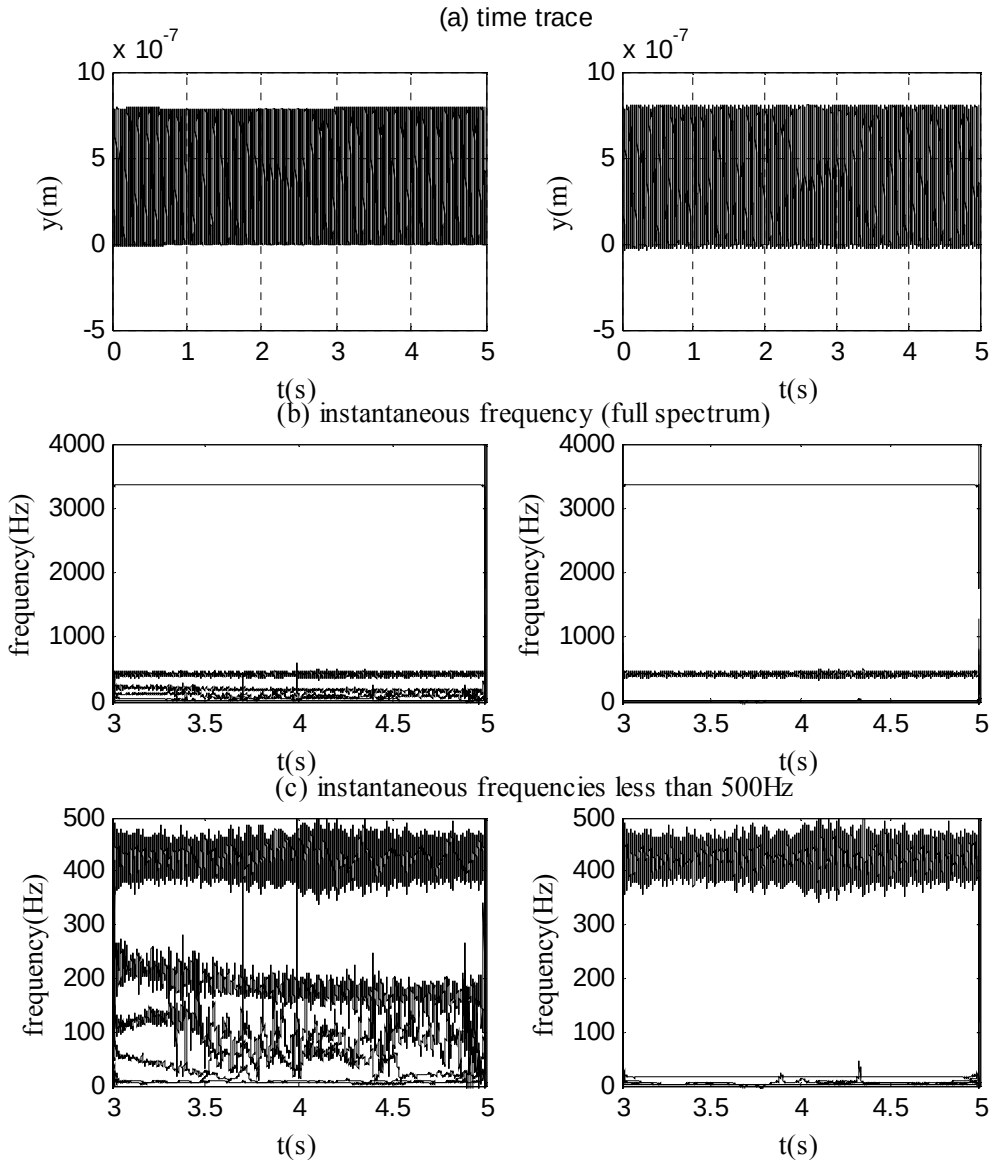

Fig.6.7 Y - direction vibration response for DOC = 1.75mm and Ω = 1000rpm with whirling of ε_1 = 0.5mm (right) and without whirling (left)

6.2 Discussions

A comparison of with- and without-whirling on machining stability was explored. It was shown that whirling is non-negligible if the fundamental dynamic characteristics of a machining process are to be fully understood. When whirling was considered with moderate eccentricity of 1.0mm, the vibration amplitudes of the workpiece were about 20 percent higher than those of without whirling case at slightly lower spindle speed. Thus, investigations without considering whirling would inevitably while adversely underestimate machining vibration amplitudes. However, when eccentricity was small, differences in vibration amplitudes between the with- and without-whirling cases were negligible. Machining dynamic responses with whirling being considered were more stable than those without whirling. It was also seen that cases without considering whirling tend to overestimate machining state as more lower frequencies bifurcated with broadband characteristics. Thus, it can be concluded that having small eccentricity due to material inhomogeneity helps stabilize machining dynamic response while keeping workpiece vibration amplitudes at the same level as the without-whirling case. Even though cutting force in the Z-direction was modeled as a nonlinear function coupled with x and y vibrations, whirling had an insignificant impact on tool motion for the feed rate considered in the section. Referring to Figs. 4.2, 4.3 and 4.9, one also noted that there was no whirling frequency component when the system dynamics was in chaotic state. Thus, whirling was found to have a negligible effect when the chaotic state of chatter occurred.

7. IMPLICATIONS OF MODEL LINEARIZATION ON CUTTING DYNAMICS

The section examines the implications of applying linear and nonlinear models to the comprehension of machining states subject to whirling and regenerative cutting force. The dynamic responses of a linearized model are evaluated against the results generated by its nonlinear version. The values used for all structure and tool parameter are kept the same as in Section 4. Since workpiece deflections induced by the exertion of cutting force components are considered, vibrations of both the tool and workpiece are examined. Nonlinearity in the nonlinear model is introduced through the presence of nonlinear cutting force and cubic nonlinear stiffness. These two terms of nonlinearity are linearized to generate the linear version. It is emphasized that the mass and the stiffness of the workpiece vary with time in both models. Details of linearization along with justifications are outlined in the immediate sub-section that follows.

7.1 Model Linearization

For the sake of continuity, the machining model developed in Section 2 is briefly re-capped. The workpiece is modeled as three rotor sections connected by a massless shaft as shown in Fig. 2.2. Rotor 1 is the unmachined section, Rotor 3 is the machined section, and the section being machined is represented by Rotor 2. Eqs. (2.1-2.56) found in Section 2 are the associated nonlinear model that describes the workpiece-tool dynamics subject to imbalance-induced whirling and regenerative cutting force.

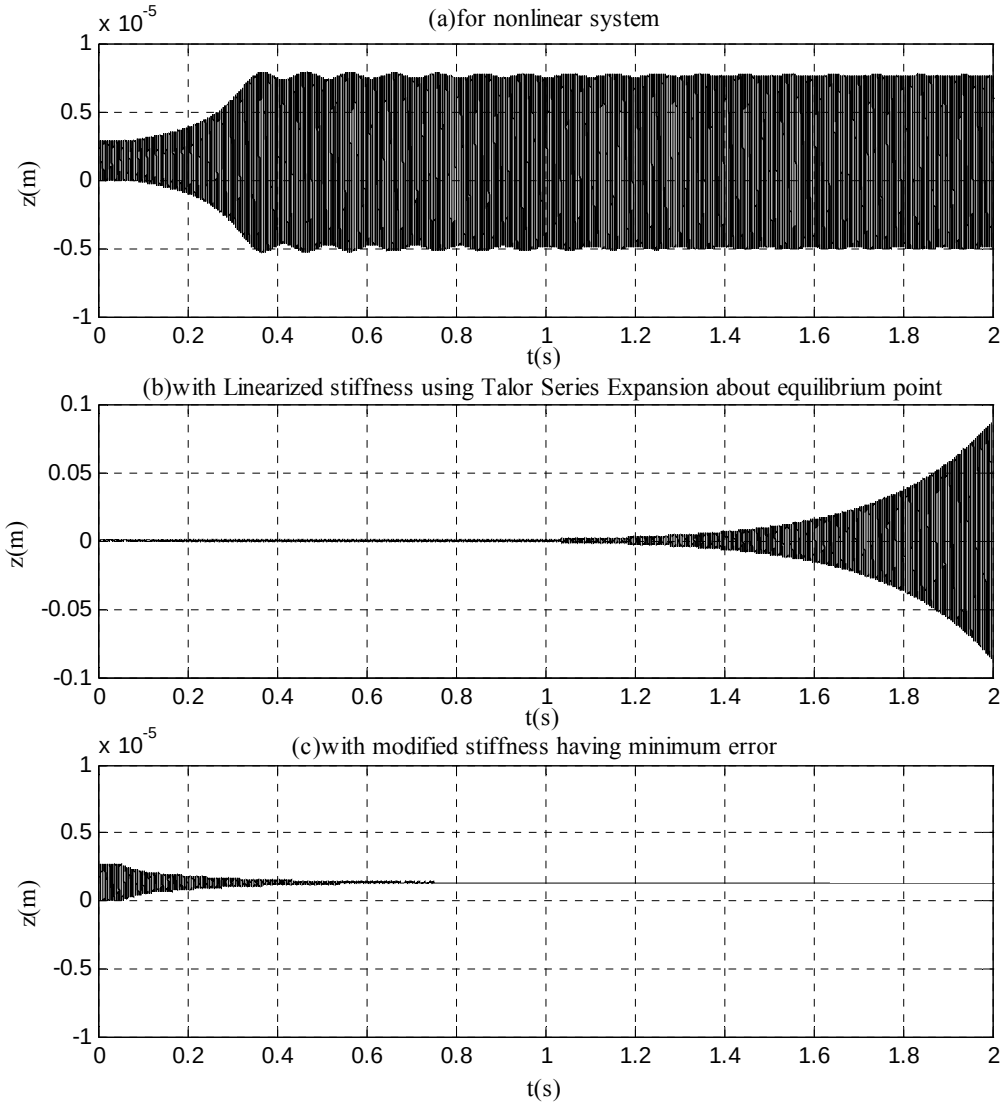

Fig.7.1 Z - direction vibration responses for DOC = 1.00mm

Whirling and deflection due to cutting force set the long workpiece to vibrate in the plane perpendicular to the spindle axis, Z. As has been observed in Section 4, the workpiece vibrates with significant amplitudes in this plane, but not along the Z-axis. Specifically, the model was so developed that workpiece motions were accounted for in the XY plane (Fig. 2.4) using equations of motion, Eqs. (7.1-7.2), and tool responses were described by the Z-direction equation of motion, Eq. (7.3). (All duplicated from Eqs. 2.36 - 2.38.)

$$f_1(t)\ddot{x}_2 + f_2(t)\dot{x}_2 + f_3(t)x_2 = f_4(t, x_2, y_2, z_t, z_t') \tag{7.1}$$

$$f_5(t)\ddot{y}_2 + f_6(t)\dot{y}_2 + f_7(t)y_2 = f_8(t, x_2, y_2, z_t, z_t') \tag{7.2}$$

$$M_Z\ddot{z}_t + k_Z z_t + k_{ZC} z_t^3 = f_9(t, x_2, y_2, z_t, z_t') \tag{7.3}$$

where $f_i(t, x_2, y_2, z_t, z_t')$ are nonlinear functions with i = 1...9.

Linearization of nonlinear equations about equilibrium points of interest is generally driven by the need for analyzing system response and developing controller. Since points of linearization play a key role in determining system dynamics, it is imperative that all essences of system dynamics are not lost to linearization. If not, understanding the underlying physics would fall short and the controller developed based on the linearized equation would be ineffective. When the equations of motion of the nonlinear machining model are linearized about $(0,0,Z_0)$ (Z_0 is the equilibrium point of the tool at (x=0, y=0) position of the workpiece selected to satisfy the ultimate goal for achieving dimensionally precise workpiece), the effect of stiffness component that is derived from the corresponding nonlinear stiffness becomes negligible. This in turn causes the system to become unstable even for the smallest DOC considered. Infinitely

growing amplitude of vibration in linearized models has been reported [30]. In order to minimize the error, nonlinear stiffness is linearized in a way that the error between nonlinear stiffness function and linearized function is minimized for a selected region. A comparison of time domain behaviors for the nonlinear and two linearized cases are shown in Fig. 7.1 for DOC = 1.00mm.

7.1.1 Linearization of Nonlinear Stiffness

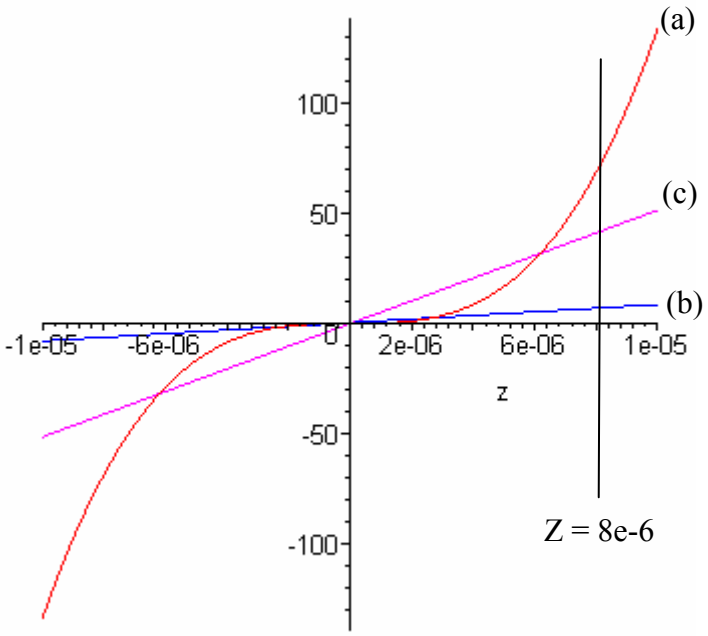

Fig. 7.2 Comparison of stiffness functions

In Fig. 7.2, the nonlinear stiffness term, $k_{ZC} z_t^{\,3}$, is shown by function (a) and the linearized stiffness term using the linear portion of the Taylor's Series Expansion, $k_{ZC}(Z_0^3 + 3Z_0^2 z_t)$, where Z_0 is the equilibrium position in the Z–direction, is represented by (b). Let (c) be the linear function, $k_{ZC} B z_t$, that gives the minimum error for the region between Z = 0 and Z = 8e-6 that encloses the origin. The region for calculating minimum error is selected due to the fact that the maximum vibration amplitude of the nonlinear system in stable condition is Z = 8e-6. The value of B can be calculated by finding (c) that gives the minimum error comparing with the nonlinear function. The squared of the error is therefore

$$E = (k_{ZC} z_t^3 - k_{ZC} B z_t)^2 \tag{7.4}$$

The error has to be squared, or else the negative and positive areas would cancel out and result in an incorrect answer. The total error can be found by integrating Eq. (7.4) over the range between 0 and 8e-6,

$$E_T = 0.005379494473 - 235352883.2B + .3064490667\text{e}19B^2 \tag{7.5}$$

Differentiating Eq. (7.5) with respect to B and equating it to zero, the value of B for the minimum error is found to be B = 0.384e-10. Fig. 7.3 illustrates the comparison of the squared error functions for (a) Taylor's series approximation about the equilibrium point and (b) modified stiffness function with B.

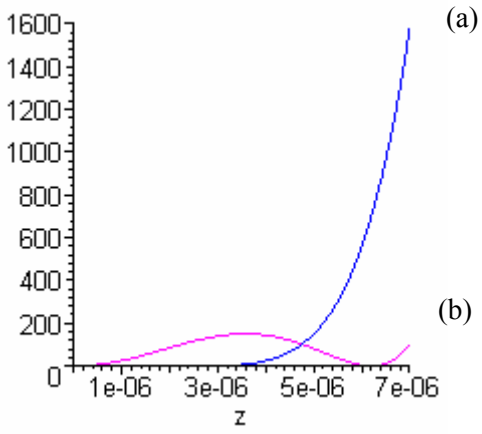

Fig. 7.3 Comparison of squared error functions

7.1.2 Linearized Model

The set of nonlinear equations, Eqs. (7.1 – 7.3), is linearized about the point (0, 0, Z_0) and using the nonlinear stiffness component determined in the previous section. The value of Z_0 depends on the cutting force. However, the cutting force always carries the term, $q = z_t - z_t'$, which goes to zero for the equilibrium state as both z_t and z_t' goes to Z_0. Hence it can be stated that the system is linearized about $x_2 = 0$, $y_2 = 0$ and $q = 0$ with the modified stiffness term mentioned earlier. In consequence, the equations of motion for the linearized model become

$$f_1(t)\ddot{x}_2 + f_2(t)\dot{x}_2 + f_3(t)x_2 = a_1\Omega^2\cos\Omega t - a_2\Omega\sin\Omega t - F_X \tag{7.6}$$

$$f_5(t)\ddot{y}_2 + f_6(t)\dot{y}_2 + f_7(t)y_2 = a_1\Omega^2\sin\Omega t + a_2\Omega\cos\Omega t + F_Y \tag{7.7}$$

$$M_Z\ddot{z}_t + (k_Z + k_{ZC}B)z_t = F_Z \tag{7.8}$$

where $F_X = F_{X0} + A_X x_2 + B_X y_2 + C_X(z_t - z_t')$ (7.9)

$$F_Y = F_{Y0} + A_Y x_2 + B_Y y_2 + C_Y (z_t - z_t') \tag{7.10}$$

$$F_Z = F_{Z0} + A_Z x_2 + B_Z y_2 + C_Z (z_t - z_t') \tag{7.11}$$

$$a_1 = m_1(t)\varepsilon_1 + m_3(t)\varepsilon_3 \tag{7.12}$$

$$a_2 = \pi \rho \dot{l} (r_1^{\,2}\varepsilon_1 - r_3^{\,2}\varepsilon_3) \tag{7.13}$$

Here $m_1(t)$ and $m_3(t)$ are masses of the 1st and 3rd rotors, respectively. The eccentricities of the 1st and 3rd rotors are ε_1 and ε_3. The density of the workpiece is ρ and $\dot{l}$ is the constant feed rate of the tool in the direction parallel to the Z-axis. The radii of 1st and 3rd rotors are r_1 and r_3, respectively. Constants A, B, C, F_{X0}, F_{Y0}, and F_{Z0} in the linearized cutting force components are dependent of cutting parameters and tool geometry. The equations of motion for the nonlinear model (Eqs. 7.1 - 7.3) and equations of motion for the linearized model (Eqs. 7.6 - 7.8) can be numerically integrated to obtain x_2, y_2, and z_t vibrations along with the cutting force components.

7.2 Description of Numerical Results

Both the linearized and nonlinear models are run for six different DOCs to generate time domain responses. All data are taken for a spindle speed at Ω = 1250rpm and 0.0965mm chip width (0.0965mm/rev feed rate). DOC = 1.62mm and 2.49mm are considered along with tool geometrical properties and cutting parameters for comparison with the available physical results in [10]. Values for M_Z, k_C, and k_{CZ} are 9kg, $5.7*10^7$ N/m and $1.34*10^{17}$ N/m^3, respectively.

7.2.1 Comparison of Models: Workpiece Vibration

Figs. 7.4-7.9 present workpiece X- and Y-direction responses for both the nonlinear and linearized models. Except for Fig. 7.9, all plots in the followings have time traces displayed on top of their respective instantaneous frequency response. Except for the cases corresponding to DOC = 1.00mm and 2.00mm, the Lyapunov spectra all demonstrate stability with zero exponents similar to figures found in Section 4. In other words, there is no difference in Lyapunov spectra between the nonlinear and linearized models for the workpiece responses. Due to this very reason, only time histories and instantaneous frequency plots are shown in Figs. 7.4 – 7.8. In Fig. 7.9, the plots on top depict time series and those immediately below give the corresponding Lyapunov exponents. All workpiece time-frequency plots have two major frequency components at 20.8 Hz and 3300Hz, which correspond to the whirling frequency and workpiece natural frequency, respectively. However, the tool natural frequency at 420Hz is not seen at most DOCs being considered. This is especially so with the responses of the linearized model. For the case of DOC = 1.00mm in Fig. 7.4, both the

nonlinear and linearized models demonstrate similar X- and Y- directions behaviors indicating a stable motion. The instantaneous frequency plots indicate a behavior of stability despite the presence of a period-doubling component at 1700Hz. Furthermore, the frequency responses of the nonlinear model demonstrate a broadband behavior that corresponds to the tool natural frequency at 420Hz. Recall that in Fig. 4.5 the Lyapunov exponent was nonzero for this case. It should be noted that the X-direction maximum vibration amplitude is about twice that of the Y- direction vibration amplitude.

When DOC is increased to 1.25mm in Fig 7.5, the time domain responses of the two models illustrate similar stable behaviors. But their frequency domain responses indicate two different states of motion. The linearized model displays period-doubling bifurcation; whereas the frequency response of the nonlinear model at DOC = 1.25mm is more stable than at DOC = 1.00mm. Note that the DOC = 1.00mm case has more frequency components. These components vanish with the increased DOC at 1.25mm. Fig. 7.6 demonstrates the dynamical responses for DOC = 1.62mm. System frequency responses for the nonlinear model are comparatively more stable than that of the linear model. On the other hand, the X- and Y- directions frequency plots for the linearized model reveal a broadband behavior that leads to ultimate instability even though the corresponding time responses seem demonstrate stability.

Increasing DOC further to 1.75mm in Fig. 7.7, X- and Y- directions behaviors of the nonlinear and linearized models become very similar. Moreover, these are highly bifurcated states of motion. Any slight disturbance would tilt the system to chaos. Fig. 7.8 demonstrates a chaotic situation associated with DOC = 2.00mm for the nonlinear system. The vibration magnitudes in both directions are seen to be growing significantly. The nonlinear model exhibits the most prominent chaotic characteristics. In contrast, the corresponding linearized system maintains constant time domain amplitude with predictable pattern. Nevertheless, both the linear and nonlinear systems display instability in the instantaneous frequency domain. Fig. 7.9 presents the time responses between 3.00 and 3.02 seconds, along with the corresponding Lyapunov spectra. Time history plots clearly show that the nonlinear and linearized models behave differently. The Y- direction Lyapunov spectrum seen in Fig. 7.9(b) for the nonlinear case exhibits a more chaotic state with larger exponents than the linearized case. Nevertheless, both the nonlinear and linearized versions display instability with positive Lyapunov exponents.

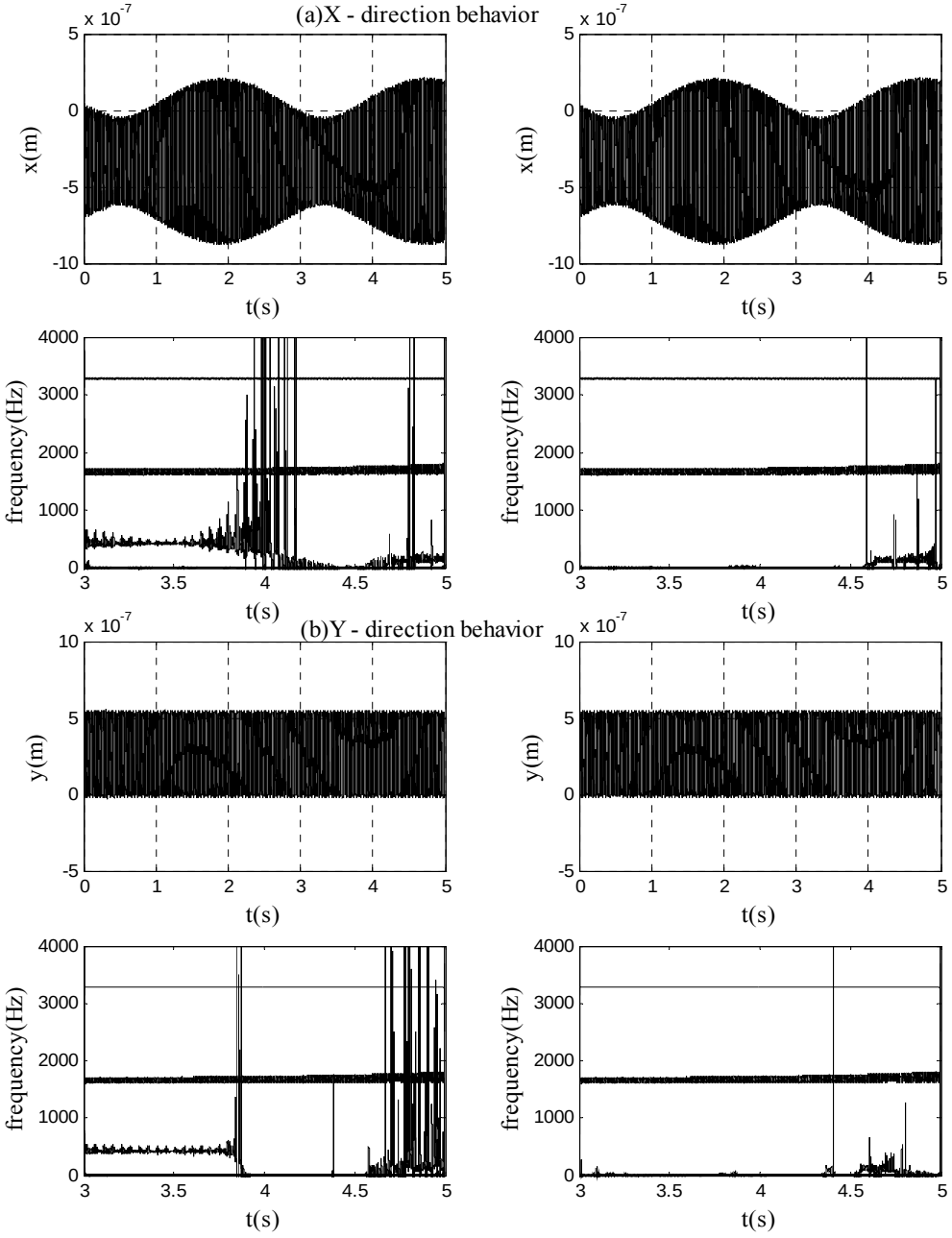

Fig. 7.4 X- and Y- direction responses for nonlinear (left) and linearized (right) models for DOC = 1.00mm at Ω = 1250rpm

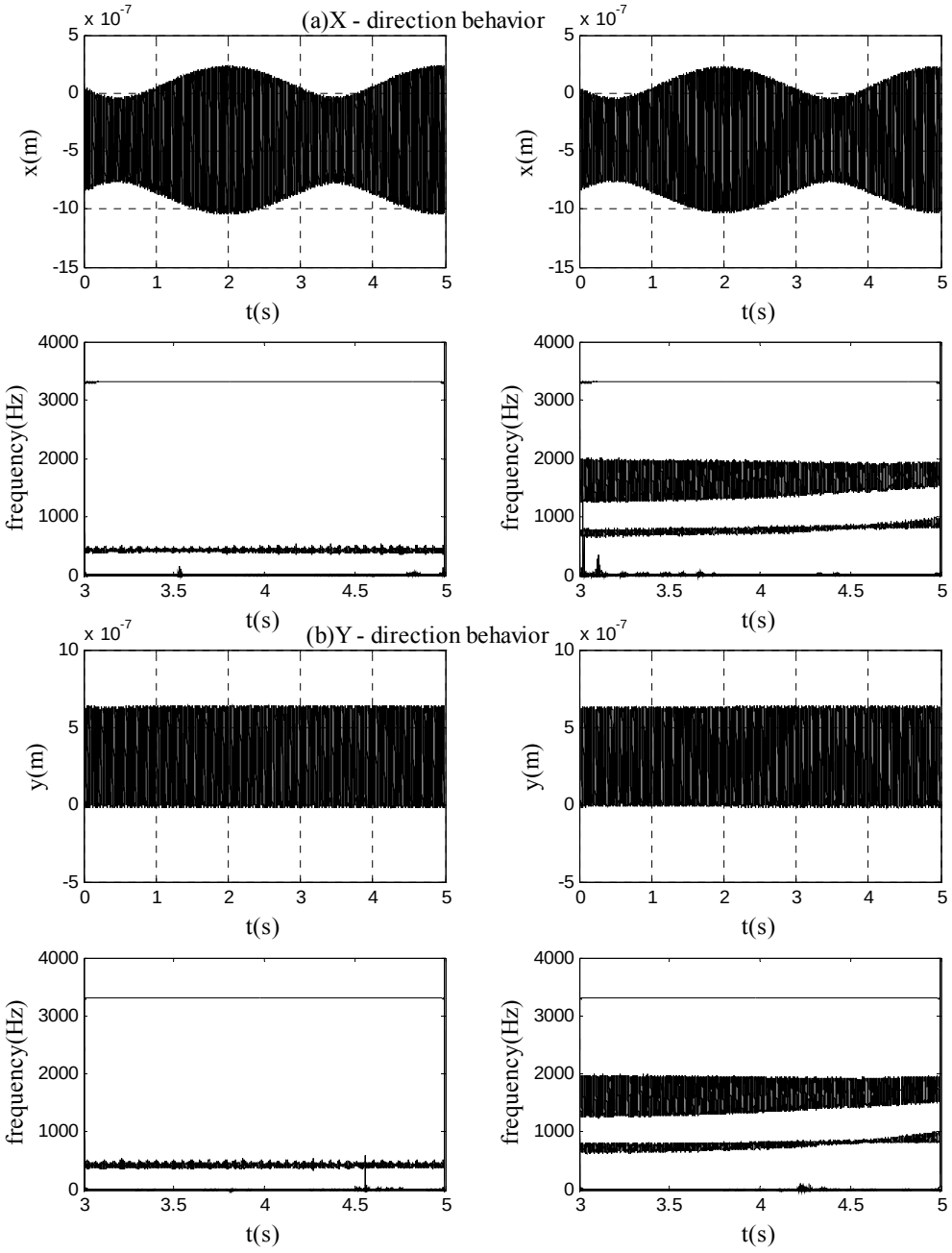

Fig. 7.5 X- and Y- direction responses for nonlinear (left) and linearized (right) models for DOC = 1.25mm at Ω =1250rpm

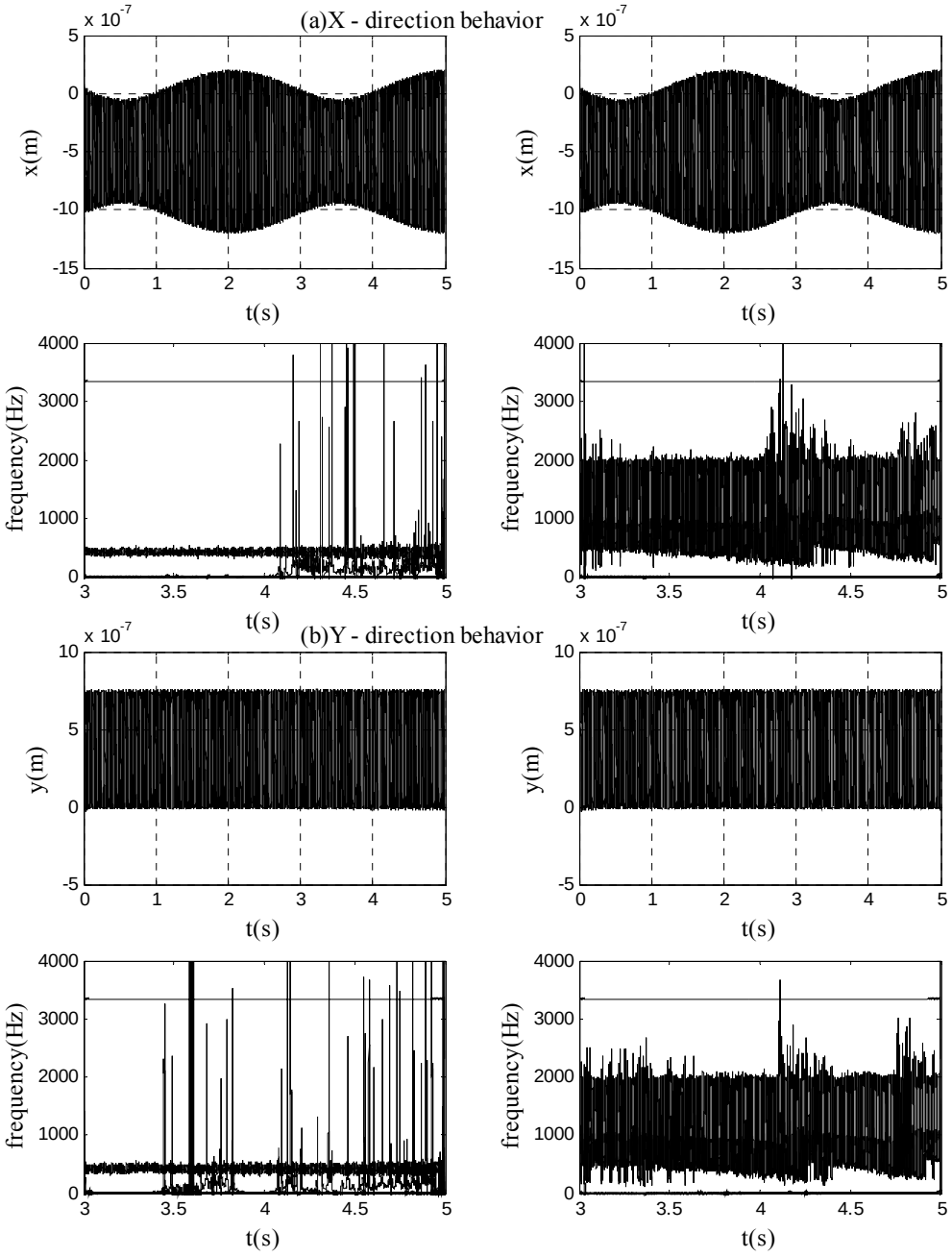

Fig. 7.6 X- and Y- direction responses for nonlinear (left) and linearized (right) models for DOC = 1.62mm at Ω = 1250rpm

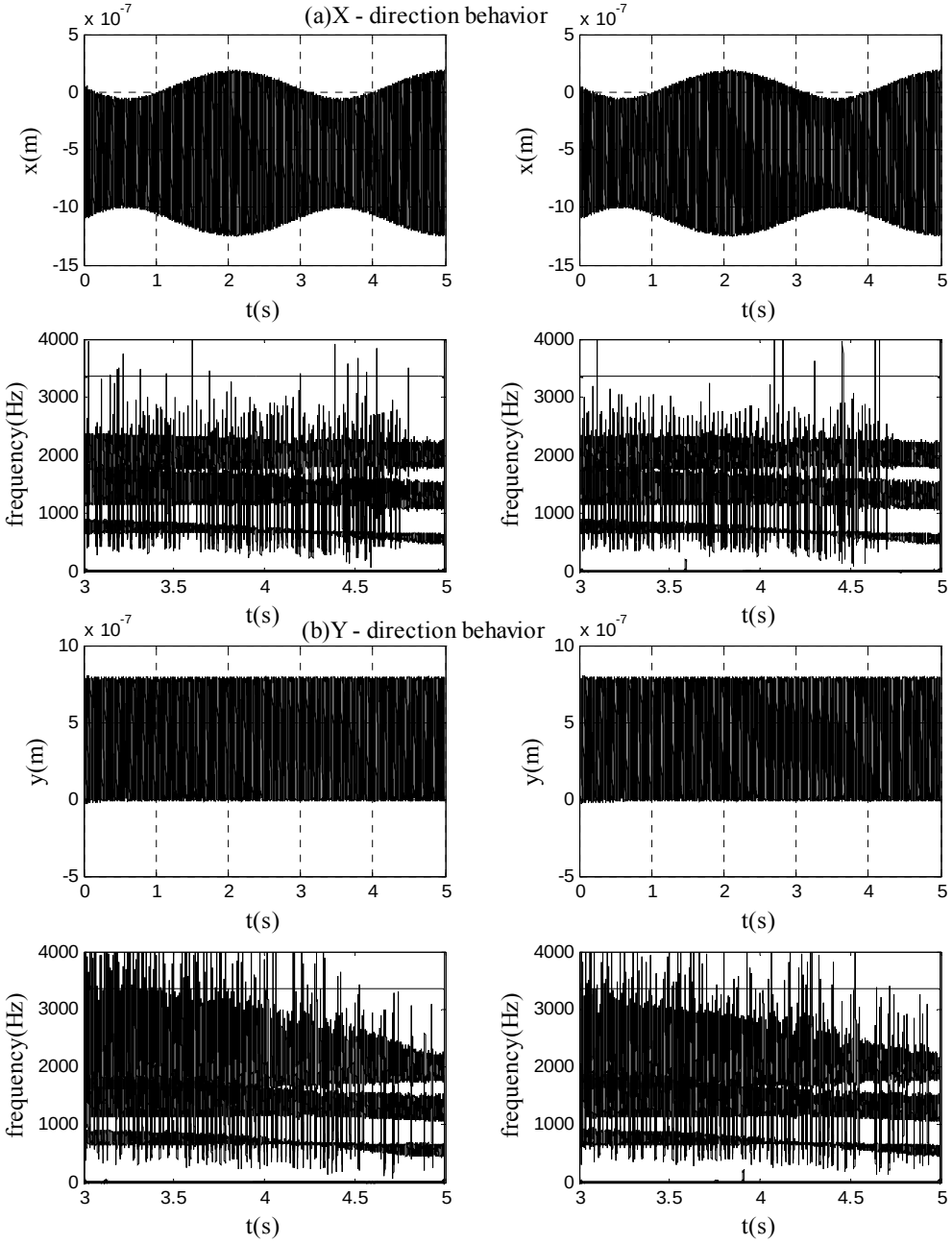

Fig. 7.7 X- and Y- direction responses for nonlinear (left) and linearized (right) models for DOC = 1.75mm at Ω = 1250rpm

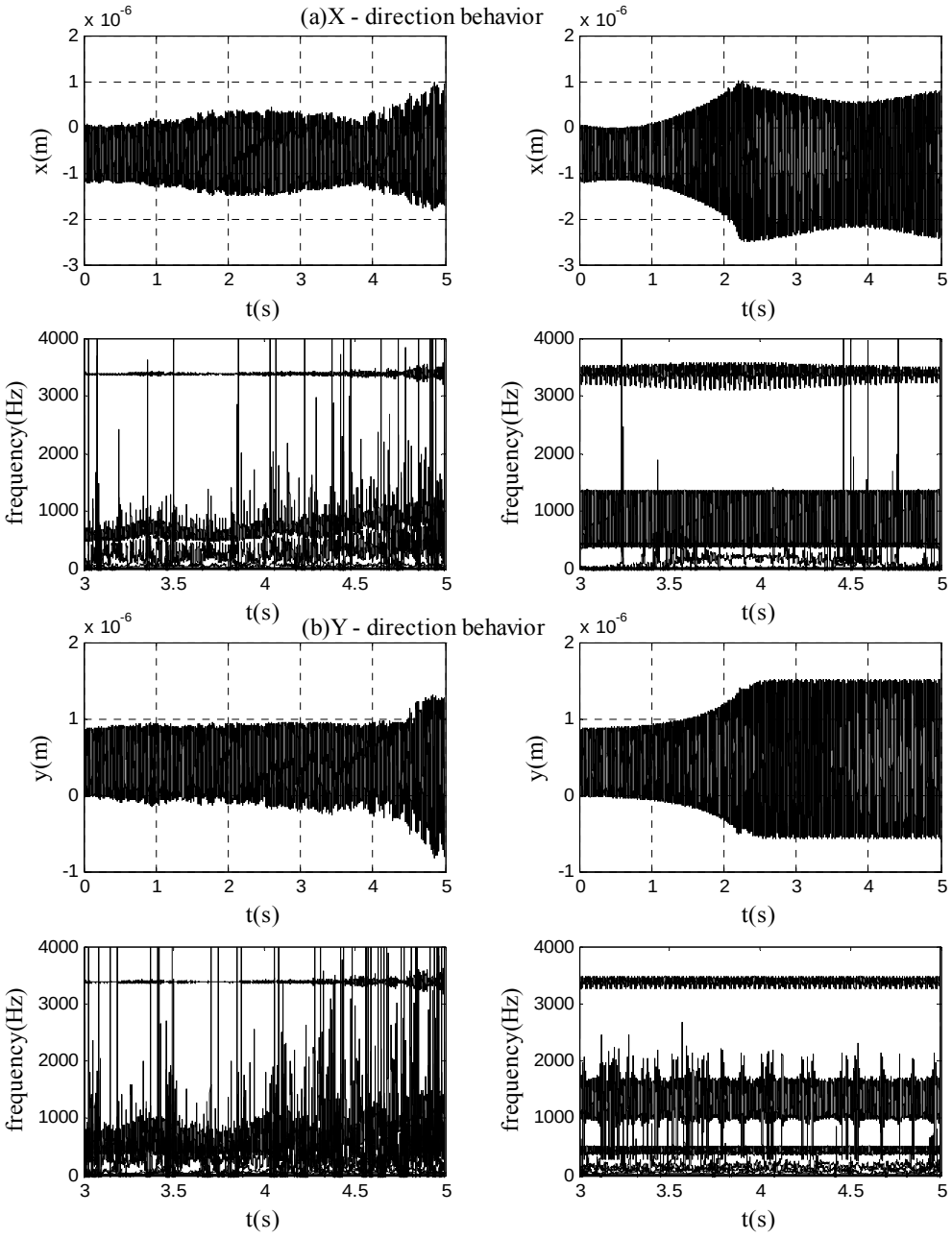

Fig. 7.8 X- and Y- direction responses for nonlinear (left) and linearized (right) models for DOC = 2.00mm at Ω = 1250rpm

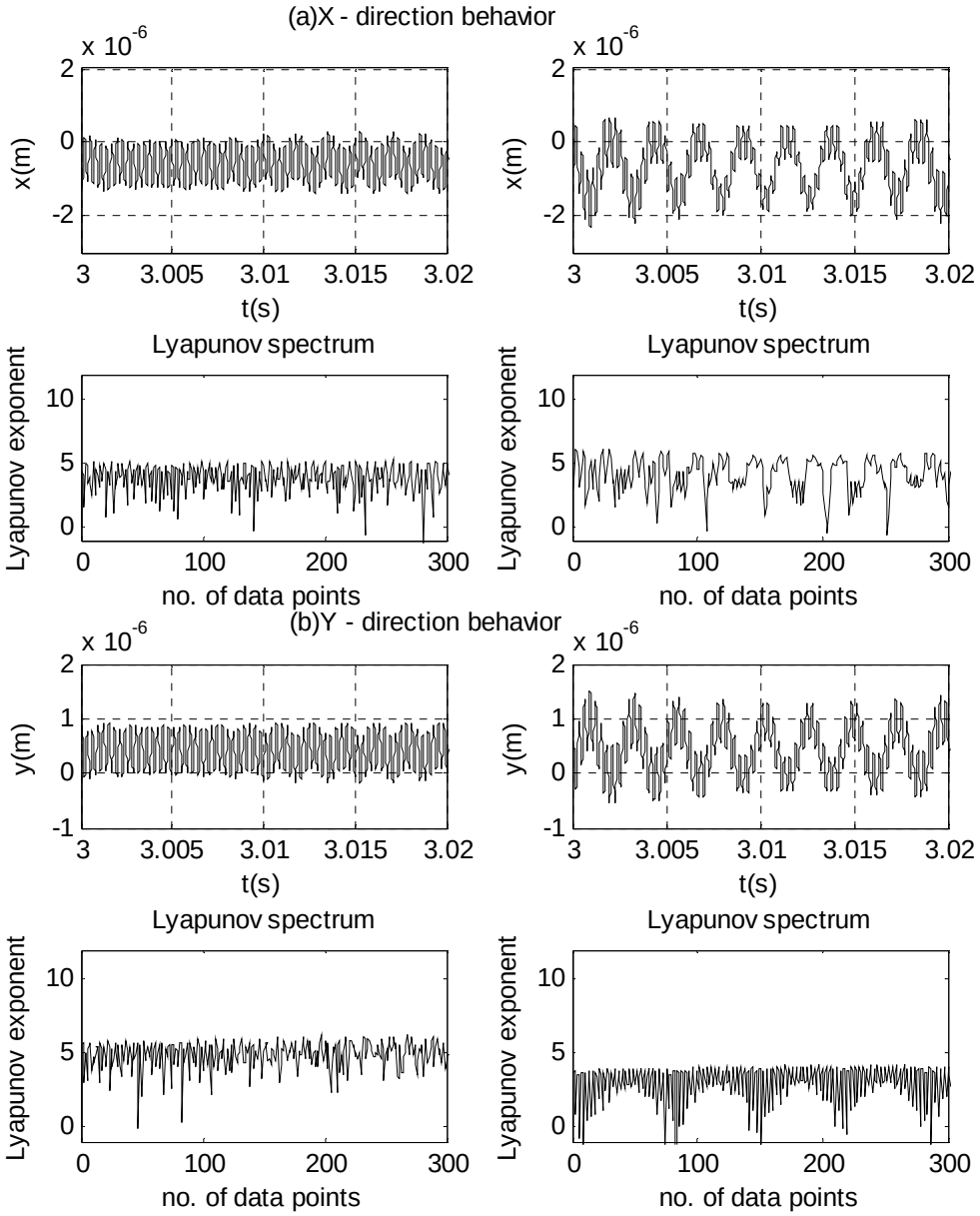

Fig. 7.9 X- and Y- direction Lyapunov spectra for nonlinear (left) and linearized (right) models for DOC = 2.00mm at Ω = 1250rpm

7.2.2 Comparison of Models: Tool Vibration

As previously described, complex tool-workpiece vibrations are realized by coupling workpiece motions in the XY-plane with tool motions in the Z-direction. It was seen in Fig. 7.1(b) that linearization about the equilibrium point at (0, 0, Z_0) resulted in an exponential growth of the tool vibration amplitude in the Z- direction. On the other hand, modifications to stiffness component are seen to bring about tool responses in the Z-direction with negligible vibration amplitudes in Figs. 7.10-7.12, where DOCs of 1.00mm, 1.25mm, 1.62mm and 1.75mm are considered. Both nonlinear and linearized models display dynamic stability with zero-exponent Lyapunov spectra (not shown). It is noted that the corresponding frequency domain responses for the linearized case as presented all demonstrate dynamic instability. While this is the case with the linearized model, the nonlinear model reveals different stages of dynamics for each DOC – an observation that is in line with the real-world experience. The major frequency component, which is the tool natural frequency at 420Hz, is seen in all plots. The Z-direction frequency response associated with DOC = 1.00mm in Fig. 7.10 illustrates more frequency components than the dynamically stable DOC = 1.25mm case at any time instance. Similar behaviors are observed for the workpiece responses in both X- and Y-directions at these two DOCs.

When DOC is increased to 1.62mm, the low frequency region exhibits a slightly broader bandwidth for the nonlinear response, as seen in Fig. 7.11(a). However, comparing with the frequency response of the corresponding linearized model, the instantaneous frequency response of the nonlinear model is relatively stable. The dynamical behaviors of the linear and nonlinear models for DOC = 1.75mm are given in Fig. 7.11(b). In contrast to the X- and Y-direction behaviors of the workpiece, the tool response in the Z-direction exhibits stability in both the frequency and time domains for the nonlinear model. With DOC being increased further to 2.00mm in Fig. 7.12, the response of the nonlinear model is clearly chaotic, while the corresponding linearized model shows a considerable growth in vibration amplitude that is approximately twice of the nonlinear model's amplitude. Time histories, frequency responses and Lyapunov spectra all indicate a chaotic motion for the nonlinear model. In addition, the linearized version does not display any chaotic behavior. The corresponding Lyapunov spectra demonstrate stability with zero exponents. Although vibrating with large amplitudes, the instantaneous frequency of the linearized model displays a relatively stable motion with only a couple of bifurcations.

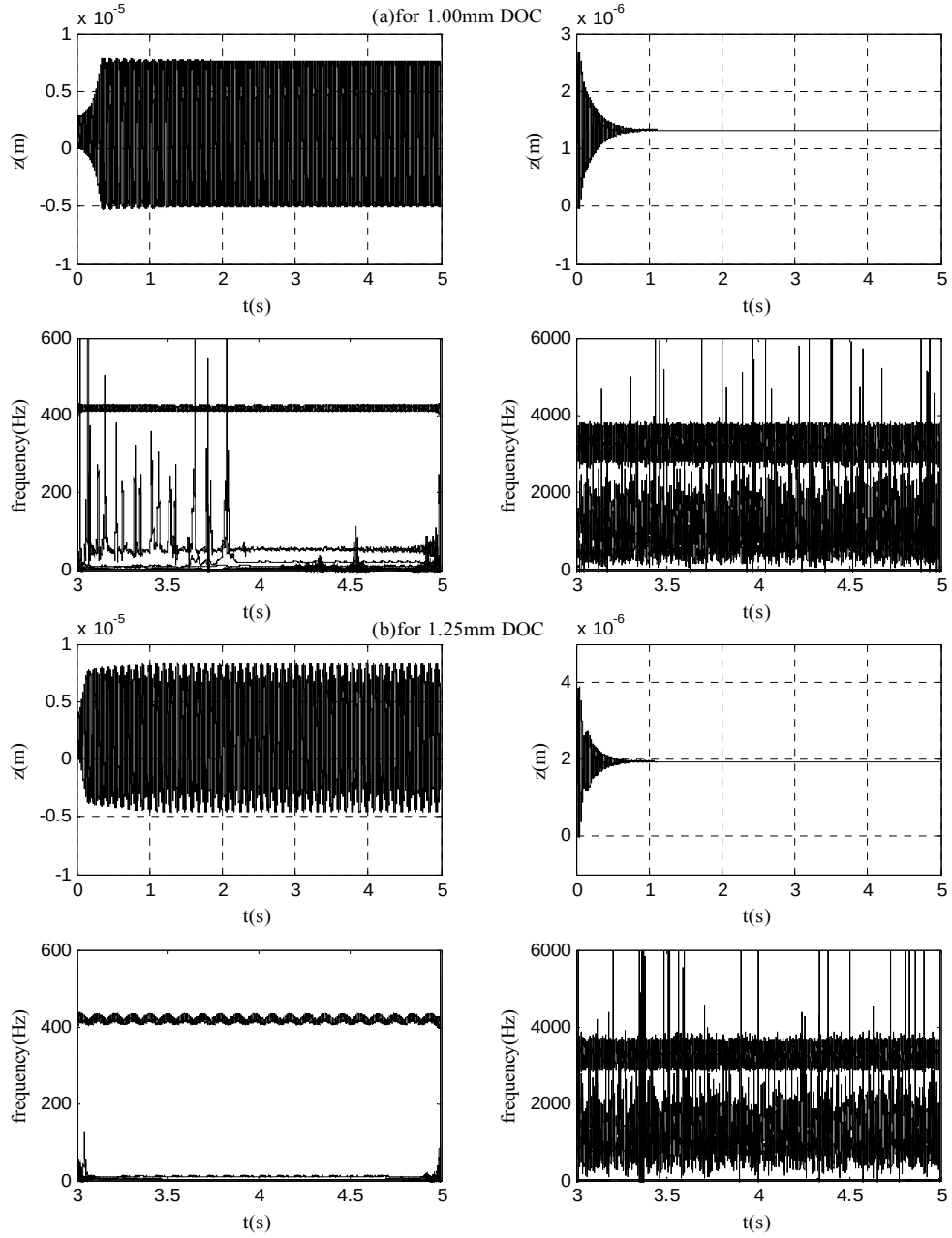

Fig. 7.10 Z - direction responses for nonlinear (left) and linearized (right) model for DOC = 1.00mm and DOC = 1.25mm at Ω = 1250rpm

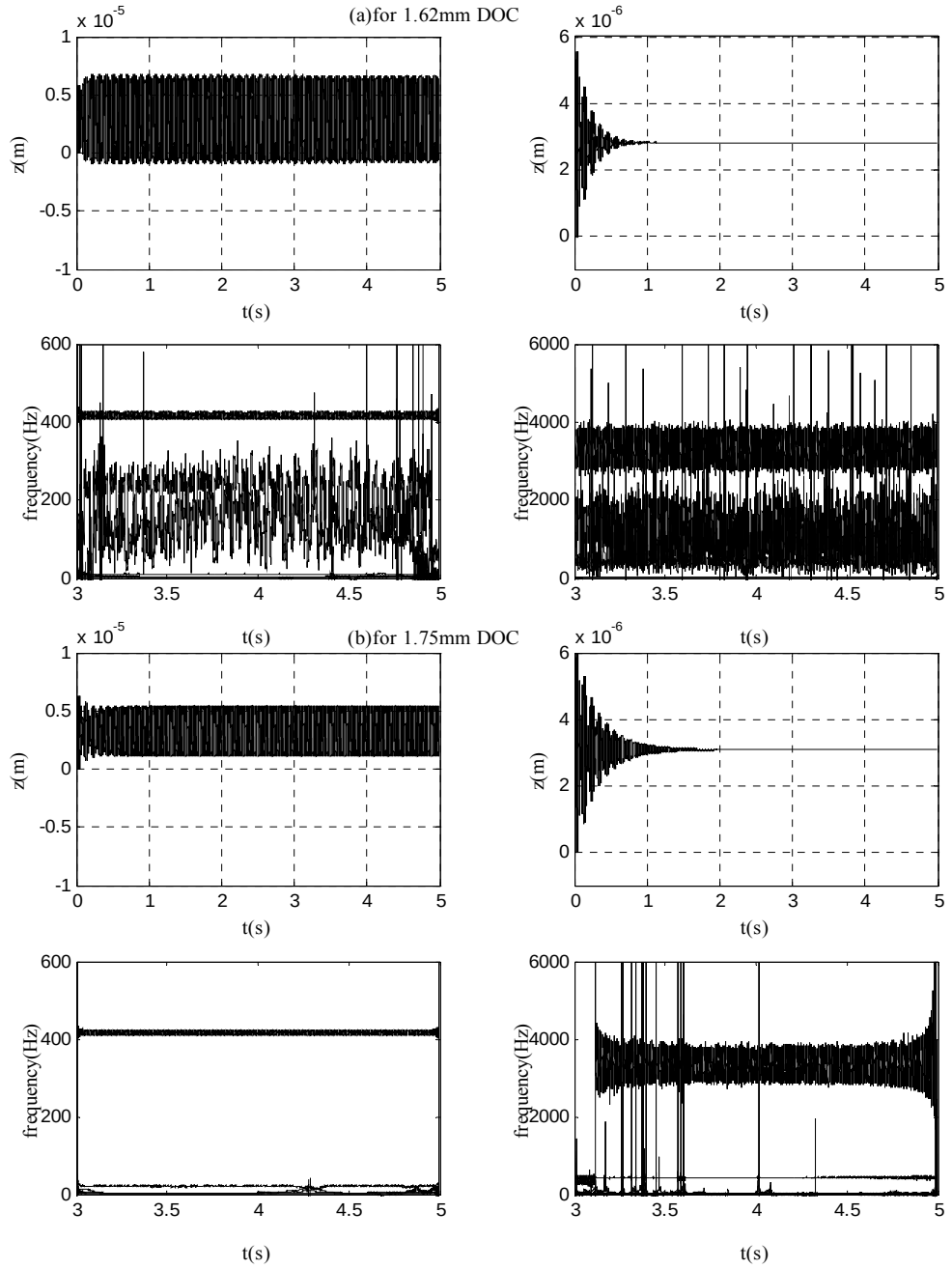

Fig. 7.11 Z - direction responses for nonlinear (left) and linearized (right) model for DOC = 1.62mm and DOC = 1.75mm at Ω = 1250rpm

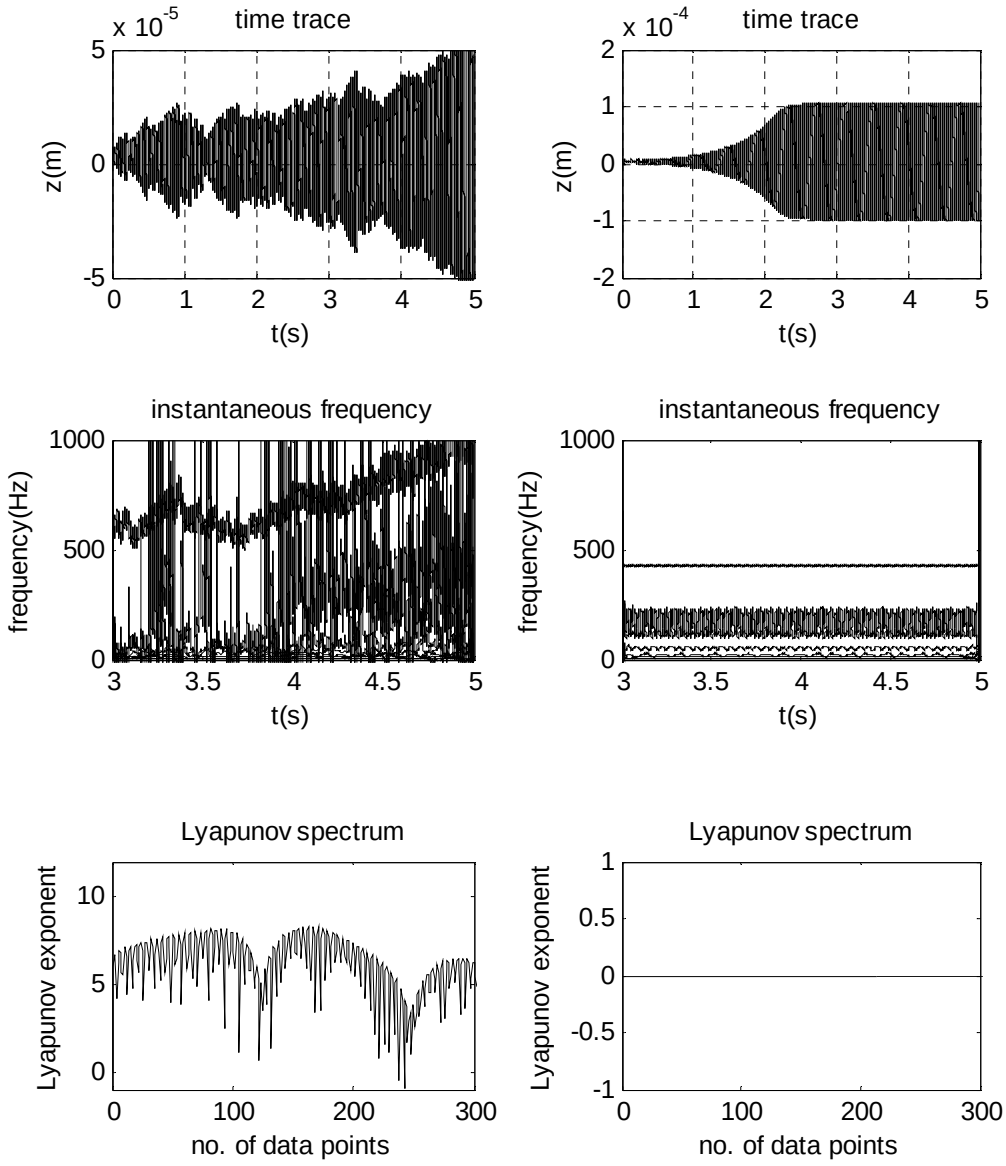

Fig. 7.12 Z - direction responses for nonlinear (left) and linearized (right) model for DOC = 2.00mm at Ω = 1250rpm

7.2.3 Comparison of Models: Experimental Results

Recall that in Section 4 the various responses of the nonlinear model agreed well with the experimental results found in [10]. Note that frequency responses illustrated in the followings all show a different tool natural frequency than was observed in [10]. The effective mass and the linear component of the stiffness adopted from [11] contribute to the differences in the excited frequency components. Also, it needs be noted that in Figs. 7.13 and 7.14 instantaneous frequency is applied, while in [10] FFT was followed for the determination of spectral responses of the experimental results. Moreover, to compare system behaviors with the experimental results, all cutting parameters including spindle speed, feed rate and DOC, along with workpiece diameter and tool geometry, are given the same values as in Case #4 in [10]. Recall the results in [10] that the Y-direction force frequency shows stability in the frequency domain at DOC = 1.62mm and instability at DOC = 2.49mm. Fig. 7.13 illustrates the instantaneous frequency responses of F_y (Y-direction cutting force component) for both the nonlinear and linearized models for DOC = 1.62mm. All plots indicate stable time and frequency domain behaviors with zero Lyapunov exponents for the DOC. The observation agrees with the physical data. In the instantaneous frequency plots in Fig. 7.14, both models exhibit instability at DOC = 2.49mm. Lyapunov spectrum for the linearized system describes a stable behavior with zero exponents. The nonlinear system, on the other hand, is a state of chaos as indicated by the positive Lyapunov exponents.

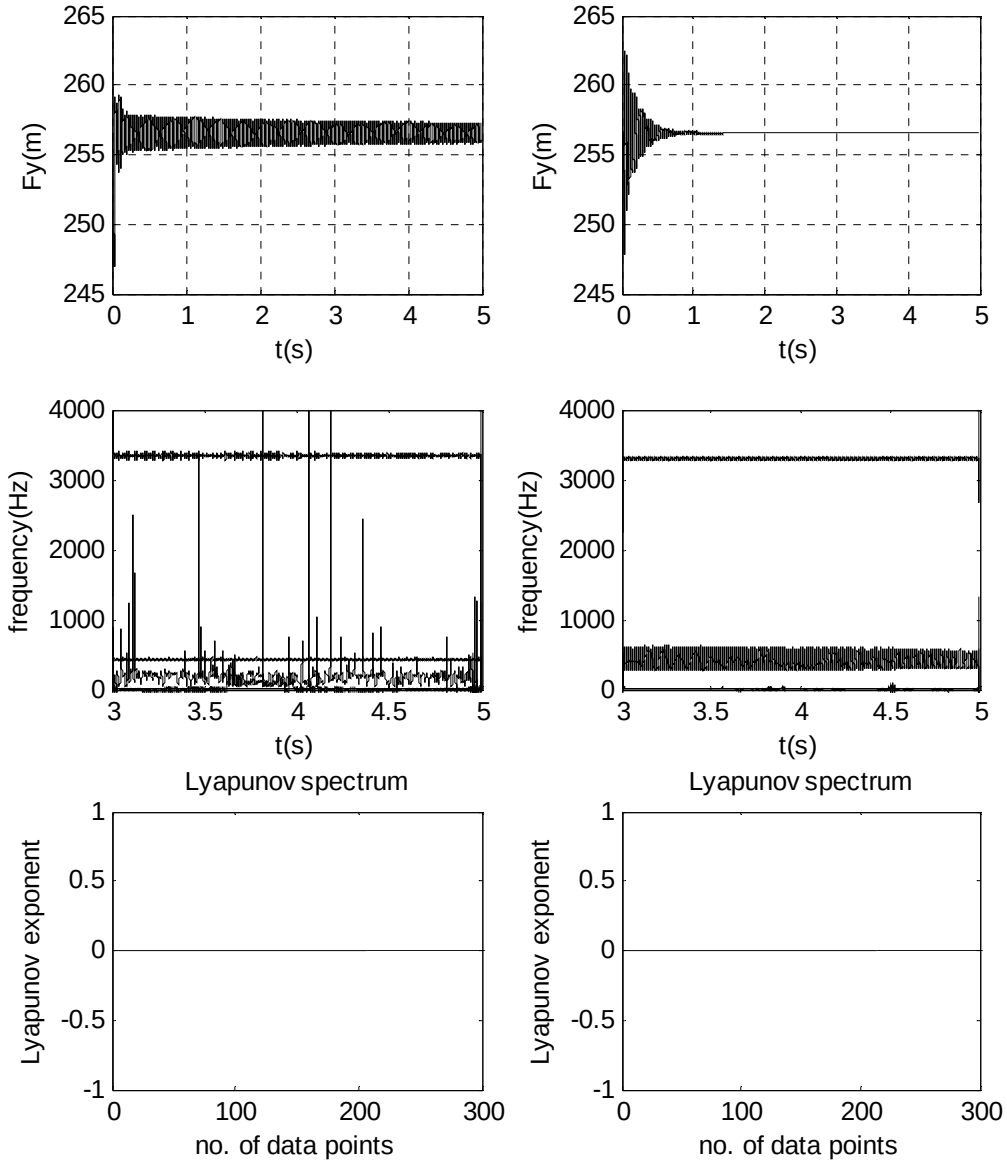

Fig. 7.13 Y- direction time responses and the associated instantaneous frequency and Lyapunov spectra for nonlinear (left) and linearized (right) cutting forces for DOC = 1.62mm at Ω = 1250rpm

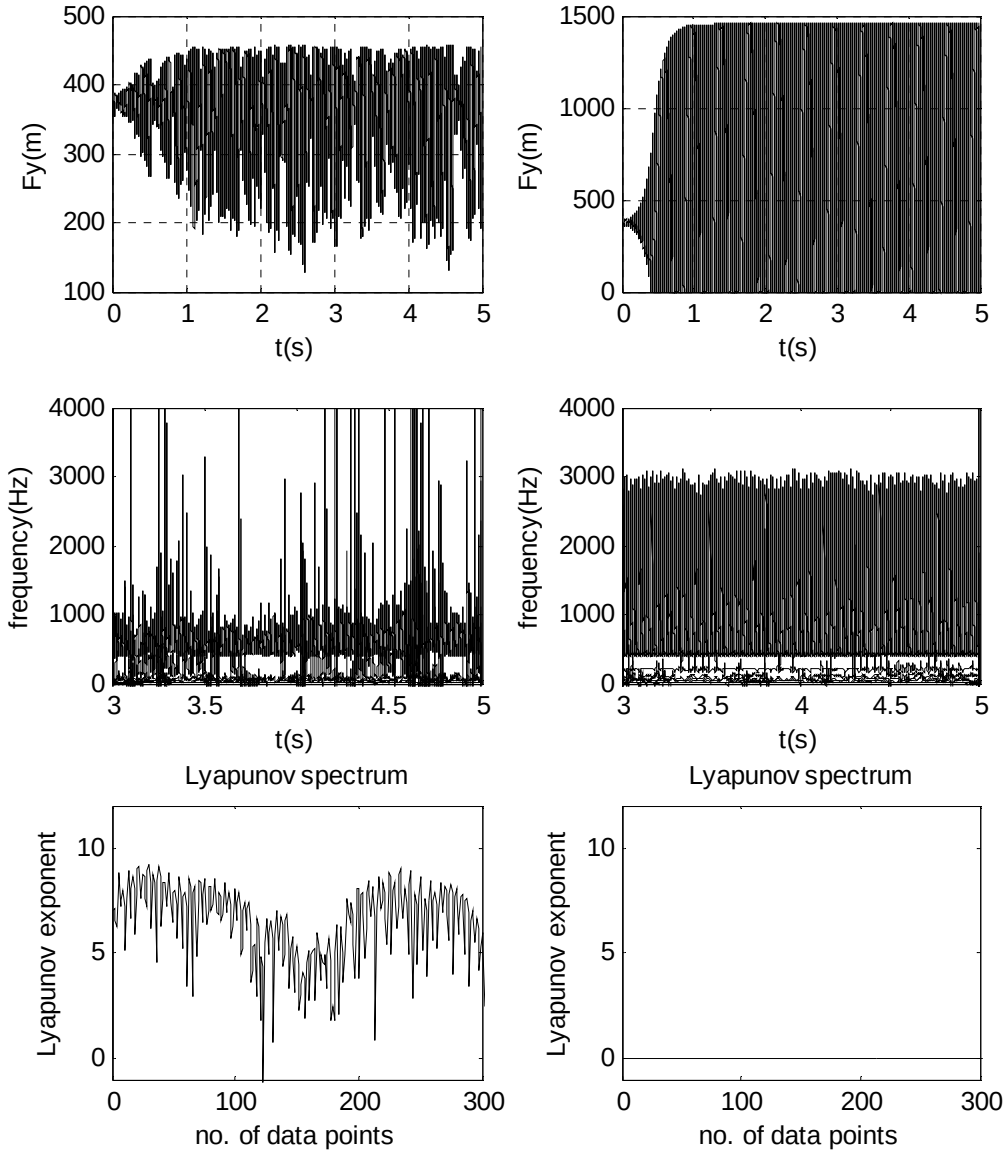

Fig. 7.14 Y- direction time responses and the associated instantaneous frequency and Lyapunov spectra for nonlinear (left) and linearized (right) cutting forces for DOC = 2.49mm at Ω = 1250rpm

Vibratory abnormality observed in the time histories of the nonlinear model at DOC = 2.49mm is consistent with the corresponding instantaneous frequencies in indicating machining instability of an extreme kind. Contrast to the temporal response of the nonlinear system, the linearized system oscillates less violently with constant tool disengagement from the workpiece (Fy = 0) and high fluctuating amplitudes. Zero-valued Lyapunov spectrum confirms that the temporal behavior is not random and thus is predictable. In the experimental study in [10], tool disengagement was never observed at this DOC. Moreover, the instantaneous frequency of F_y for the nonlinear system shows a broadband behavior oscillating near the tool natural frequency. This is in agreement with the experimental data reported in [10] where, at the particular DOC, randomness of force data was recorded.

7.3 Discussions

The modeling results of the linearized model were in major contrast to the behaviors described by the nonlinear model. It was seen from the workpiece vibration responses that the two models were similar in describing the dynamic machining states for DOCs that were less than 1.75mm. The nonlinear model demonstrated instability with nonlinear response at DOC = 2.00mm, while the linearized model exhibited motions with increased vibration amplitudes. Moreover, the workpiece instantaneous frequency of the linearized model described the machining responses of all the DOCs considered as instability of period-doubling or broadband chaotic type, which were shown to be in disagreement with published real-world data. Nearly all corresponding Lyapunov spectra indicate stability, including the case for DOC=2.49mm that should

have been chaotic. The nonlinear model, on the other hand, described a response of instability only for the cases of DOC = 2.00mm, and 2.49mm. Other than underestimating vibration amplitudes, the linearized model was in line with the nonlinear model in describing tool vibrations for all cases except for DOC = 2.00mm and 2.49mm as one of stability characterized by a finite number of frequency components. Simultaneous workpiece-tool vibrations predicted by the nonlinear model were shown to be pragmatic than the linearized counterpart in revealing the true machining state of motion. The nonlinear model also revealed in the qualitative sense the broadband behavior of the tool natural frequency associated with unstable situations. Vibration amplitudes obtained using the linearized model were diverging at certain DOCs without the commonly observed randomness in oscillations. In summary, if the underlying dynamics of turning is to be established and stability limits are to be precisely identified, linearization of nonlinear models is definitely not preferred or advisable.

8. EFFECTS OF TOOL GEOMETRY ON FINE CUTS

8.1 Introduction

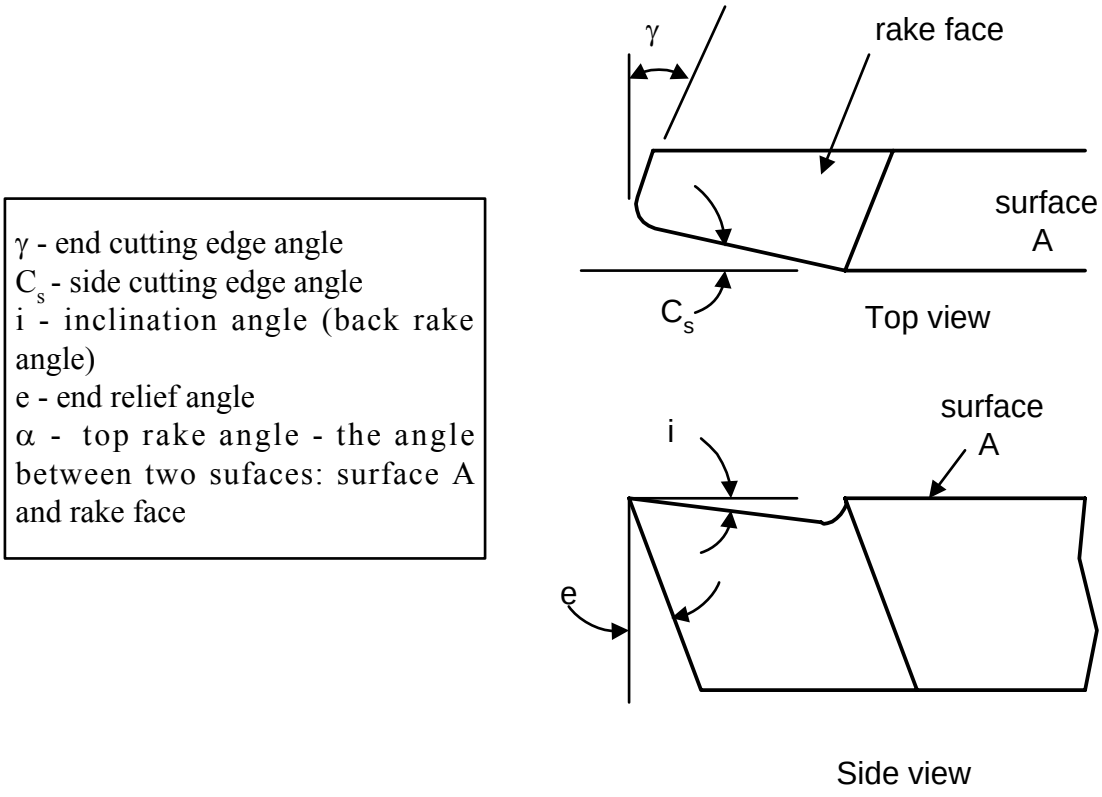

Figure 8.1 Tool angles with standard terminology

In addition to speed, feed and DOC that affect Material Removal Rate (MRR) and determines cutting force and hence power consumption, tool geometry is also one of the prominent parameters that impacts machining productivity. Surface roughness, chip

formation changes, and chip flow angle are also affected by tool geometry. Even though chip flow angle is related to tool angles [72], in the model presented herein, chip flow angle is a function only of DOC. The angles used to derive cutting forces are shown in Fig. 8.1 with standard terminology. A better view of the rake angle, α, is given in Fig. 8.2 while undergoing cutting action. Tool rake angle determines the flow of the newly formed chip. Usually the angle is of a value between +5 to -5 degrees.

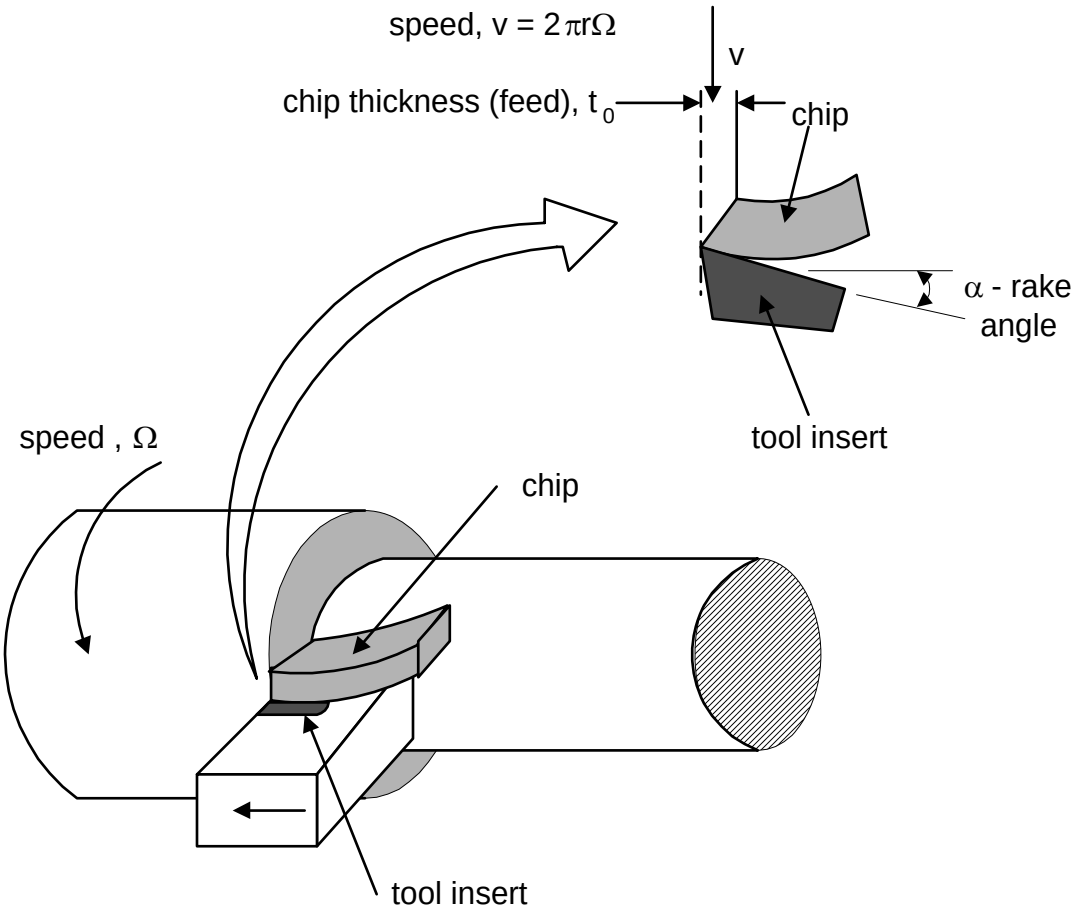

Figure 8.2 Cutting action and tool rake angle

Positive rake makes the tool sharp, but it also weakens the tool compare with negative rake [73]. Negative rake is better for rough cutting. Selection of tool geometry depends on the particular workpiece and tool materials being considered.

8.2 Numerical Results

To establish that tool angle does have significance effects on cutting stability, two sets of tool geometries are used to determine the cutting force in the followings. Their values are given in Table 8.1. Both sets are taken from the tool inserts that were used in the experiments in [10]. Since DOC considered in the numerical study is less than 1mm and can be considered as non-rough cutting, rake angles are taken positive for all cases. Recall that negative rake is better for roughing [73]. Three DOCs (0.9mm, 0.75mm and 0.5mm) are used with a 1250rpm spindle speed and 0.0965mm feed per revolution in the numerical experiment.

Table 8.1 Tool angles

Set number	Side cutting edge angle, (C_s)/(degrees)	Rake angle, (α) /(degrees)	Inclination angle, (i) /(degrees)
#1	45	3.55	3.55
#2	15	5	0

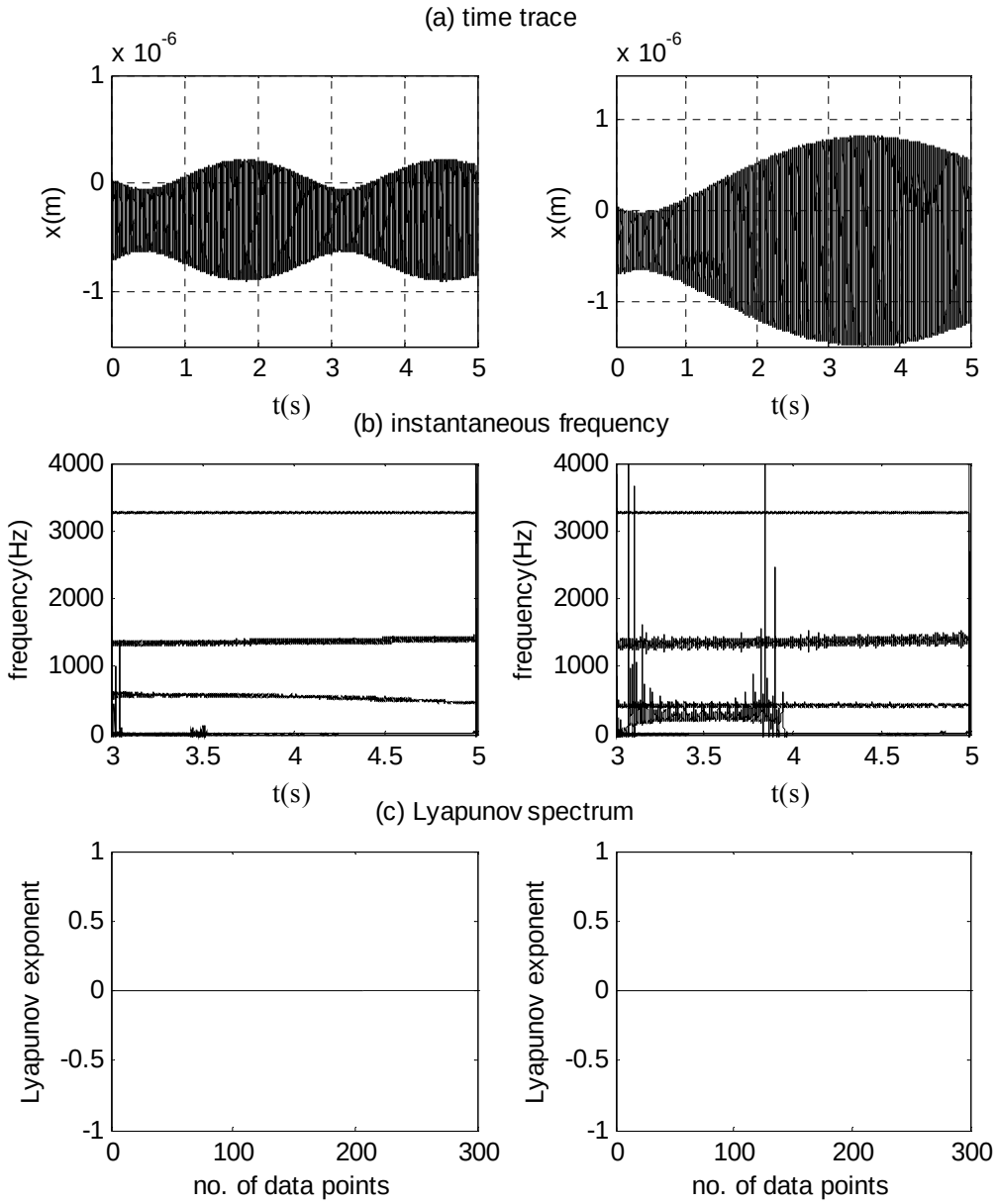

Fig. 8.3 X-direction time responses, corresponding instantaneous frequency and Lyapunov spectra for Set #1(left) and Set #2 (right) for DOC = 0.90mm at Ω = 1250rpm

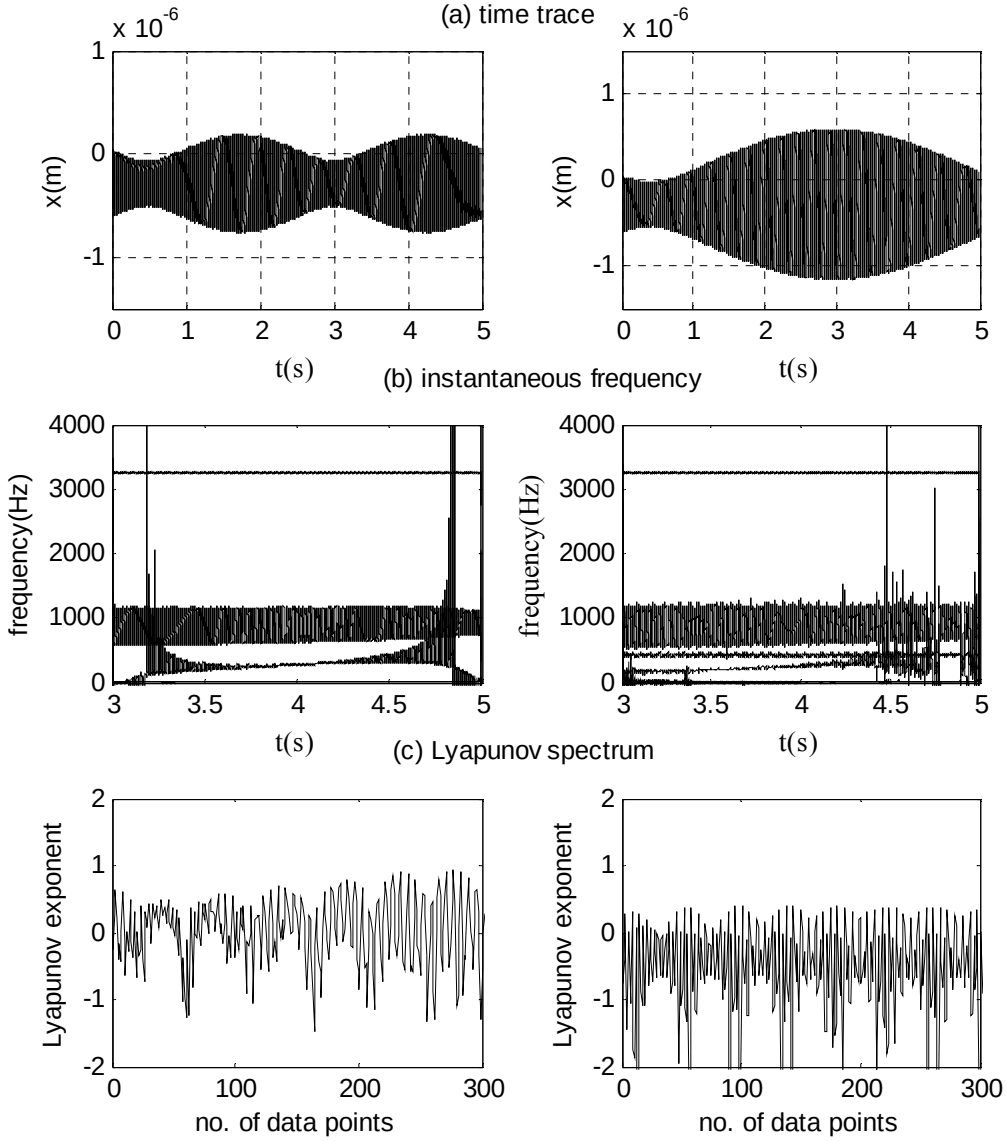

Fig. 8.4 X-direction time responses, corresponding instantaneous frequency and Lyapunov spectra for Set #1(left) and Set #2 (right) for DOC = 0.75mm at Ω = 1250rpm

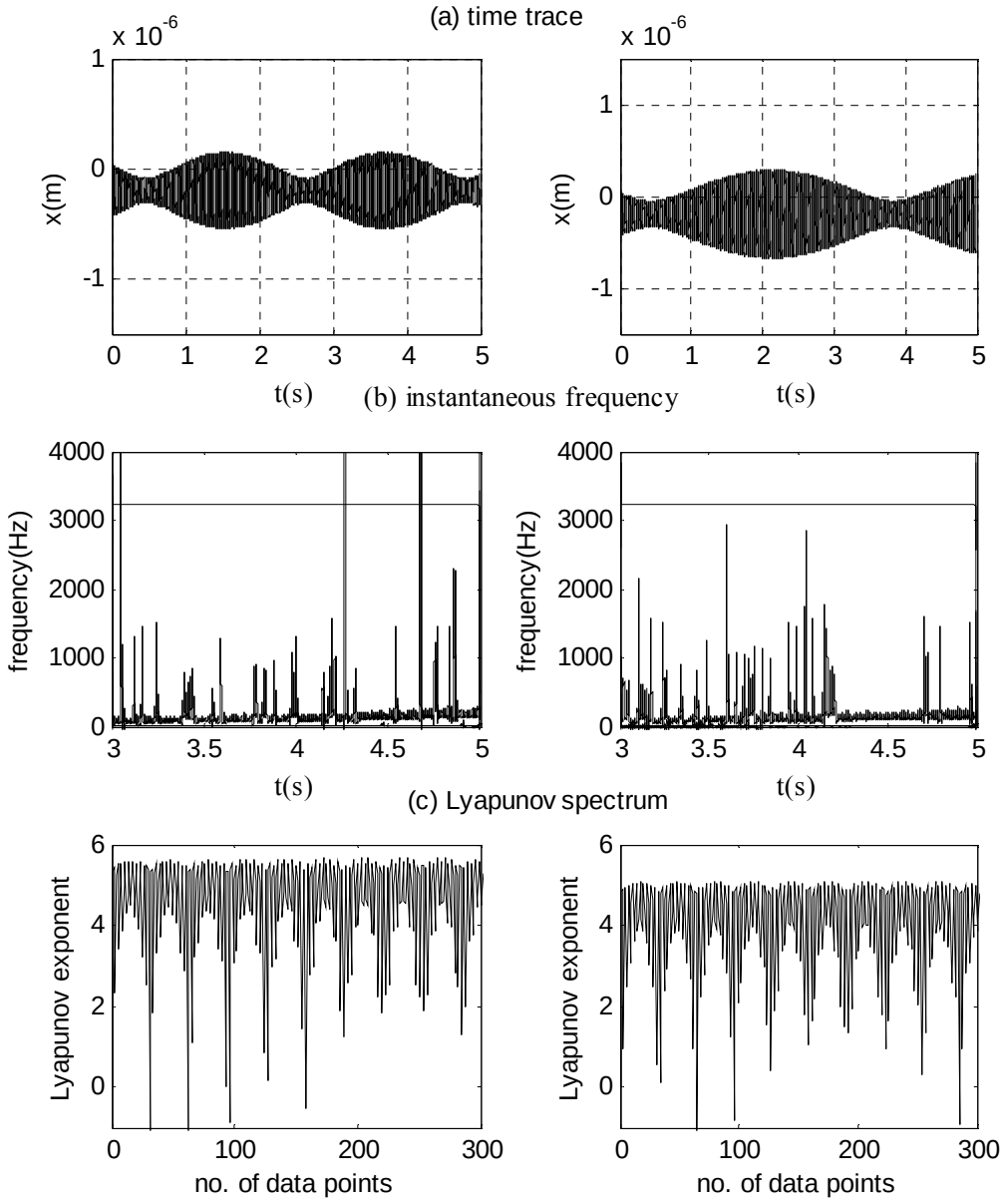

Fig. 8.5 X-direction time responses, corresponding instantaneous frequency and Lyapunov spectra for Set #1(left) and Set #2 (right) for DOC = 0.50mm at Ω = 1250rpm

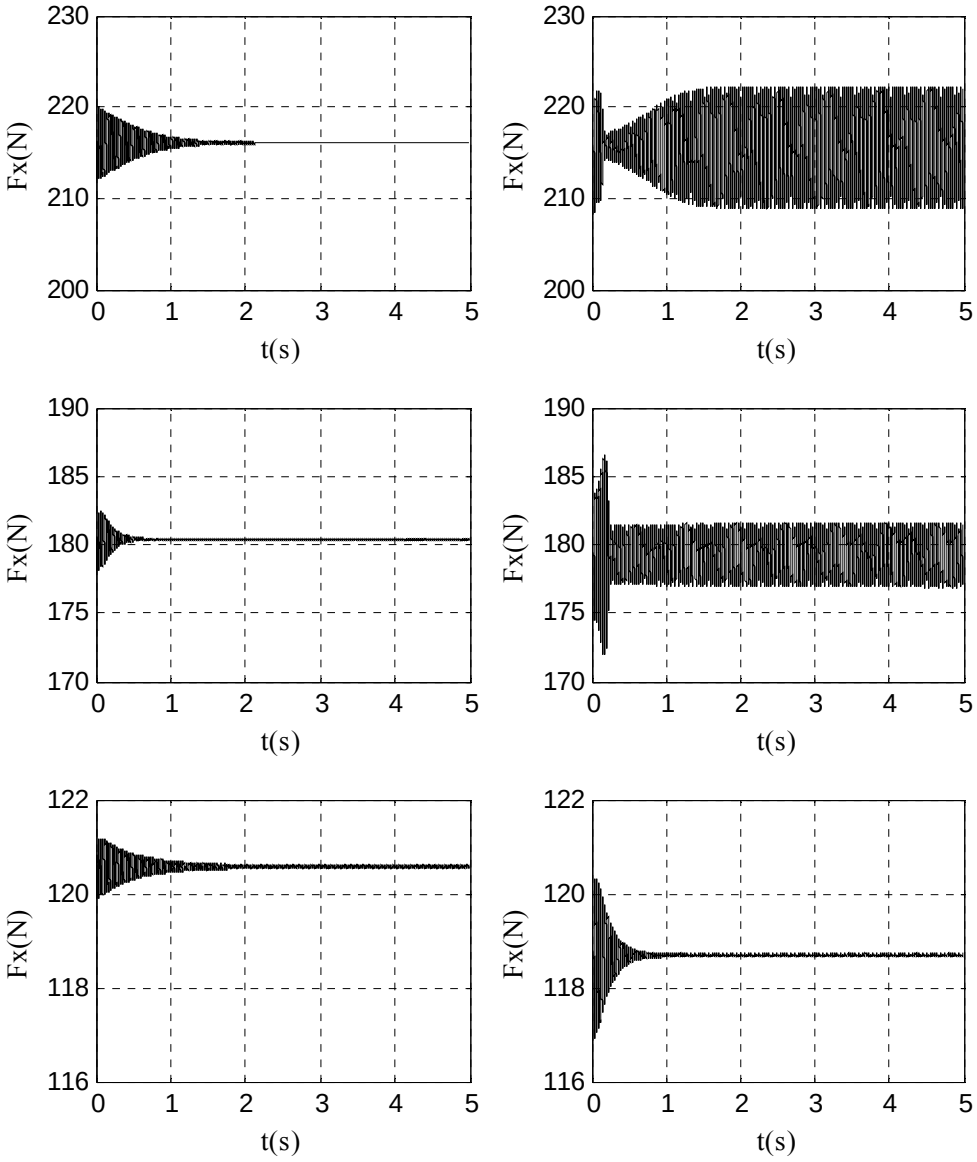

Fig. 8.6 Forces in X- direction for Set #1(left) and Set #2 (right) for DOC = 0.90mm (top), DOC = 0.75mm (middle), and DOC = 0.50mm (bottom) at Ω = 1250rpm

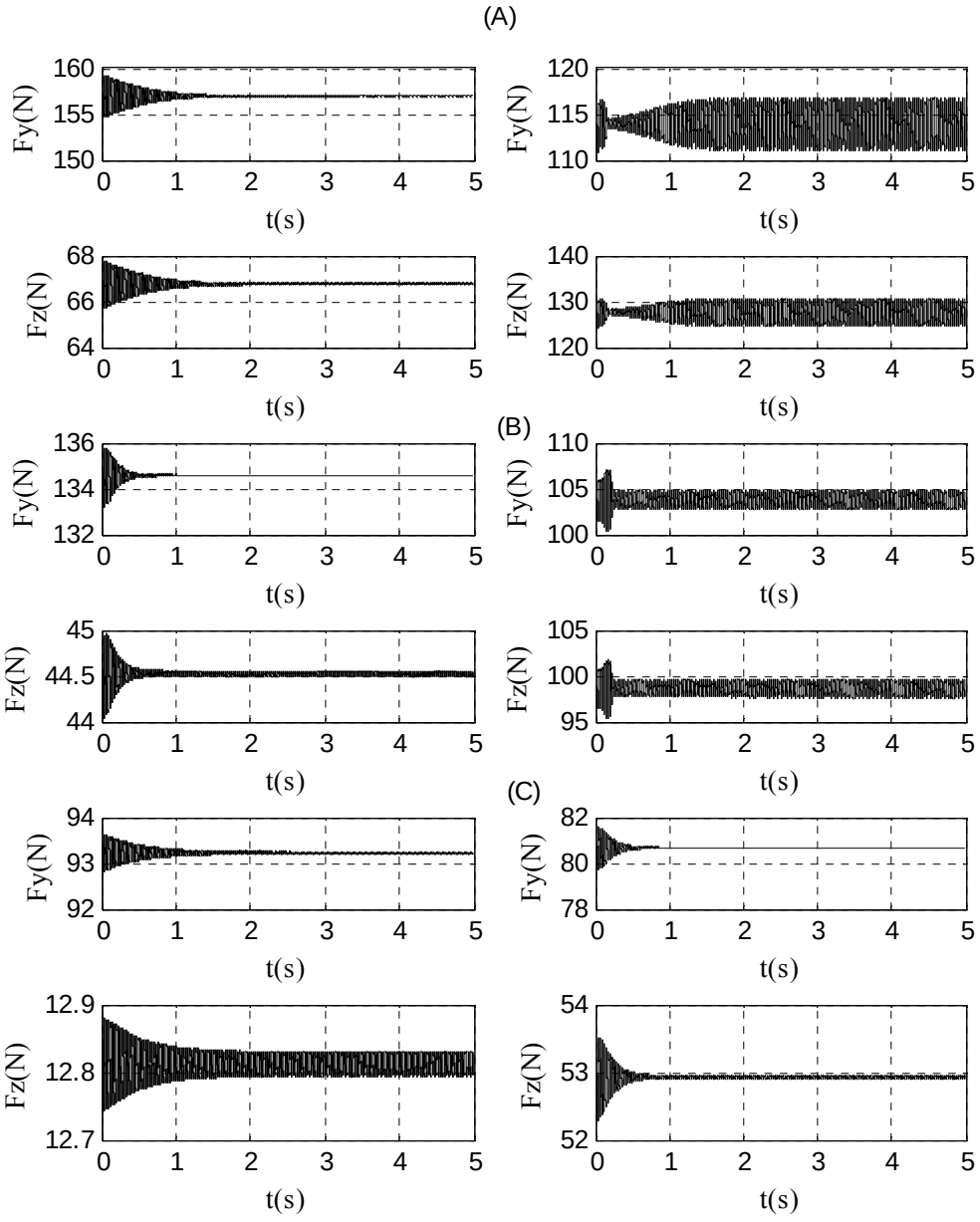

Fig. 8.7 Forces in Y- and Z-direction for Set #1(left) and Set #2 (right) for DOC = 0.90mm (A), DOC = 0.75mm (B), and DOC = 0.50mm (C) at Ω = 1250rpm

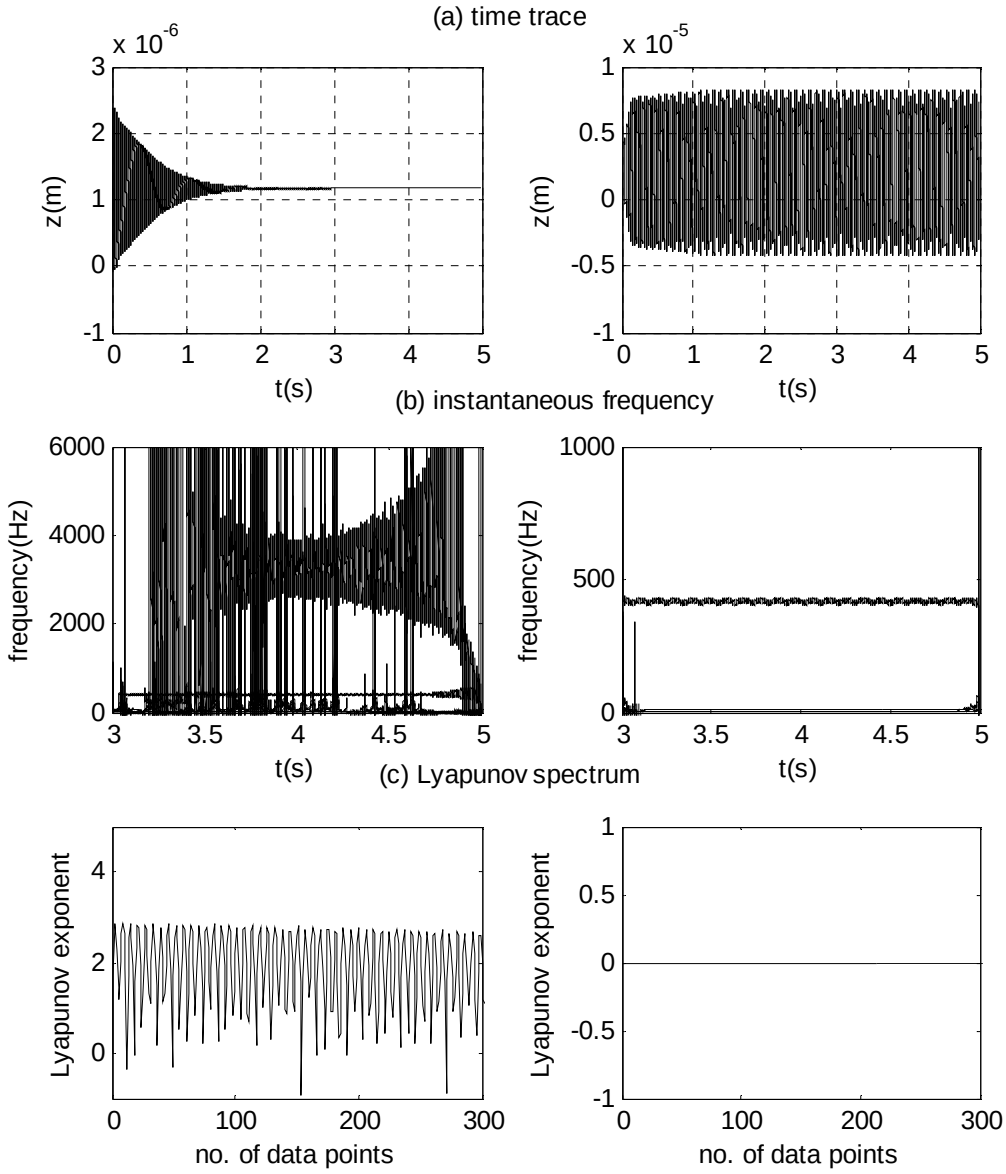

Fig. 8.8 Z-direction time responses, corresponding instantaneous frequency and Lyapunov spectra for Set #1(left) and Set #2 (right) for DOC = 0.90mm at Ω = 1250rpm

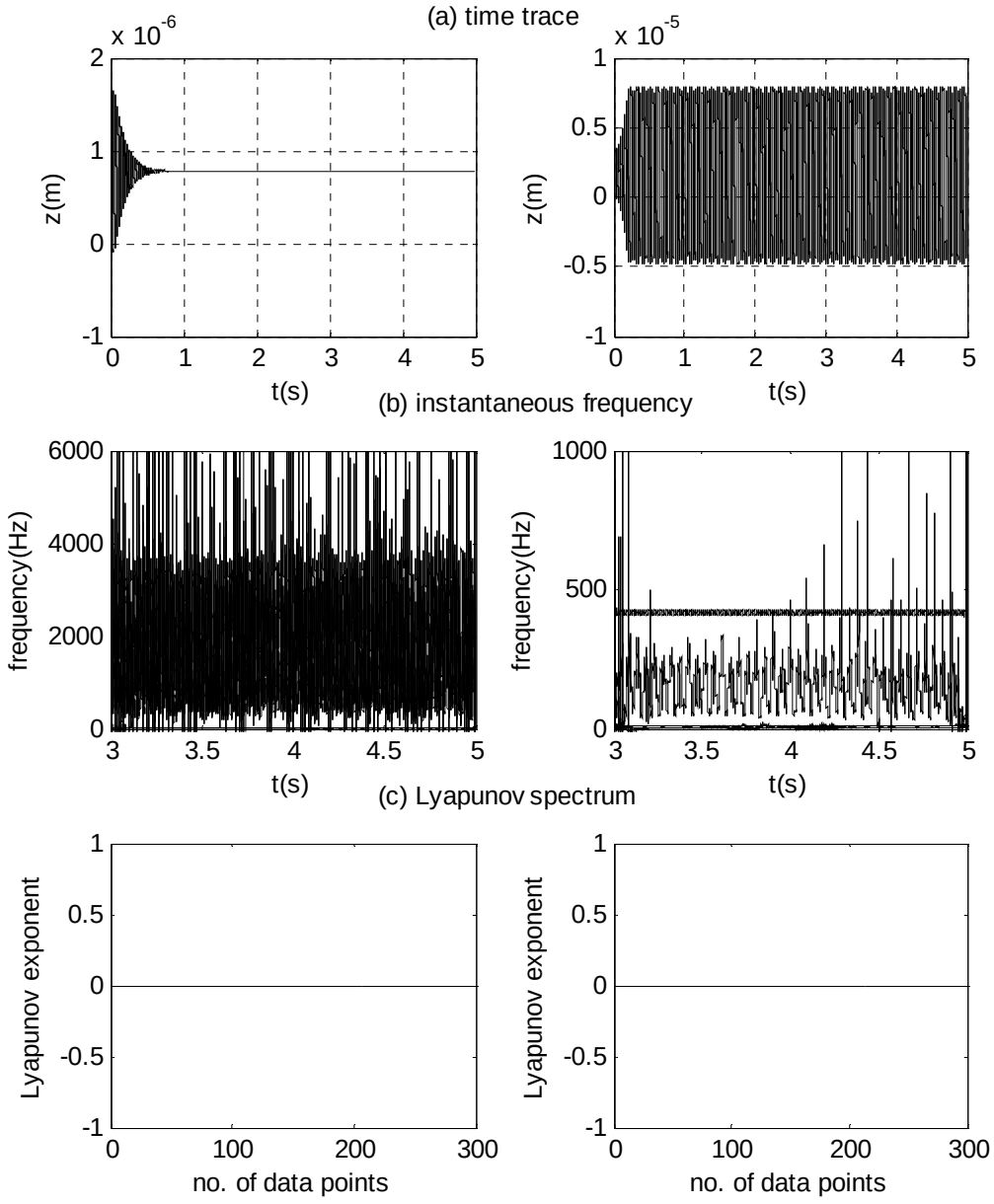

Fig. 8.9 Z-direction time responses, corresponding instantaneous frequency and Lyapunov spectra for Set #1(left) and Set #2 (right) for DOC = 0.75mm at Ω = 1250rpm

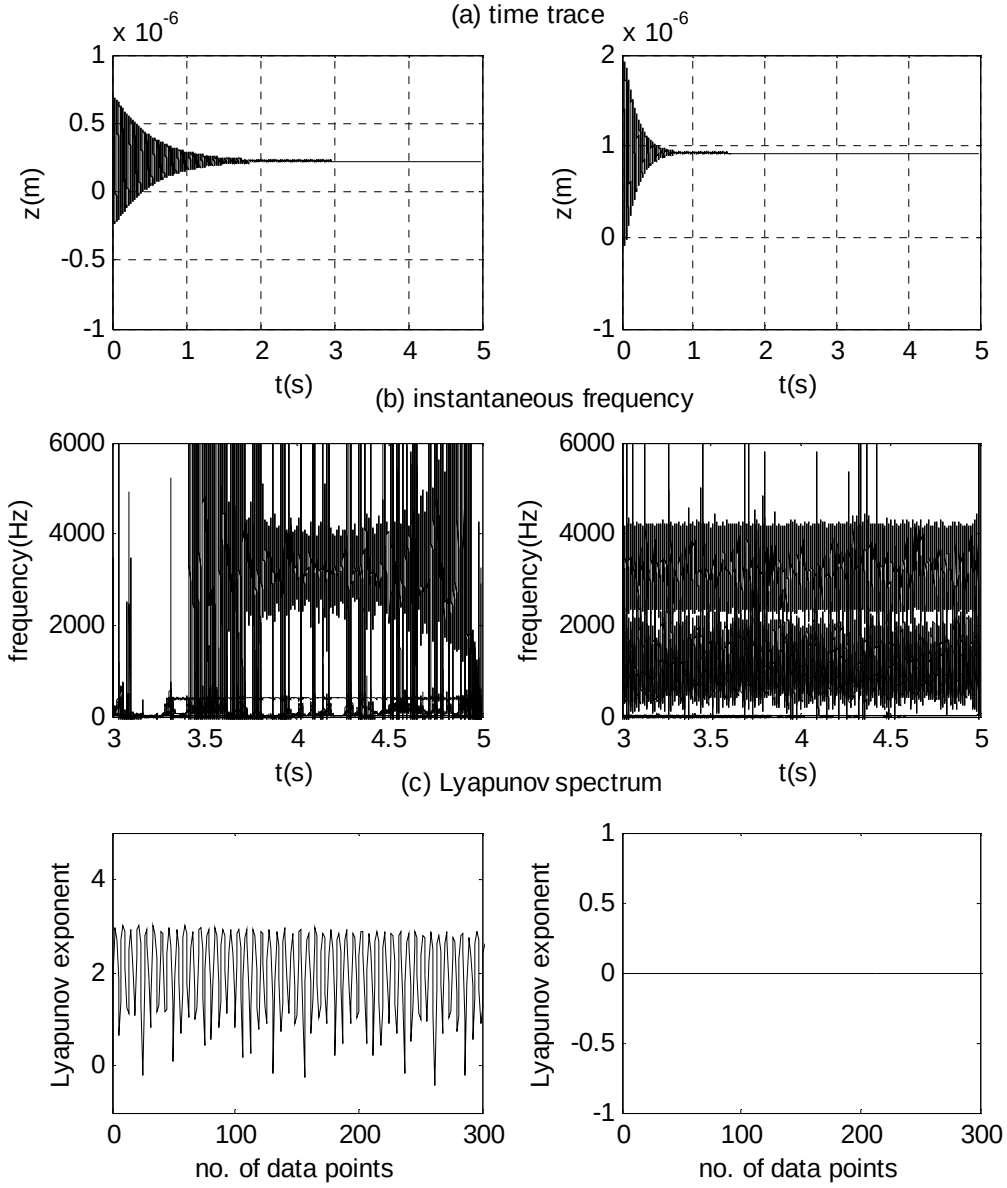

Fig. 8.10 Z-direction time responses, corresponding instantaneous frequency and Lyapunov spectra for Set #1(left) and Set #2 (right) for DOC = 0.50mm at Ω = 1250rpm

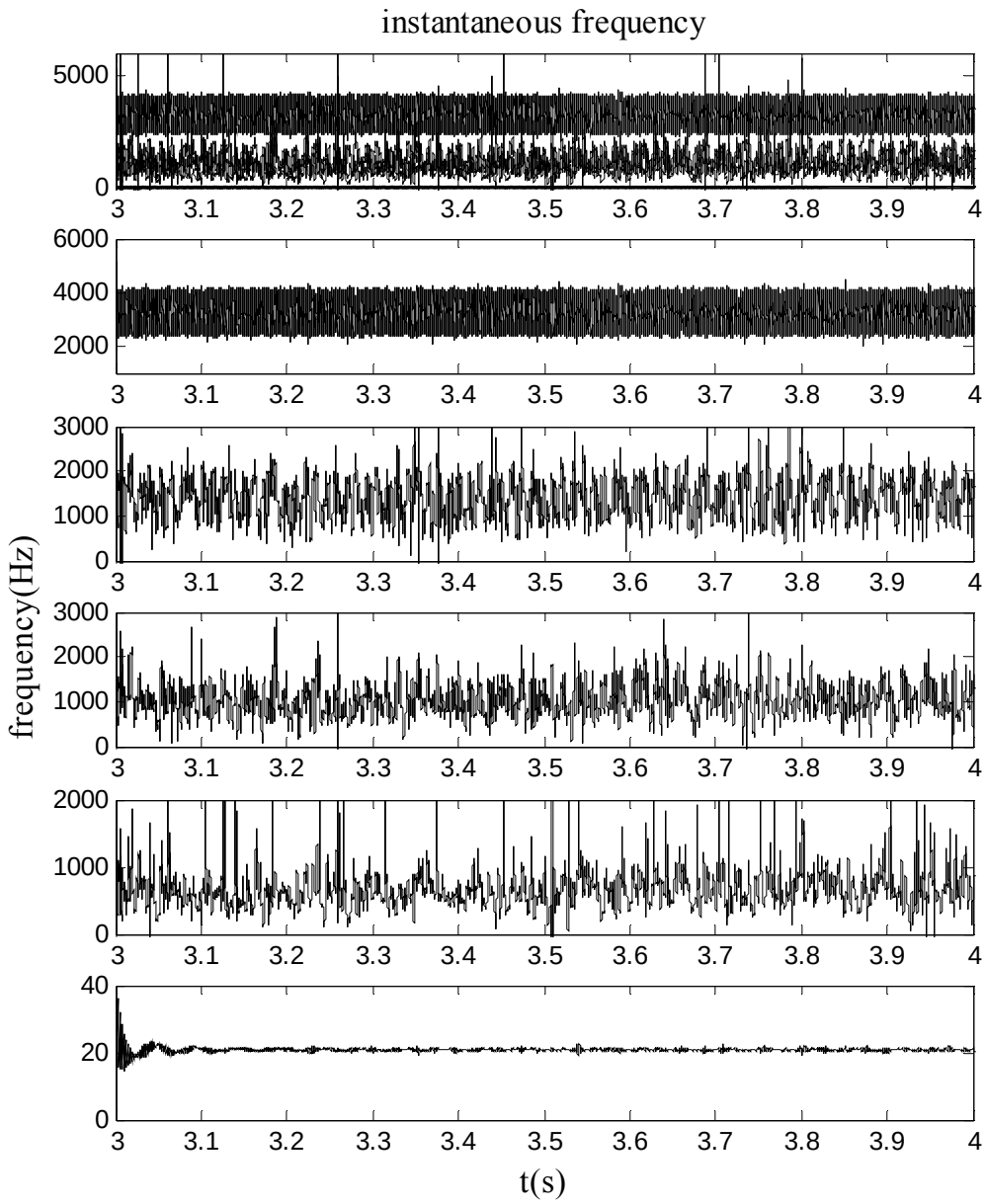

Fig. 8.11 Instantaneous frequency spectrum (top) and its mono components for

DOC = 0.50mm at Ω = 1250rpm

All figures from 8.3-8.10, except for Figs. 8.6 and 8.7 give time responses, instantaneous frequency responses between 3 to 5 seconds, and corresponding Lyapunov spectra. X-direction system responses are examined to demonstrate workpiece behaviors, and Z-direction responses are analyzed to investigate tool motions. In all figures, plots in the right column correspond to Set #1 tool geometry conditions and the left column corresponds to Set #2 tool angles. In Fig. 8.3, the X-direction vibration amplitude of Set #2 tool geometry is seen to be twice that of Set #1. However, their frequency domain behaviors are similar with a workpiece natural frequency at 3270Hz and a whirling frequency at 20.8Hz. Set #2 shows two more frequencies, one near the tool natural frequency at 425Hz and another at 250Hz, which disappears after 3.9 seconds. Set #1 has only one more tool-excited frequency. The frequency can be seen to decrease from 580Hz to 460Hz within two seconds. This implies that tool geometry is a non-negligible parameter affecting workpiece stability. Note that the Lyapunov spectra for both are evident of a relatively stable cutting situation at DOC = 0.9mm.

When DOC is decreased to 0.75mm in Fig. 8.4, there are still differences in vibration amplitudes. With the reduction of its diameter, the workpiece natural frequency decreases to 3250Hz. While whirling frequency remains the same, a 900Hz component of a wide 500Hz bandwidth dominates in both systems. It can be seen in Set #2 that a bifurcation of the tool-excited natural frequency at 425Hz diminishes after 4.8 seconds. On the other hand, Set #1 does not have a bifurcation. It has a frequency component increase from 250Hz to 400 Hz and then disappears afterwards. Both Lyapunov spectra fluctuate near zero, thus leaving a question whether the systems are

exactly stable. Further deceasing DOC to 0.5mm in Fig. 8.5, both systems show an unstable situation marked by positive Lyapunov exponents. In addition, the instantaneous frequency plots show a similar behavior for both systems with a frequency component increasing from 100Hz to 200Hz.

Relatively large force fluctuation seen in Fig. 8.6 explains the large vibration amplitudes seen for the tool geometry Set #2. Forces of large fluctuation push the workpiece to deflect more. It is interesting to note that, even though tool geometry variations are supposed to affect the cutting force, X-direction force amplitudes are almost identical for both tool geometry sets. Effects of tool geometry can be seen in the Y- and Z-direction force components in Fig 8.7. While Y-direction forces for Set #2 are less than those of Set #1, Set #2 Z-direction forces are much higher than those of Set #1. In all plots, it is seen that force responses associated with Set #1 tool geometry fluctuate less compare with those of Set #2. Figs. 8.8 through 8.10 present tool dynamical motions for DOC = 0.9mm, 0.75mm, and 0.5mm, respectively. Even though force fluctuations and vibration amplitudes are both prominent, Set #2 is relatively more stability. Of the three DOCs considered, two behave dissimilarly. In all three cases, the vibration history of Set #1 has amplitudes that are of nanometer in scale. On the other hand, Set #2 vibrates with amplitudes that are a few microns for DOC = 0.9mm and 0.75mm, and several nanometers for DOC = 0.5mm. Unlike Set #1, all Lyapunov spectra for Set #2 are evident of a stable state of dynamic response. Though having positive Lyapunov exponents, Set #2 shows instability for the DOC = 0.9mm and 0.5mm cases. Instantaneous frequency plots for DOC = 0.9mm in Fig. 8.8 confirm that Set #1

response is broadband and thus unstable, and Set #2 is stable with a clean spectrum. Although the Lyapunov spectrum in Fig. 8.9 indicates a stable state of tool motion for Set #1 at DOC = 0.75mm, the corresponding instantaneous frequency suggests otherwise. The instantaneous frequency plot for Set #2 at DOC = 0.5mm also contradicts the Lyapunov spectrum. A detail review of the individual instantaneous frequency mono-components in Fig. 8.11 reveals that the frequency at 3240Hz has bifurcated 3 times. Thus, it is a highly bifurcated state.

8.3 Discussions

Effects of tool geometry on cutting dynamics and its impact on surface finishing were investigated. Manufacturing industry has long learned to employ tool inserts with complex geometry to achieve better product surface condition. However, most models developed for understanding machining dynamics and cutting stability ignore the various effects attributable to tool geometry. One of the reasons for this is the fact that 1D machining modeling is inherently infeasible for incorporating various tool angles that are inherently 3-dimensional. Numerical experiments presented in the section deem neglecting tool geometry improbable. It was observed that variations in tool geometry can significantly impact cutting stability. A machining process can be unstable for a particular DOC using one set of tool geometry and, become stable through careful selection of proper tool inserts with different set of tool geometry, at the same DOC. This raises the question over if true dynamical stability could be identified without considering tool geometry. Thus, it is essential that tool geometry is also considered in modeling 3D turning operation to ensure proper interpretation of cutting dynamics.

9. EFFECTS OF TOOL FEED PER REVOLUTION ON CUTTING STABILITY

There are three parameters that define Material Removal Rate (MRR). Constraints dictating how fast material is removed are cutting speed, feed rate and DOC. Tool feed rate, $t_{0,}$ can be defined as the amount that tool moves in the axial direction per revolution of the workpiece [72-74]. Tool feed rate is also called "undeformed chip thickness" in turning. Feed rate can be as small as 0.00125mm per revolution for light cuts with very thin chips or as large as 2.5mm per revolution for heavy cuts. The presented model in Section 2 was derived for a feed rate ranging between 0.05mm and 0.15mm. In practice, the parameter that can be set is the tool transverse speed, f_s, in the axial direction. The relationship between feed rate and tool transverse speed is

$$f_s = t_0 \Omega / 60 \tag{9.1}$$

where f_s and t_0 are both in mm per second, and spindle speed Ω is in rpm. Because it is a major parameter in increasing MRR, this section focuses on examining the effect of t_0 on cutting stability.

9.1 Numerical Results

The model is simulated with two different feeds for comparison. A constant spindle speed of 1250rpm and six different DOCs are considered with a 0.0965mm chip thickness. Numerically integrated time response data are analyzed to obtain instantaneous frequency and the largest Lyapunov exponents for stability analysis.

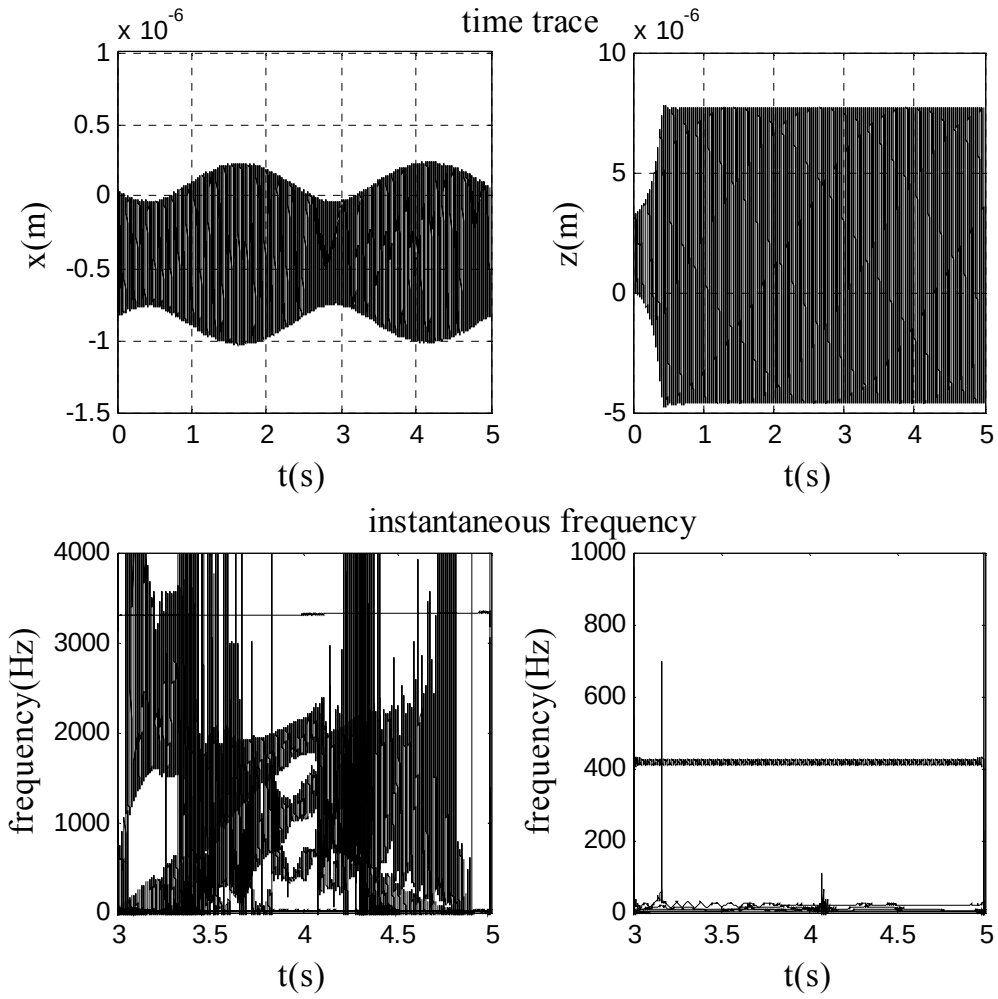

Fig. 9.1 X- (left) and Z-(right) direction model responses at DOC = 1.00mm, Ω = 1250rpm and t_0 = 0.125mm

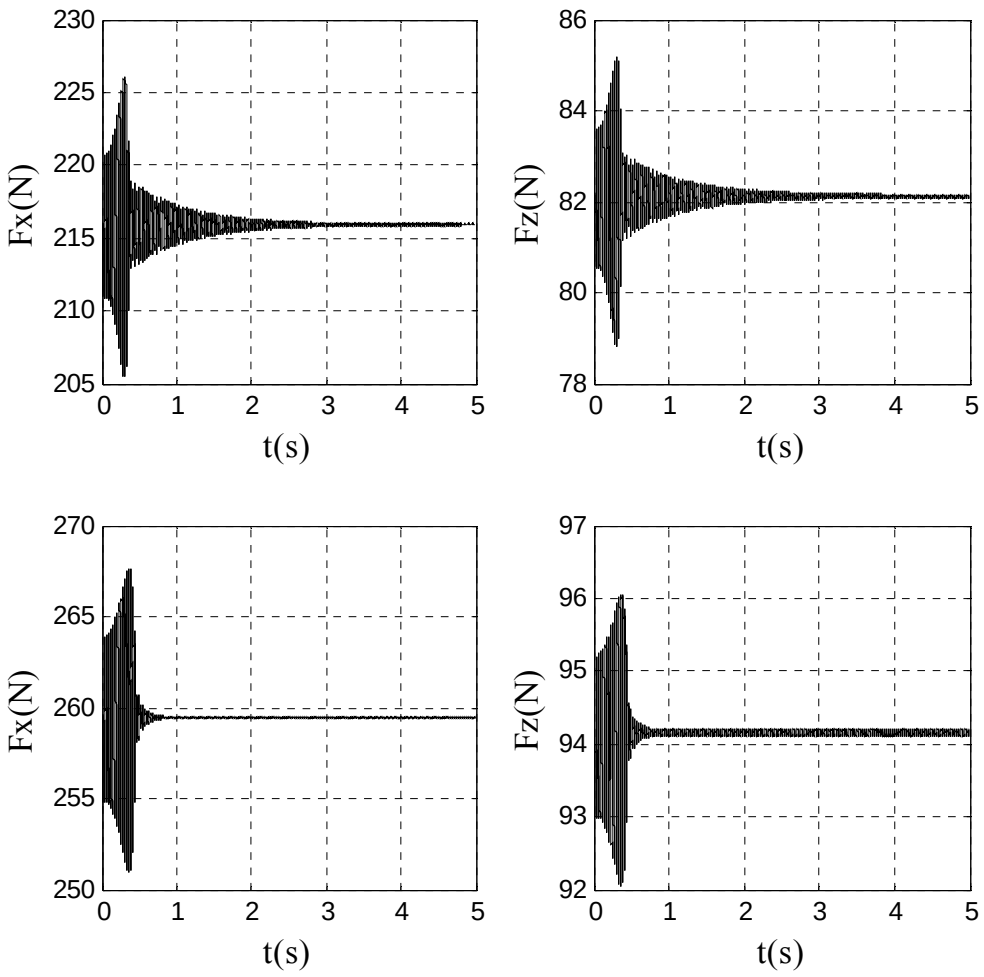

Fig. 9.2 X- and Z-direction cutting forces for t_0 = 0.0965mm (top) and t_0 = 0.125mm (bottom) at DOC = 1.00mm and Ω = 1250rpm

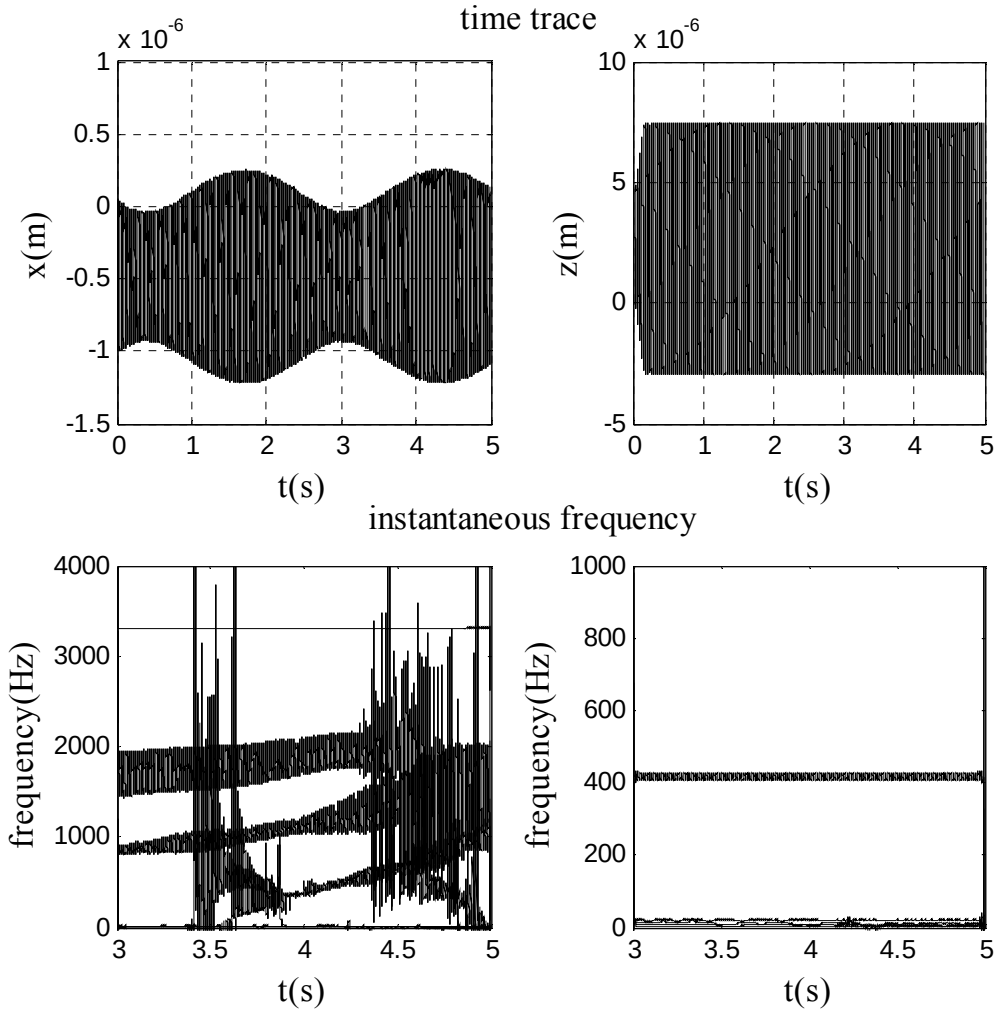

Fig. 9.3 X- (left) and Z-(right) direction model responses at DOC = 1.25mm, Ω = 1250rpm and t_0 = 0.125mm

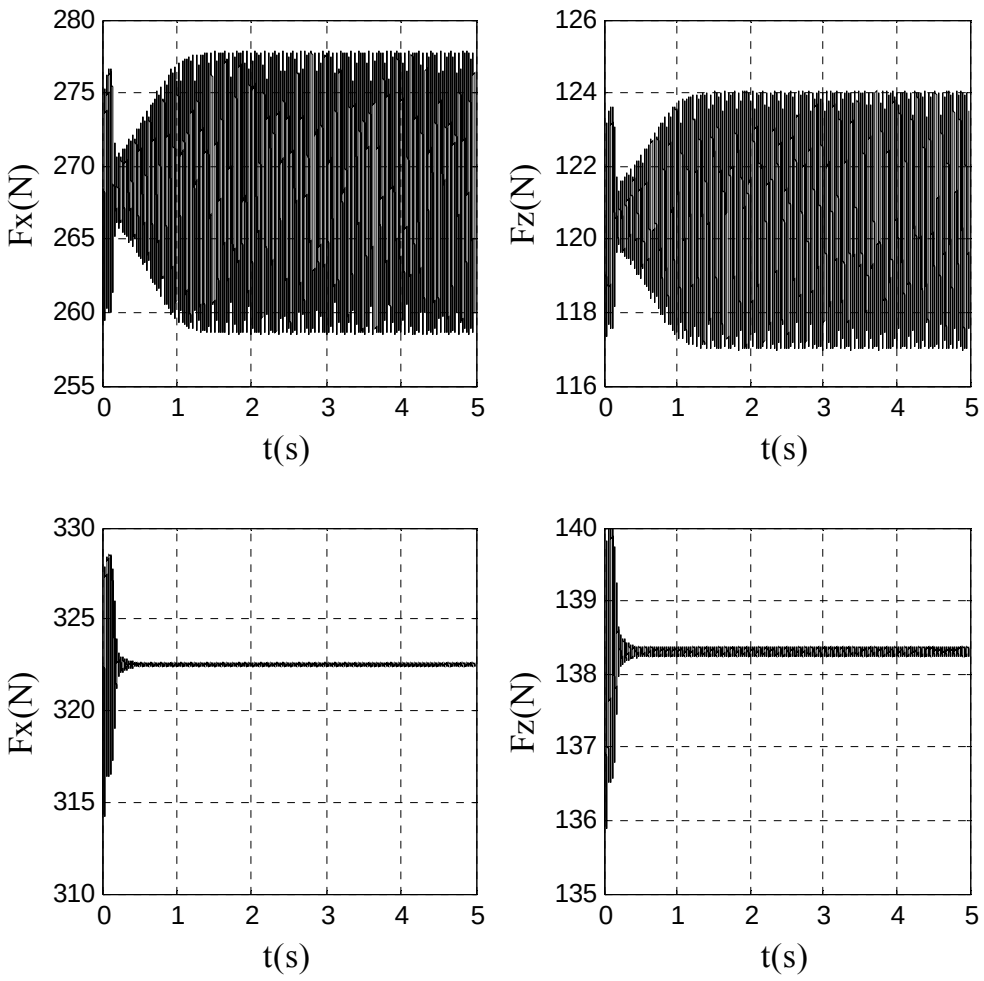

Fig. 9.4 X- and Z-direction cutting forces for t_0 = 0.0965mm (top) and t_0 = 0.125mm (bottom) at DOC = 1.25mm and Ω = 1250rpm

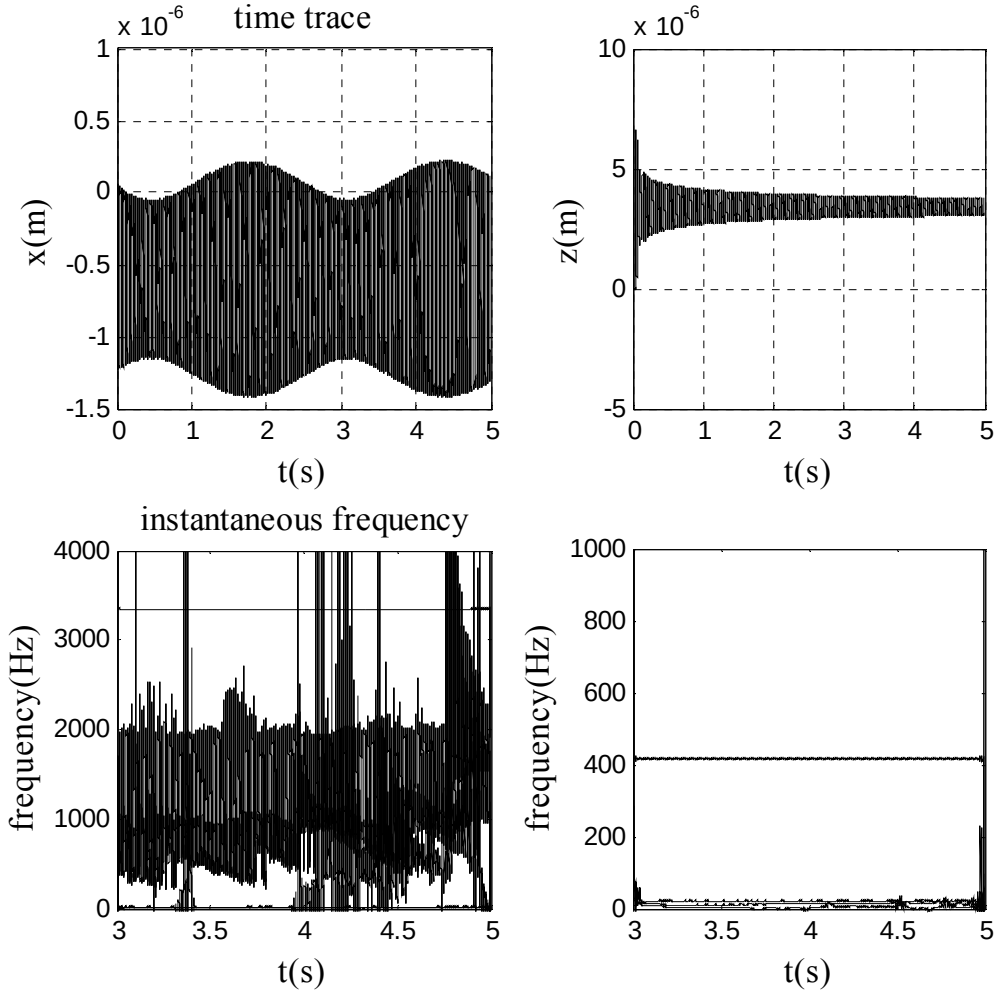

Fig. 9.5 X- (left) and Z-(right) direction model responses at DOC = 1.62mm, Ω = 1250rpm and t_0 = 0.125mm

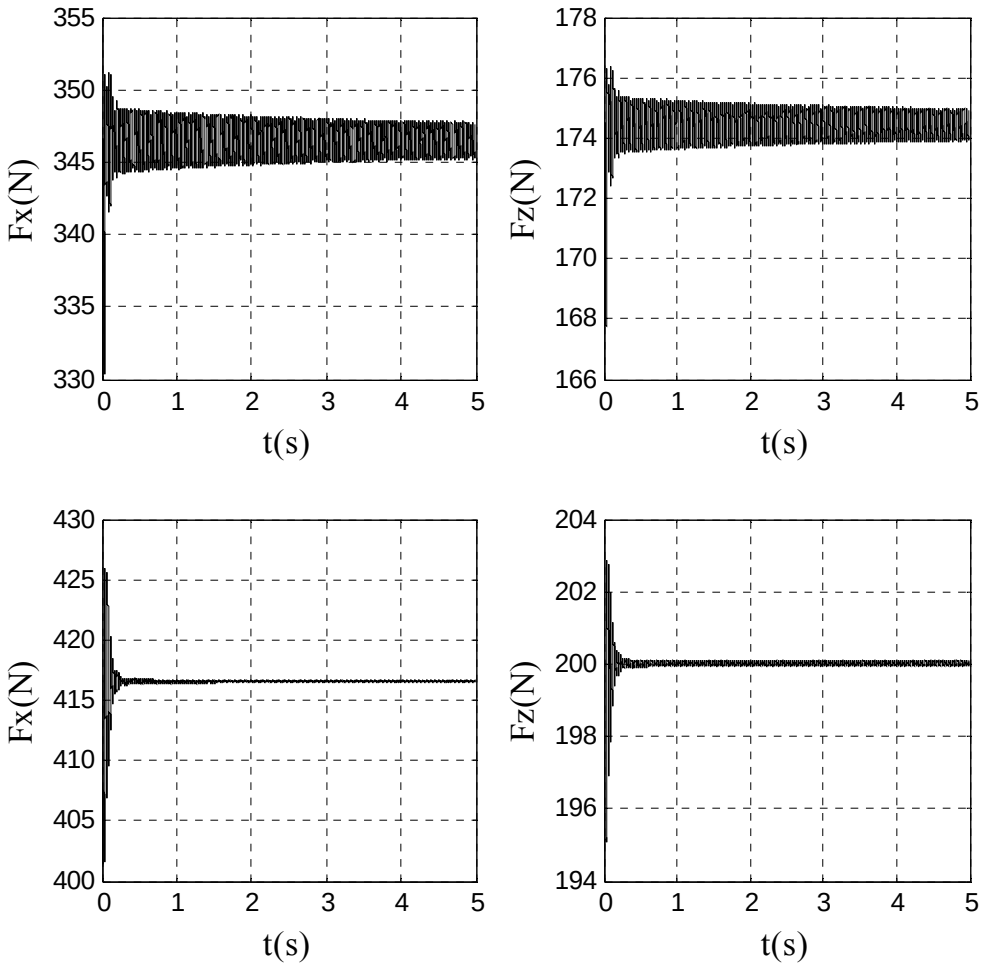

Fig. 9.6 X- and Z-direction cutting forces for t_0 = 0.0965mm (top) and t_0 = 0.125mm (bottom) at DOC = 1.62mm and Ω = 1250rpm

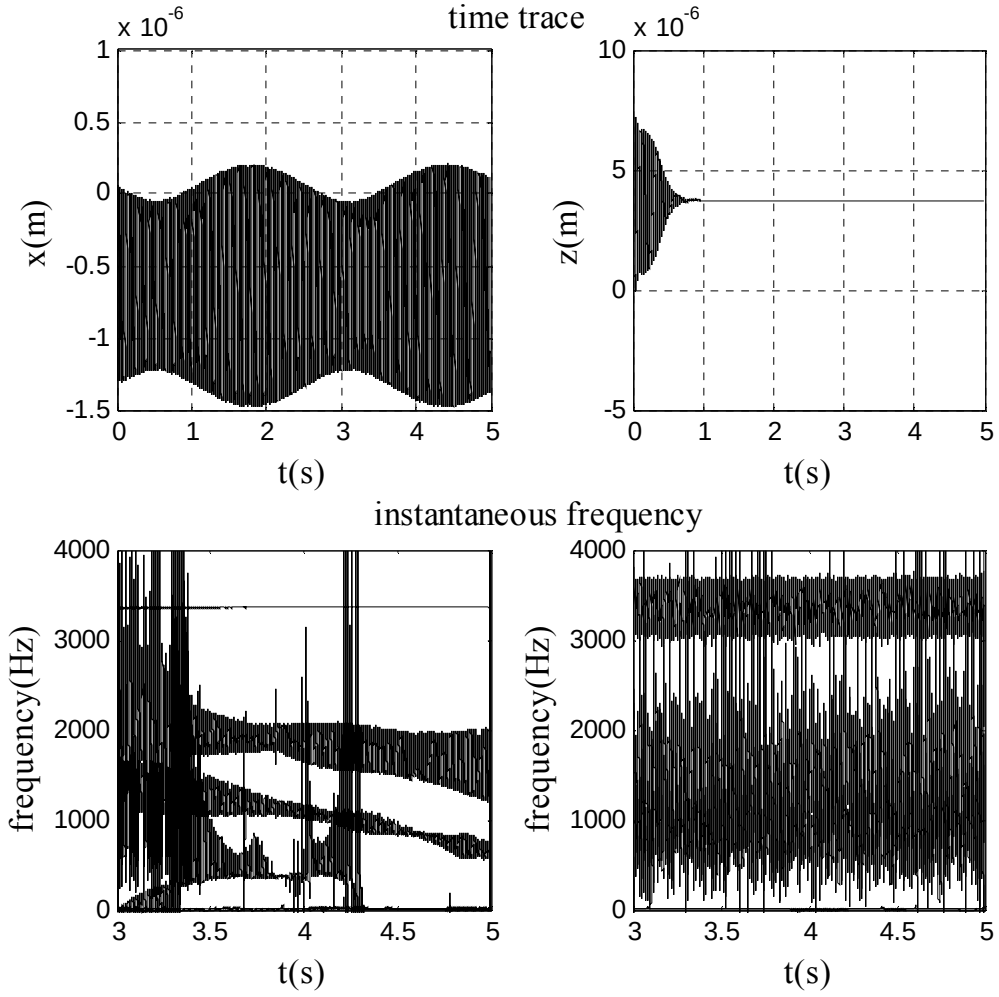

Fig. 9.7 X- (left) and Z-(right) direction model responses at DOC = 1.75mm, Ω = 1250rpm and t_0 = 0.125mm

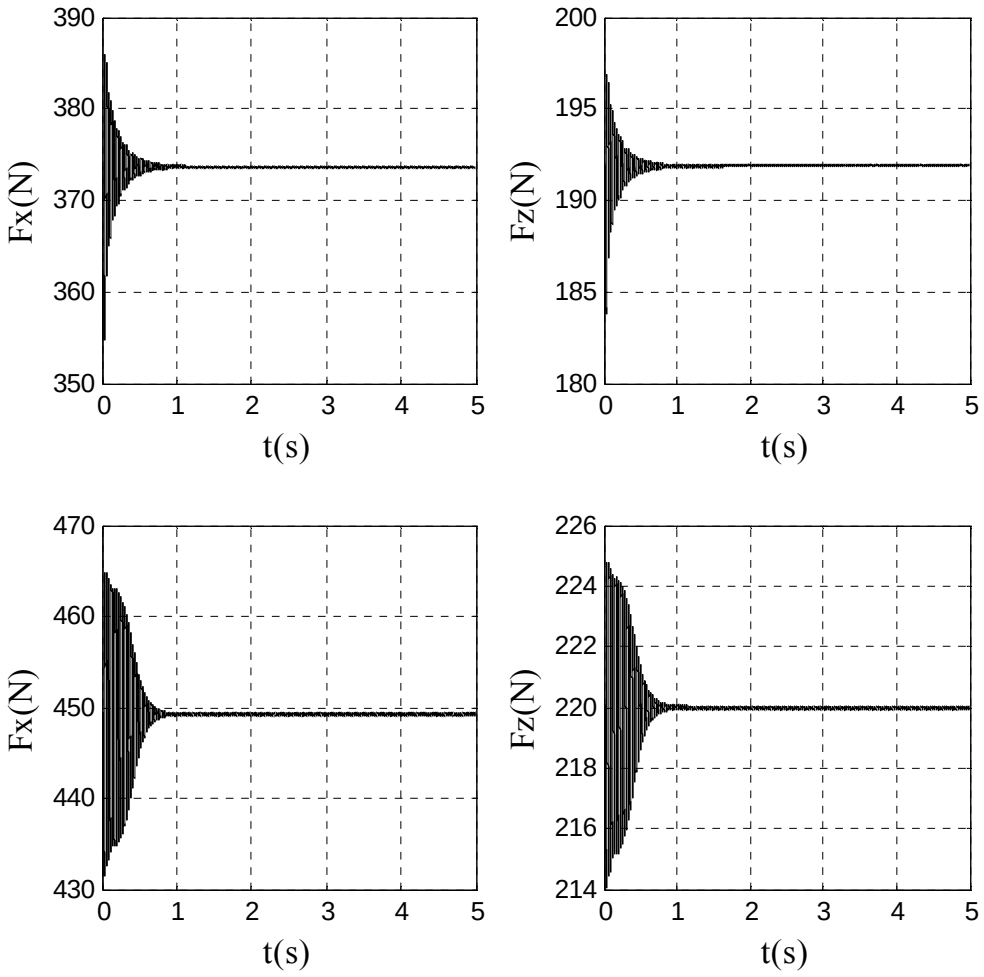

Fig. 9.8 X- and Z-direction cutting forces for t_0 = 0.0965mm (top) and t_0 = 0.125mm (bottom) at DOC = 1.75mm and Ω = 1250rpm

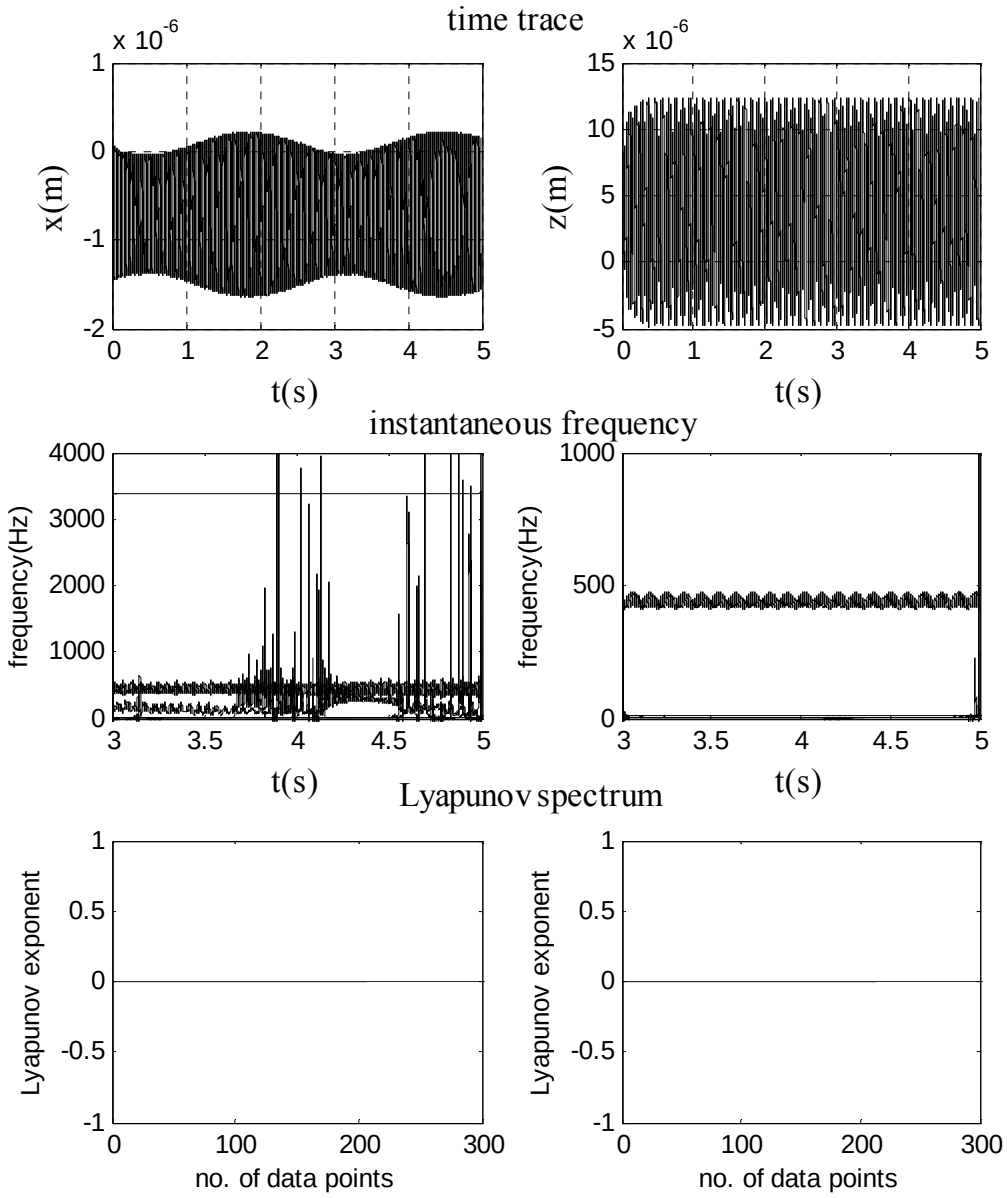

Fig. 9.9 X- (left) and Z-(right) direction model responses at DOC = 2.00mm, Ω = 1250rpm and t_0 = 0.125mm

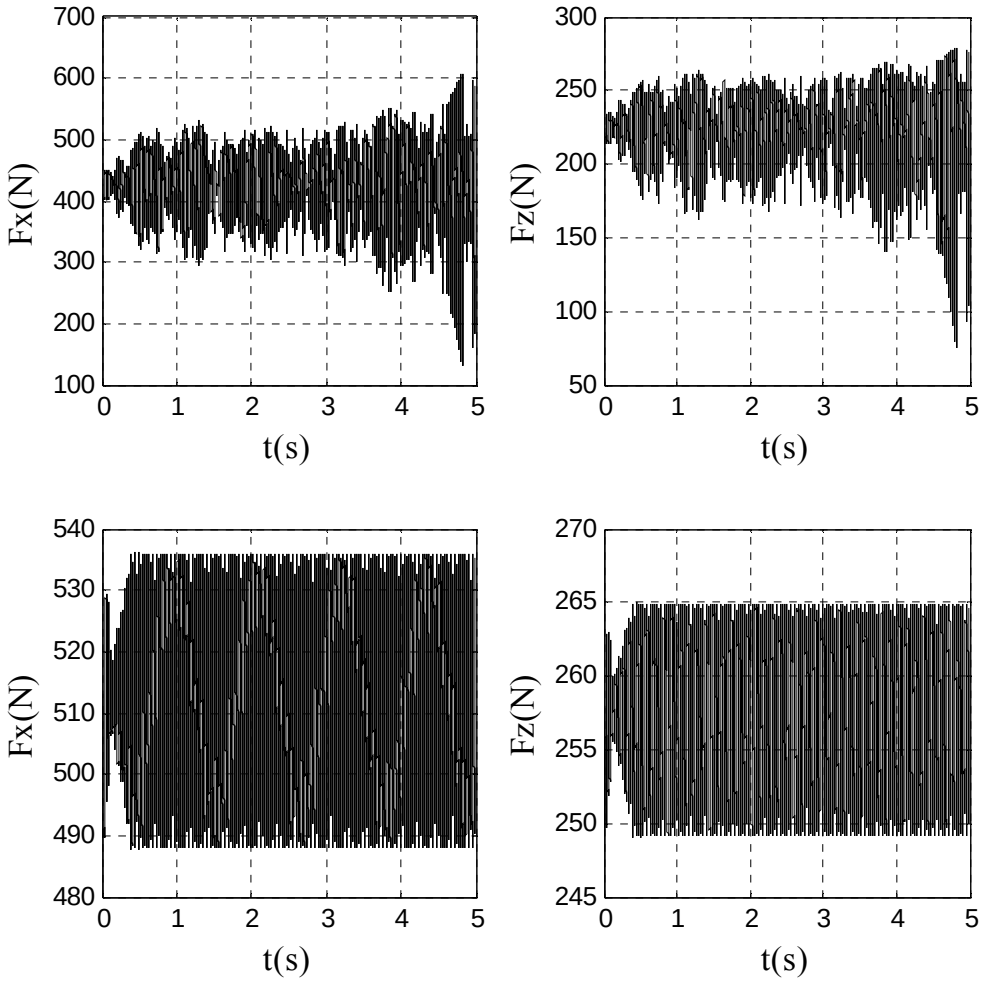

Fig. 9.10 X- and Z-direction cutting forces for t_0 = 0.0965mm (top) and t_0 = 0.125mm (bottom) at DOC = 2.00mm and Ω = 1250rpm

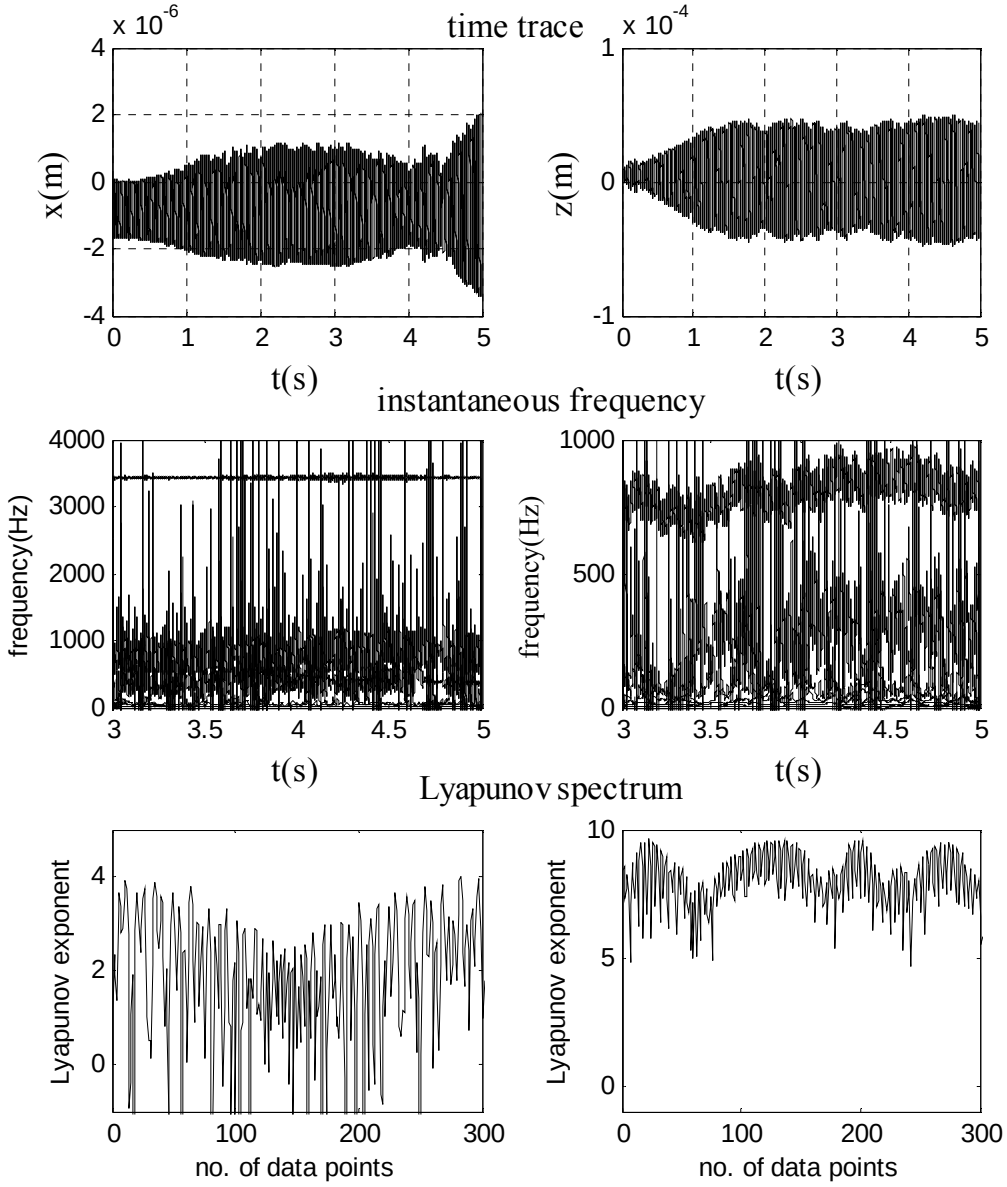

Fig. 9.11 X- (left) and Z-(right) direction model responses at DOC = 2.49mm, Ω = 1250rpm and t_0 = 0.125mm

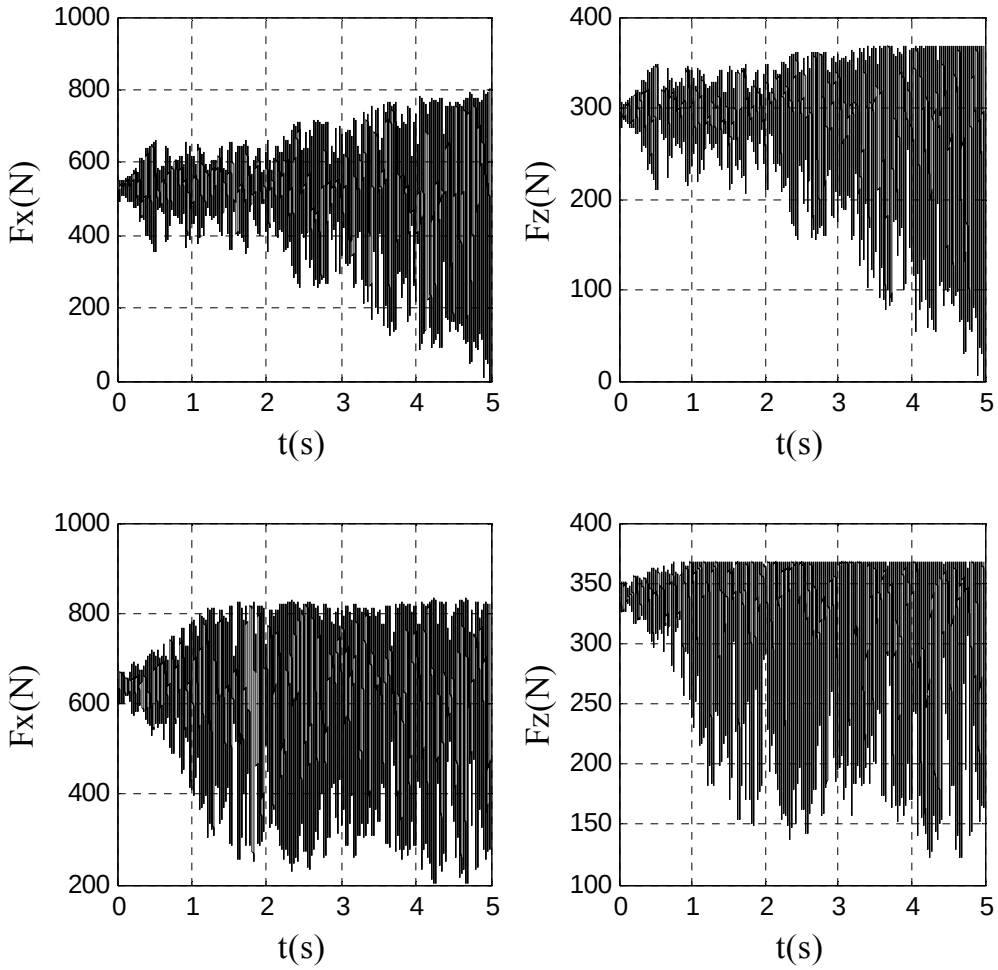

Fig. 9.12 X- and Z-direction cutting forces for t_0 = 0.0965mm (top) and t_0 = 0.125mm (bottom) at DOC = 2.49mm and Ω = 1250rpm

Figures in this subsection (9.1 - 9.12) display system dynamics for two feed rates and six different DOCs. Figs. 9.1, 9.3, 9.5, and 9.7 give the X- and Z-direction model responses corresponding to tool feed t_0 = 0.125mm and DOC = 1.00mm, 1.25mm, 1.62mm and 1.75mm, respectively. Since their respective Lyapunov spectra are all zero, only time history (top) and instantaneous frequency (bottom) are shown. These results are compared with the responses associated with the feed t_0 = 0.0965mm shown in Figs. 4.5-4.8. Fig. 9.9 carries the responses corresponding to DOC = 2.00mm. It is compared with the responses associated with t_0 = 0.0965mm in Fig. 4.9. Fig. 9.11 presents the responses corresponding to DOC = 2.49mm. Its counterpart corresponding to t_0 = 0.0965mm can be found in Fig. 4.3 (left column for X-direction response) and Fig. 4.4 (left column for Z-direction response). The corresponding X- and Z-direction cutting forces in response to DOC = 1.00mm through 2.49mm with feed t_0 = 0.0965mm and 0.125mm are shown in Figs. 9.2, 9.4, 9.6, 9.8, 9.10, and 9.12.

Comparing with the workpiece responses in Fig. 4.5, the vibration amplitudes in Fig. 9.1 associated with DOC = 1.00mm and t_0 = 0.125mm are 10% larger. While the corresponding tool vibration amplitudes do not show discernible differences, the associated instantaneous frequency of the lower tool feed (t_0 = 0.0965mm) has more frequency components. Though the time-frequency data show fewer bifurcations in the lower feed case, the one broadband component is indicative of instability, as is confirmed the same by the positive Lyapunov spectrum in Fig 4.5. The instantaneous frequency of the higher feed case has more bifurcations. Nonetheless, it is dynamically stable. Note that in Fig 9.2 the X- and Z- direction force magnitudes increase with

increasing feed rate. This is evidently true since higher chip load would result in higher cutting force.

When DOC is increased to 1.25mm in Fig 9.3, the X-direction vibration amplitude is again higher than that of the lower feed in Fig. 4.6. While the lower feed case shows stable frequency characteristics for the X-direction response, increasing feed to 1.25mm in Fig 9.3 is seen to impact stability in a negative way. The tool vibratory patterns associated with the two feed rates are very different at this DOC. Higher feed is accompanied by a 25% increase in tool vibration amplitude. Moreover, whirling frequency is readily visible in the tool instantaneous frequency plot of the higher feed rate case. In fact, whirling frequency is prominent in all instantaneous frequency plots corresponding to the case of 0.125mm feed rate. The associated cutting force components display very different behaviors in Fig. 9.4. The X-/Z-direction cutting force of the lower feed case oscillates with 18N/7N. In contrast, the case of higher feed rate oscillates with a mere 0.2N/0.1N. Note that the magnitude of the X-/Z-direction cutting force increases by 20%/15% for the higher feed rate case.

Increase DOC further to 1.62mm, the workpiece vibration patterns of the two feed rate cases in Figs. 9.5 and 4.7 are seen to be similar. However, the vibration amplitude of the higher feed rate case is 12% higher. The lower feed rate case demonstrates a broadband frequency characteristic. Tool vibratory characteristics of the two cases are visibly distinct. The case of lower feed rate has tool vibration amplitude about 10 times higher than that of the higher feed rate. This is the case when tool structural nonlinearity becomes dominant. Workpiece vibration amplitude of the higher

feed rate case, on the other hand, is always larger than the lower feed rate case. Tool instantaneous frequency plots in Fig. 9.5 illustrate that higher feed is dynamical more stable than the lower feed. Oscillation of cutting force seen in Fig. 9.6 is also smaller for the higher feed, with the magnitude showing a similar percentage increase as in previous cases.

Fig. 9.7 presents X- and Z-direction responses for DOC = 1.75mm and t_0 = 0.125mm. Compare with the responses in Fig. 4.8, it can be seen that workpiece vibration responses are similar, though the higher feed case has slightly larger vibration amplitude. Despite the fact that both responses are stable, their instantaneous frequency plots show bifurcations. Tool vibration amplitude corresponding to the higher feed rate is of a few nanometers. The lower feed rate case has its vibration amplitudes in Fig 4.8 that is 1,000 times higher. The tool instantaneous frequency response of the lower feed rate case is well behaved, while the higher feed rate case is evidently a highly bifurcated state. Cutting force oscillations for both cases in Fig. 9.8 are in the same range and of the similar characteristics as in Figs. 9.4 and 9.6.

Responses associated with DOC = 2.00mm and t_0 = 0.125mm in Fig. 9.9 show stability in both the time and frequency domains. Their corresponding Lyapunov spectra also confirm the same. In contrast, the case in Fig. 4.9 corresponding to DOC = 2.00mm and lower feed at t_0 = 0.0965mm is an instability at its worst. Moreover, the corresponding cutting forces in Fig. 9.10 show very large oscillations of hundreds of Newtons in magnitude. Forces of the higher feed rate have lower oscillation amplitudes. Extreme machining instability is seen in Fig. 9.11 where higher feed rate and DOC =

2.49mm are considered. This implies that the stability limit for t_0 = 0.125mm is in between DOC = 2.00mm and 2.49mm. Recall in Fig. 5.4 (left column) that the stability limit for t_0 = 0.0965mm feed rate is 1.84mm. Fig. 9.12 shows the corresponding X- and Z-direction cutting force components. It can be seen that the cutting forces oscillate randomly with very high amplitudes, thus signifying a state of instability.

9.2 Discussions

The effects of two feed rates (or undeformed chip thicknesses) on cutting dynamics involving whirling were studied. It was shown that tool feed impacted cutting force and workpiece and tool vibrations. X-/Z-direction cutting force magnitude was 20%/15% higher for higher feed rate. Numerical experiment performed in the section supported that increasing chip thickness induces higher chip load, and higher chip load in turn results in larger cutting forces. These higher forces induced larger workpiece deflection, thus higher vibration magnitudes. Nonlinearity of the tool structure had a dominant effect on the vibration amplitude of the tool. At high DOCs, it was seen that high feed rate contributed to stability, thus indicating that feed rate was among the parameters that impact cutting stability. It should be cautioned that these results, which were obtained by considering only two feed rates, are insufficient to conclude that higher feeds would bring about higher stability limit. Further study on investigating manipulating feed rate to achieve higher stability limit is therefore needed.

10. EFFECTS OF SPINDLE SPEED ON CUTTING STABILITY

10.1 Effect of Speed on Rough Cuts

The dynamic model is simulated using four different spindle speeds and several depth-of-cuts. Results presented in this section are only for DOC = 1.62mm. The spindle speeds considered are 750, 1000, 1250 and 1500rpm with a 0.0965mm chip thickness.

10.1.1 Workpiece Behavior

All figures(10.1-10.4) in the subsection, except for Fig. 10.5 present X- and Y-direction workpiece time responses (top), along with their corresponding instantaneous frequencies (middle) and Lyapunov exponents (bottom). The lowest spindle speed, 750rpm, considered in Fig. 10.1 displays a motion of instability at DOC = 1.62mm. Vibrations in both directions seem random and the positive Lyapunov spectra indicate chaos. These are accompanied by broadband instantaneous frequency spectra. When the speed is increased to 1000rpm, it can be seen in Fig. 10.2 that the response is remarkably stable. The time traces are periodic and the Lyapunov spectra are zero, implying that future vibrations can be predicted. Moreover, the instantaneous frequency plots show only three major frequencies that do not bifurcate. These frequencies are: workpiece natural frequency at 3343Hz, tool natural frequency at 425Hz, and whirling frequency at 16.67Hz.

Fig. 10.3 presents workpiece behaviors at 1250rpm. Time histories and Lyapunov spectra demonstrate a very stable situation at this stage, though the bandwidth

of the frequency exited by the tool natural frequency increases slightly. Overall, the workpiece is in a state of stability. When speed is increased to 1500rpm, the workpiece is seen to be in stable motion, though 4% increase in vibration amplitude is also observed (Fig. 10.4). The Lyapunov spectra also show stability with zero exponents for X-direction vibrations and negative exponents for Y-direction vibrations. X- and Y-direction cutting forces corresponding to the cases previously mentioned with four different spindle speeds are given in Fig. 10.5. Cutting forces of chaotic nature in Fig. 10.5(a) agree well with the results in Fig. 10.1. The stability indicated in Fig. 10.5(b) is qualitatively consistent with Fig. 10.2. Cutting force components in Fig. 10.5(b) are seen to be stable with relatively smaller amplitude variations compare with those in Fig. 10.5(a). When speed is increased from 1000rpm to 1250rpm, further reduction of cutting force amplitude variations is seen. Yet, since the chip load is the same with the same DOC and chip thickness, the average magnitudes of the X- and Y- direction forces remain the same. Fig. 10.5(d) presents the cutting forces associated with Ω = 1500rpm. It can be seen that the average force magnitudes are approximately the same with slight increase in amplitude variation.

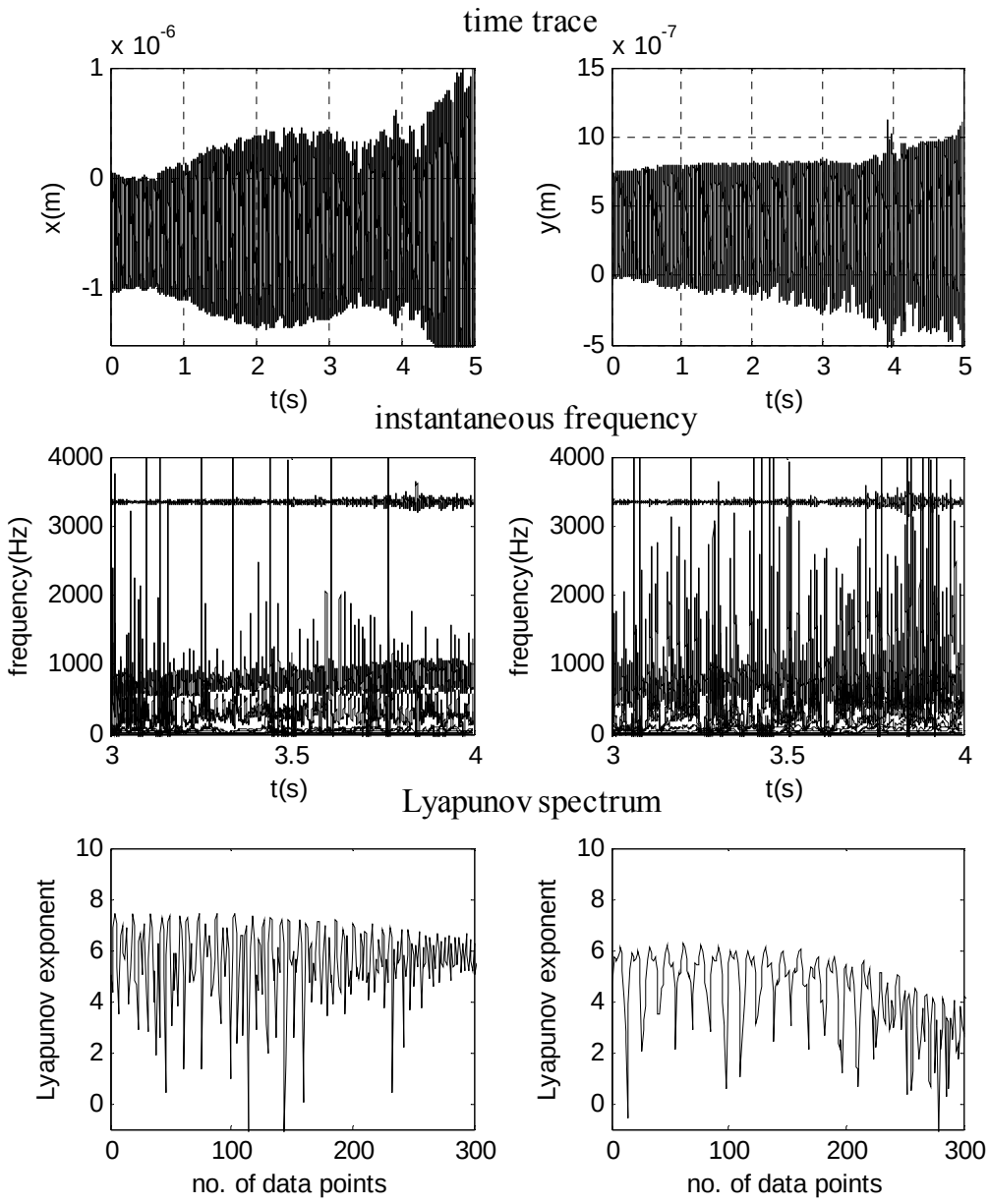

Fig. 10.1 X- (left) and Y-(right) direction workpiece responses for DOC = 1.62mm at Ω = 750rpm

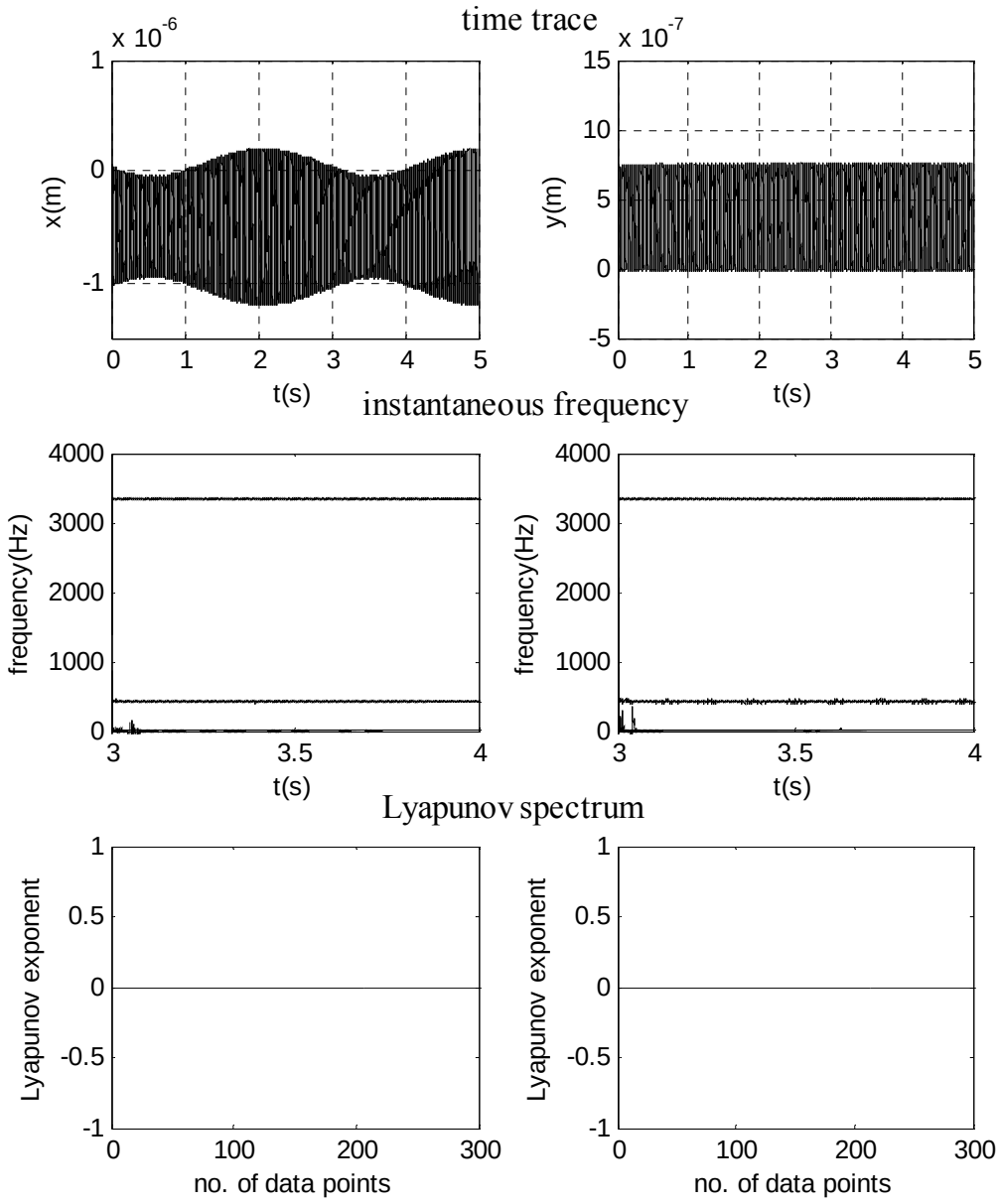

Fig. 10.2 X- (left) and Y-(right) direction workpiece responses for DOC = 1.62mm at Ω = 1000rpm

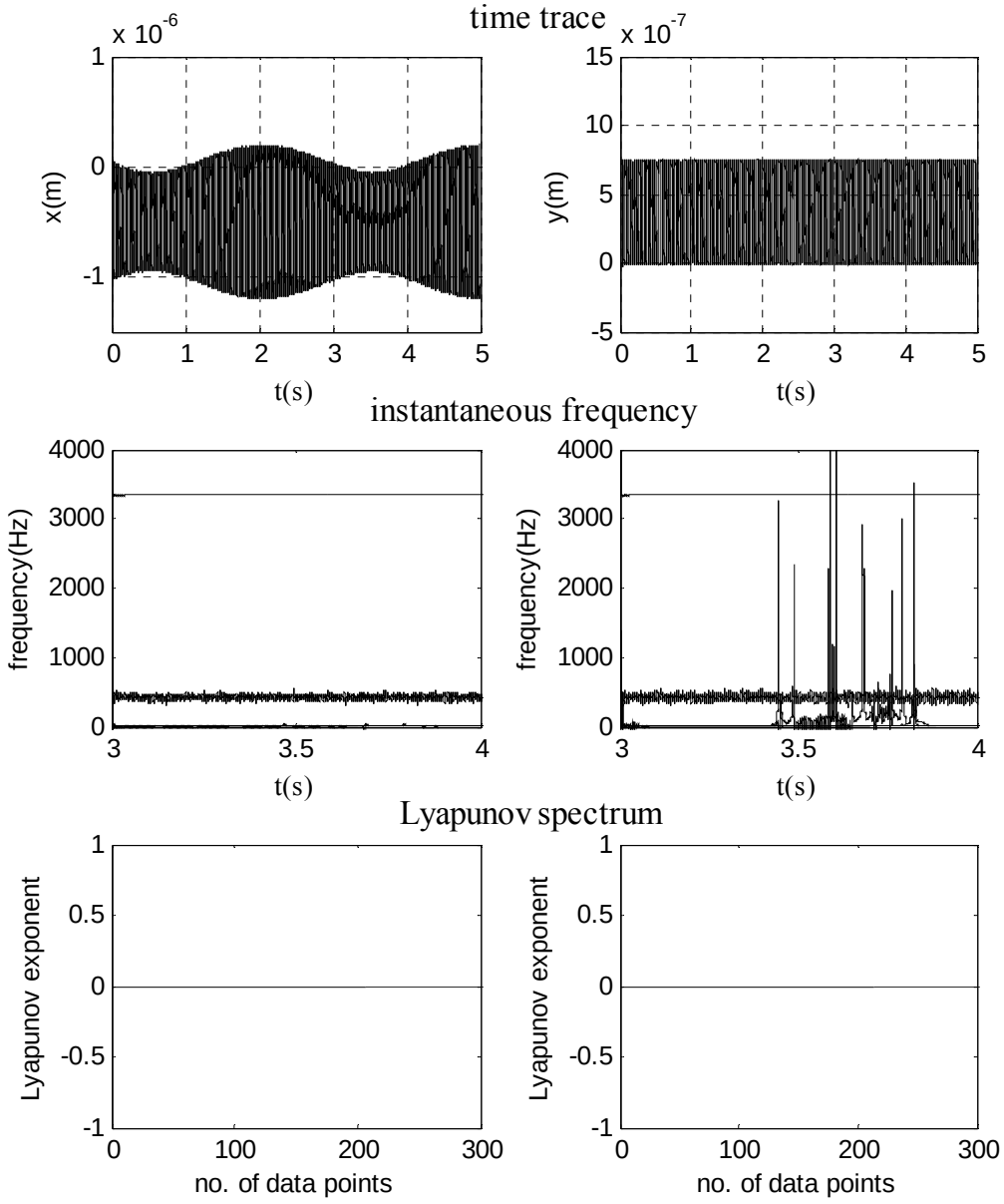

Fig. 10.3 X- (left) and Y-(right) direction workpiece responses for DOC = 1.62mm at Ω = 1250rpm

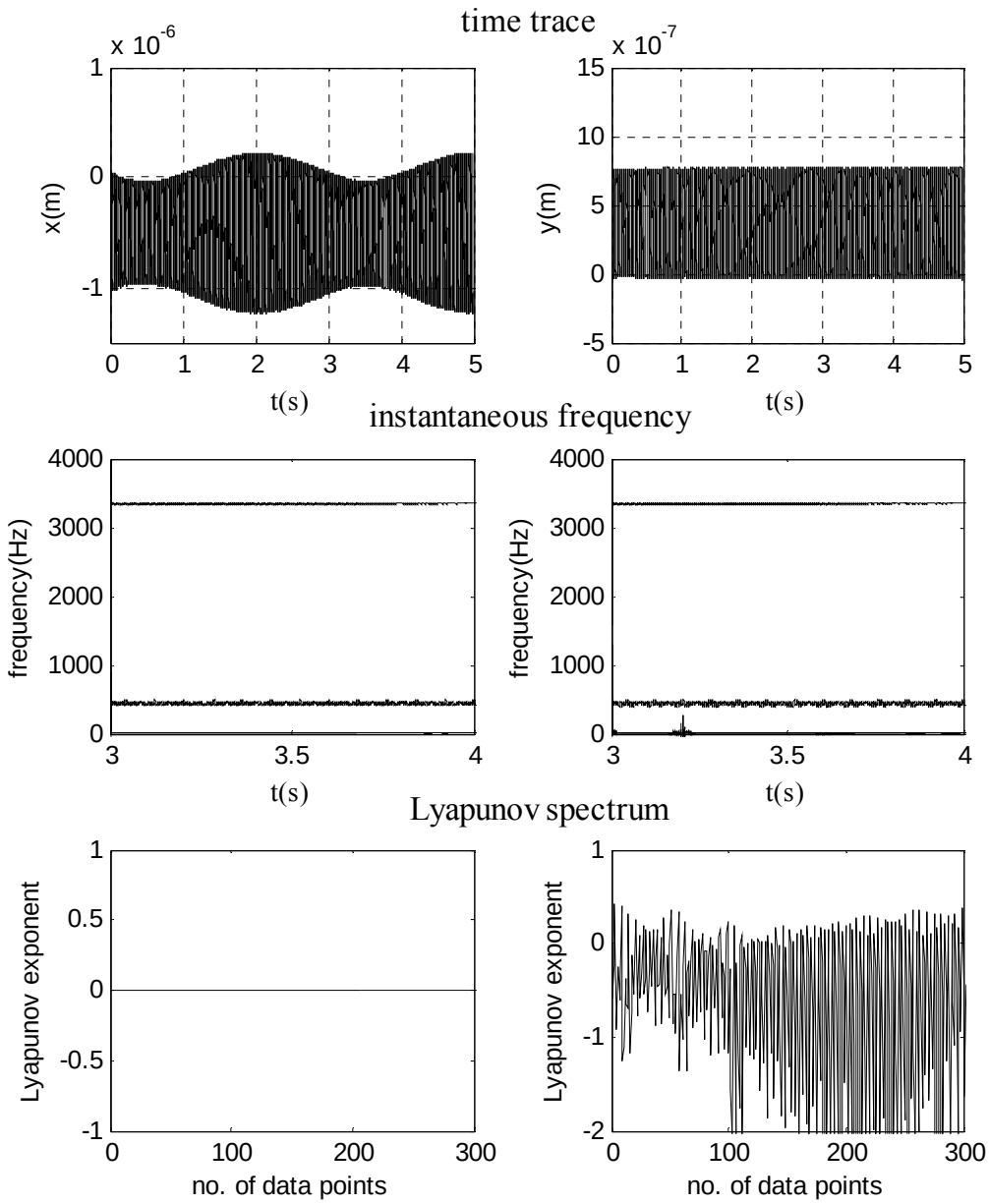

Fig. 10.4 X- (left) and Y-(right) direction workpiece responses for DOC = 1.62mm at Ω = 1500rpm

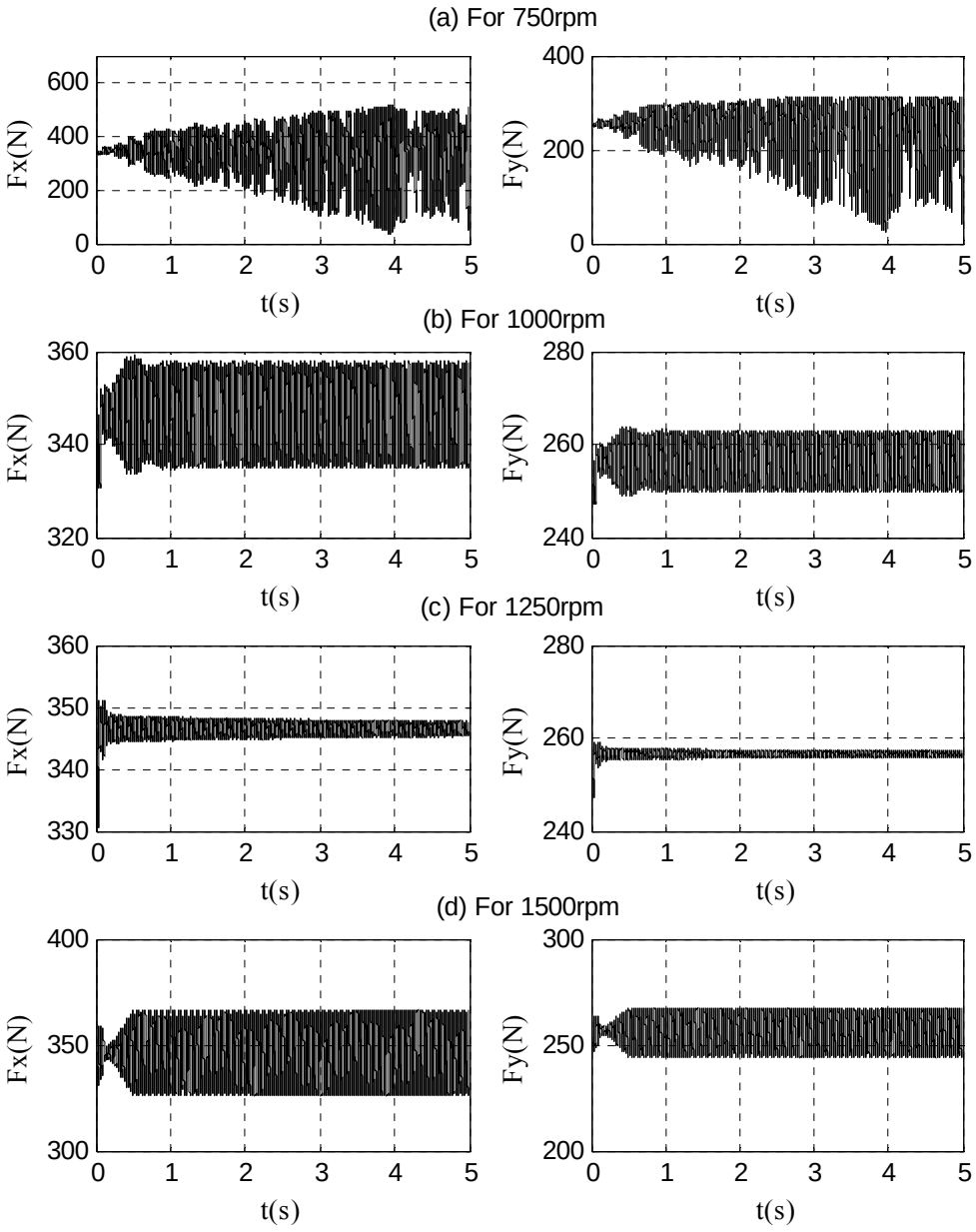

Fig. 10.5 X- (left) and Y-(right) cutting forces for DOC = 1.62mm

10.1.2 Tool Behavior

Figures in this subsection each has four subplots (a), (b), (c), and (d) presenting, respectively, tool vibration time history, Z-direction cutting force that causes tool vibration, instantaneous frequency and corresponding Lyapunov spectrum for the time data between 3 to 4 seconds. Figs. 10.6–10.9 convey the same instability states for the tool as seen of the workpiece's. Figs. 10.6 and 10.7 show the progression of tool responses from one of instability at Ω = 750rpm to one of stability at Ω = 1000rpm. Even though the workpiece is excited by the tool natural frequency subject to the action of cutting force components, the tool is not excited by the workpiece natural frequency. Similar to workpiece behaviors, the cutting force amplitude variation is reduced once the speed is increased from 1000rpm in Fig. 10.7 to 1250rpm in Fig. 10.8. Moreover, the instantaneous frequency plot displays a state of slight bifurcation with the increased speed. Increasing the spindle speed further helps maintain a stable response marked by a clean frequency spectrum. Again, the Z-direction cutting force follows the X- and Y-direction cutting forces in having the same pattern of amplitude variation (either increase or decrease) with increasing speed. Note that the response subject to higher speed remains one of stable and that different speeds have their respective stability limits.

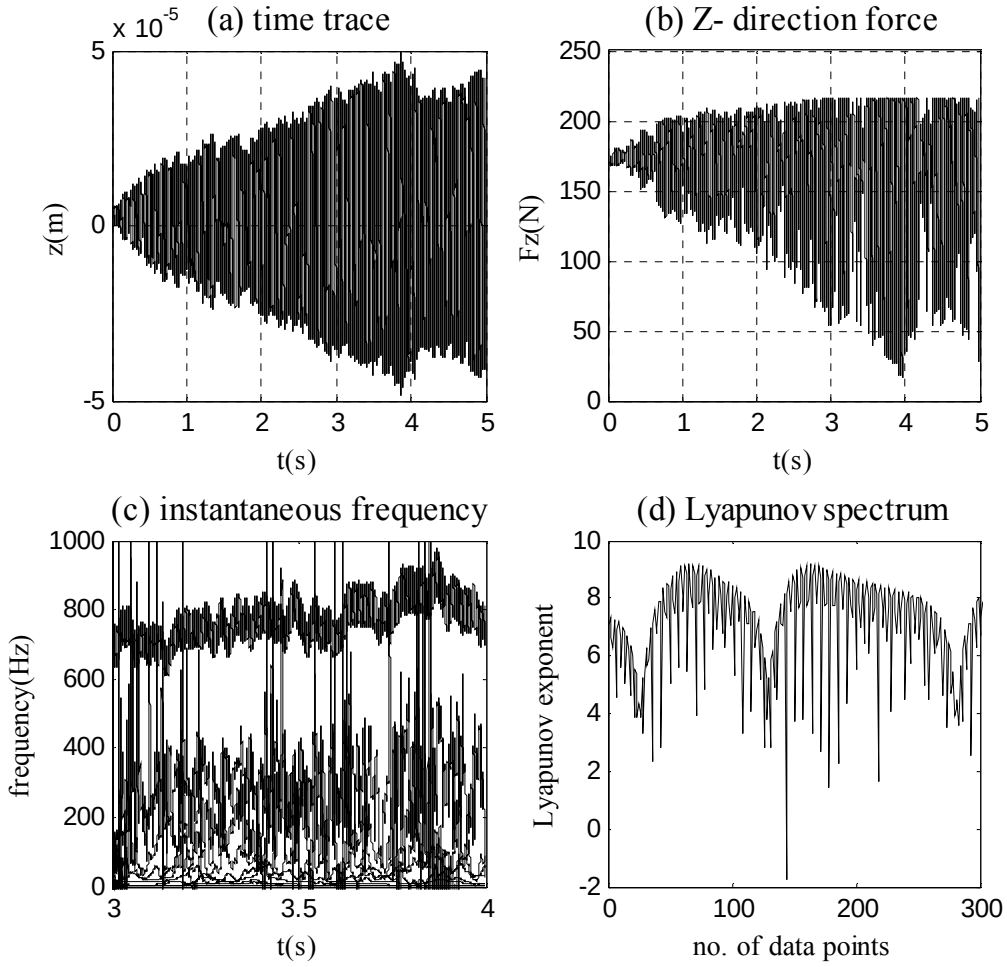

Fig. 10.6 Z- direction tool behavior for DOC = 1.62mm at Ω = 750rpm

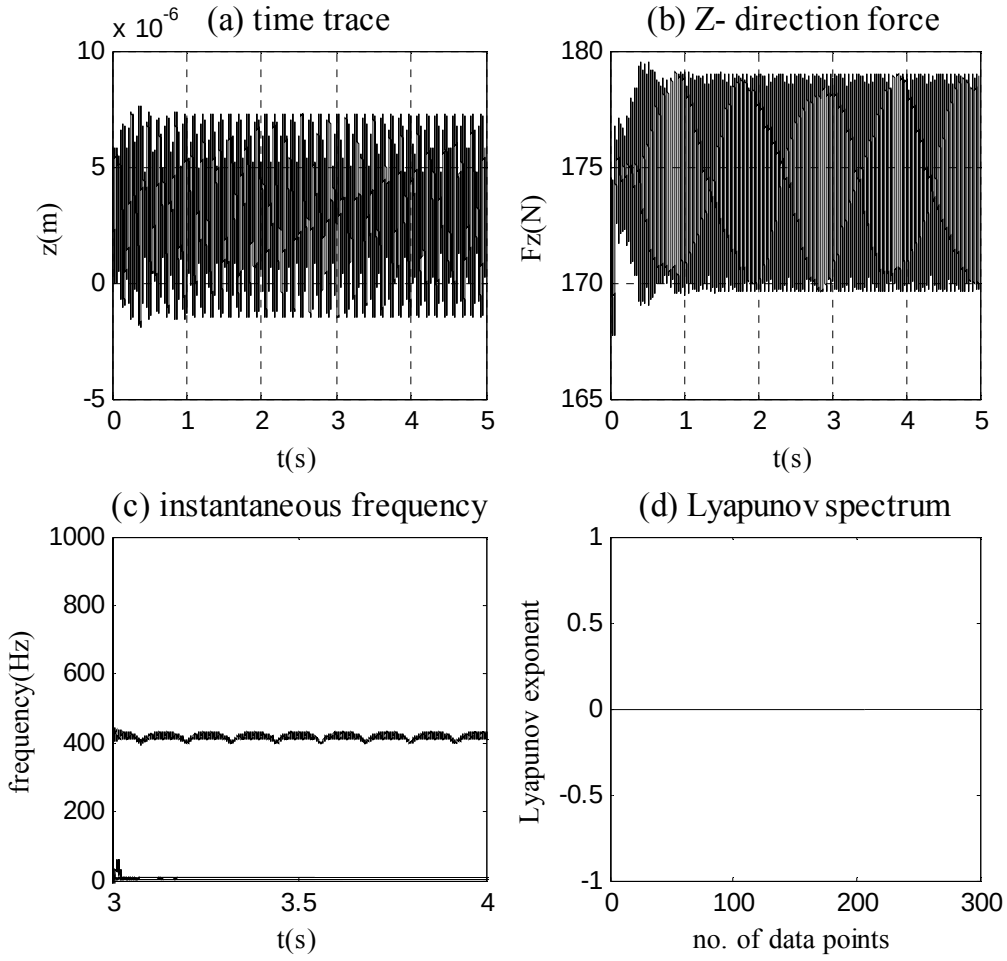

Fig. 10.7 Z- direction tool behavior for DOC = 1.62mm at Ω = 1000rpm

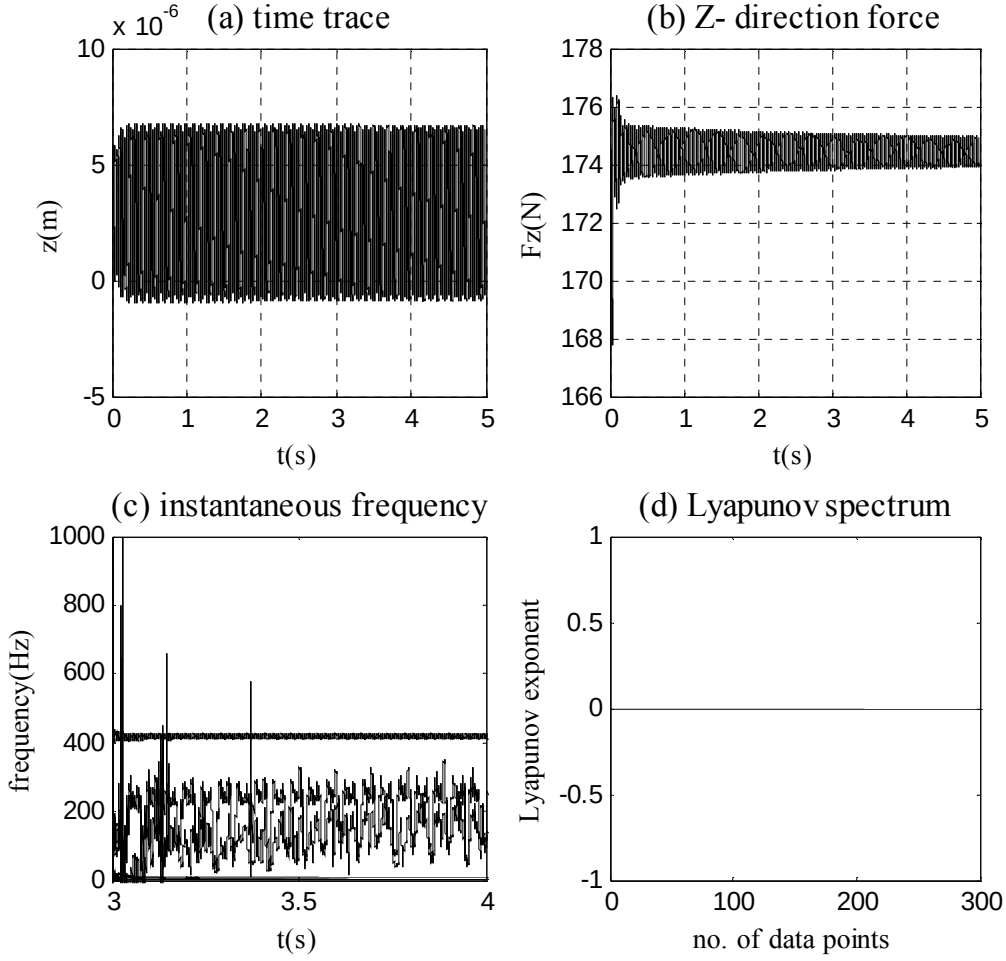

Fig. 10.8 Z- direction tool behavior for DOC = 1.62mm at Ω = 1250rpm

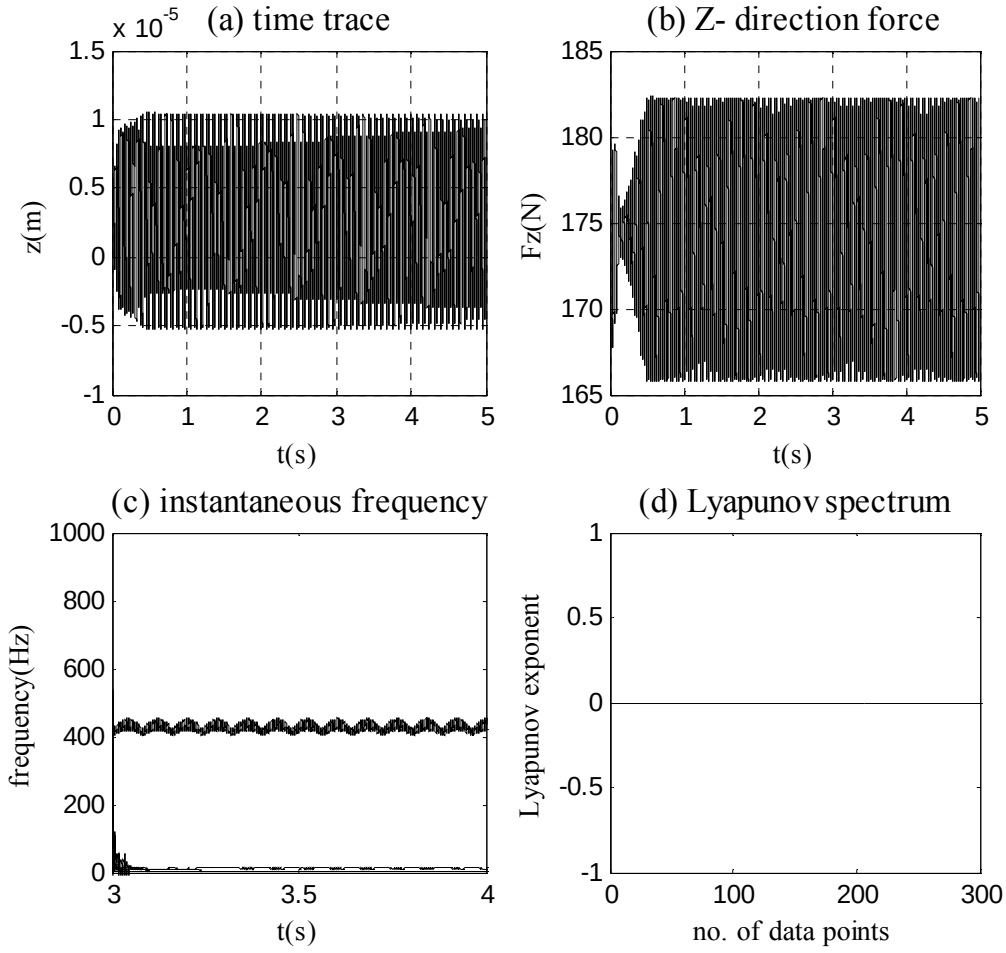

Fig. 10.9 Z- direction tool behavior for DOC = 1.62mm at Ω = 1500rpm

10.2 Stability Limits

10.2.1 Margin of Stability and Instability

After performing many numerical experiments for different DOCs, the stable-unstable margins for rough turning (at large DOCs) are found for four different speeds at 750rpm, 1000rpm, 1250rpm, and 1500rpm. Workpiece and tool vibration responses of the cutting model system that correspond to stable DOCs and unstable DOCs near the critical depth-of-cut are presented in figures that follow. X- and Z-direction vibration responses are examined to identify, respectively, the workpiece and tool stability margins. Workpiece responses found in Figs. 10.10-10.13, each illustrates a case of stability and a case of instability subject to two different DOCs at the same spindle speed. This is done to identify the margin of instability for the particular DOCs considered. The corresponding tool behaviors for the same set of DOCs are presented in Figs. 10.14–10.17. These figures are for investigating the stability limits associated with the tool. In all figures, the plots on top are time histories between 3 to 5 seconds and the middle plots are their corresponding instantaneous frequencies that demonstrate the evolution of dynamic stability and/or instability. The bottom plots provide a quantitative measure using Lyapunov spectra for determining the dynamic instability of the data windowed between 4 and 5 seconds.

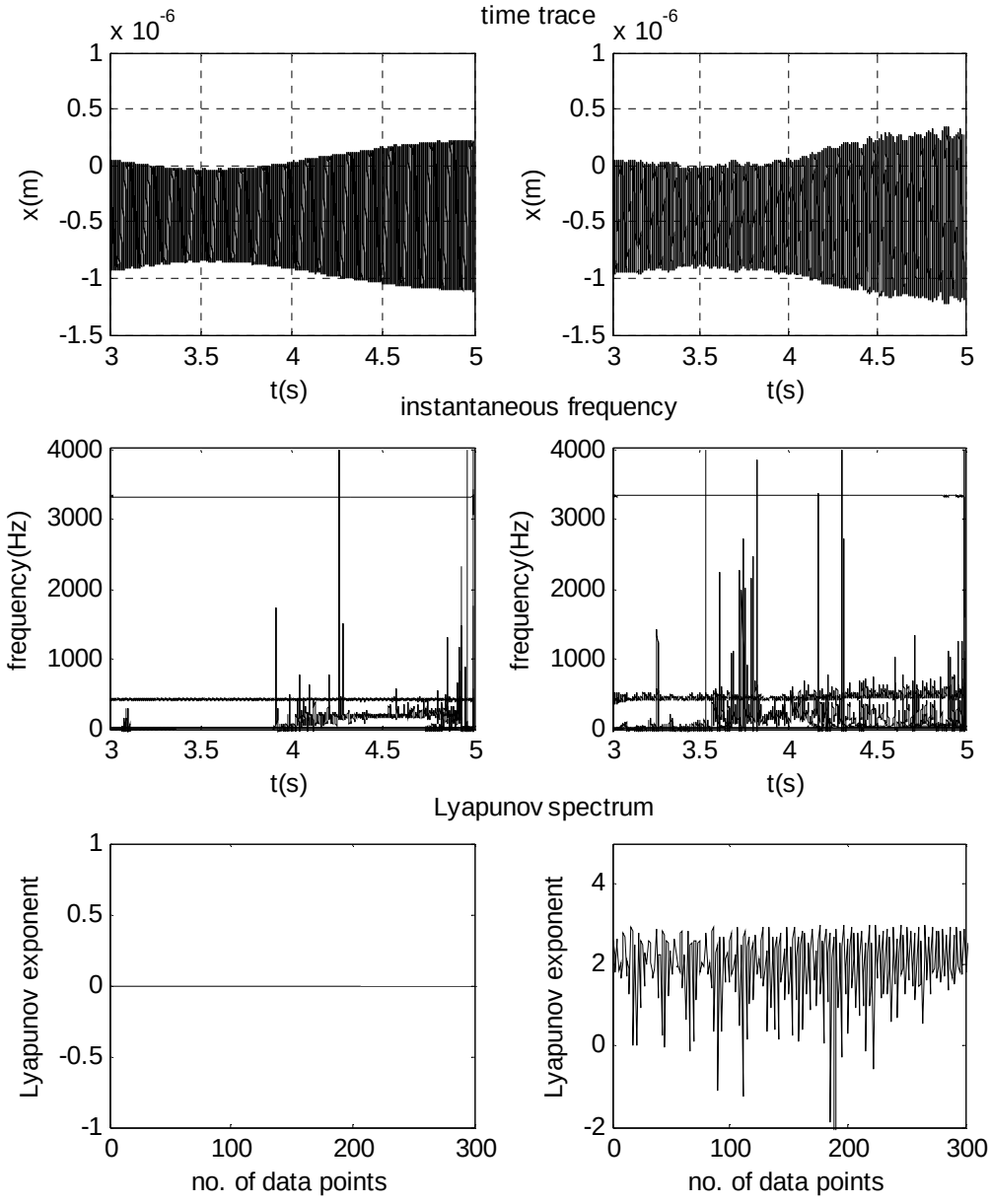

Fig. 10.10 X- direction workpiece behavior for DOC = 1.40mm (left) and DOC = 1.45mm (right) at Ω = 750rpm

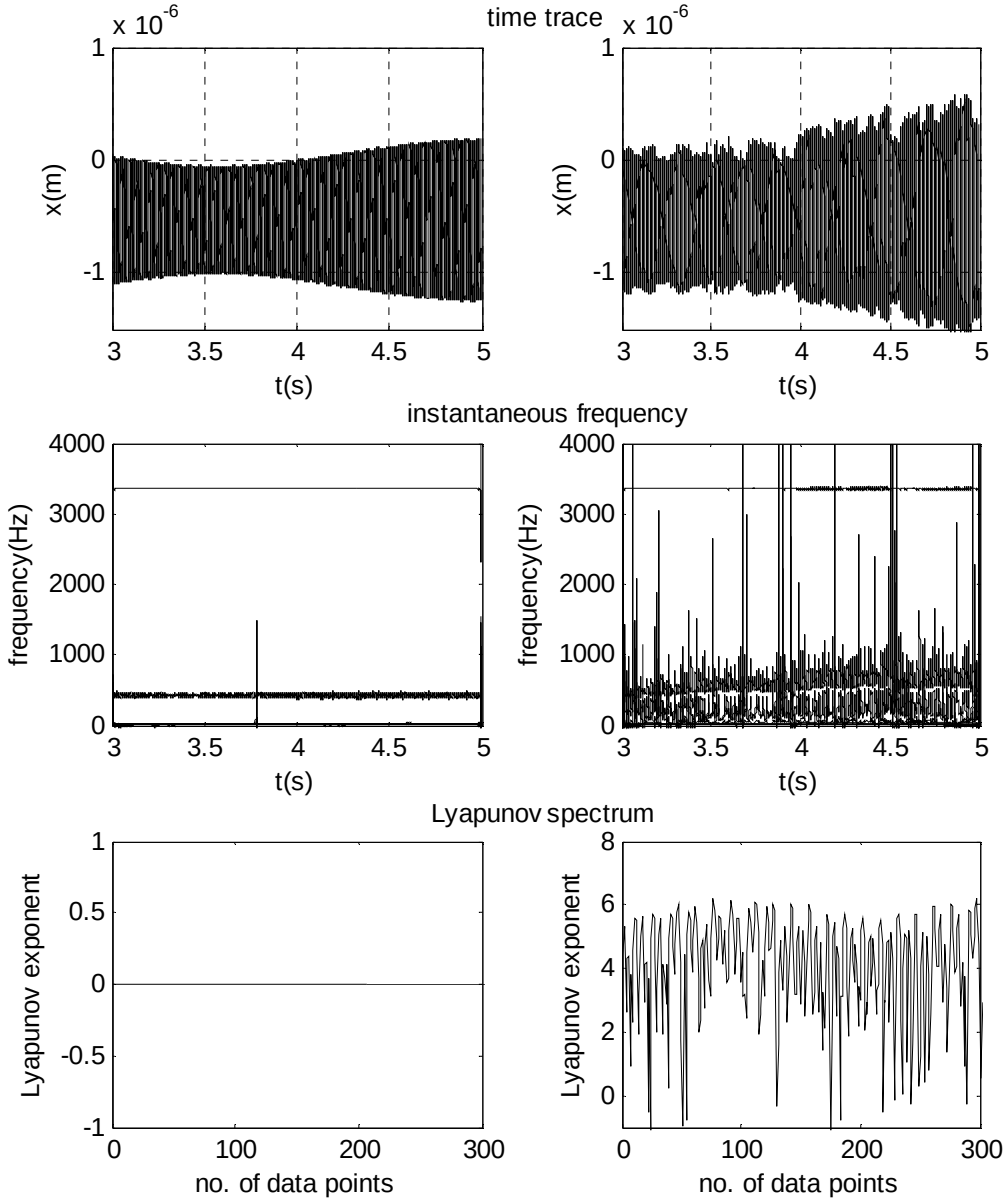

Fig. 10.11 X- direction workpiece behavior for DOC = 1.75mm (left) and DOC = 1.78mm (right) at Ω = 1000rpm

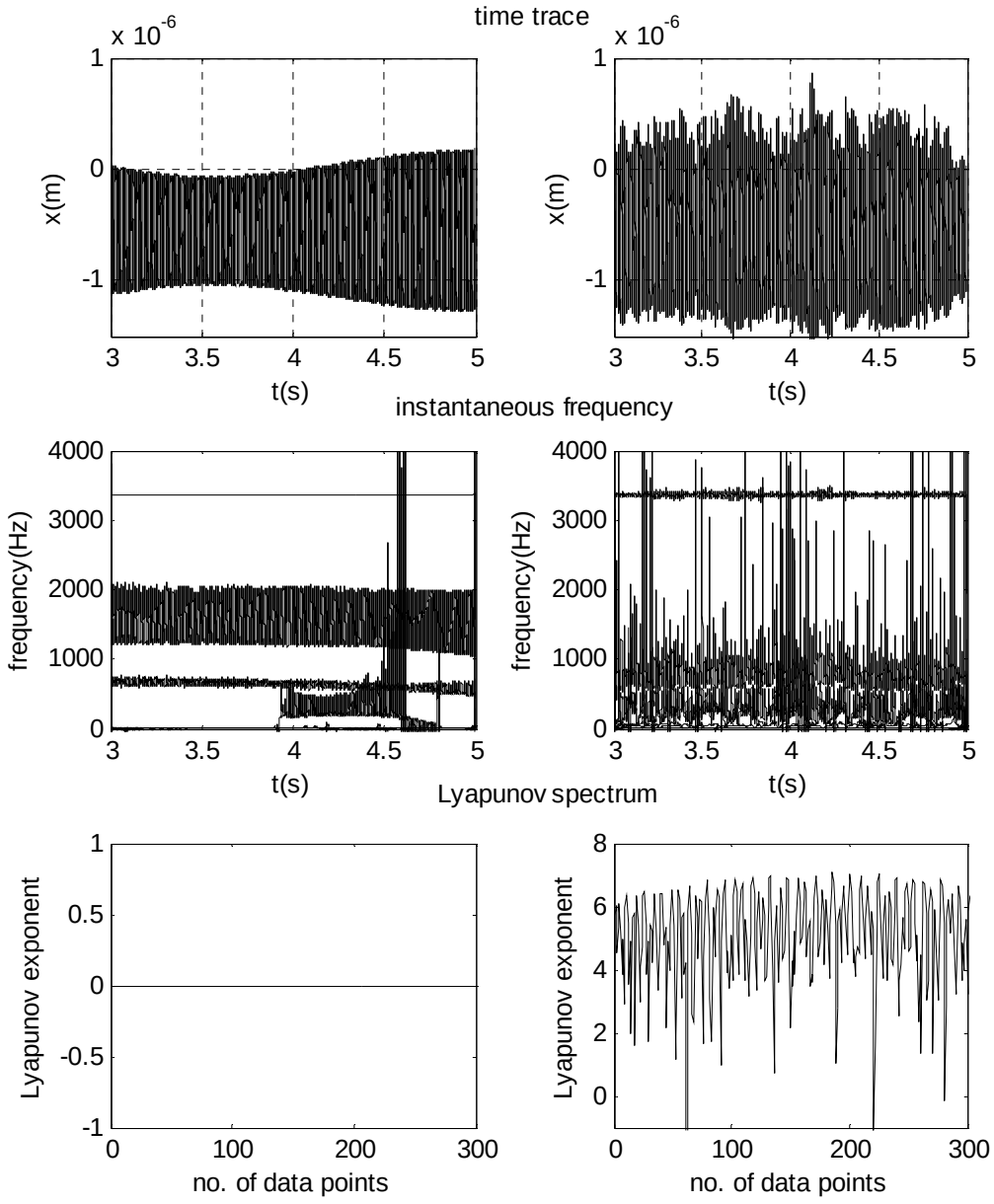

Fig. 10.12 X- direction workpiece behavior for DOC = 1.83mm (left) and DOC = 1.84mm (right) at Ω = 1250rpm

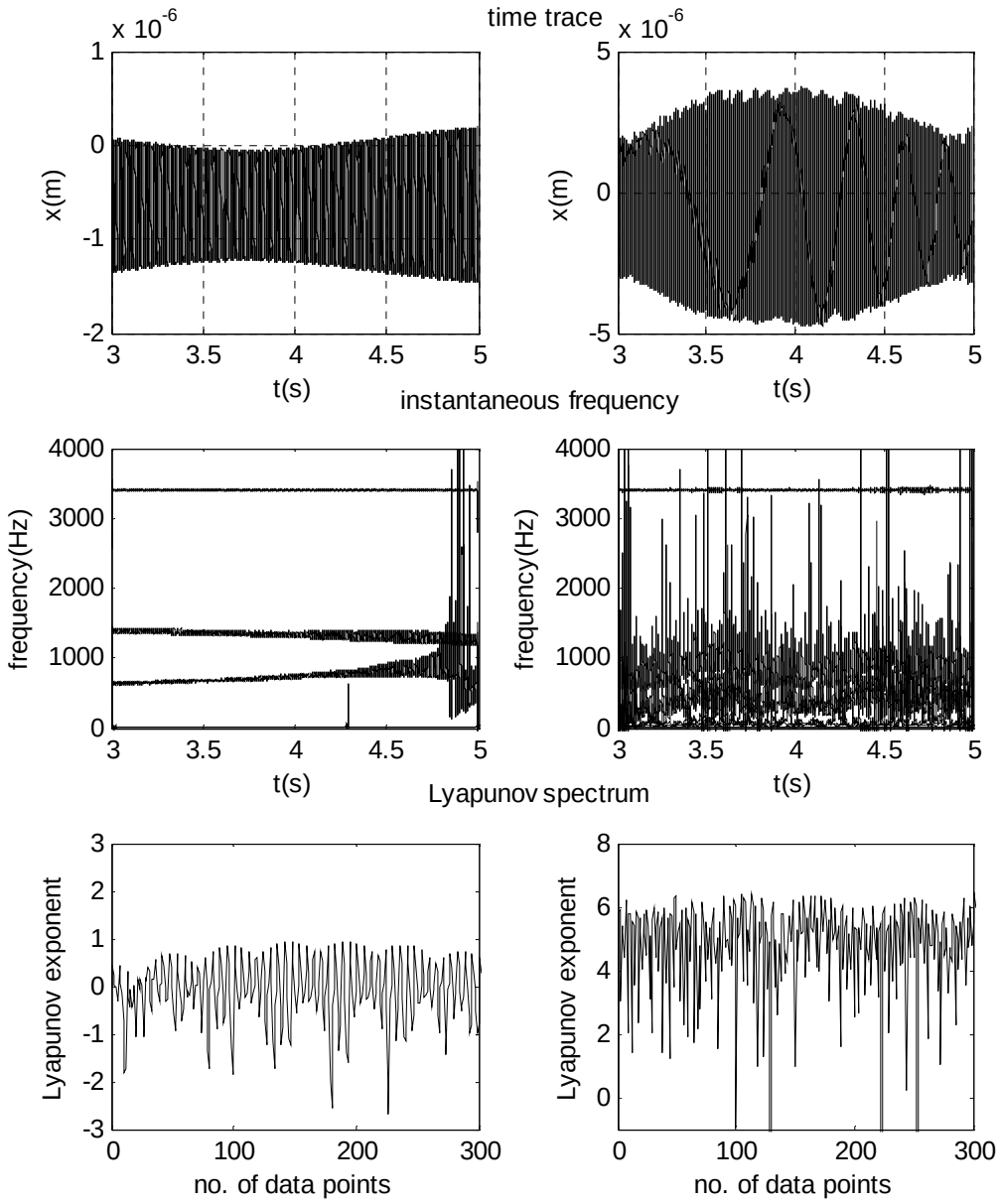

Fig. 10.13 X- direction workpiece behavior for DOC = 2.21mm (left) and DOC = 2.22mm (right) at Ω = 1500rpm

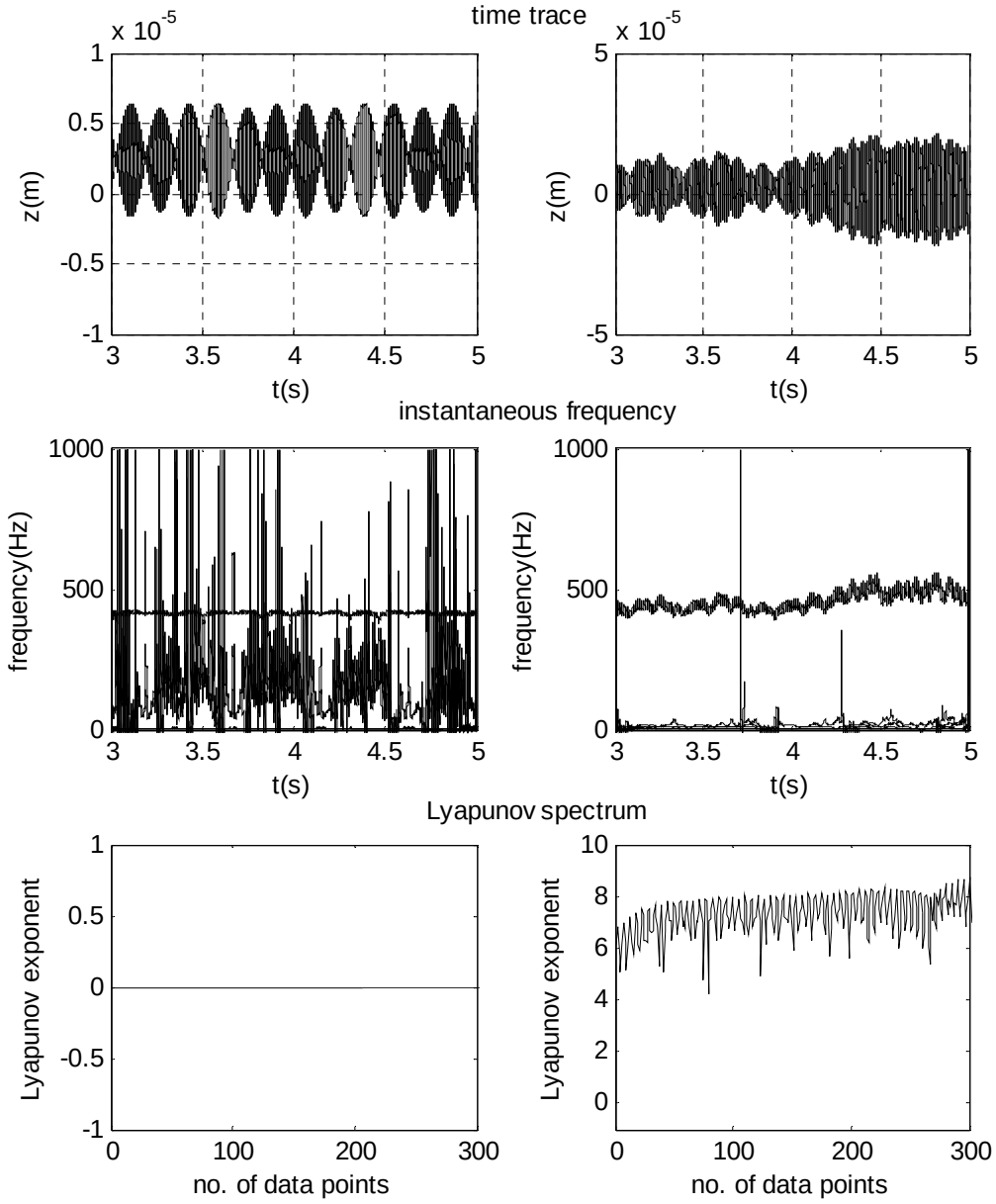

Fig. 10.14 Z- direction tool behavior for DOC = 1.40mm (left) and DOC = 1.45mm (right) at Ω = 750rpm

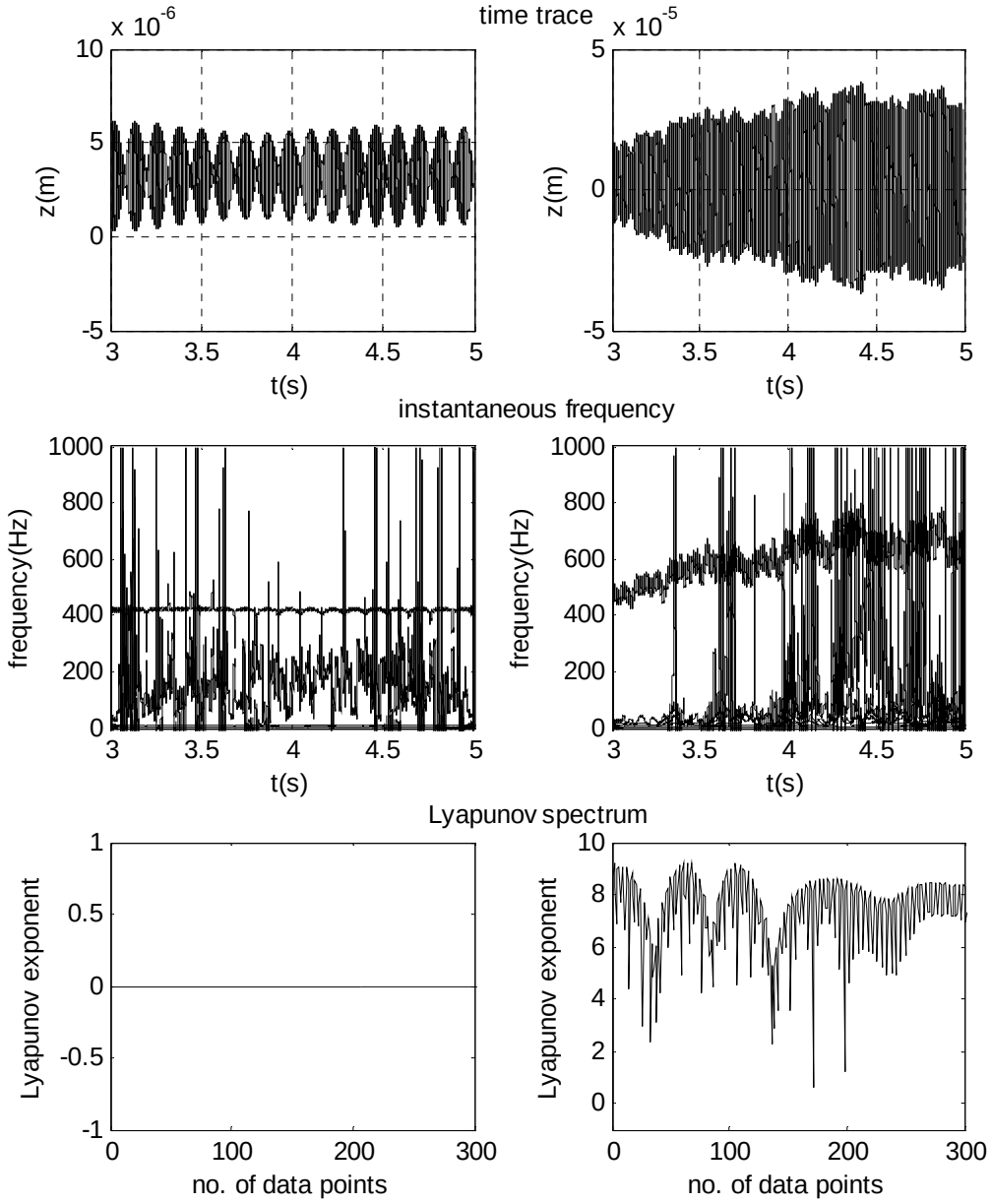

Fig. 10.15 Z- direction tool behavior for DOC = 1.75mm (left) and DOC = 1.78mm (right) at Ω = 1000rpm

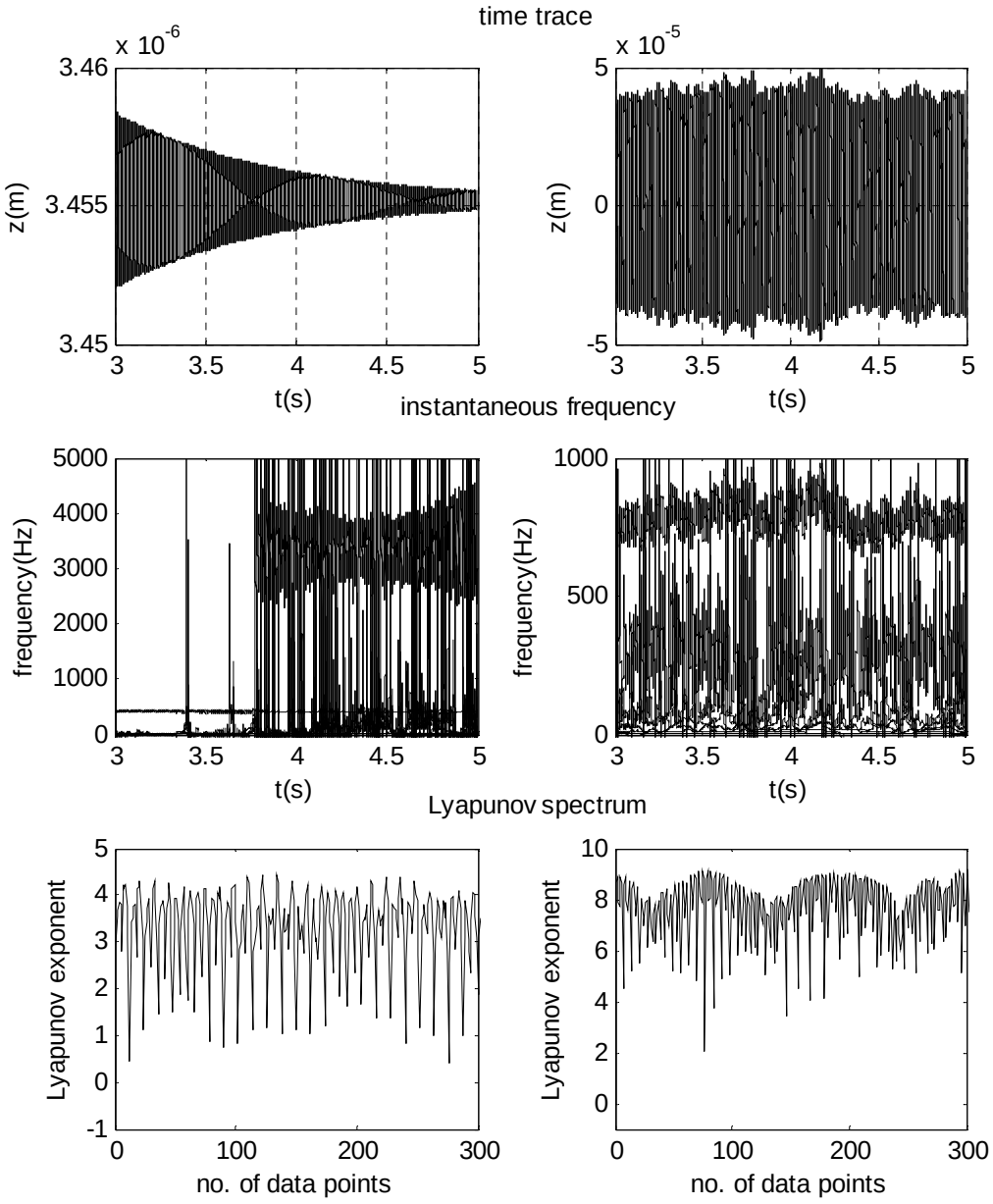

Fig. 10.16 Z- direction tool behavior for DOC = 1.83mm (left) and DOC = 1.84mm (right) at Ω = 1250rpm

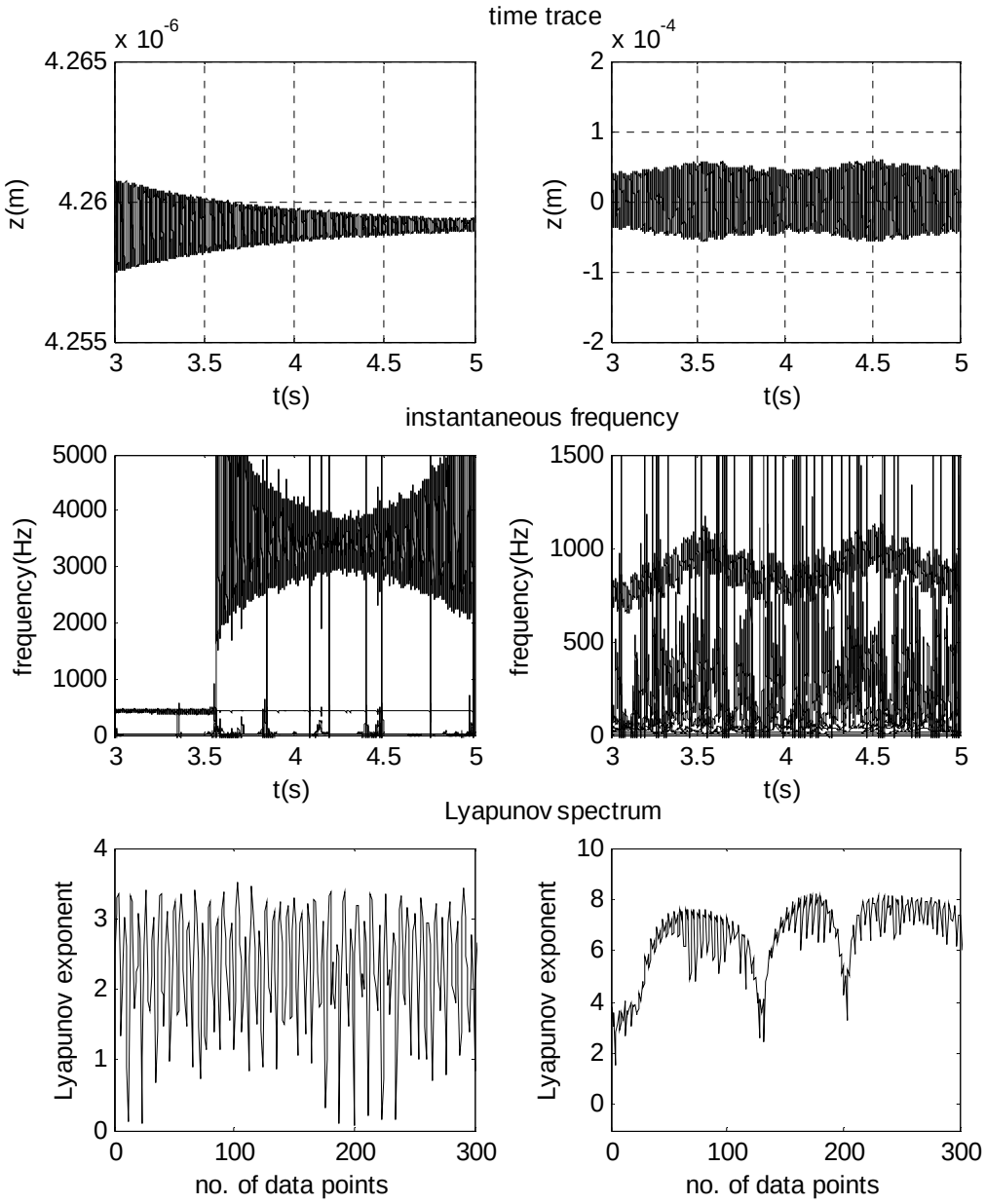

Fig. 10.17 Z- direction tool behavior for DOC = 2.21mm (left) and DOC = 2.22mm (right) at Ω = 1500rpm

Fig. 10.10 shows the workpiece behaviors at close to the critical DOC at Ω = 750rpm. It is seen that the workpiece vibrates with stability subject to DOC = 1.40mm, but becomes chaotic when DOC is increased to 1.45mm at the same speed. Zero and positive Lyapunov spectra clearly identify the two stages. The corresponding tool behavior is presented in Fig. 10.14. The time traces show random oscillations once DOC is increased from 1.40mm to 1.45mm. The corresponding Lyapunov spectra confirm the same. The instantaneous frequency shows broadband characteristics in the lower frequency region for the stable case. The frequency excited by the tool natural frequency stays unvaried with time. Unlike the 1.40mm case, when DOC is 1.45mm, the excited tool characteristic frequency varies in time. This frequency behavior can be seen in all the unstable plots of the tool in Figs. 10.14–10.17 (right column) using large DOCs.

When speed is increased to 1000rpm, the critical DOC also increases. Fig.10.11 shows the results of the workpiece vibrations corresponding to two different DOCs. It can be seen that the case corresponding to DOC = 1.75mm is very stable in both the time and frequency domains. On the other hand, having a positive Lyapunov spectrum and broadband frequency characteristics, the case with DOC = 1.78mm is an instability of chaos. The corresponding tool behaviors are found in Fig. 10.15. Similar to the case with DOC = 750rpm, violent oscillations, large vibration amplitudes and a positive Lyapunov spectrum signify an unstable state of tool motion at DOC = 1.78mm. Note that the response associated with the DOC that is only 0.03mm less than 1.78mm is one of stable.

Increasing spindle speed further to 1250rpm results in a stable state of motion, thus moving the instability margin up to the 1.83mm-1.84mm range (Fig. 10.12). Again, the associated time history, instantaneous frequency and Lyapunov spectrum of the tool all indicate a state of chaos for DOC = 1.84mm. This is in contrast with the case of DOC = 1.83mm whose zero Lyapunov spectrum indicates stability. However, the time-frequency characteristics of the DOC = 1.83mm case reveal that it is a bifurcated state. An increment of only one hundredth of a millimeter is enough to tip the stable cutting motion into dynamic instability. The tool responses in Fig 10.16 for the two DOCs convey a slightly different characteristic than the vibration results associated with the workpiece. Tool vibration amplitude is only several nanometers for the case with DOC = 1.83mm. The 0.01mm in increment induces chaotic responses of 0.1mm in vibration amplitude. The state of chaotic motion is verified the Lyapunov spectrum in Fig. 10.16. Unlike other cases considered, the instantaneous frequency shows that the tool vibrates with a frequency closer to the workpiece natural frequency at the lower DOC. This frequency component immerges after 3.8 seconds. The Lyapunov spectrum of positive exponents for this case indicates that the motion is unstable.

Fig. 10.13 shows the X- direction workpiece behaviors for DOC = 2.21mm and 2.22mm at Ω = 1500rpm. The time and frequency domain responses depict two different behaviors for the two DOCs. The Lyapunov spectrum for the lower DOC is not a straight line of zeros. It is an oscillation about zero, thus indicating that the motion is of a stable–unstable margin type. The tool behavior at this speed is comparable to the case in Fig. 10.17 where the speed was 1250rpm. The vibration amplitude grows more

than 10,000 times higher when DOC is increased by one hundredth of a millimeter from 2.21mm to 2.22mm. The instantaneous frequency for the lower DOC has a component of broadband characteristic at the workpiece natural frequency that appears after 3.5seconds. The Lyapunov spectra for both DOCs are also positive as is the case with Ω = 1250rpm. Using all the above cases in stable-unstable margin, the critical DOCs are determined for rough cutting at the various spindle speeds considered. Details will follow in the following subsection.

10.2.2 Comparison with Experimental Results

The critical DOCs that were explored in the previous subsection are compared with the experimental results in [11]. Experimentally found critical DOCs for cutting speeds in the range of 50 m/min to 300m/min are published in [11]. Using Eq. (4.1), the stability limits can be presented as the critical DOC for each corresponding cutting speed as in Table 10.1.

Table 10.1 Critical depth-of-cuts

Spindle speed / (rpm)	Cutting speed / (m/min)	Critical DOC / (mm)
750	94.7	1.40 – 1.45
1000	126.3	1.75 – 1.78
1250	157.8	1.83
1500	189.4	2.21

Fig. 10.18 illustrates a comparison of critical DOCs with experimental results subject to increasing speeds. It should be mentioned that the experimental data were taken for a short workpiece and thus the stiffness of the workpiece was higher than the modeled workpiece considered in the dissertation. It was established in previous sections that the workpiece dimensions and tool geometry affect cutting stability. However, the workpiece dimensions and tool geometry used for the research are different from the corresponding experimental setup in [11]. Still, the feed rate employed herein differs only by about 5% from those experiments. These differences would certainly contribute to the differences in stability limits.

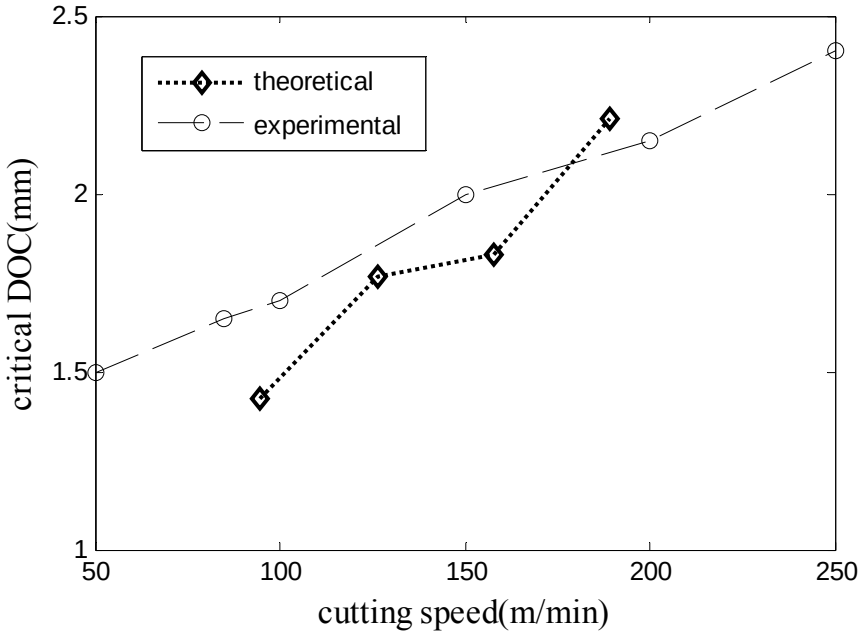

Fig. 10.18 Comparison of critical DOC with experimental data

It should be noted that the experimental results in [11] are different from the conventional stability lobes for the ranges of speed that are considered here. Contrary to one's intuition, experiments have proved that critical DOC increases with cutting speed. The machining model developed in Section 2 also suggests the same.

10.3 Stability in Fine Cuts

Cutting stability subject to DOCs less than 1.00mm is explored in this sub-section. Three different DOCs at 0.50mm, 0.75mm, and 0.90mm and four different spindle speeds at 750rpm, 1000rpm, 1250rpm, and 1500rpm are considered. The feed is 0.0965mm for all cases. All figures have three columns for time traces, instantaneous frequencies and Lyapunov spectrum. The four rows in the figures represent the results corresponds to four different speeds at a particular DOC.

10.3.1 Stability of the Workpiece

The followings considered X-direction workpiece vibrations for fine cutting. Fig. 10.19 shows the behavior of the case with DOC = 0.50mm at four different speeds. Time traces for all the four speeds seem similar and their corresponding Lyapunov spectra all demonstrate instability with positive exponents. The workpiece is excited by the tool natural frequency in all cases, except for the one at Ω = 1250rpm.

When DOC is increased to 0.75mm, the workpiece becomes more stable in Fig. 10.20. Similar to the case with DOC = 0.50mm, increasing spindle speed does not significantly alter the stability state of the workpiece for DOC = 0.75mm. All instantaneous frequency plots have a broad bandwidth component at 850Hz – 900Hz. This might be explained by the frequency-doubling of the tool natural frequency. In

addition, the Lyapunov spectra do not indicate clean-cut stability with zero exponents. But rather the exponents oscillate near zero and towards the negative side of the spectra. This can be considered as a marginal stable–unstable situation of the workpiece.

Fig. 10.21 demonstrates the workpiece behavior subject to DOC = 0.90mm. It can be seen that the workpiece is in a stable state of motion at this DOC. All the four instantaneous frequency plots illustrate similar types of bifurcated situation having whirling frequency and components other than the workpiece natural frequency. In all cases shown in Fig 10.21, one frequency is in between 450Hz – 600Hz and the other extra component is in the range of 1300Hz – 1400Hz. These frequency components do not vary with time or display broadband behaviors. The motion is periodic and stable, as is verified the same by the zero Lyapunov spectra. It is interesting to note that regardless of the speed in the range considered, the workpiece is dynamically unstable at DOC = 0.50mm. But it is marginally stable at DOC = 0.75mm and stable at DOC = 0.90mm.

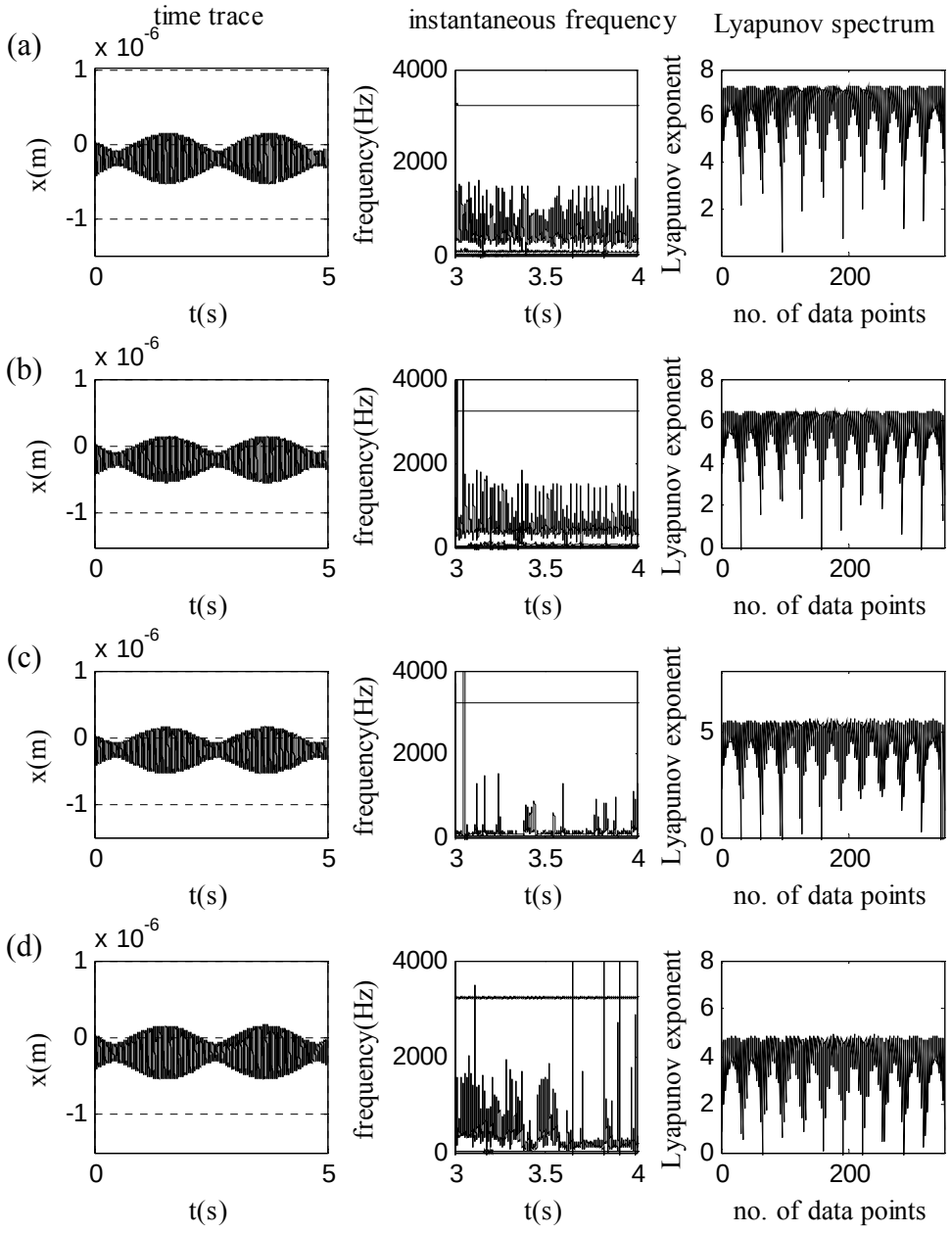

Fig. 10.19 X- direction workpiece behavior for DOC = 0.50mm at (a) Ω = 750rpm, (b) Ω = 1000rpm, (c) Ω = 1250rpm, and (d) Ω = 1500rpm

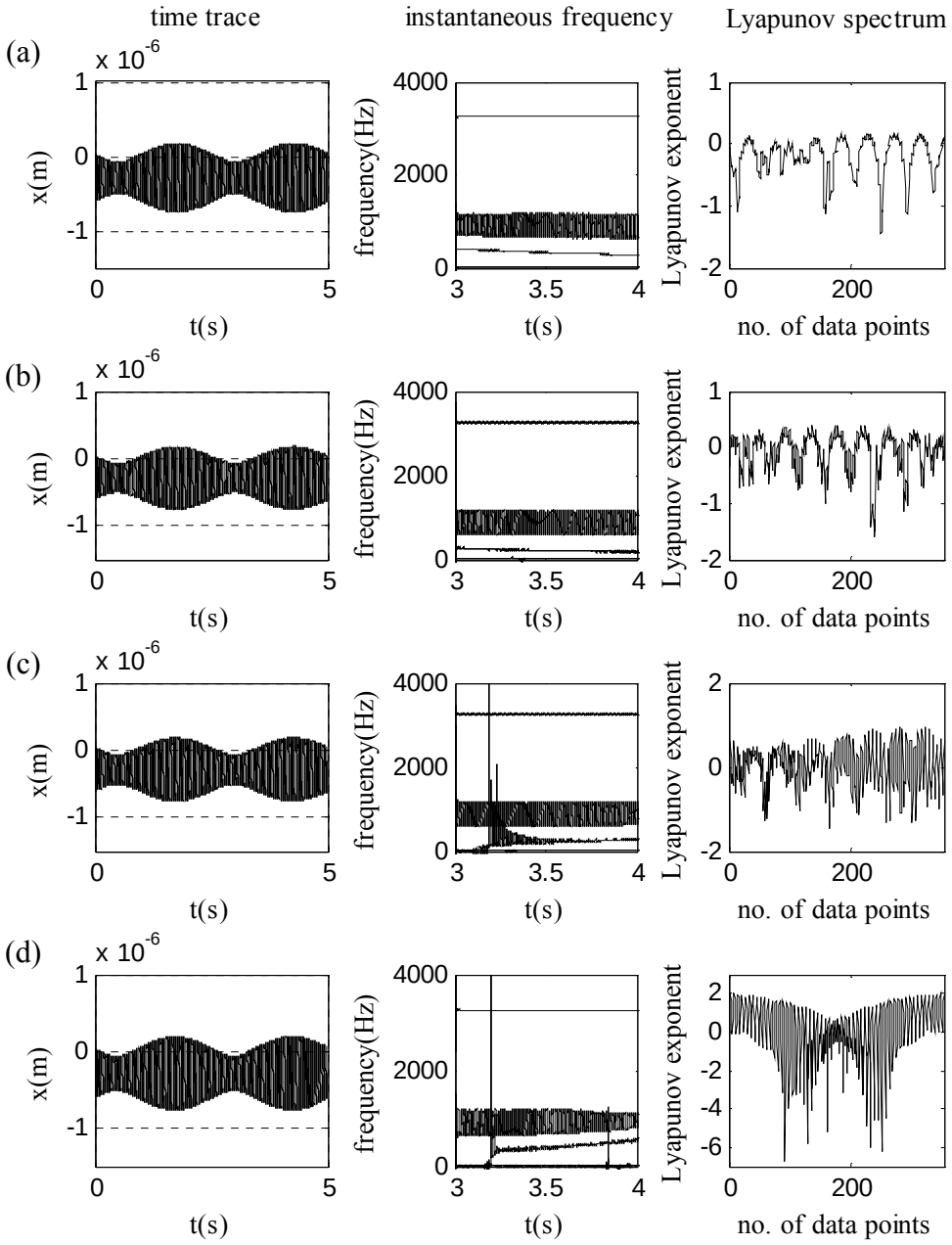

Fig. 10.20 X- direction workpiece behavior for DOC = 0.75mm at (a) Ω = 750rpm, (b) Ω = 1000rpm, (c) Ω = 1250rpm, and (d) Ω = 1500rpm

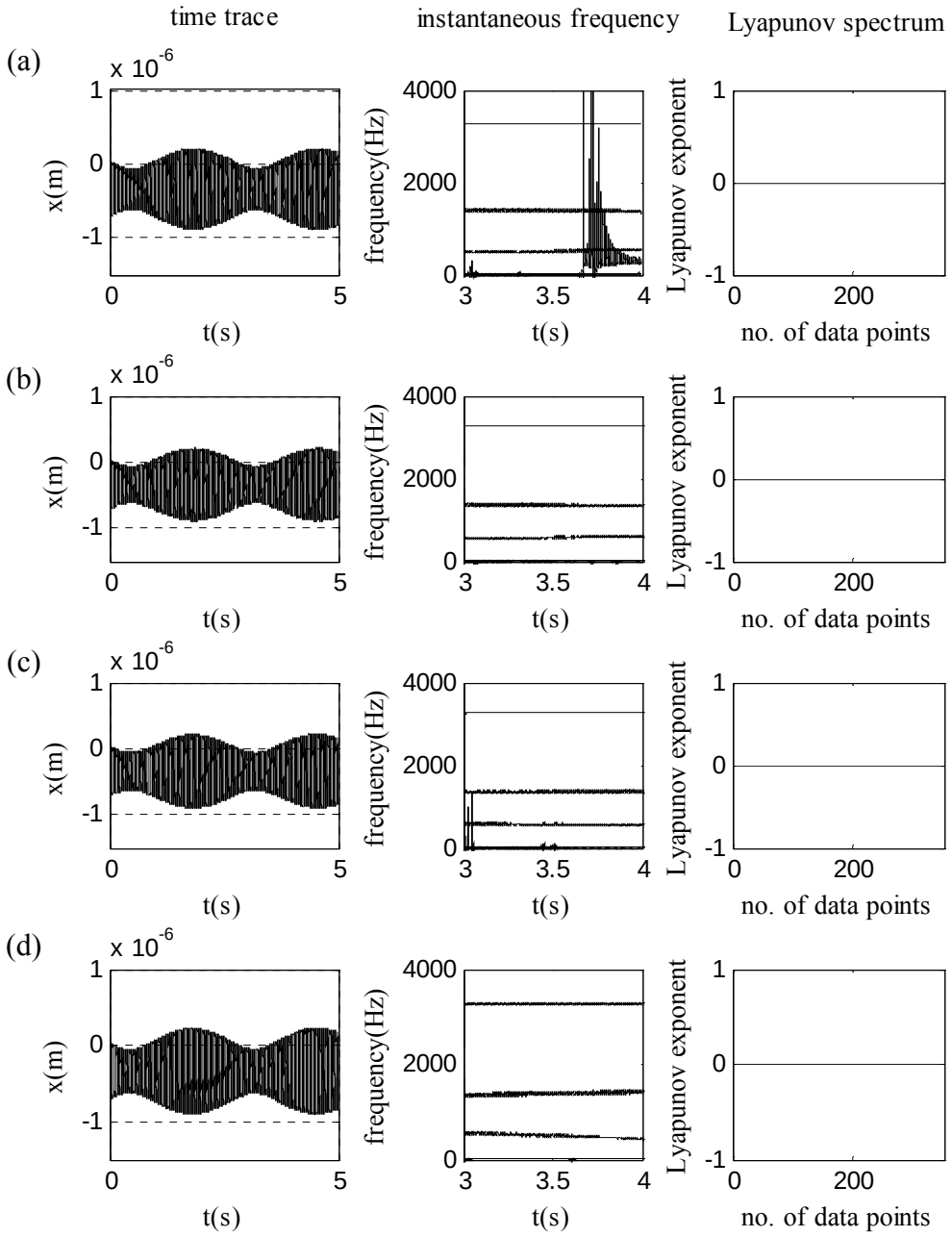

Fig. 10.21 X- direction workpiece behavior for DOC = 0.90mm at (a) Ω = 750rpm, (b) Ω = 1000rpm, (c) Ω = 1250rpm, and (d) Ω = 1500rpm

10.3.2 Stability of the Tool

The tool stability in Z-direction has been investigated in this subsection considering both time and time-frequency analysis as in pervious subsections. Fig. 10.22 shows the tool behavior for DOC = 0.50mm. It is noted that except for the 1250rpm case, all time traces look similar. In addition, the corresponding instantaneous frequency plots also show the same similarity having bifurcations only in the low frequency region without indicating any broadband behavior. When spindle speed is 1250 rpm in Fig 10.22(c), the tool is excited by the workpiece natural frequency and displays a broadband characteristic. Moreover, the associated Lyapunov spectrum indicates an unstable condition, while in all other cases the tool motion is stable with zero exponents.

When DOC is increased to 0.75mm, all speed cases display similar characteristics having very small vibration amplitudes and bifurcations in the instantaneous frequency plots (Fig. 10.23). However, all Lyapunov spectra demonstrate stable behaviors with zero exponents. Increasing DOC further to 0.90mm, two categories out of four different speeds in Fig. 10.24 are seen. The 750rpm and 1250rpm cases are alike, while 1000rpm and 1500rpm cases are comparable. Lyapunov spectra show that the 750rpm and 1250rpms cases are unstable, and the other two speed cases are stable. Many frequency components are also present in the 1000rpm and 1500rpm cases, despite that the system is stable according to the Lyapunov spectrums in Fig. 10.25.

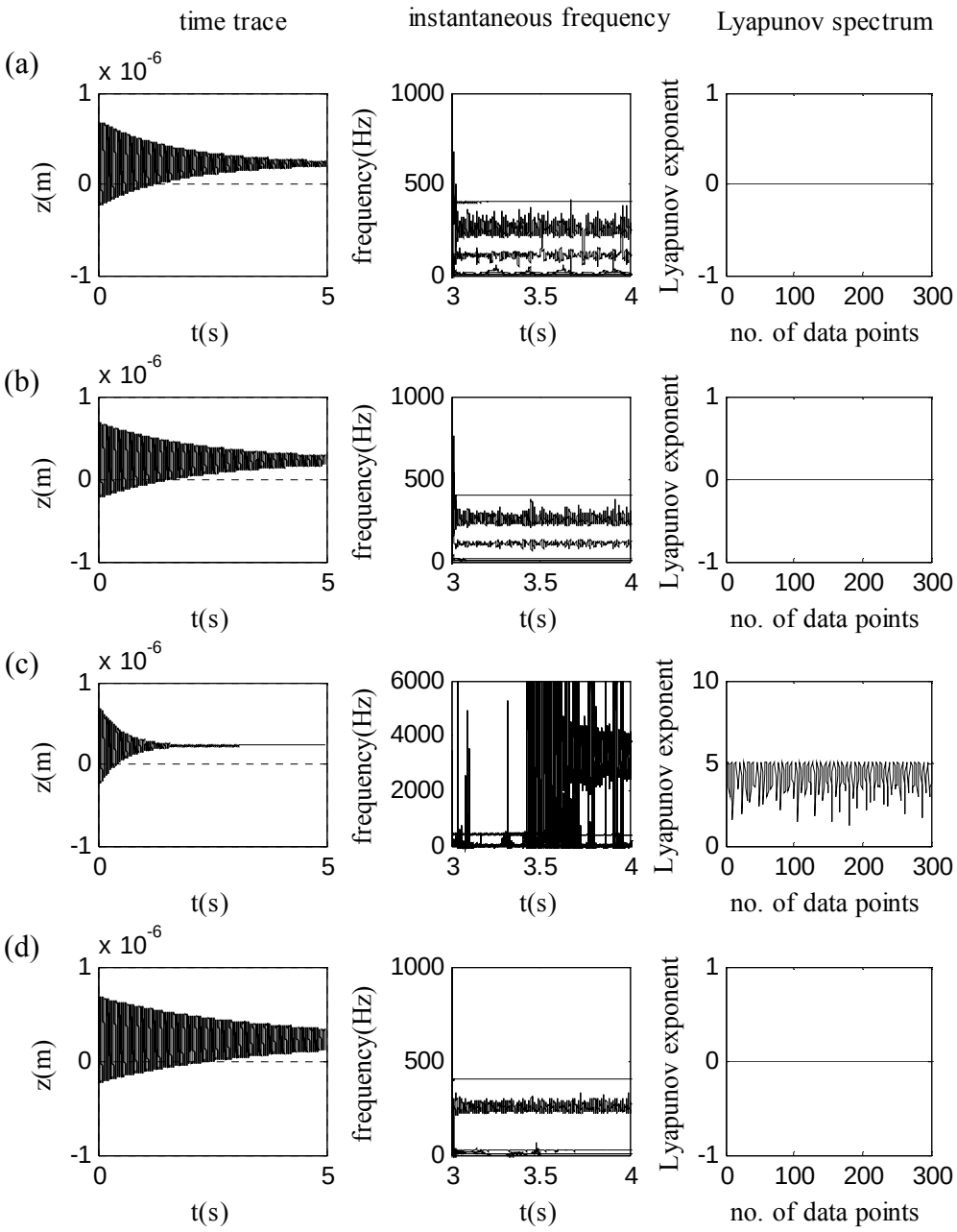

Fig. 10.22 Z- direction tool behavior for DOC = 0.50mm at (a) Ω = 750rpm, (b) Ω = 1000rpm, (c) Ω = 1250rpm, and (d) Ω = 1500rpm

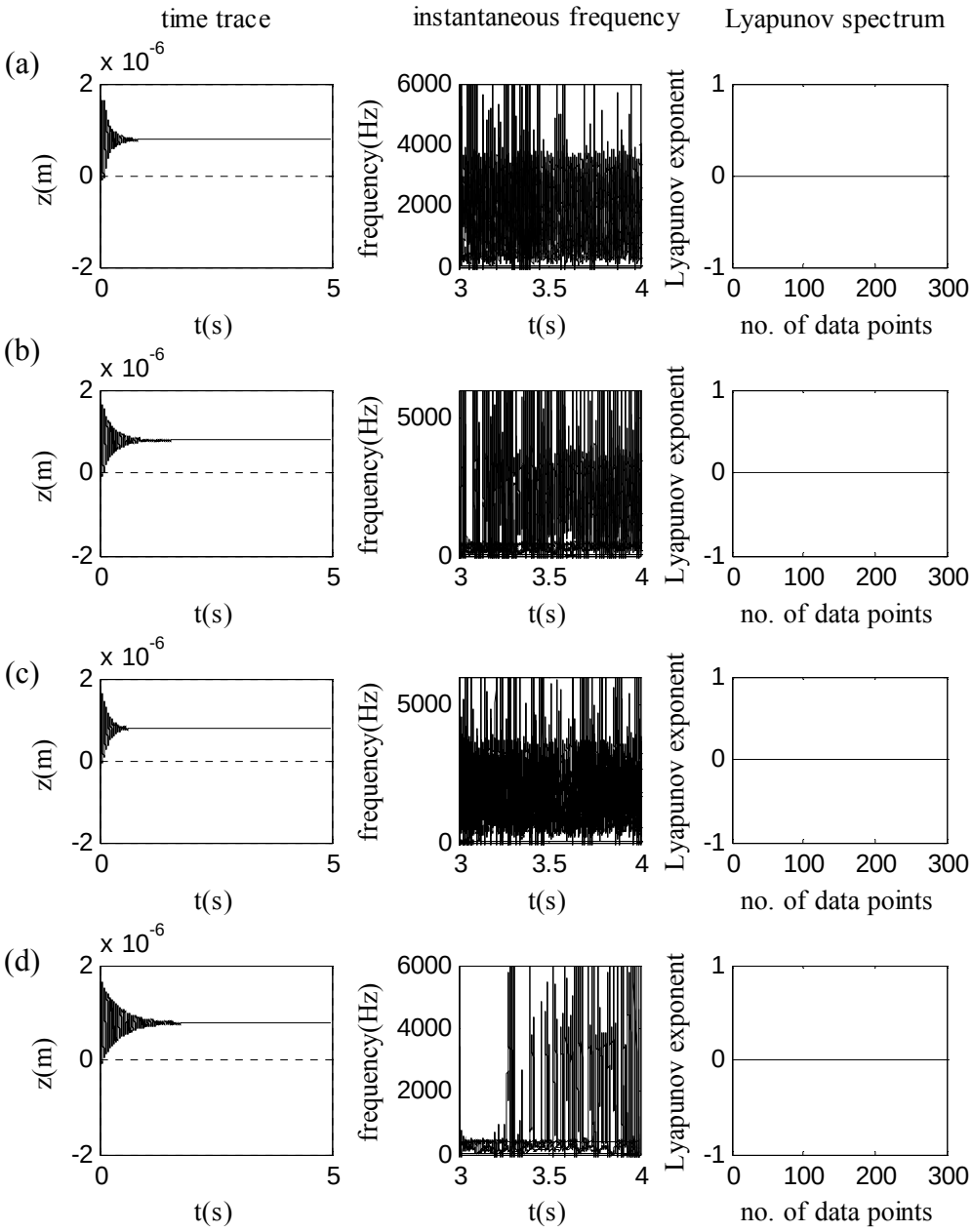

Fig. 10.23 Z- direction tool behavior for DOC = 0.75mm at (a) Ω = 750rpm, (b) Ω = 1000rpm, (c) Ω = 1250rpm, and (d) Ω = 1500rpm

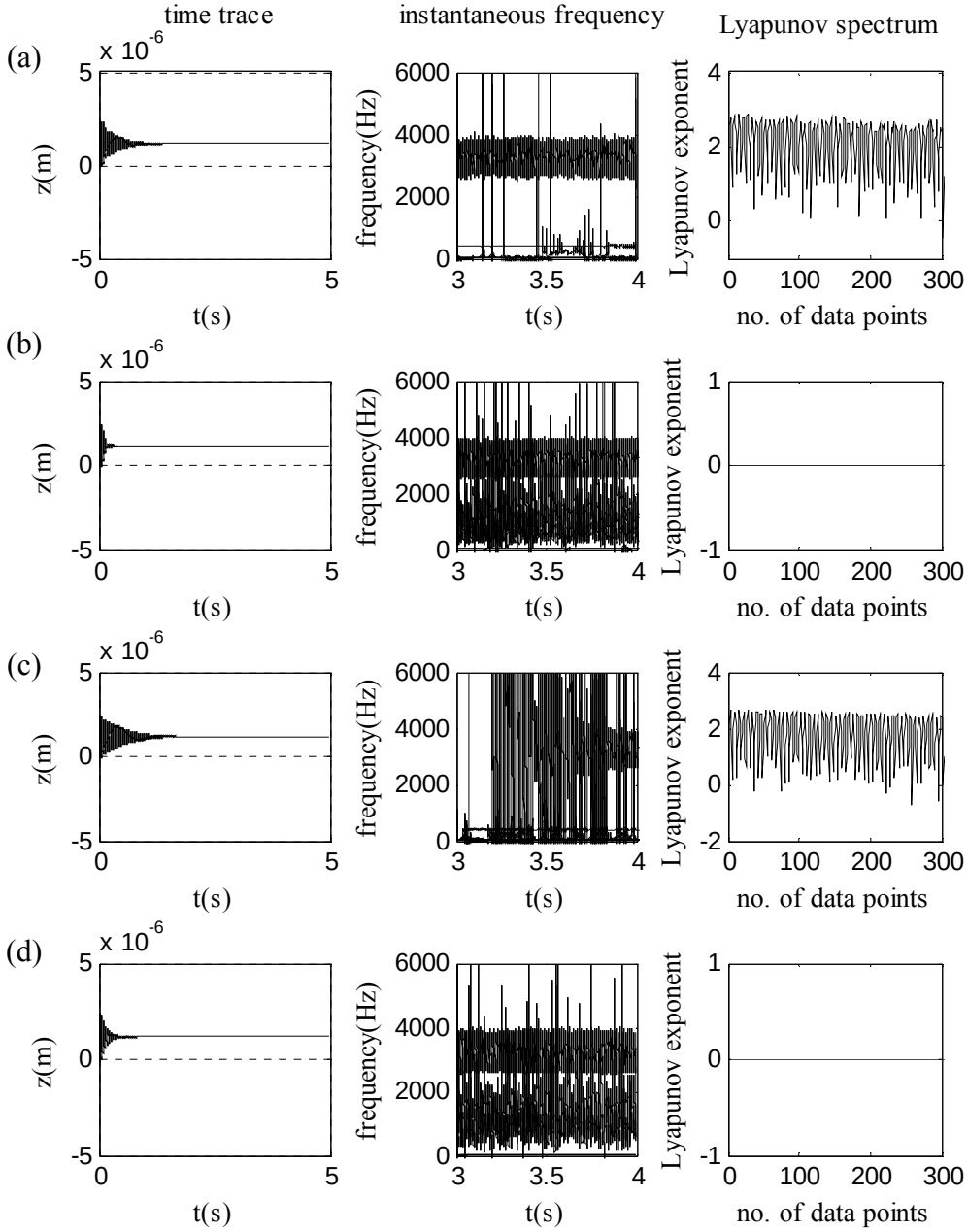

Fig. 10.24 Z- direction tool behavior for DOC = 0.90mm at (a) Ω = 750rpm, (b) Ω = 1000rpm, (c) Ω = 1250rpm, and (d) Ω = 1500rpm

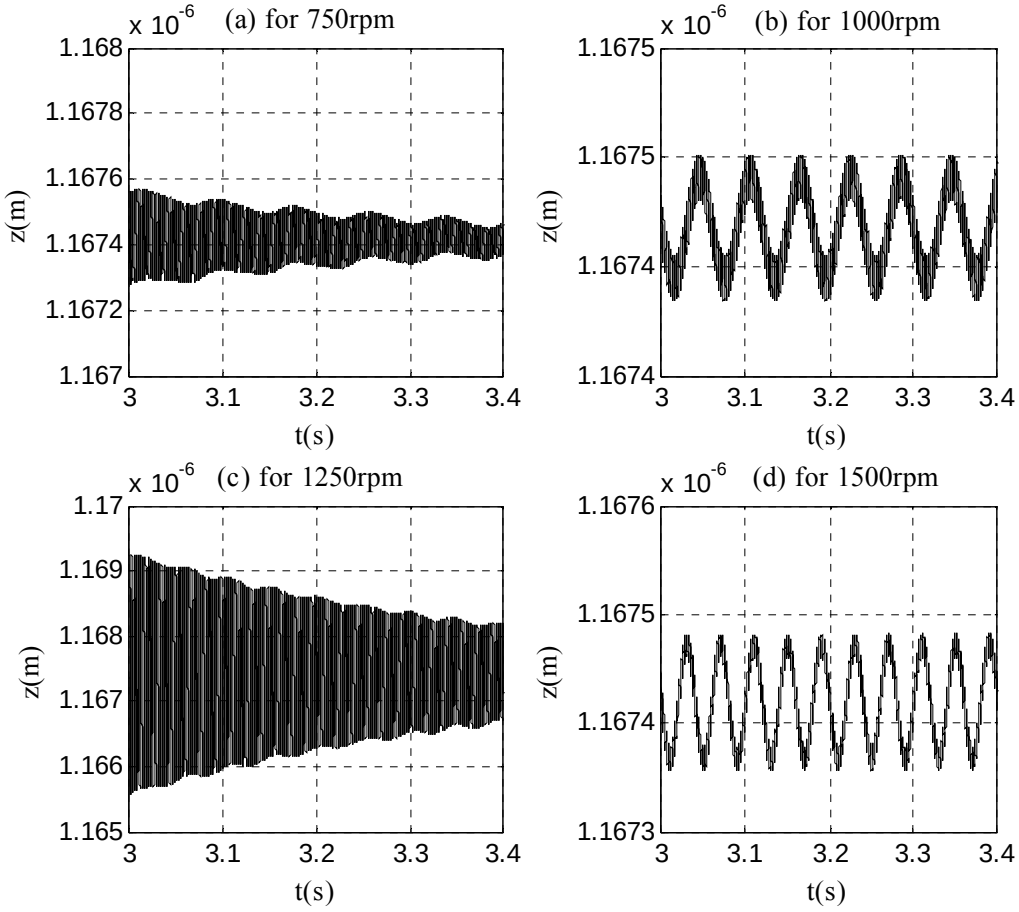

Fig 10.25 Time traces for tool vibrations between 3.0 and 3.4 seconds for 0.90mm DOC

10.3.2 Overall Stability of the System

Overall system stability can be determined by investigating the stable and unstable situations for the workpiece and the tool. The system is stable if both workpiece and tool demonstrate stable situations. If either of them displays instability, the system is unstable. Using this classification, system stability can be summarized as

in Table 10.2. Here the terms US, S, and MS stand for Unstable, Stable and Marginally Stable, respectively.

Table 10.2 System stability for fine cuts

	Spindle Speed / (rpm)			
DOC / (mm)	750	1000	1250	1500
0.90	US	S	US	S
0.75	MS	MS	MS	MS
0.50	US	US	US	US

Since the workpiece is unstable for all the speeds at DOC = 0.50mm, the system is unstable for the DOC. Moreover, the workpiece demonstrates stable–unstable situation for all four speeds considered and the tool shows highly bifurcated situations for all the cases when DOC = 0.75mm, thus making the system marginally stable. On the other hand, even though the workpiece is stable at DOC = 0.90mm for all four speeds, the tool is unstable for the 750rpm and 1250rpm cases. Thus the system is one of instability for these two cases.

10.4 Discussion

Machining stability study for rough cuts suggested that, for the speed range considered, low speeds imparted instability. However, bifurcated states could be staged in between with increasing speeds. Therefore it cannot be concluded that speed increase

would always result in stability. Using the presented cutting model, critical DOCs on the other hand were seen to increase with the increase of speed. It was shown that the observation was consistent with experimental data. It was noted that cutting force amplitude oscillations were determined by the nonlinearity of the force, not by speed increments. It was seen that both the tool and workpiece showed similar instability stages most of the times. However, when it was closer to the critical depth-of-cut, the tool reached instability first before the workpiece did. In contrast to this observation, when DOC is less than 1.00mm, most of the times when system was unstable, only the workpiece or the tool was unstable, but not both. There were few situations that both became unstable at the same time. It was noted that in all cases that the tool was unstable, the tool was excited by the workpiece natural frequency and displayed broadband behavior. However, not all cases in which the tool was excited by the workpiece natural frequency were unstable. On the other hand, almost in all cases in which the workpiece was unstable, the workpiece had a broadband frequency component near the tool natural frequency. This implies the importance of considering the workpiece-tool coupling effect in modeling cutting dynamics.

11. SUMMARY, CONTRIBUTIONS AND FUTURE WORK

11.1 Summary

A three dimensional nonlinear dynamic model for turning operation has been developed. The model incorporated regenerative effect, cutting force nonlinearity, tool nonlinearity, imbalance-induced whirling, and mass and stiffness reduction of the workpiece to realize simultaneous tool-workpiece vibrations. Model responses subject to whirling and without whirling were examined for various cases of cutting parameters including depth-of-cut, spindle speed, feed rate and tool geometry. Newmark's time integration scheme was employed in conjunction with Newton-Jacobi method to conduct numerical experiment. Stability analysis was carried out using instantaneous frequency and Lyapunov spectrum. The followings can be summarized based on the results presented and observations made in previous sections:

- Concerns over several major issues were raised and discussed; namely, neglecting workpiece vibrations in modeling turning operation, use of SDOF formulation for modeling cutting dynamics and significance of whirling and tool nonlinearity.
- The various responses of the presented 3D machining model were shown to agree favorably with experimental data established in literature.
- Negligence of workpiece vibrations will result in physically inadmissible results as discussed in Section 4.
- Workpiece dimensions impact cutting stability in a non-negligible way.

- Workpiece-tool coupling is significant in the proper interpretation of tool dynamics.
- The SDOF model overestimates machining stability by wrongly describing instability states as stable. The 1D model predicts stability limits that are higher than the stability limits determined by the 3D model. Use of SDOF models for studying cutting dynamics would inevitably generate erroneous, unreliable information.
- Whirling was found to contribute to machining stability and larger workpiece vibration amplitude.
- Whirling would affect tool dynamics only when high feed rates are considered. When critical depth of cut is reached and workpiece vibrates with instability, whirling becomes negligible.
- Responses of the linearized model disagree with real-world data. Consideration of nonlinearity in modeling machining process is crucial for understanding the underlying cutting dynamics.
- Tool geometry significantly affects cutting stability. Machining models disregarding tool geometry would miscomprehend cutting response.
- Feed rate has an impact on cutting stability. High feed could impart stability to fine turning operation. However, more elaborated investigations are needed to prove that high feed rate does contribute to higher stability limits.
- Critical DOC increases with increasing spindle speed. This observation agrees well in the qualitative sense with available physical data.

- Numerical results obtained in Section 5 supported that chatter could occur at low DOCs. This is in agreement with what [9] suggested and what [10] observed in testing. Thus, unlike conventional stability charts, the stability limits established in the work have both upper and lower stability regions.
- The stability margin for rough cuts using large DOCs can be separated from a line. However, for fine cuts using smaller DOCs there are different stability regions and no stability limits.
- Machining chatter can be associated with one of the four types of dynamic stability-instability scenarios: (1) both tool and workpiece are stable, (2) tool is stable when workpiece is unstable, (3) workpiece is stable when tool is unstable, and (4) both tool and workpiece are unstable.

11.2 Contributions and Future Work

The presented research has several contributions:

1. Provided a better understanding of the machining dynamics in turning operation involving material inhomogeneity induced whirling effect
2. Invalidated the use of linearized models for investigating machining instability
3. Signified the importance of simultaneous study of workpiece and tool vibrations
4. Provided the rationales to the technical community to reconsider the appropriateness of existing models
5. Identified critical depth of cuts for certain range of spindle speeds

6. Identified regions of tool chatter at small DOCs

In addition, the research has identified the proper analysis tools for characterizing the stability of nonlinear cutting dynamic. Insight developed through the research will help achieve higher machining productivity by producing quality products and reducing tool chatter related damages.

The presented model can be improved in several ways:

1. The model was derived for the ranges of parameters: 0.05mm < chip thickness < 0.15mm and 0.4mm < DOC < 2.5mm. Larger parameter ranges can be considered by modifying the appropriate model equations.
2. Normal and friction pressure components k_n and k_f were considered as functions of instantaneous chip thickness. However, some literature has reported that the two friction components also vary with cutting speeds. By using a series of experiments the relationship between these coefficients and cutting speed can be established. k_n and k_f can then be derived as functions of both instantaneous chip thickness and instantaneous cutting speed as an improvement.
3. The model addressed only one aspect of the complex machining process: cutting dynamics. It can incorporate cutting mechanics to account for the complex interactions between the tool and workpiece. The final model will have the various features outlined in Fig. 11.1. Note that the figure identifies four primary requirements needed to improve machining productivity and product quality.

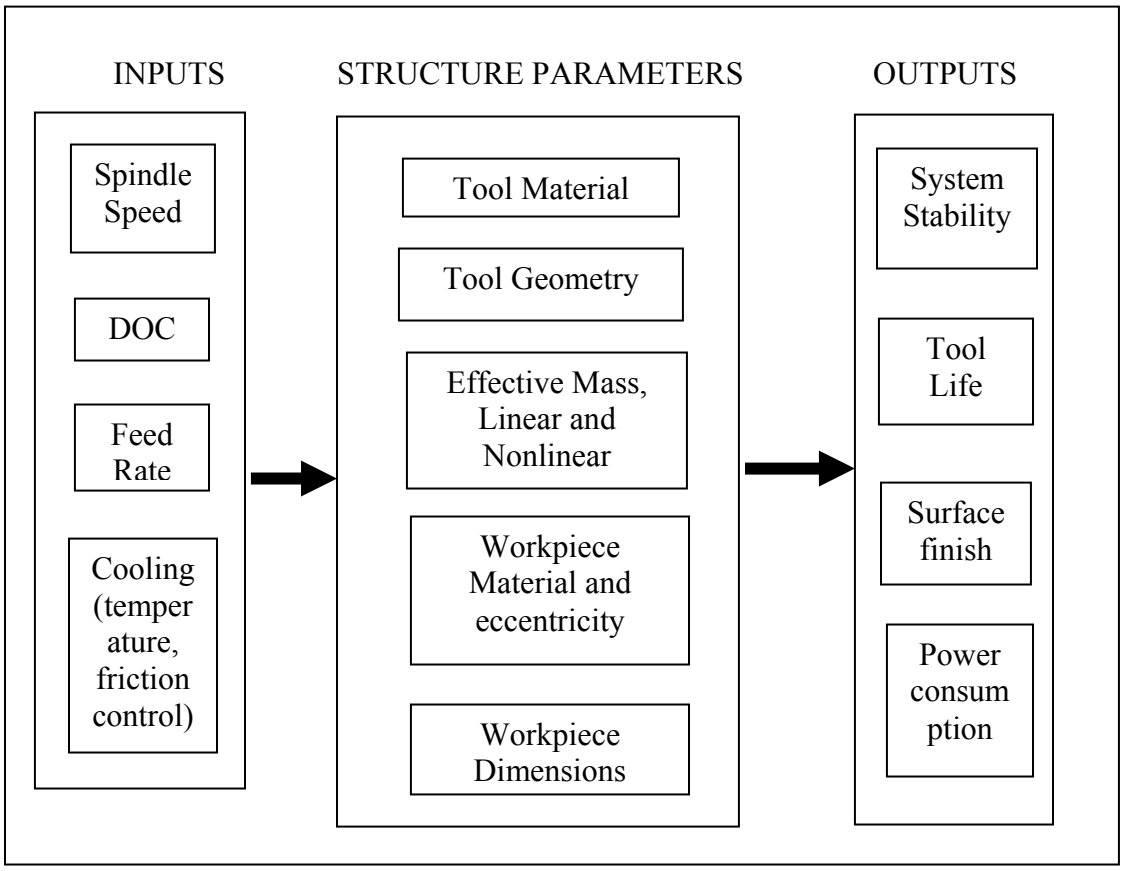

Fig 11.1 Future model

REFERENCES

1. Arnold, R. N., 1946, "The Mechanism of Tool Vibration in the Cutting of Steel," Proceedings of the Institution of Mechanical Engineering, **154**, pp. 267-284.

2. Statan, T. E. and Hyde, J. H., 1925, "An Experimental Study of the Forces Exerted on the Surface of the Cutting Tool," Proceedings of The Institution of Mechanical Engineering, **1**(2), pp.175-195.

3. Merit, H. E, 1965, "Theory of Self Excited Machine Tool Chatter: Contribution to Machine Tool Chatter," ASME Journals of Engineers for Industry, **84**, pp. 447-454.

4. Minis, I. and Yanushevsky, R., 1993, "A New Theoretical Approach for the Prediction of Machine Tool Chatter in Milling," ASME Journal of Engineering for Industry, **115** pp. 1-8.

5. Altintas, Y. and Budak, E., 1995, "Analytical Prediction of Stability Lobes in Milling," Annals of CIRP, **44**(1), pp. 357-362.

6. Chiou, Y.S., Chung, E. S., and Liang, S. Y., 1995, "Analysis of Tool Wear Effect on Chatter Stability in Turning," International Journal of Mechanical Sciences, **37**(4), pp. 391-404.

7. Schmitz T. and Donaldson R., 2000, "Predicting High-Speed Machining Dynamics by Substructure Analysis," CIRP Annals, **49**(1), pp. 303-308.

8. Clancy, B. E., and Shin, Y. C., 2002, "A Comprehensive Chatter Prediction Model for Face Turning Operation Including Tool Wear Effect," International Journal of Machine Tools and Manufacture, **42**, pp. 1035-1044.

9. Volger, M. P., DeVor R. E., and Kapoor, S. G., May 2002, "Nonlinear Influence of Effective Lead Angle in Turning Process Stability," Journal of Manufacturing Science and Engineering, **124**, pp. 473-475.

10. Rao, B. C., and Shin, Y. C., 1999, "A Comprehensive Dynamic Cutting Force model for Chatter Prediction in Turning," International Journal of Machine Tools and Manufacture, **9**(10), pp. 1631-1654.

11. Kim, J. S. and Lee, B. H., 1990, "An Analytical Model of Dynamic Cutting Forces in Chatter Vibration," International Journal of Machine Tools and Manufacture, **31**(3), pp. 371-381.

12. Moufki, A., Devillez, A., Segreti, M., and Dudzinski, D., 2006, "A Semi Analytical Model of Nonlinear Vibrations in Orthogonal Cutting and Experimental Validation," International Journal of Machine Tolls and Manufacture, **46**, pp.436-449.

13. Suh, C.S., Khurjekar, P. P., and Yang, B., 2002 "Characterization and Identification of Dynamic Instability in Milling Operation," Mechanical Systems and Signal Processing, **16**(5), pp. 829-848.

14. Deshpande, N. and Fofana, M. S., 2001 February, "Non-linear Regenerative Chatter in Turning," Robotics and Computer Integrated Manufacturing, **17**(1-2), pp 107-112.

15. Nayfeh A. H., Chin, C., and Pratt, J., Nov 1997, "Perturbation Methods in Non-linear Dynamics- Applications to Machining Dynamics," Journal of Manufacturing Science and Engineering, **119**, pp. 485-492.

16. Grabec, I., 1988, "Chaotic Dynamics of the Cutting Process," International Journal of Machine Tools and Manufacture, **28**(1), pp. 19-32.

17. Carrino, L., Giorleo, G., Polini, W., and Prisco, U., 2002, "Dimensional Errors in Longitudinal Turning Based on the Unified Generalized Mechanics of Cutting Approach, Part I: Machining Process Analysis and Dimensional Error Estimate" International Journal of Machine Tools and Manufacture, **42**(14), pp. 1517-1525.

18. Carrino, L., Giorleo, G., Polini, W., and Prisco, U., 2002, "Dimensional Errors in Longitudinal Turning Based on the Unified Generalized Mechanics of Cutting Approach, Part II: Three-dimensional Theory" International Journal of Machine Tools and Manufacture, **42**(14), pp. 1509-1515.

19. Jones, D. R. H., 1996, "Whirling Failure in a Woodworking Lathe," Engineering Failure Analysis, **3**(1), pp. 71-76.

20. Li, C.-J., Ulsoy, A. G., and Endres, W. J., 1998, "The Effect of Tool Rotation on Regenerative Chatter in Line Boring," Dynamics, Acoustics and Simulation, **98**, pp. 235-243

21. Grzesik, W., 1996, "A Revised Model for Predicting Surface Roughness in Turning," Wear, **194,** pp. 143-148.

22. Sahin, Y. and Motorcu, A.R., 2005, "Surface Roughness Model for Machining Mild Steel with Coated Carbide Tool," Materials and Design, **26**(4), pp. 321-326.

23. Thomas, M., Beauchamp, Y., Youssef, A. Y., and Masounave, J., 1996, "Effect of Tool Vibration on Surface Roughness during Lathe Dry Turning Process," Computers and Industrial Engineering, **31**(3-4), pp. 637-644.

24. Hanna, N. H. and Tobias, S. A., 1974, "Theory of Non-linear Regenerative Chatter," ASME Journal of Engineering for Industry, **96**, pp. 247-255.

25. Litak, G., 2002, "Chaotic Vibrations in a Regenerative Cutting Process," Chaos, Solutions, and Fractals, **13**(7), pp. 1531-1535.

26. Gouskov A. M., Voronov, S. A., Paris, H., and Batzer, S. A., 2002, "Nonlinear Dynamics of a Machining System with Two Independent Delays," Communications in Nonlinear Science and Numerical Simulations, **7**, pp 207-221.

27. Wiercigroch, M. and Cheng, A.H.D., 1997, "Chaotic and Stochastic Dynamics of Orthogonal Metal Cutting," Chaos, Solutions, and Fractals, **8**(4), pp 715-726.

28. Wang, X.S., Hu, J., and Gao, J.B., 2006, "Nonlinear Dynamics of regenerative Cutting Process – Comparison of Two Models," Chaos, Solutions, and Fractals, **29**(5), pp. 1219-1228.

29. Chandiramani, N. K. and Pothala, T., 2006, "Dynamics of 2DOF Regenerative Chatter during Turning," Journal of Sound and Vibration, **290**, pp. 448-464.

30. Lin, L.S. and Weng, C.I., 1990, "A Nonlinear Model for Cutting," International Journal of Machine Tools and Manufacture, **30**(1), pp. 53-64.

31. Asal, F. M. and Ulsoy, A.G., 2003, "Analysis of system of Linear Delay Differential Equations," Journal of Dynamic Systems, Measurements, and Control, **125**, pp. 215-223.

32. Vafaei, S., Rahnejat, H., and Aini, R., 2002, "Vibration Monitoring in High Speed Spindles using Spectral Analysis Techniques," International Journal of Machine Tools and Manufacture, **42**, pp. 1223-1234.

33. Berger, B. S., Minis, I., Harley, J., Rokni, M., and Papadopoulos, M., 1998, "Wavelet Based Cutting State Identification," Journal of Sound and Vibration, **213**(5), pp. 813-827.

34. Huang, N. E., Shen, Z., Long, S. R., Wu, M. C., Shih, H. H., et al, 1998, "The Empirical Mode Decomposition and the Hilbert Spectrum for Nonlinear and Non-stationary Time Series Analysis", Proceedings of the Royal Society of London Series A, **454,** pp.903 – 995.

35. Yang, B. and Suh, C. S., 2003, "Interpretation of Crack-Induced Rotor Nonlinear Response Using Instantaneous Frequency," Mechanical Systems and Signal Processing, **18**, pp. 491-513.

36. Wolf, A., Swift, J. B., Swinney, H. L., and Vastano, J. A., 1985, "Determining Lyapunov Exponents from a Time Series Analysis," Physica, **16D**, pp. 285-317.

37. Fang, N., 2002, "Machining with Tool-Chip Contact on the Tool Secondary Rake Face-Part I: New Slip Line Model", International Journal of Mechanical Sciences, **44,** pp. 2337-2354.

38. Fang, N., 2002, "Machining with Tool-Chip Contact on the Tool Secondary Rake Face-Part II: Analysis and Discussion", International Journal of Mechanical Sciences, **44,** pp. 2355-2368

39. Mei, Z., Yang, S., Shi, H., Chang, S., and Ehmann, K. F., 1994, "Active Chatter Suppression by On-Line Variation of the Rake and Clearance Angles in Turning – Principles and Experimental Investigations," International Journal of Machine Tools and Manufacture, **34**(7), pp. 981-990.

40. Fang, N. and Jawahir, S., 2002, "Analytical Predictions and Experimental Validation of Cutting Force Ratio, Chip Thickness, Chip Back Flow Angle in Restricted Contact Machining using the Universal Slip Line Model," International Journal of Machine Tools and Manufacture, **42**, pp. 681-694.

41. Lee, L.C., Lee, K.S., and Gan, C.S., 1989, "On the Correlation between Dynamic Cutting Force and Tool Wear", International Journal of Machine Tools and Manufacture, **29**(3), pp. 295-303.

42. Oraby, S.E. and Heyhurst, D.R., 1991, "Developments of Models for Tool Wear Force Relationships in Metal Cutting," International Journal of Machine Tools and Manufacture, **33**(2), pp. 125-138.

43. Chiou, R.Y. and Liang, S.Y., 2000, "Analysis of Acoustic Emission in Chatter Vibration with Tool Wear Effect in Turning", International Journal of Machine Tools and Manufacture, **40**, pp. 927-941.

44. Lee, J.H. and Lee, S.J., 1999, "One Step Ahead Prediction of Flank Wear using Cutting Force," International Journal of Machine Tools and Manufacture, **39**, pp. 1747-1760.

45. Chen, C. K. and Tsao, Y. M., 2006, "Stability Analysis of Turning Tailstock Supported Flexible Workpiece," International Journal of Machine Tools and Manufacture, **46**, pp. 18-25.

46. Olgac, N. and Hosek, M., 1998, "A New Perspective and Analysis of Machine Tool Chatter", International Journal of Machine Tools and Manufacture, **38**, pp. 783-798.

47. Moon, F. C. (editor), 1998, *Dynamics and Chaos in Manufacturing Processes,* John Wiley and Sons Inc., New York, NY.

48. Bathe, K, 1996, *Finite Element Procedures*, Prentice Hall, Inc., Englewood Cliffs, NJ.

49. Faires, J. D. and Burden, R. L., 1993, *Numerical Methods*, PWS-KENT Publishing Company, Boston, MA

50. Hopkins, R. B. 1970, *Design Analysis of Shafts and Beam,* Robert E. Krieger Publishing Company, Inc., Malabar, FL.

51. Mabie, H. H. and Ocvirk, F. W., 1975, *Mechanisms and Dynamics of Machinery,* John Wiley and Sons Inc., New York, NY.

52. Beachley, N. H. and Harrison, H. L., 1978, *Introduction to Dynamic System Analysis*, Harper and Row Publishers, New York, NY.

53. Ville, J., 1958, *Theory and Applications of the Notion of Complex Signals*, Translated by I. Seline in RAND Tech. Rept. T-92, RAND Corp., Santa Monica, CA.

54. Mandel, L., 1974, "Interoperation of Instantaneous Frequency," American Journal of Physics, **42**, pp. 840-846.

55. Boashash, B., 1992, "Estimating and Interpreting the Instantaneous Frequency" Proceedings of IEEE, **80**(4), pp. 520-568.

56. Loughlin, P. J. and Tacer, B., 1997, "Comments on the Interpretation of Instantaneous Frequency," IEEE Signal Processing Letters, **4**(5), pp. 123-125.

57. Oliveira, P.M. and Barroso, V., 1999, "Instantaneous Frequency of Multicomponent Signals" IEEE Signal Processing Letters, **6**(4), pp. 81-83.

58. Cohen, L., Loughlin, P., and Vakman, O., 1999, "On an Ambiguity in the Definition of the Amplitude and Phase of a Signal," Signal Processing, **79**, pp. 301-307.

59. Barkat, B., 2001, "Instantaneous Frequency Estimation of Nonlinear Frequency-Modulated Signals in the Presence of Multiplicative and Additive Noise," IEEE Trans. Signal Processing, **49**(10), pp. 2214-2222.

60. Yang, B. 2003, "On the Characteristics of Fault-Induced Rotor-Dynamic Bifurcations and Nonlinear Responses" Ph.D. Dissertation, Department of Mechanical Engineering, Texas A&M University, College Station.

61. Rosenstein, M. T., Collins, J. J., and De Luca, C. J., 1993, "A Practical Method for Calculating Largest Lyapunov Exponents from Small Data Sets," Physica D, **65**, pp. 117-134.

62. Casdagli, M., 1989, "Nonlinear Predictions of Chaotic Time Series," Physica D, **35**, pp. 335-356.

63. Briggs, K., 1990, "An Improved Method for Estimating Lyapunov Exponents of Chaotic Time Series," Physics Letters A, **151**(1), pp. 27-32.

64. Casdagli, M. and Eubank, S. (editors), 1992, *Nonlinear Modeling and Forecasting*, Addison-Wesley Publishing Company, New York, NY.

65. Benettin, G., Galgani, L., Giorgilli, A., and Strelcyn, J. M., 1980, "Lyapunov Characteristic Exponents for Smooth Dynamical Systems and for Hamiltonian Systems; A Method for Computing All of Them Part 1: Theory" Meccanica, **15**, pp. 9-20.

66. University of Southern California, Dynamics and Controls Group Home Page, http://www-scf.usc.edu/~vonbrem/home.html, January 16th 2006 (accessed on).

67. Sprott, J. C. and Rawlands, G., University of Wisconsin-Madison, Chaos Data Analyzer, The Academic Software Library, http://sprott.physics.wisc.edu/cda.htm, January 16th 2006 (accessed on).

68. Free Software Foundation, Inc., Boston, Massachusetts, TSTOOL Home Page http://www.physik3.gwdg.de/tstool/, January 16th 2006 (accessed on).

69. Wolf, A., Swift, J. B., Swinney, H. L. and Vastano, J. A., 1985, Determining Lyapunov Exponents from a Time Series," Physica D **16**, pp. 285-317.

70. Tjahjowidodo, T., Al-Bender, F. and Brussel, H. V., 2005, "Quantifying Chaotic Responses of Mechanical Systems with Backlash Component," Mechanical Systems and Signal Processing, Available online 7 November 2005

71. Enescu B., Ito K., Radulian M., Popescu E., and Bazacliu O., 2005, "Multifractal and Chaotic Analysis of Vrancea (Romania) Intermediate-depth Earthquakes: Investigation of the Temporal Distribution of Events," Pure and Applied Geophysics, **162**, pp. 249-271.

72. Childs T. H. C., Maekawa, K., Obikawa, T., and Yamane, Y., 2000, "*Metal Machining: Theory and Applications*", Arnold Publishers, London, Great Britain.

73. Michigan Technological University's Turning Information center, http://www.mfg.mtu.edu/cyberman/machining/trad/turning/turn.html, February 09th 2006 (accessed on).

74. Trent, E. M. and Wright, P. K. 2000, *"Metal Cutting: Fourth Edition"* Butterworth Heinemann, Boston, MA.

VITA

Ms. Achala Viomy Dassanayake was born in Kandy, Sri Lanka. In March 1993, she enrolled as a freshman at University of Peradeniya, Sri Lanka and completed the degree of Bachelor of Science in Production Engineering in July 1997. After having two years working experience as an instructor and a production engineer, Ms. Dassanayake was admitted into the Mechanical Engineering M.S. program at Texas A & M University in August 1999. She completed her M.S. degree in December 2001 and subsequently in August 2006 was conferred a doctoral degree from the same engineering program. Her research interests are in modeling dynamical systems, linear and nonlinear vibration analysis, machining operations and manufacturing and design.

Ms. Achala V. Dassanayake can be reached at V.C. 191, Ampitiya, 20160, Sri Lanka, or via email at achalatamu@yahoo.com.